ADVANCED DESIGN EVALUATION OF PLANAR STEEL FRAMES COMPOSED OF GENERAL NONPRISMATIC I-SECTION MEMBERS

A Dissertation
Presented to
The Academic Faculty

by

Oğuzhan Toğay

In Partial Fulfillment
of the Requirements for the Degree
Doctor of Philosophy in the
School of Civil and Environmental Engineering

Georgia Institute of Technology
December 2018

ADVANCED DESIGN EVALUATION OF PLANAR STEEL MEMBERS AND FRAMING SYSTEMS

Approved by:

Dr. Donald W. White, Advisor
School of Civil and Environmental Engineering
Georgia Institute of Technology

Dr. Glaucio Paulino
School of Civil and Environmental Engineering
Georgia Institute of Technology

Dr. Arash Yavari
School of Civil and Environmental Engineering
Georgia Institute of Technology

Dr. Barry Goodno
School of Civil and Environmental Engineering
Georgia Institute of Technology

Dr. Dewey H. Hodges
School of Aerospace Engineering
Georgia Institute of Technology

Date Approved: October 29, 2018

To Elif, for all her love and support

ACKNOWLEDGEMENTS

I would like to dedicate this dissertation to my precious wife Elif, who is the most valuable person of my life. I also would like to thank my family that has supported me throughout this time. I wish to express my deepest gratitude for the guidance provided by my advisor, Dr. Donald White. I am deeply indebted to him for his support and patience, and for the tremendous amount of time and effort he has dedicated to mentoring this thesis work. I could not have imagined having a better advisor and mentor for my Ph.D. study.

I also wish to thank the other members of my committee, Dr. Arash Yavari, Dr. Glaucio Paulino, Dr. Dewey H. Hodges and Dr. Barry J. Goodno. Their comments and suggestions have been very helpful.

I wish to thank all my fellow students- Ryan, Ajinkya, Lakshmi, Woo Yong, Thanh, Evan, Esmaeel and Ajit for their help and support.

I would like to also thank to Turkish Ministry Education for giving me the opportunity to have my education in this level.

TABLE OF CONTENTS

LIST OF TABLES

LIST OF FIGURES

LIST OF SYMBOLS AND ABBREVIATIONS

A Gross cross-sectional area

A_e Effective cross-section area corresponding to a given axial compression force, accounting for plate local buckling effects

A_g Gross cross-sectional area

C_b Beam moment gradient and load height factor

C_w Warping constant

D_{cT} Depth of the web in compression

D_{cp} Depth of the web in compression for the fully-plastic cross-section

E Modulus of elasticity of steel, taken equal to 29000 ksi

G Shear modulus of elasticity of steel, taken equal to 11200 ksi

F_L Magnitude of flexural stress in the compression flange at which flange local buckling or lateral torsional buckling is taken to be influenced by yielding in the AISC Specification

F_{cr} Column critical buckling stress

F_e Member internal axial compression stress at incipient elastic buckling of the member or structural system

F_{el} Elastic local buckling stress

F_y Specified minimum yield stress

F_{yc} Specified minimum yield stress of the compression flange

I Moment of inertia in the plane of bending

I_x Moment of inertia about the major principal axis

I_y Moment of inertia about the minor principal axis

I_{yc} Moment of inertia of the compression flange about the axis of the web

J St. Venant torsional constant

K Column or beam effective length factor

L Member length

L_b Member unbraced length between the braced points

L_p Prismatic beam unbraced length limit within which the AISC nominal lateral torsional buckling (LTB) resistance under uniform bending is equal to the plateau resistance $M_{max.LTB}$

L_r Prismatic beam unbraced length limit beyond which the nominal AISC lateral torsional buckling (LTB) resistance is taken as the theoretical elastic LTB resistance

M_e Elastic lateral torsional buckling moment of the member for the case of zero axial compressive force

$M_{e\tau}$ Member maximum buckling moment equal to $\tau_{ltb} M_{e\tau}$

M_{max} Largest potential moment that can be developed in the beam cross-section considering the three potential governing limit states of compression flange yielding, compression flange local buckling, and tension flange yielding

$M_{max.FLB}$ Largest potential moment that can be developed in the beam cross-section considering only the compression flange local buckling limit state

$M_{max.LTB}$ Largest potential moment that can be developed prior to lateral torsional buckling for sufficiently short member lengths, considering only the lateral torsional buckling limit state; commonly referred to as the LTB "plateau resistance," and referred to in the AISC Specification as the limit state of yielding or compression flange yielding

$M_{max.TFY}$ Largest potential moment that can be developed in the beam cross-section considering only the tension flange yielding limit state

M_n Member nominal flexural strength

M_p Cross-section plastic bending moment

M_u Cross-section internal moment corresponding to a given ASCE LRFD load combination

M_{yc} Moment at nominal yielding of the extreme fiber of the compression flange

M_{ycT} Moment at first yielding of the compression flange

P_e Member internal axial compression force at incipient elastic buckling of the member or structural system

$P_{e\tau}$ Member axial force equal to $\tau_a P_e$

P_n Member nominal axial resistance

P_u Cross-section internal axial load corresponding to a given ASCE LRFD load combination

P_y Cross-section yield axial load, equal to $A_g F_y$

P_{ye} Yield axial load based on the effective cross-section area, taken equal $A_e F_y$

Q_x First moment of the gross cross-sectional area about the reference axis of the cross-section

R_b Cross-section bend buckling strength reduction factor, AASHTO (2015) notation, represented by the symbol R_{pg} in the AISC Specification

R_h Hybrid girder factor from AASHTO (2015)

R_{pc} AISC LRFD web plastification factor, or effective plastic section modulus considering web slenderness effects

S_x Elastic section modulus

S_{xc} Elastic section modulus to the extreme fiber of the compression flange for major-axis bending

SRF Stiffness reduction factor employed for the buckling analysis

UC Unity check value with respect to the cross-section maximum strength

X Cross-section major-axis flexural to St. Venant torsional property ratio, taken as $\sqrt{S_{xc}h_o / J}$

Y Intermediate factor used in calculating τ_{ltb} for compact and noncompact web I-sections

a Distance between the neutral axis and the center of the compression flange

b_f Width of flange

d Full nominal depth of the cross-section

f Member axial stress equal to $\Gamma P_u / A_e$

h Clear distance between the flanges less the fillet radius for rolled I-sections; clear distance between the flanges for welded I-sections

h_c Twice the distance from the centroid of the cross-section to the inside face of the compression flange less the fillet radius for rolled I-sections, and to the inside face of the compression flange for welded I-sections

h_o Distance between the flange centroids

m normalized cross-section moment $\Gamma M_u / \phi_b M_{yc}$

r_t radius of gyration of the compression flange plus one-third of the web area in compression due to the application of major-axis bending moment alone

Γ Applied design load scale factor

ΓM_u Cross-section internal moment corresponding to a given value of the load scale factor Γ

ΓP_u Cross-section axial force corresponding to a given value of the load scale factor Γ

β_T Provided torsional bracing stiffness

β_{br} Provided lateral bracing stiffness

β_x Cross-section monosymmetry factor

β_i Ideal bracing stiffness, defined as the bracing stiffness at which the member or structure and its bracing system buckle at the required design load

ϕ AISC LRFD resistance factor on bracing stiffness, equal to 0.75

ϕ_b AISC LRFD resistance factor for flexure

ϕ_c AISC LRFD resistance factor for axial compression

γ Eigenvalue obtained from the buckling analysis, equal to the multiple of the current loading corresponding to buckling, given the stiffness properties associated with the current loading state

τ_a Column inelastic stiffness reduction factor not including the additional factors 0.9 x 0.877 x A_e/A_g

τ_b Stiffness reduction factor applied to the member flexural rigidity for a second-order load-deflection analysis per the AISC Direct Analysis Method

τ_{ltb} Beam lateral torsional buckling stiffness reduction factor not including the additional factors $0.9R_b$

ζ Angle of the force point within the normalized x-y interaction plot of the cross-section axial and moment strength ratios

λ_{rw} Noncompact web slenderness limit

M_p Plastic Moment

R_b Web bend buckling strength reduction factor

R_h Hybrid Factor

UC Unity Check

Q_x First moment of the area about the reference axis of the cross-section

r_t Effective radius of gyration for lateral-torsional buckling

INBA Inelastic Nonlinear Buckling Analysis

SRF Stiffness Reduction Factor

TFY Tension Flange Yielding

FLB Flange Local Buckling

DM Direct Analysis Method

LTB Lateral Torsional Buckling

TWOS Thin-Walled Open-Section

SUMMARY

This research provides a new comprehensive approach for the design of structural steel members and framing systems via an Inelastic Nonlinear Buckling Analysis (INBA) employing column, beam and beam-column inelastic stiffness reduction factors derived from the ANSI/AISC 360 Specification. The resulting procedure provides a relatively rigorous check of member and frame design resistances accounting for member cross-section double- or single-symmetry, nonprismatic member geometry, continuity effects across braced points, as well as lateral and/or rotational restraint from other framing including a wide range of types and configurations of stability bracing. With this approach, no separate checking of the corresponding Specification member stability design resistance equations is required. The buckling analysis captures these resistances. No calculation of effective length (K) factors and moment gradient and/or load height (C_b) factors, is necessary. The buckling analysis directly captures the fundamental mechanical responses associated with these design strength factors. This approach is coupled with the AISC Direct Analysis Method (the DM), for calculation of pre-buckling displacement effects, to fully satisfy the stability design requirements of the AISC Specification. Member cross-section based strength limit states are checked, given the internal forces calculated using the AISC DM requirements. The key concepts of this advanced design evaluation approach are developed, and a variety of applications of the method are demonstrated. Results from the recommended approach and from routine application of the DM are compared to results from test simulations satisfying the requirements of Appendix 1.3 of the AISC Specification.

Procedures are developed to solve for the load level corresponding to the most critical buckling or cross-section strength limit state of the ANSI/AISC 360 Specification. From prior research as well as from the validation studies conducted in this work, it is observed that the Flange Local Buckling (FLB) and Tension Flange Yielding (TFY) limit states in Chapter F of the ANSI/AISC 360 Specification tend to underestimate the true I-section member flexural resistances as the web and/or the compression flange become increasingly slender. This research develops an improved approach for calculation of the resistances corresponding to these limit states, considering the development of the spread of yielding in flexural tension (TFY) using mechanics of materials concepts, and accounting for the cross-section plate post-buckling resistance based on the unified effective width approach from Chapter E of the AISC Specification for FLB limit states.

CHAPTER 1. INTRODUCTION

Within the context of the Effective Length Method of design (the ELM), engineers have often calculated inelastic buckling effective length (K) factors to achieve a more accurate and economical design of columns (Yura, 1971; Disque, 1973; Hajjar & White, 1997). This process involves the determination of a stiffness reduction factor, τ, which captures the loss of rigidity of the column due to the spread of plasticity, including initial residual stress effects, as a function of the magnitude of the column axial force. Several different τ factor equations are in use in practice, but there is only one that fully captures the implicit inelastic stiffness reduction associated with the AISC column strength curve. This tau factor typically is referred to as τ_a. What many engineers do not realize is that the ELM does not actually require the calculation of K factors at all. The column theoretical buckling load can be calculated directly and used in the design equations rather than being determined implicitly via the use of K.

Furthermore, if the stiffness reduction factor, SRF = 0.9 x 0.877 x τ_a, is incorporated within a direct buckling analysis, the calculations may be set up such that, if the member or structure buckles at a given multiple of the required design load, ΓP_u in Load & Resistance Factor Design (LRFD), the load ΓP_u is equal to the factored design strength $\phi_c P_n$. If the load multiplier Γ corresponding to the buckling load is greater than 1.0, with the column stiffnesses calculated based on 0.9 x 0.877 x τ_a, the member or structure satisfies the AISC Specification column strength requirements without the need for further checking. The column strength requirements are inherently included in the buckling calculations.

The above approach can be applied not only to account for column end rotational restraint from supports or another structural framing, but also it can be employed to directly evaluate the column strength given the modeled stiffness of any type or combination of bracing. Furthermore, since the bracing stiffness requirements of the AISC Specification Appendix 6 are based on multiplying the *ideal* bracing stiffness, which is the bracing stiffness necessary to achieve a column buckling strength equal to the required column axial load, by a factor of $2/\phi = 2/0.75$ in LRFD, a buckling analysis that incorporates the column τ_a factor(s) can be used as a more rigorous method to design column stability bracing. Even more exciting and powerful is that the above approach can be extended to the member and stability bracing design of beams and beam-columns.

In design, these Stiffness Reduction Factors can be used to determine the strength of the desired members or systems. An Inelastic Nonlinear Buckling Analysis (INBA) that uses these SRFs streamline the evaluation of member stability while also providing greater rigor. This is particularly the case for general non-prismatic members with doubly- or singly-symmetric cross-sections, and subjected to complex bracing conditions (for instance beam-columns with bracing along only one flange). INBA involves a geometric nonlinear analysis of a planar structure for design loads applied within its plane, which captures in-plane pre-buckling displacement effects, combined with a general three-dimensional buckling analysis to capture predominantly out-of-plane member and system buckling resistances. While INBA is used to design for member and/or structural system buckling, separate cross-section strength checks of the Specification (AISC 2016) limit states are conducted directly given the second-order internal forces determined from the planar geometric nonlinear analysis. Tension Flange Yielding, Compression Flange Local

Buckling, member shear strengths, etc. can be checked on a cross-section basis while the INBA evaluates the member and system stability limit states. The load level associated with the most critical limit state defines the capacity of the structure.

The Flange Local Buckling (FLB) and Tension Flange Yielding (TFY) limit states in Chapter F of the ANSI/AISC 360 Specification (AISC 2016) tend to underestimate I-section member flexural resistances as the web and/or the compression flange become increasingly slender (Toğay and White 2018). The characterization of FLB only considers the compression flange buckling strength without accounting for its reserve postbuckling capacity. The FLB limit state check can be improved by implementing a form of the unified effective width approach, which recognizes the postbuckling resistance of slender flange elements. For the TFY limit state, the current equations limit the moment capacity of singly-symmetric slender-web I-section members with $S_{xt} < S_{xc}$ to the first yield of the tension flange, where S_{xt} and S_{xc} are the elastic section moduli to the tension and compression flanges respectively. However, the actual cross-section typically is able to develop extensive yielding of the tension flange and the tension region of the web. For the TFY limit state, simple calculations can be configured from mechanics of materials concepts, recognizing the ability of the region in flexural tension to develop extensive spread of yielding. These calculations eliminate the conservatism of the TFY equations while accurately characterizing the associated member structural stability.

In light of above information, the primary objectives of this research are:

1) Development of beam and beam-column stiffness reduction factors (SRF) for inelastic buckling analysis. The stiffness reduction factor developed from the AISC

specification column strength curve has been used extensively in prior engineering practice (Yura, 1971; Disque, 1973; Hajjar & White, 1997). The comparable stiffness reduction factor for beams can be derived based on the AISC Specification lateral torsional buckling equations. After deriving this stiffness reduction factor, it is proposed to calculate the stiffness reduction factor for beam-columns via an interpolation between the column and beam stiffness reduction factors.

2) Improvements on Flange Local Buckling (FLB) and Tension Flange Yielding (TFY) limit states can be provided to improve the predictions of the strength limit states in general. The FLB limit state calculation can be improved by employing the unified effective width approach (Peköz 1986) to recognize the postbuckling resistance of noncompact and slender flanges. This change results in significantly better correlations with experimental test and test simulation results for beam-column cases with cross-sections having slender elements. For TFY improvements, it is proposed that the spread of yielding in the tension zone of the web is proposed to be included for the section moment capacity calculations for section types in which $S_{xt} < S_{xc}$. In the limit that the web of the cross-section is slender, it is proposed that the member flexural resistance should be based on reductions applied to the moment at first nominal yielding of the compression flange, considering early spread of yielding in flexural tension.

Considering the above objectives, the supporting objectives for this research are:

1) For application of beam-column strength reduction factors, the suggested bilinear curve by AISC (2016) Specification tends to over-estimate the strength of certain

members around the “knee” region of the curves. This research aims to propose a better fit to test simulation results.

2) Although the Inelastic Buckling Analysis is a robust application to solve systems or members, this analysis type is not suited for hand calculation. For this purpose, another objective of this research is to build a comprehensive software framework for advanced design evaluation utilizing the above approaches. A current prototype software system that implements the above methods, SABRE2, has been developed by the author and others. This software system is implemented in MATLAB (MathWorks Inc. 2016). However, a number of the characteristics of MATLAB prohibit the extension of this software system to more comprehensive frame analysis capabilities. The Python (Python Software Foundation 2018) programing language potentially provides a more effective foundation for this type of software. A key component of this research is therefore to implement and expand the above capabilities in Python.
3) Based on the above improvements to the FLB and TFY limit states equations along with the recommendations from Subramanian et al. (2018) for the Lateral Torsional Buckling (LTB) characterization, updates to the unified flexural provisions equations from White (2008) are recommended.
4) The above INBA with SRFs needs to be validated along with the updated limit states pertaining to TFY and FLB. The validation addresses doubly- and singly-symmetric prismatic and non-prismatic members.
5) Finally, the application of these approaches is demonstrated via a series of examples.

CHAPTER 2. INELASTIC BUCKLING ANALYSIS USING SPECIFICATION-BASED STIFFNESS REDUCTION FACTORS

Inelastic Nonlinear Buckling Analysis (INBA) generally is a buckling analysis that considers both material nonlinearity and pre-buckling displacements. For general beam-column members, pre-buckling displacements commonly have a measurable influence on the structural capacity. As such, the AISC Specification generally requires the use of a second-order load-deflection analysis to determine the load effects. The specific INBA approach proposed here involves the use of a Direct Analysis Method (DM) solution for the pre-buckling load-deflection analysis, the parameters of which are defined by the AISC (2016) Specification provisions, but replaces the member stability based resistance equations of the Specification by equivalent inelastic buckling analysis solutions.

This is a promising approach to obtain the most accurate column design axial resistance, since it allows the engineer to more rigorously account for the inelastic characteristics of the different members at the strength limit state, continuity effects across braced points with adjacent member lengths and various member end and intermediate restraints.

The inelastic buckling analysis employed in this work utilizes stiffness reduction factors that many engineers are accustomed to for members subjected to concentric axial loading. However, it also uses stiffness reduction factors associated with the Specification lateral torsional buckling (LTB) equations to allow for the evaluation of beam LTB responses. The recommended INBA solution uses a basic interpolation between the column

and beam inelastic stiffness reduction factors to address general beam-column member stability limit states.

Application of this approach requires a Thin-Walled Open-Section (TWOS) frame element for the buckling calculations. This type of element typically has seven degrees of freedom at each joint or nodal location – three translations, three rotations, and one warping degree of freedom. This allows for the essential consideration of member warping rigidity in the evaluation of member stability limit states involving torsion.

2.1 Open-Section Thin-Walled Frame Finite Element

The Inelastic Nonlinear Buckling Analysis procedures employed in this research achieve their solution efficiency by calculating the member inelastic stiffnesses using Stiffness Reduction Factors (SRFs) obtained from the Specification resistance equations, as well as by modeling the general member behavior using a 3D corotational frame element based on thin-walled open-section beam theory. The element formulation is adopted from Chang (2006) and Jeong (2014). The element uses seven degrees of freedom at each joint or nodal location – three translations, three rotations, and one warping degree of freedom. and is based in essence on Vlasov kinematics (Vlasov 1963). The element kinematic assumptions are:

- Shear deformations within the plane of the cross-section plates are negligible. Therefore, plane sections remain plane and normal to the deformed axis of the member, with the exception of the cross-section warping displacements.
- The cross-section profile remains unchanged, for example, web-distortion and flange or web local buckling of the cross-section is not captured by the element.

- The element displacements and rotations may be large, but the element strains are small.

Cubic Hermitian shape functions are used for interpolation of the element independent transverse displacements. Cubic Hermitian interpolation is also employed for the element twist rotations in the version of this element implemented by Jeong (2014) and in the current version. Lastly, for the axial displacements, linear interpolation is employed within the element co-rotational frame.

A straight line between the element nodal points is used as the reference configuration of the element (Total Lagrangian-Corotational Approach). The element utilizes a local reference frame that rotates with the chord between the element end nodes. The rotations of the frame element with respect to this reference frame are assumed to be finite but small, e.g., the sine of the angle between the deformed axis and the reference frame may be approximated by the angle, and the cosine of the angle between the deformed axis and the reference frame may be approximated as 1.0.

2.2 Column Inelastic Buckling Analysis using the AISC Inelastic Stiffness Reduction Factor

The column inelastic stiffness reduction factor (τ_a) is the most appropriate of various stiffness reduction estimates for the AISC design assessment of steel columns via buckling analysis. This is because τ_a is derived inherently from the AISC column strength curve. Therefore, when configured properly with a buckling analysis, the internal axial force in the column(s) is equal to $\phi_c P_n$ at incipient buckling of the analysis model. The τ_a factor accounts implicitly for residual stress and initial geometric imperfection effects, as well as

the traditional higher margin of safety specified by AISC for slender columns. This factor is not the most appropriate inelastic stiffness reduction for a second-order load-deflection analysis, such as an analysis conducted to satisfy the requirements of the Direct Analysis Method of design (the DM). The separate τ_b factor has been adopted by AISC for use with the Direct Analysis Method. The τ_b factor is intended to account predominantly just for nominal residual stress effects. If used with a second-order load-deflection analysis per the DM, the τ_a factor gives higher internal forces and correspondingly lower strength predictions. This is because the engineer would effectively be double-counting geometric imperfection effects in the DM if τ_a were used, since geometric imperfections are modeled explicitly as part of the DM calculation of the internal forces. It is recommended that τ_a can be used, along with an eigenvalue buckling analysis, to provide a rigorous assessment of the member resistances, given the internal forces obtained from the above DM second-order load-deflection analysis. The use of τ_a in a buckling analysis allows the engineer to obtain a rigorous prediction of column strengths per the AISC column strength equations, accounting for continuity effects across braced points and lateral and/or rotational restraint from other framing, including general stability bracing. With this approach, no separate checking of the corresponding underlying Specification member resistance equations is needed. The mechanical responses associated with effective length (K) factors are captured rigorously without the difficulty of determining these factors. Refined estimates of the member strengths are obtained without the modeling of detailed member out-of-straightness imperfections.

An expression for τ_a can be derived as follows. The derivation is shown only in the context of LRFD to keep the developments succinct.

Generally, one can write the factored column design resistance as

$$\phi_c P_n = 0.9\,(0.877)\,P_{e\tau} = 0.9\,(0.877)\,\tau_a\,P_e \tag{1}$$

where 0.9 is the resistance factor in the AISC Specification for column axial compression, 0.877 is a factor applied generally to the elastic column buckling resistance in the AISC Specification to obtain the nominal column elastic buckling resistance (accounting for geometric imperfection and partial yielding effects for columns that fail by theoretical elastic buckling, as well as an implicit increased margin of safety for slender columns in AISC), and τ_a is the column inelastic stiffness reduction factor. The column inelastic buckling load, considering just τ_a and not considering the additional 0.9 and 0.877 factors, may be written as

$$P_{e\tau} = \tau_a\,P_e \tag{2}$$

where again, P_e is the theoretical column elastic buckling load.

For $\frac{P_{e\tau}}{P_y} > \frac{4}{9}\left(\text{i.e., for } \frac{\phi_c P_n}{\phi_c P_y} > 0.390\right)$, the AISC column inelastic strength equation may be written as

$$\frac{\phi_c P_n}{\phi_c P_y} = 0.658^{\frac{\tau_a P_y}{P_{e\tau}}} \tag{3}$$

The column resistance factor, ϕ_c, is included within the numerator and denominator on the left-hand side of this expression due to the fact that the inelastic buckling solution in this work aims to provide the column factored resistance, $\phi_c P_n$. Substituting the relationship

$$P_{e\tau} = \frac{P_n}{0.877} \tag{4}$$

from Eq. (1) into Eq.(2), one obtains

$$\frac{\phi_c P_n}{\phi_c P_y} = 0.658^{\frac{0.877\tau_a P_y}{P_n}} \tag{5}$$

Then, after taking the natural logarithm of both sides of this equation, one can solve for τ_a as follows:

$$\ln\left(\frac{\phi_c P_n}{\phi_c P_y}\right) = \ln\left(0.658^{\frac{0.877\tau_a P_y}{P_n}}\right) \tag{6}$$

$$\ln\left(\frac{\phi_c P_n}{\phi_c P_y}\right) = 0.877\tau_a \frac{P_y}{P_n}\ln\left(0.658\right) \tag{7}$$

$$\tau_a = -2.724\,\frac{\phi_c P_n}{\phi_c P_y}\ln\left(\frac{\phi_c P_n}{\phi_c P_y}\right) \tag{8}$$

Equation (8) has been used widely for column inelastic buckling calculations in the context of the AISC Specification. This equation can be applied most clearly by substituting an internal axial force ΓP_u for $\phi_c P_n$, such that τ_a can be thought of conceptually as an effective reduction on the member flexural rigidity (EI) at a given level of axial load in LRFD. As such, the τ_a equation becomes, for $\left(\frac{\Gamma P_u}{\phi_c P_y} > 0.390 \right)$,

$$\tau_a = -2.724 \frac{\Gamma P_u}{\phi_c P_y} \ln\left(\frac{\Gamma P_u}{\phi_c P_y} \right) \tag{9}$$

The above equation is valid only for column buckling load levels that are within the inelastic buckling range.

For $\left(\frac{\Gamma P_u}{\phi_c P_y} \leq 0.390 \right)$, elastic buckling controls and

$$\tau_a = 1 \tag{10}$$

The above τ_a expressions can be employed with buckling analysis capabilities, such as those provided by the program Mastan2 (Ziemian and McGuire 2016), or the capabilities developed in this research, to explicitly (or "directly") calculate the maximum column strength for any axially loaded problem.

The most streamlined application of τ_a with a buckling analysis to determine column strength is as follows:

1. Construct an overall buckling analysis model for the problem at hand.

2. Apply the desired factored loads from a given LRFD load combination to the above model. These applied loads produce the column internal axial forces P_u.
3. Reduce the elastic modulus of the structural members, E, by 0.9 x 0.877 = 0.7893.
4. Reduce the member moments of inertia by τ_a, based on P_u, using Eqs. (9) and (10)with $\Gamma = 1$. (Alternately, this step and step 3 may be replaced by a single step where either the elastic modulus E or the moment of inertia I is reduced by the net stiffness reduction factor, $SRF = 0.9 \times 0.877 \times \tau_a$.)
5. Solve for the inelastic buckling load of the above model. Vary the applied loads by the common applied load scale factor Γ, calculate the τ_a values based on the scaled load levels (using the corresponding internal loads ΓP_u), and solve for the multiple of the current loading, γ, at which the system buckles. Iterate on these calculations until $\gamma = 1$, indicating that the system buckles at the load level Γ specified at the start of the buckling analysis. The corresponding internal axial forces ΓP_u in the model at incipient buckling are then "directly" equal to the column axial capacities $\phi_c P_n$.

This is a promising approach to obtain the most accurate column design axial strengths, accounting for the inelastic characteristics of the different members at the strength limit state, continuity effects across braced points with adjacent member lengths and various other member end and intermediate restraints, all within the context of the AISC (2016) column design equations.

Given the above developments, it is useful to specify a terminology associated with the above stiffness reduction factors. The factor τ_a is referred to as the "base" column

stiffness reduction factor, whereas the factor SRF = 0.9 x 0.877 x τ_a is referred to as the net stiffness reduction factor. When calculating the factored column resistances for design, the inelastic buckling analysis solution is in effect derived from the net stiffness reduction factor.

Traditionally, the Effective Length Method (ELM) has been used with a basic version of this approach to determine the influence of end rotational restraint on columns. The member restraints need not be limited to just column end rotational restraints though. When applied to column buckling problems, the above procedure gives an accurate estimate of the column strength accounting for the restraint offered by the bracing system. The engineer simply needs to include the lateral (and more generally, also torsional) stiffnesses provided by the bracing system in the buckling analysis.

In fact, as stated in this section, rather than solving for the column buckling load for a given set of bracing stiffnesses, one can consider a given LRFD applied factored loading P_u (with $\gamma = 1$) and then solve for the required bracing stiffnesses necessary to develop the critical buckling strength equal to this factored load level. These bracing stiffnesses are commonly referred to as the *ideal bracing stiffness* values, β_i, corresponding to a given desired load level P_u.

Some engineers have suggested that $0.8\tau_b$, the general stiffness reduction used in the AISC Direct Analysis Method, should be used for all problems including calculation of column inelastic buckling loads (Geschwindner L.F. (2010)). This is certainly possible, but such an approach misses the clear advantage of having a buckling analysis procedure that can determine directly the value of $\phi_c P_n$ accounting for all end and intermediate

restraint effects. This issue can be understood by comparing the net stiffness reduction factors 0.9 x 0.877 x τ_a and 0.8τ_b as shown in Fig. 1. The factor 0.8τ_b generally does not give an accurate estimate of the column strength $\phi_c P_n$ when used in a buckling analysis calculation. It does give an appropriate estimate of the column strengths if used as part of a second-order analysis in which appropriate geometric imperfections are included per the requirements of the DM.

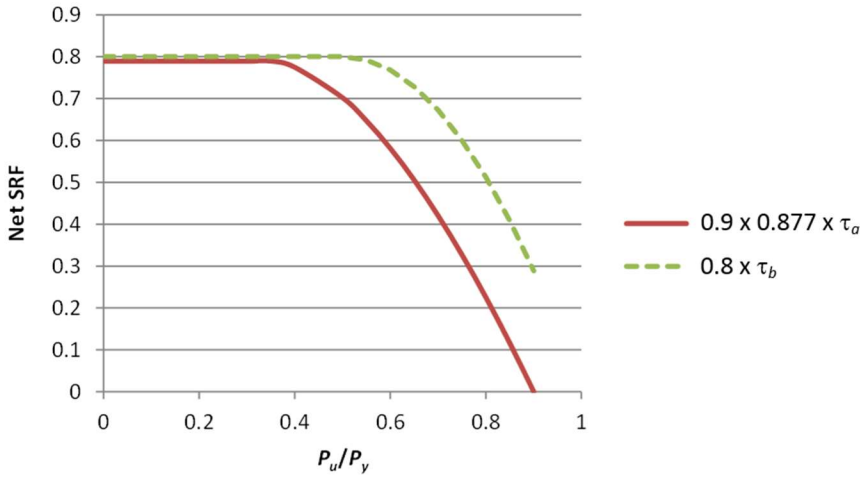

Figure 1. Comparison of the net column stiffness reduction factors 0.9 x 0.877 x τ_a and 0.8τ_b.

2.3 Net Stiffness Reduction Factor (SRF) for Columns with Slender Cross-Section Elements

The 2016 AISC Specification (AISC 2016) has adopted a unified effective width approach to characterize the axial resistance of members having slender cross-section elements under uniform axial compression. Using this approach, the member axial resistance is expressed simply as

$$\phi_c P_n = 0.9 F_{cr} A_e \tag{11}$$

where F_{cr} is the column critical stress determined using the member gross cross-section properties and A_e is the cross-section effective area obtained by summing the effective widths times the thicknesses for all the cross-section elements. In many practical situations, the most economical welded I-section members have slender webs. Beam-type rolled wide flange sections, i.e., sections that have a depth-to-flange width d/b_f greater than about 1.7, also often have slender webs. Therefore, it is important to define how the column inelastic *SRF*s should be determined for these cases. Stated succinctly, the column net *SRF* may be written as

$$SRF = 0.9 \text{ x } 0.877 \text{ x } \tau_a \frac{A_e}{A_g} \tag{12}$$

for these cross-section types, where τ_a is calculated from Eqs. (9) and (10).

In addition, it is recommended that the plate effective widths should be calculated based on the axial stress $f = \Gamma P_u / A_{e(Fy)}$ in evaluating $A_{e(Fy)}$ in Eq. (12). As such, since A_e is dependent on f, while f is also dependent on A_e, A_e and f generally must be solved for iteratively. These iterations are reasonably fast and are simple to handle numerically. For manual calculation, f may be taken conservatively as F_y. For columns with simply-supported end conditions, the above calculations produce the same result as the unified effective width equations in the 2016 AISC Specification (AISC 2016), since at the strength limit, $\Gamma P_u = \phi_c P_n$. For columns with general end and intermediate restraints, the above calculations account for the idealized relative stiffnesses in the structural system with the

same rigor as the more basic method for nonslender element members explained in Section 2.2.

2.4 Inelastic Lateral Torsional Buckling (LTB) Analysis using Stiffness Reduction Factors Derived from the AISC LTB Strength Curves

A stiffness reduction factor for beam lateral torsional buckling (LTB) can be developed in a similar fashion to the development of the above column stiffness reduction factor. Similar to the use of column stiffness reduction factors, the Specification LTB resistance equations can be replaced by an inelastic buckling solution using the beam SRFs, thereby accounting more rigorously for continuity, end restraint and moment gradient effects on the member LTB resistances. Those stiffness reduction factors for LTB are developed for the first time in this research.

Similar methods have been developed in the prior research by Trahair and Hancock (2004) and Trahair (2009 and 2010) and have been shown to provide accurate estimates of column, beam and beam-column resistances for various types of geometries, loadings and member restraints. More recently, Kucukler et al. (2015a & b) have developed comparable procedures in the context of design to Eurocode 3.

Generally, one can write the factored AISC LRFD beam LTB design resistance as

$$\phi_b M_n = \phi_b R_b M_{e\tau} = 0.9 R_b \tau_{ltb} M_e \tag{13}$$

where M_e represents the theoretical beam elastic LTB resistance, $M_{e\tau}$ represents the beam inelastic LTB resistance, and R_b is the web bend buckling strength reduction factor, equal to 1.0 for a compact or noncompact web I-section. The term τ_{ltb} is the base stiffness

reduction factor corresponding to the nominal AISC LTB strength curves. Net stiffness reduction factor (SRF) based on this τ_{ltb} can be calculated with multiplication of the resistance factor (ϕ_b). The derivation of this factor parallels the derivation of the base column stiffness reduction factor, τ_a, presented in Section 2.3. The derivation of τ_{ltb} is presented below.

For all types of I-section members, when $m \le \frac{R_b F_L}{F_{yc}}$, where $m = \frac{\Gamma M_u}{\phi_b M_{yc}}$,

$$\tau_{ltb} = 1 \tag{14}$$

For compact and noncompact web I-section members with $\frac{F_L}{F_{yc}} < m < \frac{\phi_b M_{max.LTB}}{\phi_b M_{yc}}$, where $\phi_b M_{max.LTB} = 0.9 R_b R_{pc} M_{yc}$, the following τ_{ltb} equation is applicable for the range of $L_p \le L_b \le L_r$. For these types of sections, the above L_p limit may be converted to an $\frac{M_e}{M_{yc}}$ limit as follows:

$$\frac{M_e}{M_{yc}} = \frac{\pi^2 E}{\left(\frac{L_b}{r_t}\right)^2 F_{yc}} \sqrt{1 + \frac{0.07794}{X^2}\left(\frac{L_b}{r_t}\right)^2} \tag{15}$$

where M_e is the elastic lateral torsional buckling strength and M_{yc} is the yield moment with respect to the compression flange. By substituting $L_b = L_p = c_p r_t \sqrt{\frac{E}{F_{yc}}}$, these equations may be written as

$$\frac{M_e}{M_{yc}} = \frac{\pi^2}{c_p{}^2} \sqrt{1 + \frac{0.07794}{X^2} c_p{}^2 \frac{E}{F_{yc}}} \tag{16}$$

where c_p is 1.1 in the current AISC (2016) Specification, and 0.63 in the recommended procedures from Subramanian et al. (2018).

In applying the τ_{ltb} formula derived in the following, the L_p limit is addressed by limiting $\frac{\Gamma M_u}{\phi_b M_{yc}}$ to a maximum of $\frac{\phi M_{\max.LTB}}{\phi M_{yc}}$. When $\frac{\Gamma M_u}{\phi_b M_{yc}}$ is limited in this manner, τ_{ltb} is the value of the inelastic stiffness reduction factor that causes the maximum buckling moment to be equal to $\phi M_{\max.ltb}$. In the inelastic buckling analysis, if the maximum cross-section moment is larger than $\phi M_{\max.ltb}$, then τ_{ltb} is reduced until $\Gamma M_u = \phi M_{\max.ltb}$.

In addition, the L_r limit is handled by setting τ_{ltb} to 1.0 when $\frac{\Gamma M_u}{\phi_b M_{yc}}$ is less than $\frac{F_L}{F_{yc}}$.

For intermediate values of $\frac{\Gamma M_u}{\phi_b M_{yc}}$, the inelastic LTB tau factor is derived as follows for compact- and noncompact-web members, starting with Eq. (15). After squaring each side of this equation and collecting terms, one obtains

$$\left(\frac{M_e}{M_{yc}}\right)^2\left(\frac{L_b}{r_t}\right)^4 - 0.07794\frac{\pi^4}{X^2}\left(\frac{E}{F_{yc}}\right)^2\left(\frac{L_b}{r_t}\right)^2 - \pi^4\left(\frac{E}{F_{yc}}\right)^2 = 0 \tag{17}$$

Upon using the quadratic formula to determine $\frac{L_b}{r_t}$, then simplifying:

$$\frac{L_b}{r_t} = \sqrt{\frac{0.07794\frac{\pi^4}{X^2}\left(\frac{E}{F_{yc}}\right)^2 + \sqrt{\left[0.07794\frac{\pi^4}{X^2}\left(\frac{E}{F_{yc}}\right)^2\right]^2 + 4\left(\frac{M_e}{M_{yc}}\right)^2\pi^4\left(\frac{E}{F_{yc}}\right)^2}}{2\left(\frac{M_e}{M_{yc}}\right)^2}} \tag{18}$$

Taking the $\frac{1.95}{\left(\frac{M_e}{M_{yc}}\right)}\left(\frac{E}{XF_{yc}}\right)$ term outside of the square root to simplify the equation, the following is obtained:

$$\frac{L_b}{r_t} = \frac{1.95}{\left(\frac{M_e}{M_{yc}}\right)}\left(\frac{E}{XF_{yc}}\right)\sqrt{1+\sqrt{1+6.76\left(\frac{X^2F_{yc}}{E}\right)^2\left(\frac{M_e}{M_{yc}}\right)^2}} \tag{19}$$

Next, the X term can be taken into the square root to obtain a more streamlined equation:

$$\frac{L_b}{r_t} = \frac{1.95}{\left(\frac{M_e}{M_{yc}}\right)}\left(\frac{E}{F_{yc}}\right)\sqrt{\frac{1}{X^2} + \sqrt{\frac{1}{X^4} + 6.76\left(\frac{F_{yc}}{E}\right)^2\left(\frac{M_e}{M_{yc}}\right)^2}} \tag{20}$$

Replacing M_e with $\frac{\Gamma M_u}{\tau_{ltb}}$ gives

$$\frac{L_b}{r_t} = \frac{1.95}{\left(\frac{\Gamma M_u}{\tau_{ltb} M_{yc}}\right)}\left(\frac{E}{F_{yc}}\right)\sqrt{\frac{1}{X^2} + \sqrt{\frac{1}{X^4} + 6.76\left(\frac{F_{yc}}{E}\right)^2\left(\frac{\Gamma M_u}{\tau_{ltb} M_{yc}}\right)^2}} \tag{21}$$

In addition, $\frac{\Gamma M_u}{\tau_{ltb} M_{yc}}$ can be expressed as

$$\frac{\Gamma M_u}{\tau_{ltb} M_{yc}} = R_{pc}\left[1 - \left(1 - \frac{F_L}{R_{pc} F_{yc}}\right)\frac{\frac{L_b}{r_t} - \frac{L_p}{r_t}}{\frac{L_r}{r_t} - \frac{L_p}{r_t}}\right] \tag{22}$$

Substituting $\frac{L_b}{r_t}$ from Eq. (21) into Eq. (22) gives

$$\frac{\Gamma M_u}{\tau_{ltb} M_{yc}} = R_{pc}\left[1-\left(1-\frac{F_L}{R_{pc}F_{yc}}\right)\frac{\frac{1.95}{\left(\frac{1}{\tau_{ltb}}\right)\left(\frac{\Gamma M_u}{\tau_{ltb}M_{yc}}\right)}\left(\frac{E}{F_{yc}}\right)\sqrt{\frac{1}{X^2}+\sqrt{\frac{1}{X^4}+6.76\left(\frac{F_{yc}}{E}\right)^2\left(\frac{\Gamma M_u}{\tau_{ltb}M_{yc}}\right)^2\left(\frac{1}{\tau_{ltb}}\right)^2}}-\frac{L_p}{r_t}}{\frac{L_r}{r_t}-\frac{L_p}{r_t}}\right] \tag{23}$$

After further mathematical simplifications, the following equation is obtained:

$$\left\{\left[\frac{\left(1-\frac{\Gamma M_u}{\tau_{ltb}M_{yc}}\frac{1}{R_{pc}}\right)}{\left(1-\frac{F_L}{R_{pc}F_{yc}}\right)}\left(\frac{L_r}{r_t}-\frac{L_p}{r_t}\right)+\frac{L_p}{r_t}\right]\left(\frac{\Gamma M_u}{\tau_{ltb}M_{yc}}\right)\left(\frac{F_{yc}}{E}\right)\left(\frac{1}{1.95}\right)\right\}^2-\left(\frac{\tau_{ltb}}{X}\right)^2 \tag{24}$$

$$=\sqrt{\frac{{\tau_{ltb}}^4}{X^4}+6.76\left(\frac{F_{yc}}{E}\right)^2\left(\frac{\Gamma M_u}{\tau_{ltb}M_{yc}}\right)^2{\tau_{ltb}}^2}$$

in which

$$Y = \left[\frac{\left(1 - \frac{\Gamma M_u}{\tau_{ltb} M_{yc}} \frac{1}{R_{pc}} \right)}{\left(1 - \frac{F_L}{R_{pc} F_{yc}} \right)} \left(\frac{L_r}{r_t} - \frac{L_p}{r_t} \right) + \frac{L_p}{r_t} \right] \left(\frac{\Gamma M_u}{\tau_{ltb} M_{yc}} \right) \left(\frac{F_{yc}}{E} \right) \left(\frac{1}{1.95} \right) \tag{25}$$

$$T = \frac{\tau_{ltb}}{X} \tag{26}$$

and

$$X^2 = \frac{S_{xc} h_o}{J} \tag{27}$$

Using these coefficients, Eq. (24) can be simplified to

$$Y^2 - T = \sqrt{T^2 + 6.76 X^2 \left(\frac{F_{yc}}{E} \right)^2 \left(\frac{\Gamma M_u}{\tau_{ltb} M_{yc}} \right)^2 T} \tag{28}$$

Solving for *T*, the following equation is obtained:

$$T = \frac{Y^4}{\left[6.76 X^2 \left(\frac{F_{yc}}{E} \right)^2 \left(\frac{M_n}{M_{yc}} \right)^2 + 2Y^2 \right]} \tag{29}$$

Substituting $\frac{\tau_{ltb}}{X}$ for *T,* the following expression can be written for τ_{ltb}:

$$\tau_{ltb} = \sqrt{\frac{Y^4 X^2}{\left[6.76X^2\left(\frac{F_{yc}}{E}\right)^2 m^2 + 2Y^2\right]}} \tag{30}$$

For compact- and noncompact-web members the net stiffness reduction factor is

$$SRF = 0.9\ \tau_{ltb} \tag{31}$$

Conversely, for slender-web I-sections with $\frac{R_b F_L}{F_{yc}} < m < \frac{\phi_b M_{max}}{\phi_b M_{yc}}$, where $m = \frac{\Gamma M_u}{\phi_b M_{yc}}$, the following simpler form is obtained in comparison to Eq. (30). The L_p limit may be converted to an $\frac{M_e}{M_{yc}}$ limit as follows:

$$\frac{M_e}{M_{yc}} = \frac{\pi^2 E}{\left(\frac{L_b}{r_t}\right)^2 F_{yc}} \tag{32}$$

Substitute $L_b = L_p = c \times r_t \sqrt{\frac{E}{F_{yc}}}$, where again c is 1.1 for current AISC (2016) Specification, whereas 0.63 for recommended procedure from Subramanian et al. (2018) as explained in Section 3.3.

Within the inelastic buckling range:

$$m = R_b \left[R_h - \left(R_h - \frac{F_L}{F_{yc}} \right) \left(\frac{\sqrt{\frac{M_{yc}}{M_e}} - \frac{c}{\pi}}{\sqrt{\frac{M_{yc}}{M_L}} - \frac{c}{\pi}} \right) \right] \tag{33}$$

Substituting $\frac{\Gamma M_u}{\tau_{ltb}}$ for M_e, Eq. (34) may be written as

$$m = R_b \left[R_h - \left(R_h - \frac{F_L}{F_{yc}} \right) \left(\frac{\sqrt{\frac{\tau_{ltb}}{m}} - \frac{c}{\pi}}{\sqrt{\frac{M_y}{M_L}} - \frac{c}{\pi}} \right) \right] \tag{34}$$

The inelastic LTB tau factor for slender web sections is obtained from Eq. (34) as:

$$\tau_{ltb} = \frac{m}{R_b} \left[\frac{\left(R_h - m \frac{1}{R_b} \right)}{\left(R_h - \frac{F_L}{F_{yc}} \right)} \left(\sqrt{\frac{F_{yc}}{F_L}} - \frac{c}{\pi} \right) + \frac{c}{\pi} \right]^2 \tag{35}$$

and the corresponding net stiffness reduction factor is

$$SRF = 0.9\, R_b\, \tau_{ltb} \tag{36}$$

where R_h is the hybrid cross-section factor, which is not addressed in the ANSI/AISC 360 Specification, but is addressed by similar strength equations in the AASHTO LRFD Specifications (AASHTO 2005). Furthermore, for both compact- and noncompact-web

sections, one can write

$$m = \frac{\Gamma M_u}{\phi_b M_{yc}} = \frac{\Gamma M_u}{\phi_b M_{\max.LTB} / R_{pc}} = R_{pc} \frac{\Gamma M_u}{\phi_b M_{\max.LTB}} = R_{pc} \frac{\Gamma M_u}{\phi_b M_{\max}} \frac{M_{\max}}{M_{\max.LTB}} \qquad (37)$$

where $\phi_b M_{\max}$ is the general "plateau strength" taken as the minimum of the independent flexural strengths calculated for the LTB plateau strength, flange local buckling (FLB) strength, and tension flange yielding (TFY) strength as applicable:

$$\phi_b M_{\max} = \min\left(\phi_b M_{\max.LTB}, \phi_b M_{n.FLB}, \phi_b M_{n.TFY}\right) \qquad (38)$$

The advantage of writing *m* as shown in Eq. (37) is that the ratio $\frac{\Gamma M_u}{\phi_b M_{\max}}$ varies from zero to a maximum value of 1.0, as does $\frac{\Gamma P_u}{\phi_c P_{ye}}$. These ratios facilitate the description of an interpolated beam-column net *SRF* discussed subsequently.

For slender-web I-sections, one can write

$$m = \frac{\Gamma M_u}{\phi_b M_{yc}} = \frac{\Gamma M_u}{\phi_b M_{\max.LTB} / R_b R_h} = R_b R_h \frac{\Gamma M_u}{\phi_b M_{\max.LTB}} = R_b R_h \frac{\Gamma M_u}{\phi_b M_{\max}} \frac{M_{\max}}{M_{\max.LTB}} \qquad (39)$$

where

$$M_{max.LTB} = R_h M_{yc} \qquad (40)$$

Figures 2 and 3 illustrate how τ_{ltb} varies relative to the well-known column inelastic stiffness reduction factor τ_a for representative beam- and column-type W sections respectively. The behavior of τ_{ltb} for slender-web I-sections is similar to that shown for the beam-type W21x44 section.

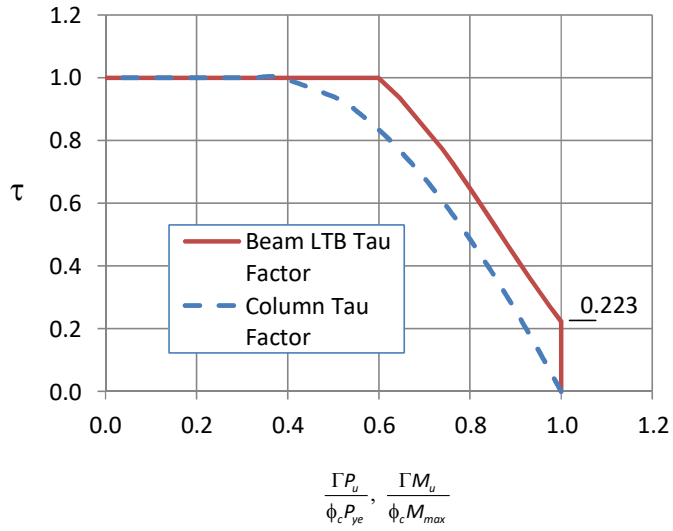

Figure 2. Column and beam τ factors for a W21x44 representative beam-type wide-flange section.

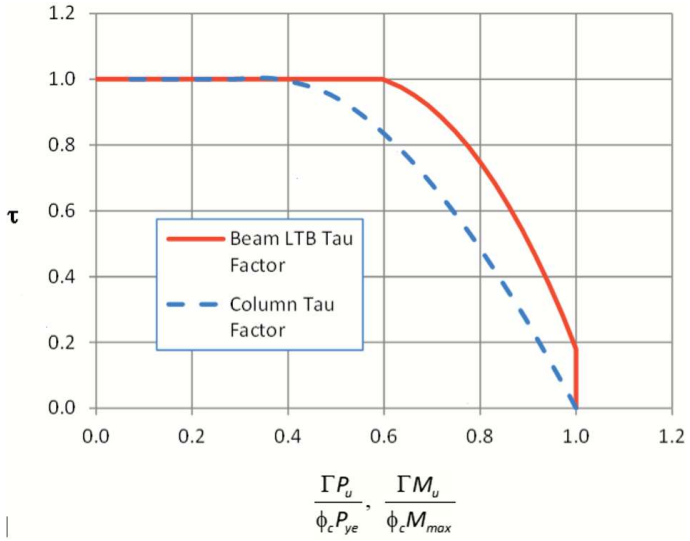

Figure 3. Column and beam τ factors for a W14x257 representative column-type wide-flange section.

The LTB inelastic stiffness reduction factor, τ_{ltb}, tends to be somewhat larger (i.e., reduces the capacity less) than the corresponding column inelastic stiffness reduction factor, τ_a, for a given normalized load ratio $\frac{\Gamma P_u}{\phi_c P_{ye}}$ or $\frac{\Gamma M_u}{\phi_b M_{\max}}$. It should be noted that based on the AISC LTB strength curves, I-section beams still have significant effective inelastic stiffness when ΓM_u reaches the plateau resistance $\phi_b M_{max}$. For the above W21x44 and W14x257 examples, τ_{ltb} = 0.223 and 0.180 respectively when this level of loading is reached.

In addition to the above, if the internal moment at incipient buckling, ΓM_u, is larger than the corresponding $\phi_b M_{max}$ at the most critically loaded cross-section, based on an analysis in which the τ_{ltb} values are calculated using the corresponding internal moments throughout the length of the members, the "plateau strength" has been reached at the critical cross-section; hence, the design strength is the applied load level at which the internal moment at the critical cross-section is equal to $\phi_b M_{max}$.

Since both of the above example cross-sections are doubly symmetric and have compact flanges, $\phi_b M_{max} = \phi_b M_{max.LTB}$. For doubly-symmetric sections having a noncompact or slender compression flange, or singly-symmetric sections with a noncompact or slender compression flange and $h_c > h$ (usually associated with the compression flange being smaller than the tension flange), flange local buckling (FLB) governs the plateau resistance and $\phi_b M_{max} = \phi_b M_{max.FLB}$. For singly-symmetric sections with $h_c < h$, either FLB or tension flange yielding (TFY) can govern for the plateau resistance. For doubly- or singly-symmetric sections with compact webs and compact flanges, $\phi_b M_{max} = \phi_b M_{max.LTB}$

$= \phi_b M_{max.FLB} = \phi_b M_{max.TFY} = \phi_b M_p$, or as stated in the AISC Specification, the governing limit state is "yielding" and the other limit states do not apply.

For proper calculation of the LTB resistance from a buckling analysis, several requirements must be satisfied:

1. In the context of doubly-symmetric I-section members, the buckling analysis software must rigorously include the contributions from warping rigidity EC_w as well as the St. Venant torsional rigidity GJ and the lateral bending rigidity EI_y.
2. In addition, for singly-symmetric I-section members, the buckling analysis must account rigorously for the behavior associated with the shear center differing from the cross-section centroidal axis, which relates to the monosymmetry factor, β_x, in analytical equations for the LTB resistance of these types of beams.
3. The $SRF = 0.9\ R_b\ \tau_{ltb}$ should be applied equally to each of the elastic stiffness contributions GJ, EC_w and EI_y, at a given cross-section, for the execution of the buckling analysis. Physically, it can be argued that the effective reduction in the St. Venant torsional rigidity of an inelastic beam is not as large as the reduction in the effective EI_y and EC_w values. However, the use of an equal reduction on all three rigidities (at a given cross-section) is simple and sufficient. Furthermore, equal reduction on all three cross-section rigidities reproduces the beam LTB resistance from the AISC Specification equations exactly for cases involving uniform bending and simply-supported end conditions.
4. A separate SRF of 0.9 x 0.877 x τ_a should be applied to the elastic stiffness contributions EA, EI_x and EQ_x (where Q_x is the first moment of the area about the

reference axis of the cross-section, equal to zero when the reference axis is the cross-section centroidal axis, but non-zero in cases such as singly-symmetric section members, where it is common for the shear center to be taken as the reference axis in the structural analysis). For beam members subjected to zero axial load, $\tau_a = 1$. Beam-column members are addressed subsequently. Furthermore, it should be noted that for singly-symmetric sections, the moment about the centroidal axis must be used generally in the calculation of τ_{ltb}.

5. The internal force state upon which the buckling analysis is based is to be determined using the elastic properties of the structure, using the rules specified in Chapter C or Appendix 7 of the AISC Specification. If the Effective Length Method of design is employed, the nominal elastic properties of the structure are used in the above load-deflection analysis to determine the internal forces. If the Direct Analysis Method of design is employed, all the cross-section elastic stiffnesses are reduced generally by $0.8\tau_b$. In this case, AISC Chapter C also gives rules permitting the use of $\tau_b = 1$ if additional system initial geometric imperfection effects are included in the load-deflection analysis. Also, AISC Chapter C and Appendix 7 specify required nominal initial imperfections of the points of intersection of the members in the structure (i.e., "system imperfections", or equivalent Notional loads, corresponding to these imperfections.

In general, the AISC Chapter C and Appendix 7 requirements entail that a general inelastic nonlinear buckling analysis must be used to assess the member resistances. This is a buckling analysis in which the pre-buckling displacement effects are considered, via the use of a second-order load-deflection analysis to determine the internal forces. Given a

selected level of applied load and the corresponding internal forces, the *SRF*s are calculated for the buckling analysis, and then the buckling analysis is performed to evaluate the member resistances. If the buckling eigenvalue γ is greater than 1.0, the buckling resistance is greater than the current load level.

In some cases, the member failure mode determined from the buckling analysis may involve an overall buckling of the entire structural system; however, in many situations, the member failure will involve a localized member buckling involving several unbraced lengths in the vicinity of a critical region, or failure by reaching general yielding, FLB or TFY limit state.

For problems involving only beam members or involving concentrically loaded columns with negligible pre-buckling displacements, an inelastic linear buckling analysis provides an acceptable solution. This type of bucking analysis entails the use of a first-order elastic analysis to determine the system internal forces, followed by the calculation of the corresponding *SRF*s and the execution of the buckling analysis.

It should be apparent that the above inelastic LTB solutions are not manual engineering solutions. However, for that matter, neither is the general second-order elastic analysis of an indeterminate frame. Although engineers can conduct approximate analysis to perform initial sizing of the members in an indeterminate frame structure, commonly they do not rely on these analyses, manual moment distribution calculations, etc. for final design at this day and time. With the appropriate software implementation of the above τ_a and τ_{ltb} calculations using a frame element based on thin-walled open-section beam theory, the above procedure is quite easy to apply. The software performs the appropriate elastic

matrix analysis of the structure to determine the required member internal forces. Then it performs an inelastic eigenvalue buckling analysis based on these forces to evaluate the design. If the software automatically handles the internal inelastic stiffness reductions based on the magnitude of the internal forces, the inelastic buckling analysis is relatively straightforward to apply. The software SABRE2-V2 (Toğay et al. 2018) automates and satisfies all the above requirements for general doubly- or singly-symmetric I-section members with prismatic or non-prismatic stepped and/or tapered geometries, as well as frames composed of these types of members.

This approach can be quite powerful to provide highly accurate consideration of end restraints, continuity across braced points, general moment gradient, finite bracing stiffness effects, and nonprismatic geometry on the LTB resistance of beam and frame members. One key attribute of the power of this approach is that, similar to the τ_a approach for column buckling, once one has determined the load level corresponding to incipient inelastic buckling using the τ_{ltb} factor, the internal forces in the model at the buckling load correspond precisely to the design moment resistances $\phi_b M_n$. This allows the consideration of any and all restraints from bracing and member end conditions to be directly and automatically considered in the design assessment, by including them in the structural analysis model. Regarding the assessment of the required stiffnesses for stability bracing, this assessment is accomplished as a direct and integral part of the calculation of the member LTB resistances. If the buckling eigenvalue γ is greater than 1.0 from the buckling analysis, with the internal element stiffnesses calculated based on the τ_{ltb} equations given the internal forces at a load level Γ, then the beam has sufficient design strength for LTB at that load level. In addition, SABRE2 calculates the $\phi_b M_{max}$ values associated with flange

local buckling and tension flange yielding (based on Eq. (38)), as applicable, and checks these. If the critical beam cross-section reaches $\phi_b M_{max}$, with the reference load taken as the required loading from a given LRFD load combination, the system maximum load is governed by reaching this "plateau resistance" prior to the occurrence of LTB. (Note that other limit states such as web crippling, connection limit states, etc. must be checked separately, just as they would be in ordinary design.)

2.5 Proposed Stiffness Reduction Factors for Beam-Columns

Traditional beam-column strength interaction equations utilize a simple interpolation between the member axial strength in the absence of bending, $\phi_c P_n$, and the member flexural strength in the absence of axial loading, $\phi_b M_n$. Given the stiffness reduction factors $SRF = 0.9 \times 0.877 \times \tau_a \frac{A_e}{A_g}$ for axial load only cases and $SRF = 0.9 R_b \tau_{ltb}$ for bending only cases, one might expect that a simple interpolation between these stiffness reduction factors would provide an accurate representation of the net *SRF* for beam-column members. The current interaction between beam and column strengths given by the AISC specification is the bilinear interaction (Fig. 4). The stiffness reduction factors for beams can be used for loadings along the x-axis of this plot, and the SRF for columns can be used for loadings along the y-axis. Appropriate SRFs for beam-column members potentially can be determined by an interpolation between the beam and the column SRF values.

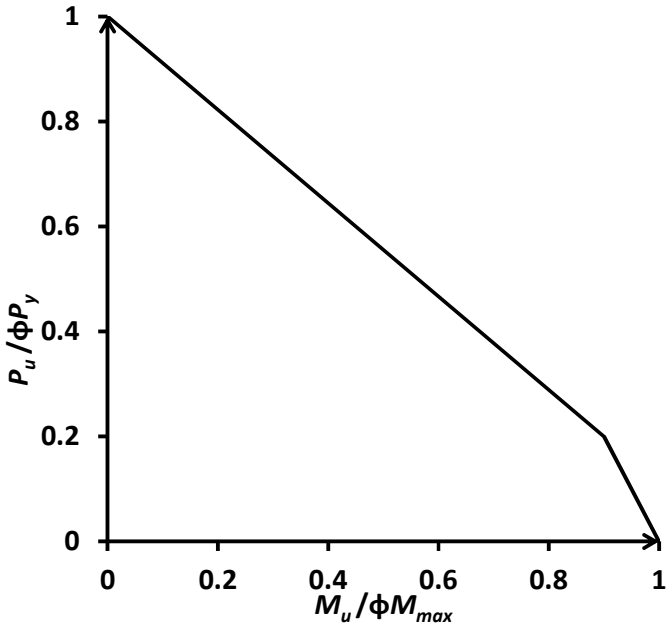

Figure 4. Beam-column interaction plot

In this research, it is found that the following interpolation procedure between the cross-section column and beam net SRF values provides an accurate characterization of I-section beam-column strengths for I-section members in which the flanges and/or webs are compact in flexure, and the cross-section plates are nonslender under axial compression:

1. The unity check value with respect to the cross-section maximum strength is obtained using the equations

$$UC = \frac{\Gamma P_u}{\phi_c P_{ye}} + \frac{8}{9}\frac{\Gamma M_u}{\phi_c M_{\max}} \quad \text{for } \frac{\Gamma P_u}{\phi_c P_{ye}} \geq 0.2 \tag{41}$$

and

$$UC = \frac{\Gamma P_u}{2\phi_c P_{ye}} + \frac{\Gamma M_u}{\phi_c M_{\max}} \quad \text{for } \frac{\Gamma P_u}{\phi_c P_{ye}} < 0.2 \tag{42}$$

2. The above *UC* value is employed in the τ_a and τ_{ltb} equations instead of the ratios

$\frac{\Gamma P_u}{\phi_c P_{ye}}$ and $\frac{\Gamma M_u}{\phi_c M_{\max}}$.

3. The angle

$$\zeta = \text{atan}\left(\frac{\Gamma P_u / \phi_c P_{ye}}{\Gamma M_u / \phi_b M_{\max}}\right) \tag{43}$$

is calculated. This angle is the orientation of the current force point within a normalized x-y interaction plot of the axial and moment strength ratios for a given cross-section.

4. The net SRF representing the beam-column response is determined using the interpolation equation

$$SRF = \left(\frac{\zeta}{90^o}\right) 0.9 \times 0.877 \times \tau_a \frac{A_e}{A_g} + \left(1 - \frac{\zeta}{90^o}\right) 0.9 R_b \tau_{ltb} \tag{44}$$

This *SRF* value is applied to EC_w, EI_y and *GJ*. In addition the SRF calculated using 0.9 x 0.877 x $\tau_a \frac{A_e}{A_g}$, which is calculated using $\frac{\Gamma P_u}{\phi_c P_{ye}}$ instead of UC, is applied to *EA* and EI_x.

A linear interpolation is recommended in place of Eqs. (41) and (42) for members having noncompact or slender flanges or webs in flexure, or having any slender cross-section plates under uniform axial compression. This is addressed subsequently in Section 3.4.

All the SRFs and intermediate calculations to obtain the SRFs in this chapter are presented in the context of LRFD (Load and Resistance Factor Design Specifications). For Allowable Strength Design (ASD),

$$SRF = \left(\frac{\zeta}{90^o}\right)0.9 \times \frac{0.877}{\Omega_c} \times \tau_a \frac{A_e}{A_g} + \left(1 - \frac{\zeta}{90^o}\right)0.9\frac{R_b}{\Omega_b}\tau_{ltb} \tag{45}$$

where

$$\zeta = \text{atan}\left(\frac{\Omega_c P_a / P_{ye}}{\Omega_b M_u / M_{\max}}\right) \tag{46}$$

In the equations for τ_a and τ_{ltb}, the $\frac{\Gamma P_u}{\phi_c P_{ye}}$ and $\frac{\Gamma M_u}{\phi_c M_{\max}}$ values are replaced by $\frac{\Omega_c \Gamma P_a}{P_{ye}}$ and $\frac{\Omega_b \Gamma M_u}{M_{\max}}$. Similarly, the Unity Check (UC) equations for ASD are as follows:

$$UC = \frac{\Omega_c \Gamma P_a}{P_{ye}} + \frac{8}{9}\frac{\Omega_b \Gamma M_u}{M_{\max}} \quad \text{for } \frac{\Omega_c \Gamma P_a}{P_{ye}} \geq 0.2 \tag{47}$$

and

$$UC = \frac{\Omega_c \Gamma P_u}{2P_{ye}} + \frac{\Omega_b \Gamma M_u}{M_{\max}} \quad \text{for } \frac{\Omega_b \Gamma P_a}{P_{ye}} < 0.2 \tag{48}$$

CHAPTER 3. IMPROVED REPRESENTATION OF FLANGE LOCAL BUCKLING, TENSION FLANGE YIELDING AND LATERAL-TORSIONAL BUCKLING FLEXURAL LIMIT STATES

In metal building frames, it is common to use a constant flange width within the fabricated segments of frame members, while stepping the thickness of the flange (as well as tapering of the web depth and stepping of the web thickness) to achieve significant design economy. In these cases, it is not uncommon for the flanges to be classified as slender by the AISC flexural design rules in the vicinity of inflection points or regions of low bending moment. The current Specification provisions (AISC 2016) do not recognize flange postbuckling strength in flexural compression, although they do account for flange postbuckling strength under uniform axial compression.

The AISC(2016) Compression Flange Local Buckling (FLB) predictions match well with experimental test results for typical cases within the stockier (i.e., smaller $\lambda_f = b_f/2t_f$) range corresponding to inelastic flange local buckling. However, the AISC FLB predictions have been shown to be significantly conservative for flanges classified as slender by the AISC flexural resistance rules. Figure 5 shows comparisons of the AISC predictions to experimental data collected by White and Jung (2008) focusing primarily on inelastic FLB. One can observe from these tests, and from other studies such as Seif and Schafer (2009), that the AISC FLB resistance equations tend to give a conservative estimate of the true FLB resistance for members having a slender compression flange (i.e.,

$\lambda_f / \lambda_{fr} > 1$). This is due to the substantial postbuckling strength of slender compression flanges.

Prior AISC and AASHTO developments have accepted this conservatism. The AASHTO (2017) Specifications limit the flange slenderness to $b_f/2t_f = 12$ as a precaution against flange welding distortion as well as to ensure robustness of rectangular flange plates during fabrication and construction. However, there are applications where a more accurate characterization of slender flange local buckling resistances can be beneficial.

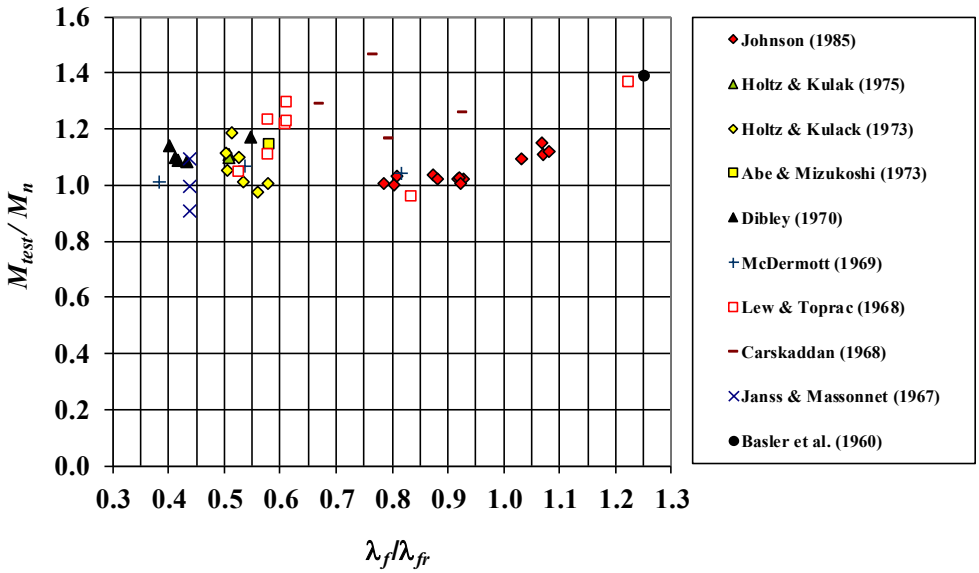

Figure 5. M_{test}/M_n versus λ_f / λ_{fr} for 11 rolled and 36 welded I-section experimental tests in which the flexural resistance is governed by FLB (AISC 2016), adapted from White and Kim (2008a).

Figure 6 presents the same experimental tests presented in Fig. 5 using the recommended FLB procedure in this chapter. From this figure, one can observe that the predictions with the recommended procedure provides a better correlation with the experimental tests. The largest gain in strength by using the recommended procedure is detected approximately 40%, and the most conservative predictions, which is

approximately 48% conservative, reduced to 31% conservative. An outlier case, which is from Lew & Toprac (1968), is 18% unconservative. This case is a hybrid girder test involving Grade 100 flanges, and a Grade 36 web. The previsions presented here are not intended for these types of extreme hybrid cross-section members. The predictions are acceptable for hybrid members having only one change in the grade of the steel between the flanges and webs, such as Grade 70 flanges and Grade 50 webs.

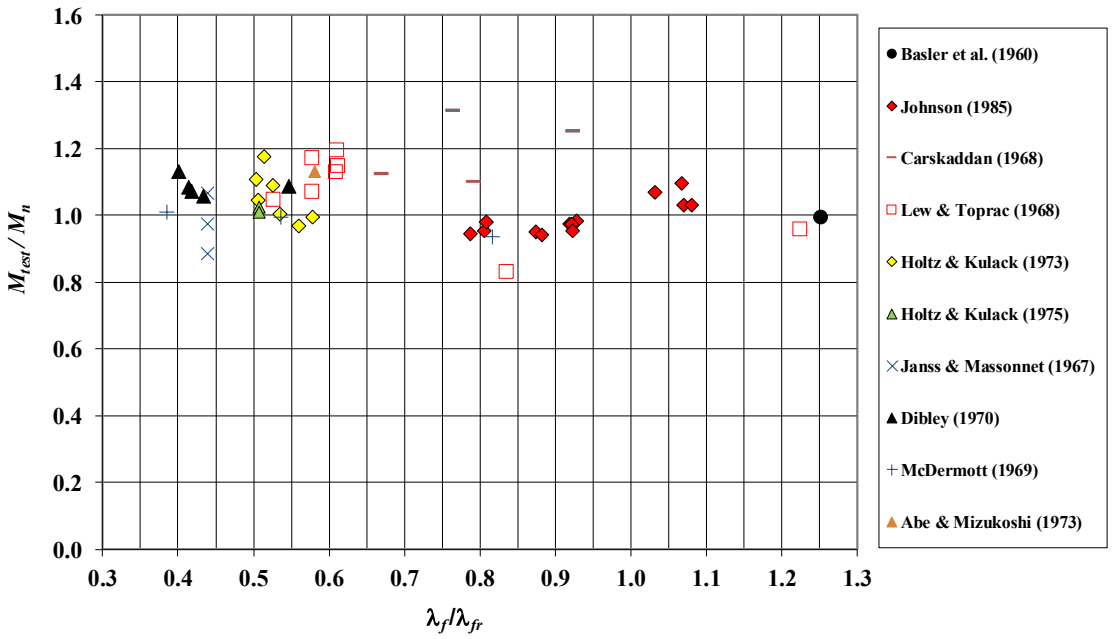

Figure 6. M_{test}/M_n versus λ_f / λ_{fr} for 11 rolled and 36 welded I-section experimental tests in which the flexural resistance is governed by FLB (recommended procedure), adapted from White and Kim (2008a).

Figure 7 compares the AISC (2016) predictions, and recommended predictions discussed subsequently in this section, to test simulation results from Toğay and White (2017) for a set of identical simply-supported beam-columns with doubly-symmetric cross-sections having a slender compression flange and a noncompact web in flexure (all elements classified as slender in uniform axial compression), subjected to different ratios

of primary bending moment and axial compression (The Finite Element Analysis test simulation procedures employed in this research are detailed in Appendix A.). The AISC (2016) flexural resistances are governed by the FLB limit state for these members, resulting in up to 34 % conservatism relative to the test simulation results.

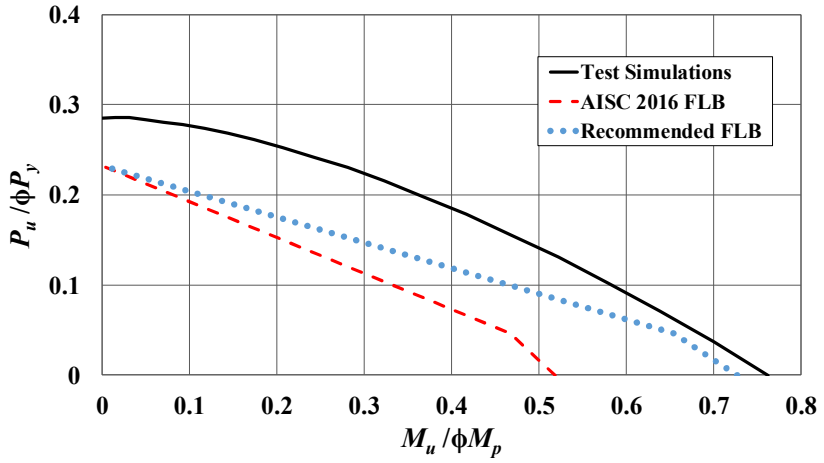

Figure 7. Strength envelopes from test simulation, the AISC (2016) column and FLB flexural strength provisions, and the AISC column and recommended FLB flexural strength provisions, torsionally and flexurally simply-supported doubly-symmetric I-section members with b_f = 6.5 in., t_f = 0.1806 in. ($b_f/2t_f$ = 18), h = 19.8 in., t_w = 0.1787 (h/t_w = 111), and $L_x = L_y = L_z = L_b$ = 13 ft, subjected to axial force and moment gradient loading with an applied moment at one end.

A succinct modification of the current flexural strength provisions to recognize the compression flange postbuckling resistance is possible. An important attribute of the Specification equations that must be preserved is the accurate characterization of FLB resistance, larger than the compression flange yield moment and up to the plastic moment of the cross-section, for I-sections having noncompact flanges and noncompact or compact webs. Approaches in other standards that characterize the FLB postbuckling strength of a slender flange, but then do not recognize the ability of a noncompact flange section to achieve strengths larger than the yield moment to the compression flange, are deficient for

common design situations involving compact or noncompact flanges and noncompact or compact webs.

For slender-web singly-symmetric members, the AISC Specifications have traditionally employed a Tension Flange Yield (TFY) limit state check simply equal to the yield moment of the tension flange, M_{yt}. In prior practice, engineers have sometimes used singly-symmetric sections with a smaller tension flange to achieve highly optimized designs. These types of sections are efficient, since the depth of web in compression is reduced by shifting of the neutral axis toward the larger compression flange, and since the tension flange does not need to be as large for purposes of design efficiency (because it is in tension rather than in compression). Numerous studies, e.g., Subramanian and White (2017d), have shown that the TFY strength check can be quite conservative for slender-web I-section members. Figure 8 illustrates this conservatism in the AISC (2016) procedures, and improvements gained by the recommended procedures discussed subsequently, relative to test simulation results for a set of simply-supported beam-columns. These 10 ft long members are singly-symmetric and are subjected to uniform primary bending. The right-hand quadrant of the plot corresponds to flexural compression on the larger flange. For this direction of bending, the AISC TFY limit state check governs the flexural resistance for $P_u = 0$. In the left-hand quadrant, the flexural resistance for $P_u = 0$ is governed for these members by FLB. The detailed behavior associated with the strength curves in Fig. 8 is explained in detail for similar members with $L_b = L_x = L_y = L_z = 5$ ft later in this section.

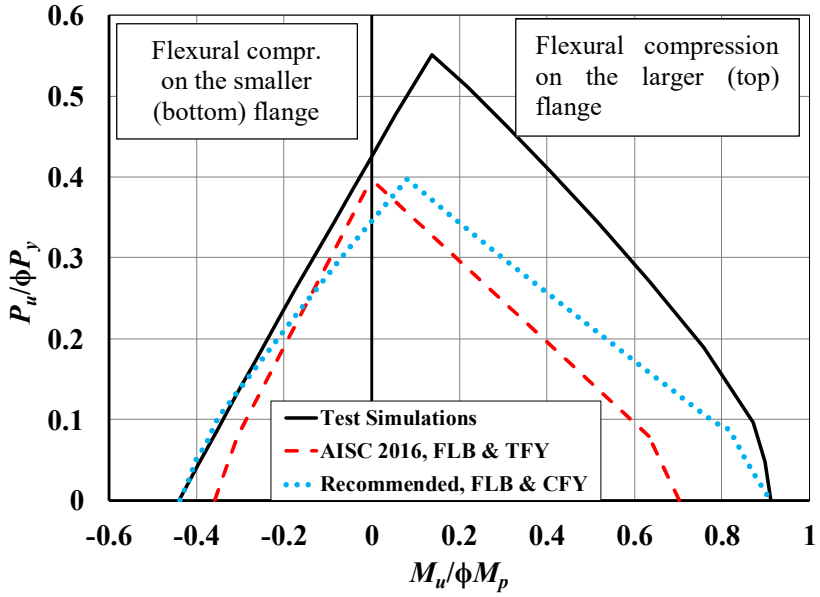

Figure 8. Strength envelopes from test simulation, the AISC (2016) column and flexural strength provisions, and the AISC column and recommended flexural strength provisions, torsionally and flexurally simply-supported singly-symmetric I-section members with $b_{fc} = b_{ft} = 8.0$ in., $t_{fc} = 0.75$ in. $t_{ft} = 0.25$ in., $h = 37.0$ in., $t_w = 0.1875$ in., and $L_x = L_y = L_z = L_b = 10$ ft, subjected to uniform primary bending moment and axial compression.

If a member's web and compression flange are compact, and the member is sufficiently braced, the AISC Specification predicts a flexural capacity equal to the fully plastic moment, M_p. However, in the limit that the web is slender, the Specification has traditionally limited the resistance to the yield moment to the tension flange, M_{yt}. This estimate has been shown to be substantially conservative relative to resistances obtained from test simulation (Subramanian and White 2017a). Noncompact-web members are also handled quite conservatively in the present Specification as the web becomes thinner.

It is observed that for members where the current TFY limit state controls, eliminating the Tension Flange Yield check and calculating the member yield moment to the compression flange, M_{yc}, accounting for the early spread of yielding within the tension zone, gives a better characterization of the flexural resistance. The modified calculation of

M_{yc} can be written in a succinct closed form. This form is the *true* moment at first yielding of the compression flange, and is designated specifically as M_{ycT}, i.e., the yield moment to the compression flange, considering the early yielding of the tension flange and the spread of yielding within the tension zone.

In addition to the Tension Flange Yielding (TFY) and Flange Local Buckling (FLB) limit states improvements, for sections which employ slender plates under axial compression, or noncompact or slender plates under flexural compression, it is observed that the interaction between axial and flexural strengths is close to linear. Figure 8 shows the interaction curve of flexural and axial strength of a built-up section which has slender flange under both axial and flexural loading. The left quadrant of the figure for the test simulation results shows the linear interaction between the axial and flexural loading. The proposed changes TFY and FLB limit states calculations, improve the overall accuracy of the beam-column strength predictions.

3.1 Improved Characterization of Flange Local Buckling (FLB) Limit States

For cases involving FLB, the conservatism associated with the current buckling-based calculation can be rectified by recognizing the compression flange postbuckling resistance via an application of the unified effective width approach. The following is one way of accomplishing this.

For sections with a slender compression flange in flexure:

a) The effective width of the flange is calculated directly given the flange elastic buckling stress

$$F_{el} = \frac{0.9Ek_c}{(b_f / 2t_f)^2} \tag{49}$$

and the assumption that the compression flange stress within the effective width is F_y at the strength limit in flexure. The terms $F_{e\ell}$ and F_y are substituted into Winter's unified effective width equation,

$$b_e = b_f \left(1 - 0.22\sqrt{\frac{F_{e\ell}}{F_y}}\right)\sqrt{\frac{F_{e\ell}}{F_y}} \tag{50}$$

b) The location of the neutral axis for the effective cross-section, relative to the inside of the compression flange, D_{ce}, and the effective section modulus corresponding to the compression flange, S_{xce}, are determined.

c) The FLB resistance, considering the flange postbuckling strength, is then determined as $R_{pg}M_{yce}$, where M_{yce} is the yield moment to the compression flange for the effective section and R_{pg} is the web bend buckling strength reduction factor, equal to 1.0 for compact- and noncompact-web sections, and calculated as discussed in Section 4 for slender-web sections.

For sections having a noncompact flange in flexure:

a) The effective width reduction based on the noncompact flange slenderness limit, λ_{rf}, is applied to the compression flange (regardless of the actual flange slenderness), and the corresponding $R_{pg}M_{yce}$ is determined using the procedure

explained above. This establishes an "anchor point" corresponding to the flange postbuckling resistance at $\lambda = \lambda_{rf}$, labeled as $M_{yce(\lambda r)}$ in Fig. 9.

b) A modified linear interpolation is then employed between the anchor points (λ_{rf}, $M_{yce(\lambda r)}$) and (λ_{pf}, M_{maxFLB}), where M_{maxFLB} is the plateau resistance equal to M_p for a compact-web section, $R_{pc}M_{yc}$ for a noncompact-web section, and $R_{pg}M_{yc}$ for a slender web section. This gives the improved estimate of the inelastic FLB resistance illustrated in Fig. 9. (Note: M_{ycT} is substituted for M_{yc} in the case of cross-sections that exhibit early tension flange yielding.)

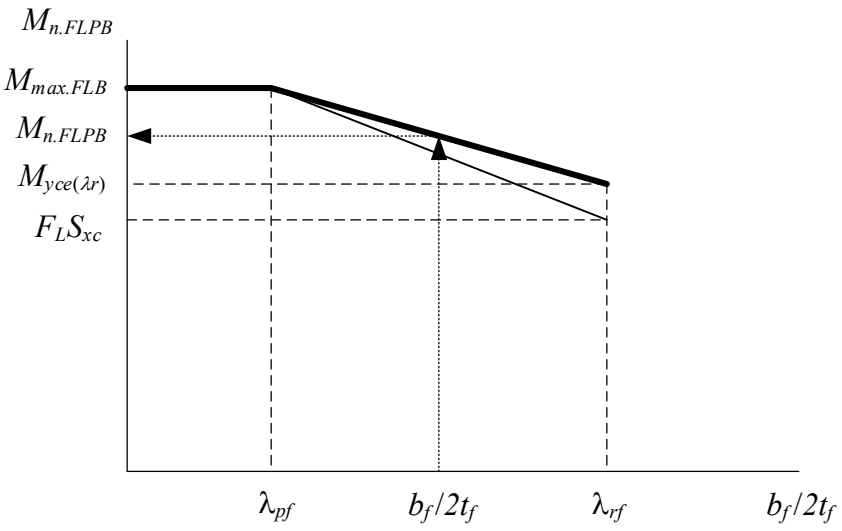

Figure 9. Calculation of compression flange local postbuckling (FLPB) resistance within the inelastic FLB range.

The above calculation preserves the clear qualities of the AISC FLB resistance calculations in for common cases with noncompact and compact I-section flanges, while recognizing the additional resistance associated with the flange local postbuckling response of slender flanges. White and Kim (2008a & b) report reliability indices for FLB that are somewhat larger than the target value of 2.6 for statically determinate beam tests, based on

the current AISC (2016) FLB equations. The above update results gives a reliability index estimates closer to 2.6.

The updates mentioned above significantly improve the FLB resistance predictions corresponding to $P_u = 0$ in Figs. 7 and 8. The updates also improve the overall prediction of the strengths under combined flexure and axial load. It should be noted that the strength predictions for high axial load cannot be improved significantly relative to the results shown here unless a more accurate column strength curve were adopted. An improved representation of the shape of the beam-column strength curve can be obtained by using Inelastic Buckling Analysis (Toğay et al. 2018)

3.2 Improved Characterization of Tension Flange Yielding (TFY) Limit States

When a singly-symmetric section is subjected to flexure with the larger flange in compression, the flexural resistance can be governed by tension flange yielding (TFY). If the section has a slender-web, the TFY resistance can be quite conservative. While the AISC (2016) TFY limit is equal to the plastic moment capacity ($\phi_b M_p$) for compact-web I sections, the TFY limit is equal to the tension flange yield strength ($\phi_b M_{yt}$) for slender-web sections.

For cases in which first yielding is encountered at the tension flange (and for which the TFY resistance check is currently employed), one can account for the early yielding on the tension side of the neutral axis in the calculation of the yield moment to the compression flange. This modified yield moment is referred to as M_{ycT}. A representative flexural stress profile associated with this calculation is shown in Fig. 10. Mechanistically, the use of M_{ycT} is more rigorous than the use of M_{yc}, since M_{ycT} captures the influence of yielding on the

tension side of the neutral axis. This modified yield moment can be employed with the FLB calculations discussed previously, as well as within the LTB equations, to provide an accurate characterization of the FLB and LTB limit states, including the impact from early yielding in flexural tension. The TFY limit state calculations are in effect folded into the determination of M_{ycT}. No explicit TFY limit state check is required in this updated approach. The resulting calculations are explained further below.

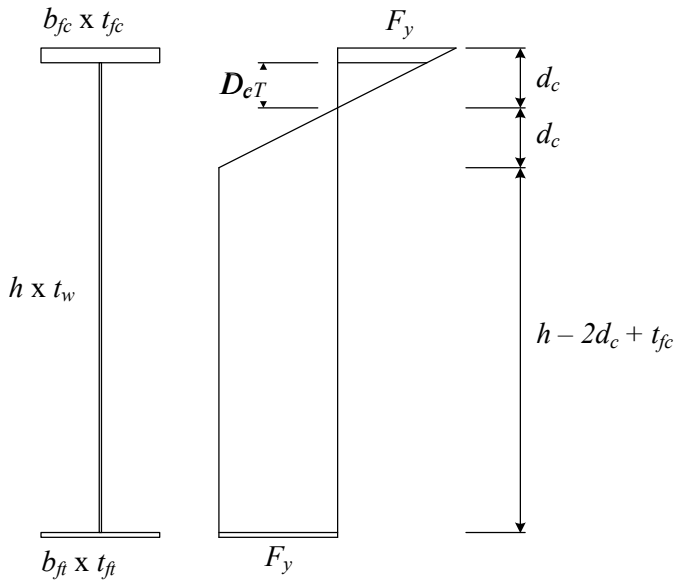

Figure 10. Representative flexural stress profile associated with the calculation of M_{ycT}, considering early yielding on the tension side of the neutral axis.

A simple set of equations can be derived for the calculation of M_{ycT} by working with the flange forces at the flange centroids, rather than considering rectangular stress blocks associated with the flange forces (see Fig. 10). This streamlined calculation of M_{ycT} requires the distance from the top (extreme fiber) of a rectangular compression flange to the neutral axis, d_c. This variable is determined such that the net longitudinal force from the stress distribution in Fig. 10 is equal to zero:

$$d_c = \frac{\Delta A + \sqrt{\Delta A^2 + 2A_{fc}A_{wfc} - A_{wfc}^2}}{4t_w} \tag{51}$$

where:

$$\Delta A = A_{ft} + A_w + A_{wfc} - A_{fc} \tag{52}$$

and

$$A_{ft} = b_{ft}t_{ft}, \quad A_w = ht_w, \quad A_{fc} = b_{fc}t_{fc}, \quad A_{wfc} = 2t_{fc}t_w \tag{53}$$

Given d_c, the depth of the web in compression, D_{cT}, is obtained as shown in Fig. 10 is calculated as

$$D_{cT} = d_c - t_{fc} \tag{54}$$

For welded built-up sections,

$$h_c = 2D_{cT} \tag{55}$$

When $D_{cT} > 0$ (neutral axis located within the web)

$$M_{ycT} = F_y\left[\frac{A_{fc}}{d_c}\left(\frac{D_{cT}t_{fc}}{2} + \frac{t_{fc}^2}{3}\right) + A_{ft}\left(h + \frac{t_{ft}}{2}\right) + \frac{t_w}{2}\left(h^2 - t_{fc}^2 - \frac{7d_c^2}{3} + 3d_c t_{fc} - \frac{D_{cT}^3}{3d_c}\right)\right] \tag{56}$$

For cases where D_{cT} in Eq. (54) becomes negative, the plastic neutral axis is located in the compression flange and the neutral axis associated with first yielding of the compression flange also tends to be in the compression flange. For this case, M_{ycT} may be approximated with good accuracy as the fully plastic moment M_p.

Given the above calculations of D_{cT} and M_{ycT}, these values are substituted for the terms D_{cT} and M_{yc} in the flowcharts presented in Section 3.3, which detail a recommended unified calculation of the flexural resistance for general homogeneous I-section members.

3.3 Improved Characterization of Lateral-Torsional Buckling (LTB) Limit States

Prior to discussing the details of the INBA procedures, it is essential to discuss an important change that is needed to the AISC/AASHTO flexural resistance equations to allow for accurate capture of experimental test and advanced test simulation results by the refined proposed inelastic buckling analysis procedures.

Subramanian et al. (2018) propose that, in light of additional experimental and advanced test simulation data generated since the original calibration of the unified provisions, as well as the availability of simple estimates of inelastic LTB effective length factors and the emergence of practical capabilities that accurately account for inelastic end restraint effects, several modifications of the unified, AISC and AASHTO resistance equations should be considered:

1. The value of L_p (limiting laterally unbraced length for the limit state of yielding) should be taken as $0.63 r_t \sqrt{E / F_y}$.

2. The nominal compression flange stress, at which yielding and geometric imperfection effects start to impact the LTB resistance, should be reduced to F_{yr} (AASHTO) and F_L (AISC) = $0.5F_{yc}$.

3. The noncompact web slenderness limit (λ_{rw}) should be set as

$$\lambda_{rw} = \max\left(5.7\sqrt{\frac{E}{F_{yc}}}, \min\left((3.1+2.5\frac{A_{fc}}{A_{wc}})\sqrt{\frac{E}{F_{yc}}}, 4.6\sqrt{\frac{E}{F_{yc}}}\right)\right) \quad (57)$$

Subramanian et al. (2018) show that these changes result in a more uniform level of reliability, as a function of the LTB slenderness, consistent with the minimum target of $\beta = 2.6$ for statically determinate beams intended in the AISC LRFD Specification (AISC 2010).

In Fig. 11, an example beam-column plot for DS-1, a W21x44 rolled section with 144 in unbraced length, is provided. This figure shows the results from calculations using the following methods:

- Appendix 1.3* - Refined test simulations based on Appendix 1.3 of the AISC (2016) Specification using one-half of typical nominal residual stresses and geometric imperfections. (Further specifics of the Finite Element Analysis test simulation procedures employed in this research are detailed in Appendix A.)

- INBA* - Direct Analysis Method solutions using Inelastic Nonlinear Buckling Analysis based on the AISC (2016) resistance equations modified as discussed above
- DM* - Routine DM solutions using the AISC (2016) Specification provisions with the above flexural resistance changes recommended in Sections 3.1 and 3.2, and Subramanian et al. (2018)
- Appendix 1.3 - Refined test simulations per AISC (2016) using typical full nominal residual stresses and geometric imperfections
- INBA - Direct Analysis Method solutions using Inelastic Nonlinear Buckling Analysis based on the AISC (2016) resistance equations
- DM - Routine Direct Analysis Method solutions using the current AISC (2016) flexural resistance equations (Griffis and White 2013)

The nominal residual stresses for rolled I-section members and the nominal geometric imperfections considered in the Appendix 1.3* calculations in this work are discussed in the Appendix. Subramanian and White (2016) show that these reduced nominal residual stresses and geometric imperfections are necessary for advanced test simulation results to provide a close correlation with experimental test data for I-type cross-sections. Consequently, the Appendix 1.3* solution is employed as the benchmark finite element simulation in this work. As can be observed from Fig. 11, without modifying the AISC flexural resistance equations, the moment capacity is predicted too optimistically. When the results from Appendix 1.3 of AISC Specifications solutions (using full nominal residual stresses and geometric imperfections) are compared to the DM solutions based on

the current Specification flexural resistance equations, the over-prediction by the DM solutions is substantial.

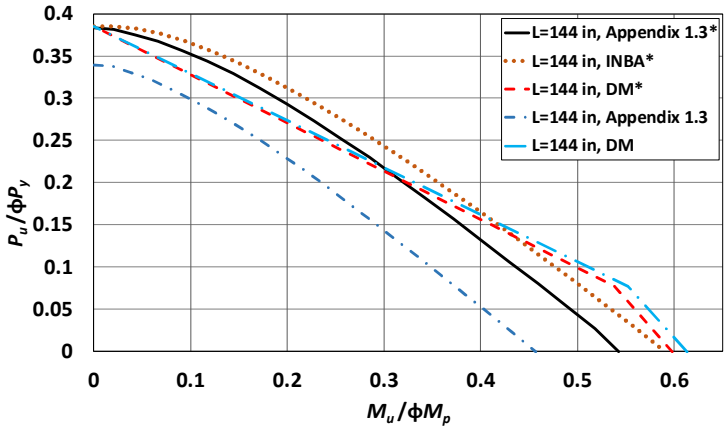

Figure 11. DS-1 (W21x44) L=144 in, comparison of uniform primary moment results versus recommended results

3.4 Beam-Column Interaction Improvement

When the member is under both axial and flexural loading, the τ_a and τ_{ltb} equations are calculated using the unity check (UC) values instead of the $\Gamma P_u/\phi_c P_{ye}$ and $\Gamma M_u/\phi_b M_{max}$ ratios (Section 2.5). White, Jeong et al. (2016) shows a close correlation between the corresponding INBA predicted strengths and I-section beam-column resistances.

For certain cases, the bilinear interaction is observed to result in unconservative results near to the knee region. The reason for the unconservative differences is that the bilinear interaction curve is based on planar frame plastic zone analysis results. This type of analysis does not account for the three-dimensional beam-column limit states behavior, including the influence of local buckling and cross-section distortion. Column-type sections with relatively thick flanges and webs typically are better able to develop the strengths associated with this "knee." When the member cross-section has slender plates

under uniform axial compression, or noncompact or slender plates under flexural compression, the beam-column resistances are characterized more accurately by the linear instead of the bilinear strength interaction curve (see Fig. 12).

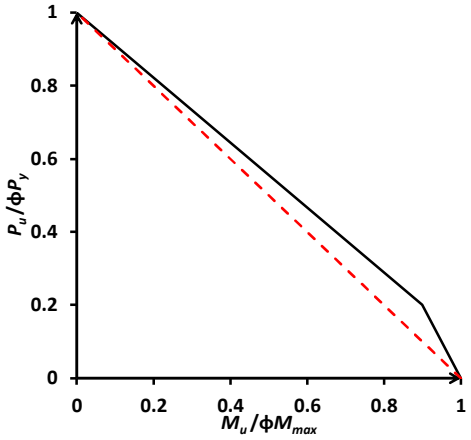

Figure 12. Beam colum linear and bilinear cross-section strength interaction plot

1. When the section has slender plates under axial compression, or noncompact or slender plates under flexural compression,

$$\text{UC} = \Gamma P_u / \phi_c P_{ye} + \Gamma M_u / \phi_b M_{max} \tag{58}$$

2. Otherwise, the UC equations are taken from the AISC 2016 Specifications as

$$\text{UC} = \Gamma P_u / \phi_c P_{ye} + 8/9\, \Gamma M_u / \phi_b M_{max} \qquad \text{for } \Gamma P_u / \phi_c P_{ye} \geq 0.2 \tag{59}$$

$$\text{UC} = \Gamma P_u / 2\phi_c P_{ye} + \Gamma M_u / \phi_b M_{max} \qquad \text{for } \Gamma P_u / \phi_c P_{ye} < 0.2 \tag{60}$$

3.5 Summary of Changes to the Unified Flexural Resistance Provisions

White (2008) provides a detailed overview of the so-called "unified flexural resistance provisions" developed as part of the major updates to the AASHTO LRFD Specifications in 2004 and the AISC Specification in 2005. White (2008) provides flowcharts that illustrate the overall organization of the unified calculations. Minor differences between the finalized AASHTO and AISC provisions and the unified provisions are explained where they occur.

Figures 13 through 15 show a modified form of the flowcharts from White (2008). These updated flowcharts implement the recommended changes discussed above in Sections 3.1 and 3.2 in the context of homogeneous I-section members. Furthermore, these flowcharts implement updates to the AISC LTB resistance calculations recommended by Subramanian, Jeong et al. (2018) necessary to address low-reliability index estimates in the intermediate inelastic LTB range, particularly for welded I-section members. The flowcharts in Figs. 13 through 15 utilize the terms D_c and M_{yc} for the depth of the web from the inside of the compression flange to the neutral axis at the nominal first yielding of the compression flange and the yield moment to the compression flange, respectively. The corresponding values D_{cT} and M_{ycT} discussed in Section 3.2 are substituted into D_c and M_{yc} in cases where early yielding occurs at the tension flange, i.e., when $M_{yt} < M_{yc}$. (It should be noted that S_{xc} in Figs. 13 through 15 is the elastic section modulus to the compression flange, without any consideration of early tension flange yielding.) All the variables in Figs. 13 through 15 are expressed using the AISC (2016) notation, with the exception of $2D_c$, which is expressed in the AISC Specification as h_c. The term R_{pg} is denoted by R_b and the term F_L (the "nominal compressive strength above which the inelastic buckling limit

states apply") is denoted by F_{yr}, in AASHTO (2017). Equation numbering in Fig. 13 to 15 are numbered with respect to figure number of the equation (e.g., F13-1: Figure 13-Equation 1).

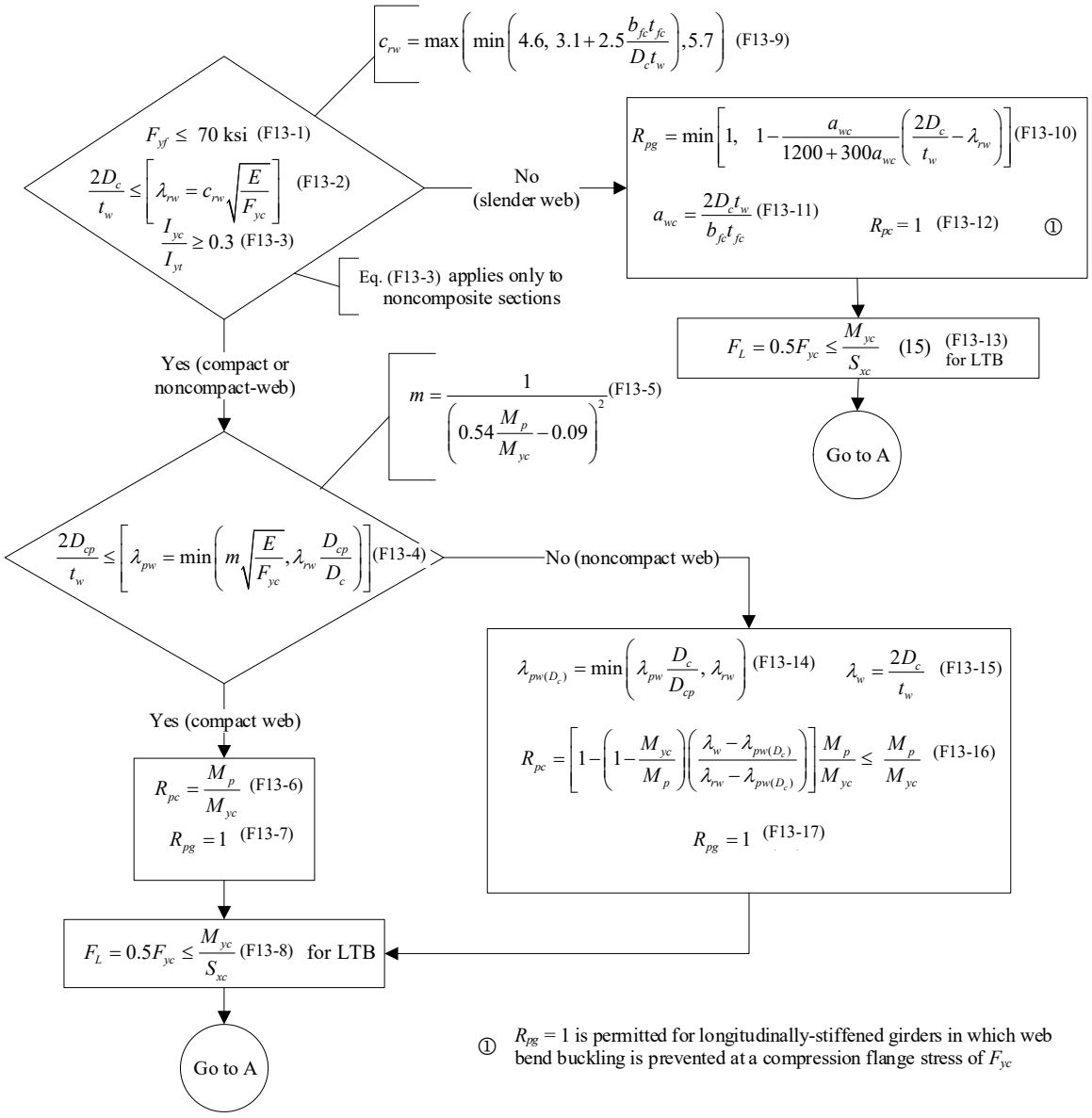

Figure 13. Calculation of the web slenderness based parameters, R_{pc} and R_{pg}, and the nominal compressive strength above which inelastic buckling limit states apply, F_L.

The recommended modifications to the original "unified" flowcharts are as follows:

- In Eq. F13-2 (see Fig. 13), the coefficient 5.7 in the corresponding AISC (2016) equation is replaced by the coefficient c_{rw}. This coefficient is defined in Eq. F13-9. This modification is based on observations by Subramanian and White (2017b), from physical tests and test simulations, that I-girders with relatively small flanges compared to the web area exhibit a minor reduction in their flexural resistances when their webs are near the current noncompact web limit. That is, noncompact-web girders of this nature tend to perform more like slender-web girders.
- In the flowchart cells containing Eqs. F13-6, F13-7, F13-16, F13-17 and F14-1, F14-2, the calculation of R_{pt} is eliminated. The recommended calculations no longer require any explicit calculation of Tension Flange Yielding (TFY). The TFY response is folded into the calculation of $M_{yc} = M_{ycT}$ for cross-sections having a larger compression flange such that $M_{yt} < M_{yc}$.
- Equations F13-8 and F13-13 are modified to $F_L = 0.5F_{yc}$ pertaining to Lateral Torsional Buckling. This is based on the recommendations from Subramanian et al. (2018) addressing low-reliability index estimates in the intermediate inelastic LTB range. Engineers often consider F_L to simply represent residual stress effects. However, there is far more to F_L than just the consideration of residual stresses. This term also accounts for the reduction in the LTB capacity at intermediate unbraced lengths due to amplification of initial geometric imperfections by stability effects. It should be noted that the updated provisions no longer require F_L in the determination of the FLB resistance, other than in the calculation of λ_{rf} where it is

recommended that F_L for FLB may be taken simply as $0.7F_y$ for homogeneous cross-section members. The term F_LS_{xc} is replaced by $M_{yce(\lambda r)}$ as discussed below

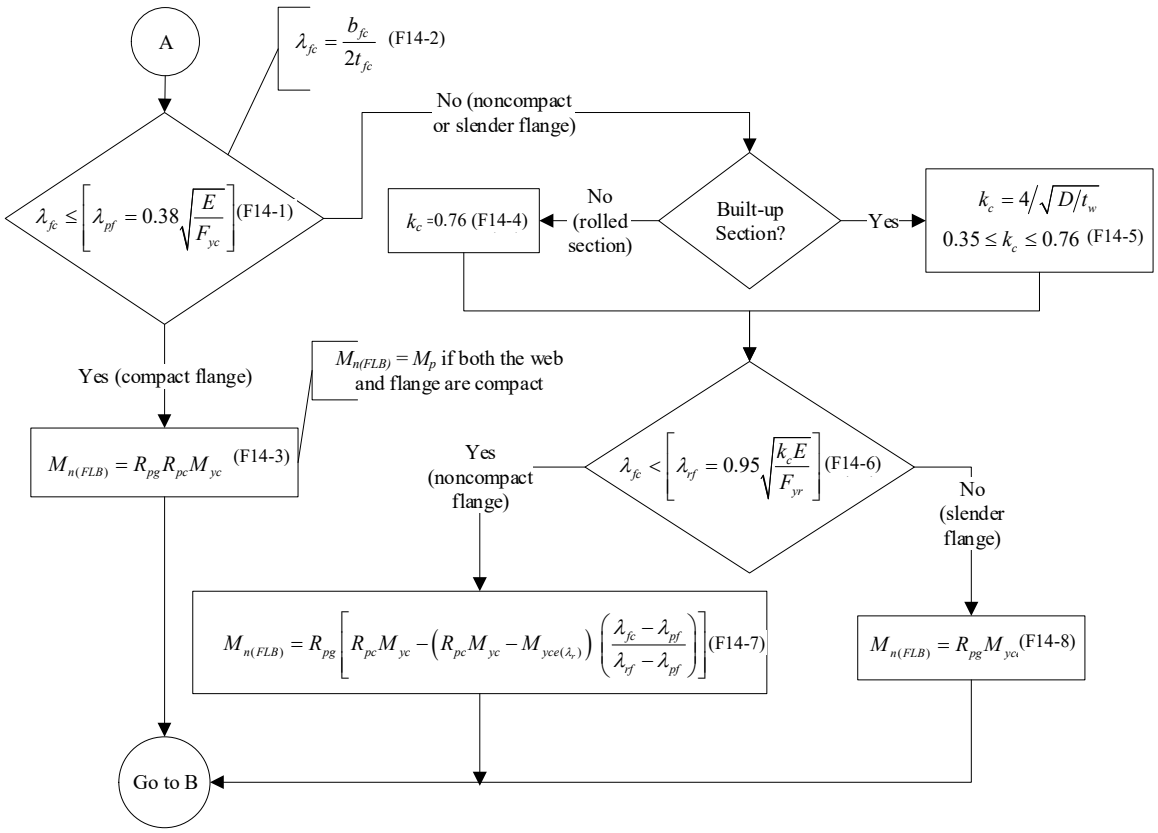

Figure 14. Flange Local Buckling strength calculations.

- Equation F15-1 in Fig. 15 is modified from the original unified equation for L_p to again address low-reliability index estimates in the intermediate inelastic LTB range (Subramanian et al. 2018). In addition, this modified equation recognizes that test simulations commonly show a smaller "plateau length" than indicated by the original unified provisions (Greiner and Kaim 2001, Kim 2010, Subramanian and White 2017b & c).

- Equations F15-9 and F15-10 specify the limit on the moment above which inelastic buckling limit states apply. This moment is taken as F_LS_{xc} as in the prior unified

provisions. However, in the case of highly singly-symmetric cross-sections with the larger flange in compression, $M_{yc} = M_{ycT}$ potentially can be smaller than $F_L S_{xc}$. In this extreme case, M_{ycr} is taken equal to M_{ycT}.

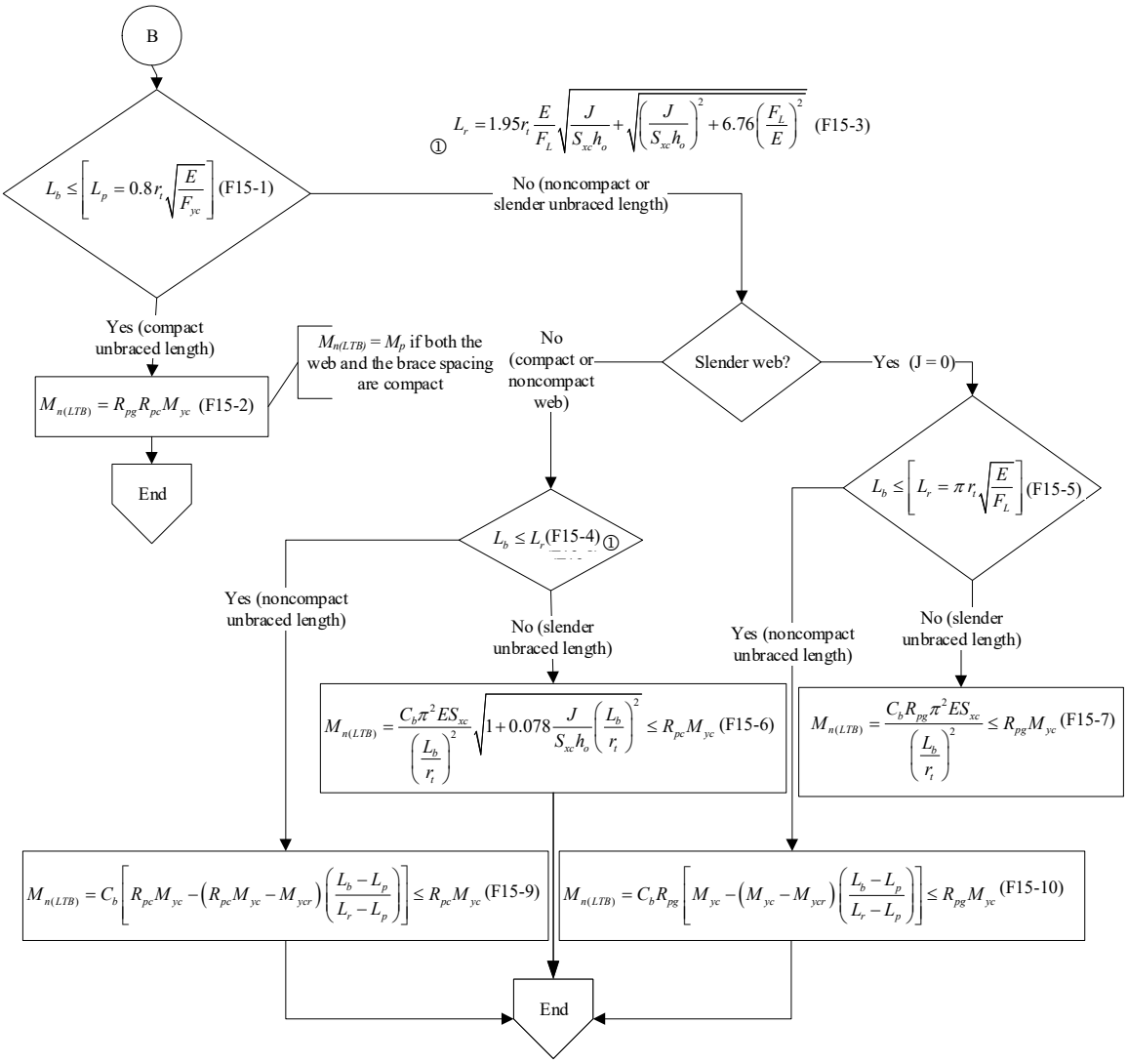

Figure 15. Lateral Torsional Buckling strength calculations

White (2008) shows a fourth flowchart for the calculation of $M_{n(TFY)}$. As stated above, the TFY limit state check is replaced by the consideration of early yielding in flexural tension in the calculation of the yield moment to the compression flange, M_{ycT}. This relegates Tension Flange Yielding to a secondary role in the calculation of the flexural

resistance, similar to the manner that the original unified flexural resistance equations relegated Web Local Buckling to a secondary role in the calculation of the FLB and LTB resistances.

CHAPTER 4. VALIDATION AND DEMONSTRATION

The proposed inelastic buckling analysis procedures utilize stiffness reduction factors that many engineers are accustomed to for members subjected to concentric axial loading. However, they also use stiffness reduction factors associated with the Specification lateral torsional buckling equations to allow for the evaluation of beam LTB responses. The recommended INBA solution uses a basic interpolation between the column and beam inelastic stiffness reduction factors to address general beam-column member stability limit states. For the limit states, the recommendations for Flange Local Buckling (FLB) and Tension Flange Yielding (TFY) are employed which are explained in Chapter 3. This approach employs a Thin-Walled Open-Section (TWOS) frame element for the buckling calculations. This element has seven degrees of freedom at each joint or nodal location – three translations, three rotations, and one warping degree of freedom, which allows for the important consideration of member warping rigidity in the evaluation of member stability limit states involving torsion. The INBA solutions presented in this dissertation are conducted using the SABRE2-V2 software (Toğay et al. 2018).

In the following presentations, a postfix "*" is appended to the names INBA and DM to emphasize that these calculations are all based on modified AISC flexural resistance equations recommended in Section 3. In addition, the postfix "*" is also appended to Appendix 1.3, to emphasize that the test simulation solutions are based on one-half the residual stresses and geometric imperfections as recommended by Subramanian and White (2017a) (See Appendix A for a detailed description of the Finite Element Analysis test simulation procedures employed in this research.). In addition to the INBA* and DM*

solutions, current AISC (2016) solutions are also provided with current Lateral Torsional Buckling (LTB), Flange Local Buckling (FLB), and Tension Flange Yielding (TFY) calculations.

4.1 Prismatic Member Studies

This section assesses the accuracy of two Direct Analysis Method solutions. One is referred to routine Direct Analysis Method and uses the AISC stability-based resistance equations, and the other is an explicit inelastic buckling analysis to determine buckling based resistances. The proposed Inelastic Nonlinear Buckling Analysis (INBA*) procedure, as well as the conventional DM procedure, are evaluated for prediction of the lateral torsional buckling resistance of a wide range of doubly-symmetric and singly-symmetric I-section members.

The test simulations considered in this section are beam, column and beam-column tests considering the following types of members and loadings:

- Doubly-Symmetric Cross-Section Members
  - Uniform bending loading
  - Moment gradient loading
  - Uniformly distributed loading
- Singly-Symmetric Cross-Section Members
  - Uniform bending loading
  - Moment gradient loading

4.1.1 *Overview of Approach for General Evaluation Relative to Test Simulations*

For the evaluation of Inelastic Buckling Analysis (INBA) and Direct Analysis Method (DM) with the recommended changes in Chapter 3, a normalized beam-column plot is used. In this plot, the normalization is performed using the Appendix 1.3* maximum axial strength ($P_{sim,max}$) and maximum flexural strength ($M_{sim,max}$) values (Fig. 16).

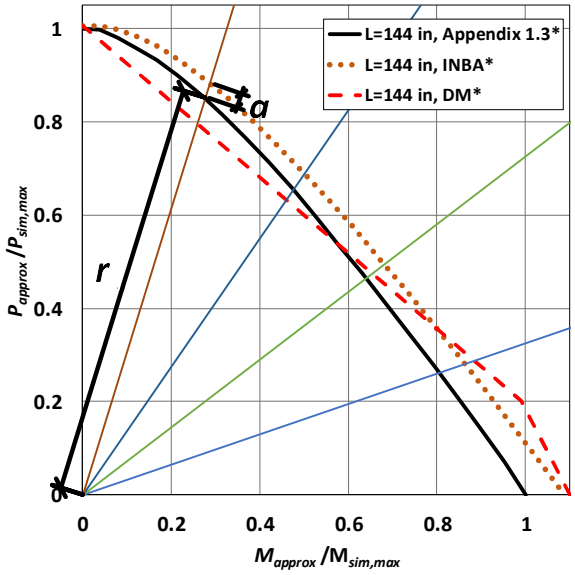

Figure 16. Normalized Beam-Column Interaction Plot (Example Case: DS-1 L = 144 in Uniform Moment Loading)

Using six equally spaced radial lines on the normalized interaction plot, the percentage differences in the DM*, INBA*, and DM solutions, relative to the Appendix 1.3* solutions, are calculated as

$$Difference\ wrt.\ Appendix\ 1.3^*(\%) = \left(\frac{a}{r}\right) \times 100 \tag{61}$$

where r is the distance from the origin to the Appendix 1.3* result, and *a* is the distance between either Appendix 1.3* and INBA* results, Appendix 1.3* and DM* results, or Appendix 1.3* and DM results. A positive difference, as illustrated by the dimension lines shown in Fig. 16, indicates that the prediction is conservative relative to the test simulation resistance, whereas a negative difference indicates that the prediction is unconservative relative to test simulation resistance.

The 0^o line corresponds to the flexural (beam) loading case, while the 90^o line corresponds to the pure axial compression case. The difference plots are generated with the values from Eq. (61) for each of the cross-section cases and load combinations.

For singly-symmetric cases, since the application of the moment is both in positive and negative direction, 180^o line is also generated. That line corresponds to the negative moment application. The plots are generated with the difference with respect to Appendix 1.3* values from Eq. (61) for each of the cross-section cases and load combinations.

The differences with respect to the Appendix 1.3* results are provided in box and whiskers style format plots for all doubly-symmetric and singly-symmetric sections. In these plots, the black "x" inside the boxes represents the mean of each data set. The bottom and top of the grey boxes represent the first (Q_1) and third (Q_3) quartile points, respectively. The bottom whisker is displayed at the most extreme data value within $Q_1 - 1.5 \times IQR$, and the top whisker is displayed at the most extreme data value within $Q_3 + 1.5 \times IQR$, where IQR is the interquartile range, calculated as $Q_3 - Q_1$. In addition, the solid horizontal lines inside the boxes represent the median value of the data sets. Data values that fall outside of the range between $Q_1 - 1.5 \times IQR$ and $Q_3 + 1.5 \times IQR$ are referred

as outlier data points. These data points are displayed as small black circular symbols in the plots.

4.1.2 *Doubly-Symmetric Prismatic Beam-Columns*

Three different loading configurations are examined for doubly-symmetric cross-sections. First, uniform primary moment cases with nine prismatic cross-sections are tested (Fig. 17). Second, moment gradient cases using the same prismatic cross-section set are evaluated (Fig. 18). Lastly, various W21x44 beam-columns subjected to uniformly distributed lateral load are studied (Fig. 19). A total of 609 + 588 + 63 = 1260 test simulations are conducted.

Figure 17. Uniform positive primary moment load configuration

Figure 18. Positive moment gradient load configuration

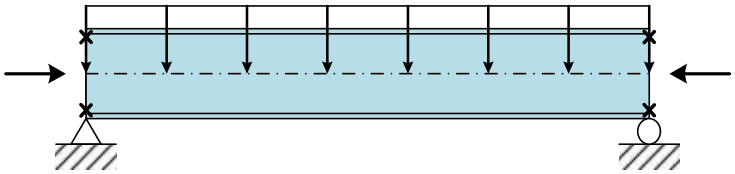

Figure 19. Uniformly distributed lateral load configuration

All the members are flexurally and torsionally simply-supported at their ends. That is:

(a) The end rotations within the plane of the member are free (unrestrained),

(b) One vertical support is in essence an idealized pin and the other is an idealized roller within the plane of the member,

(c) The member out-of-plane end rotations are free (unrestrained), and

(d) The member end cross-sections are free to warp (i.e., the two member flanges are free to "cross-bend" in opposite directions at member ends).

Specialized multi-point constraints as discussed by Kim (2010) are applied at the member ends in the finite element simulation models to achieve the above kinematic end conditions. In addition, the members do not have any intermediate lateral bracing. As such, their effective lengths $L_{cx} = L_{cy} = L_{cz}$ are all equal to their laterally unbraced length L. Subramanian et al. (2018) compare the results of INBA solutions to a relatively comprehensive database of I-section flexural tests involving various loading and end restraint conditions. Nine different cross-sections are considered in this study as summarized by Table 1. Members with short, intermediate and long unbraced lengths are considered for each of these sections. Member lengths (L) is set for short length less than L_p (Section 3.3). For intermediate lengths, L is set to a length between L_p and L_r. Finally, for long unbraced lengths, L is set to a length longer than L_r.

Table 1.Doubly-symmetric I-sections considered in validation studies (b_f = 6.5 in, d_w = 19.8 in).

Case	Description	t_f (in)	t_w (in)	$A_{fillets}$ (in^2)	$b_f/2t_f$	d_w/t_w
1	W21x44 Section	0.4500	0.3500	0.22	7.22	56.57
2	Equivalent Welded Section	0.4500	0.3500	0.00	7.22	56.57
3	Noncompact Web	0.4500	0.1787	0.00	7.22	110.80
4	Slender Web	0.4500	0.1238	0.00	7.22	160.00
5	Noncompact Flange	0.2708	0.3500	0.00	12.00	56.57
6	Noncompact Flange & Noncompact Web	0.2708	0.1787	0.00	12.00	110.80
7	Noncompact Flange & Slender Web	0.2708	0.1238	0.00	12.00	160.00
8	Slender Flange & Noncompact Web	0.1806	0.1787	0.00	18.00	110.80
9	Slender Flange & Slender Web	0.1806	0.1238	0.00	18.00	160.00

4.1.2.1 Member Strength Envelopes and Plots of Differences Relative to Test Simulation Studies, Doubly-Symmetric Members Subjected to Uniform Primary Bending

Beam-column interaction plots that compare the INBA*, DM*, and DM results with the Appendix 1.3* solutions are provided in this subsection. The plots are provided for all the cases for the uniform primary moment loading conditions shown in Table 1.

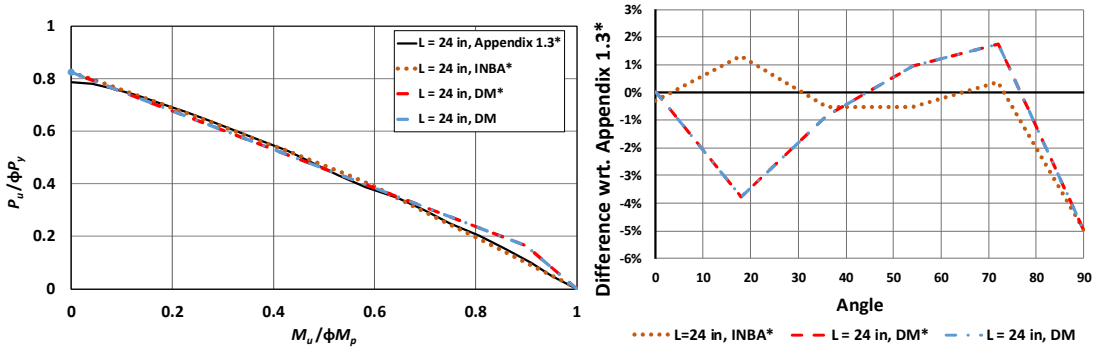

Figure 20. DS-1, uniform moment, beam-column strength curves and difference with respect to Appendix 1.3* curves (Lb=24 in, 60 in, 102 in, 144 in, 192 in)

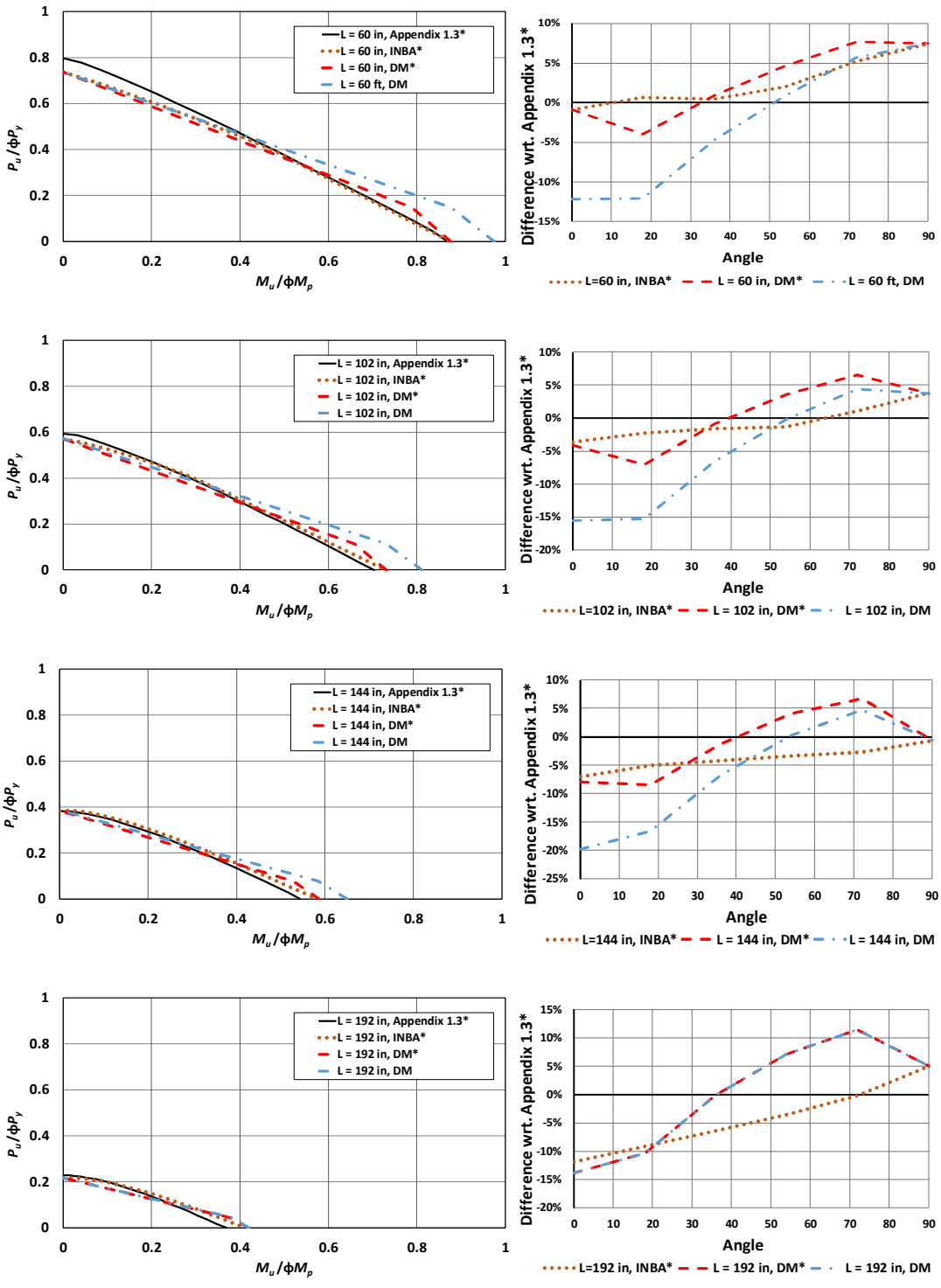

Figure 20 (continued). DS-1, uniform moment, beam-column strength curves and difference with respect to Appendix 1.3* curves (L_b=24 in, 60 in, 102 in, 144 in, 192 in)

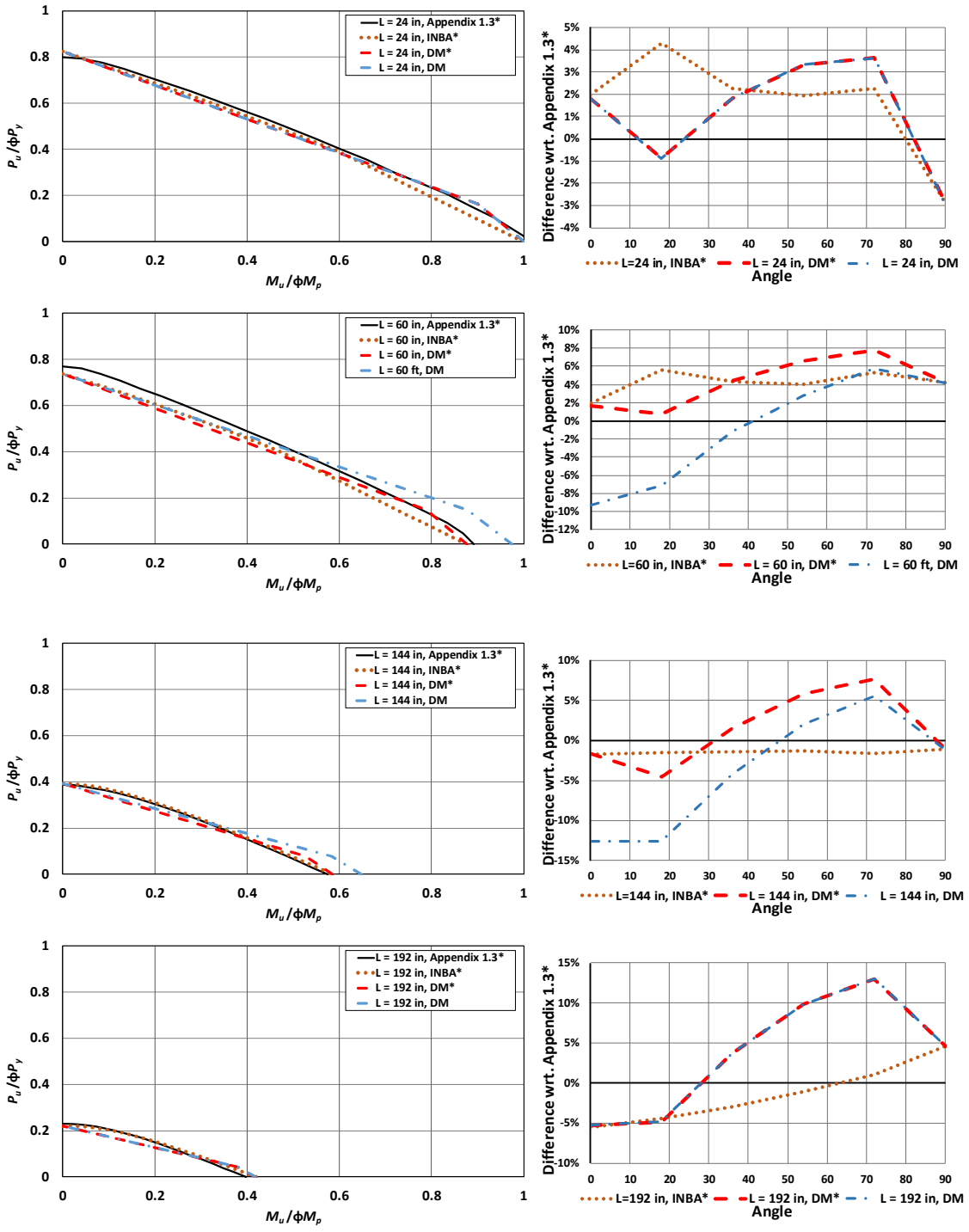

Figure 21. DS-2, uniform moment, beam-column strength curves and difference with respect to Appendix 1.3* curves (L_b=24 in, 60 in, 144 in, 192 in)

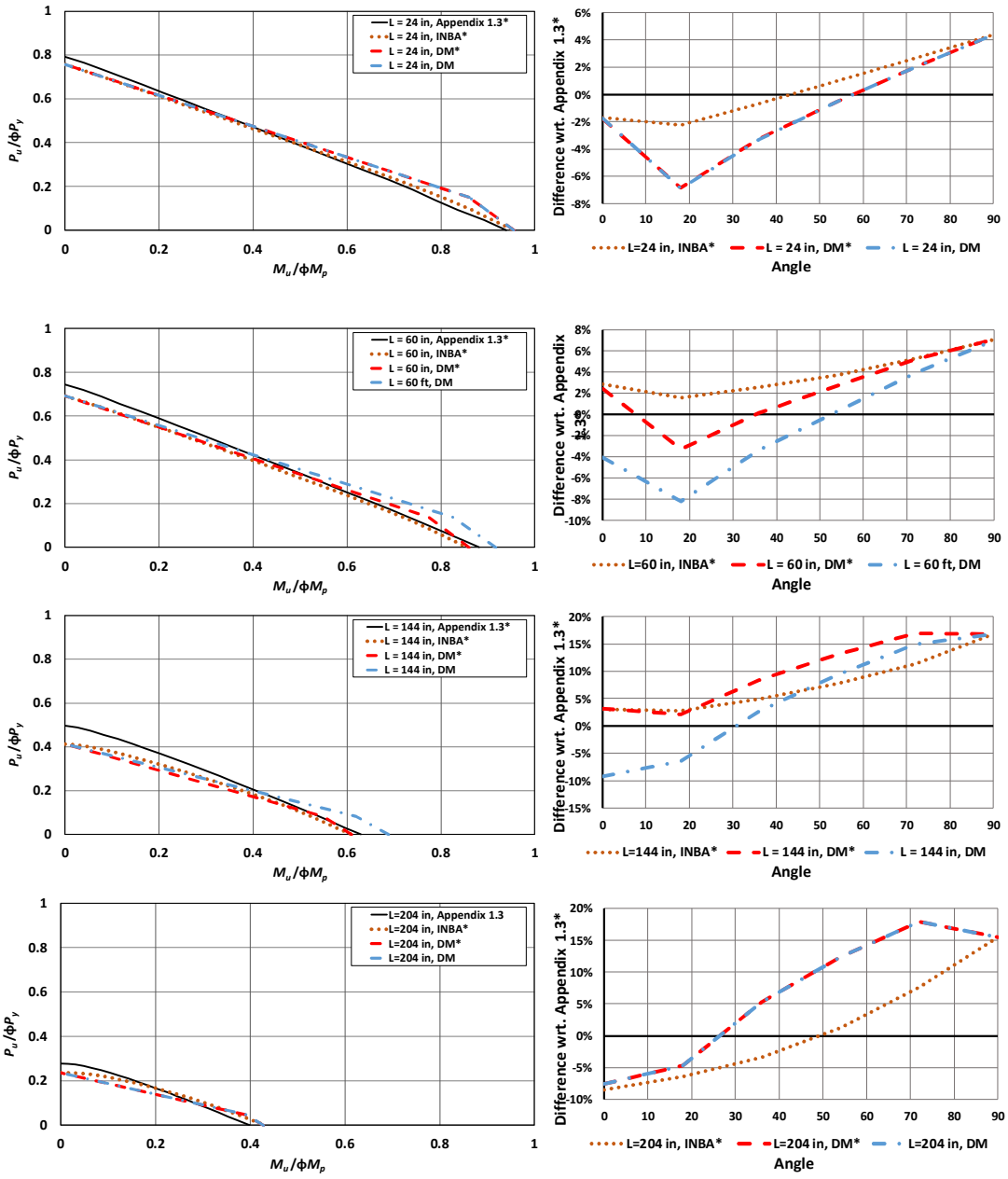

Figure 22. DS-3, uniform moment, beam-column strength curves and difference with respect to Appendix 1.3* curves (L_b=24 in, 60 in, 144 in, 204 in)

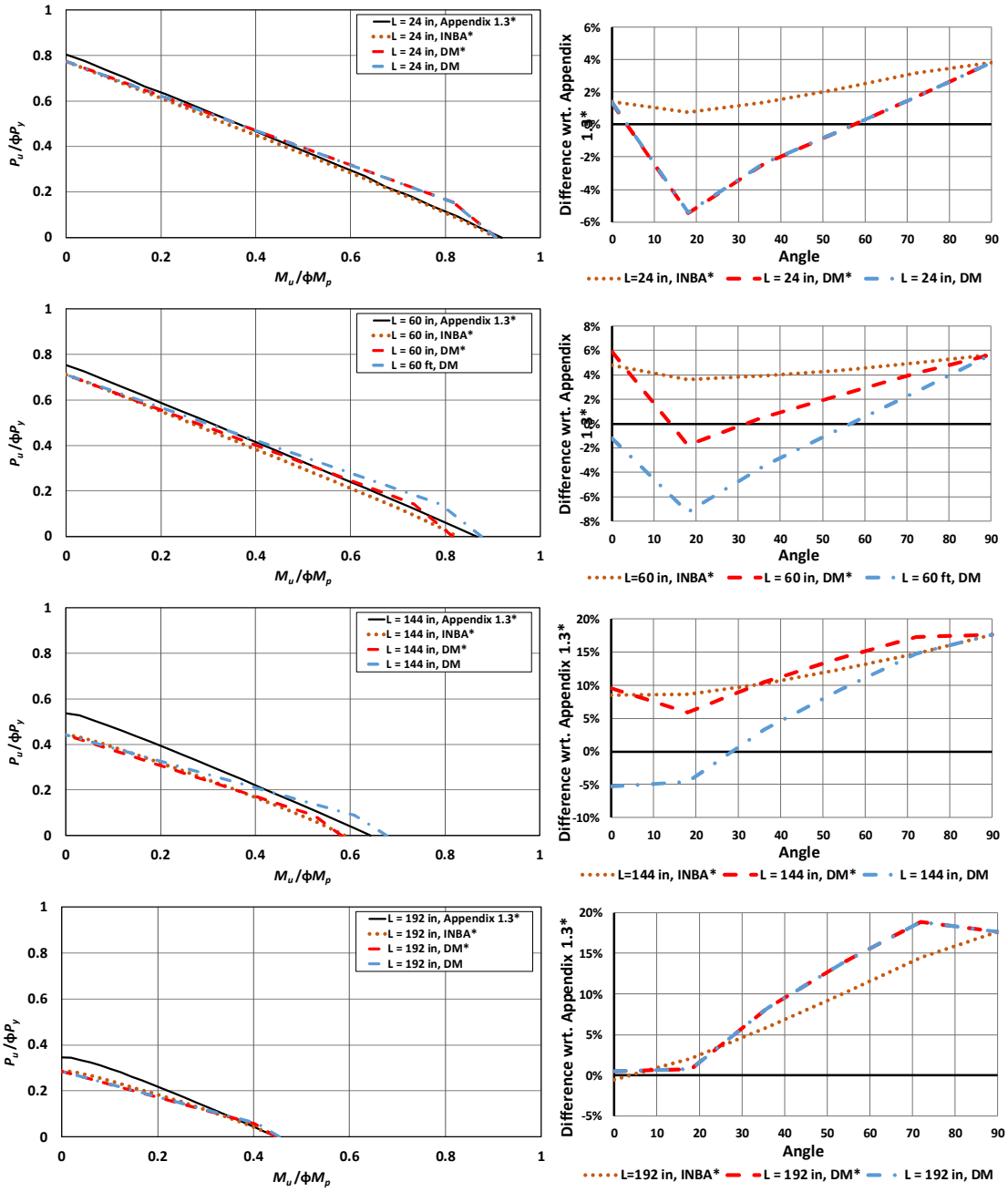

Figure 23. DS-4, uniform moment, beam-column strength curves and difference with respect to Appendix 1.3* curves (L_b=24 in, 60 in, 144 in, 192 in)

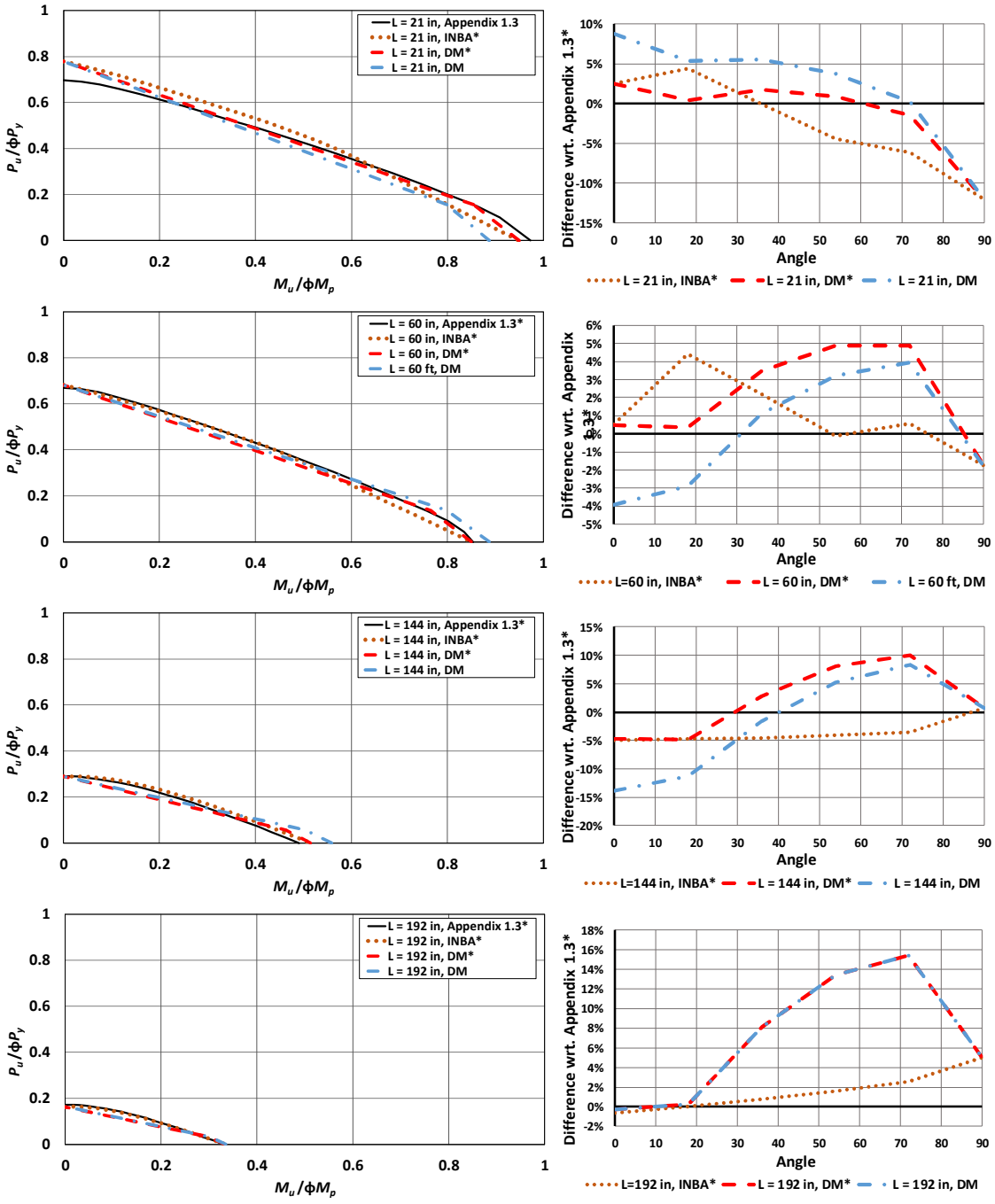

Figure 24. DS-5, uniform moment, beam-column strength curves and difference with respect to Appendix 1.3* curves (L_b=21 in, 60 in, 144 in, 192 in)

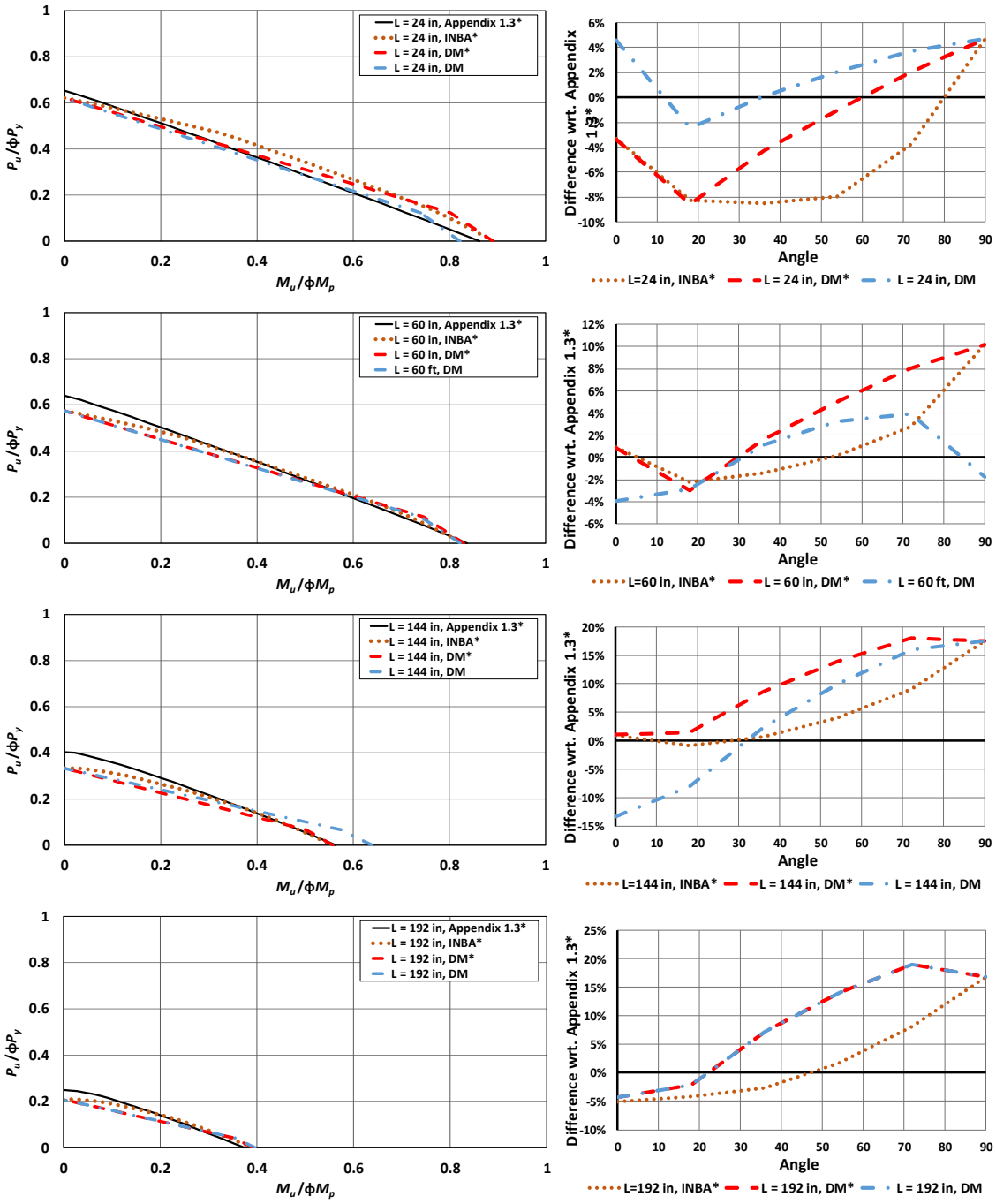

Figure 25. DS-6, uniform moment, beam-column strength curves and difference with respect to Appendix 1.3* curves (L_b=24 in, 60 in, 144 in, 192 in)

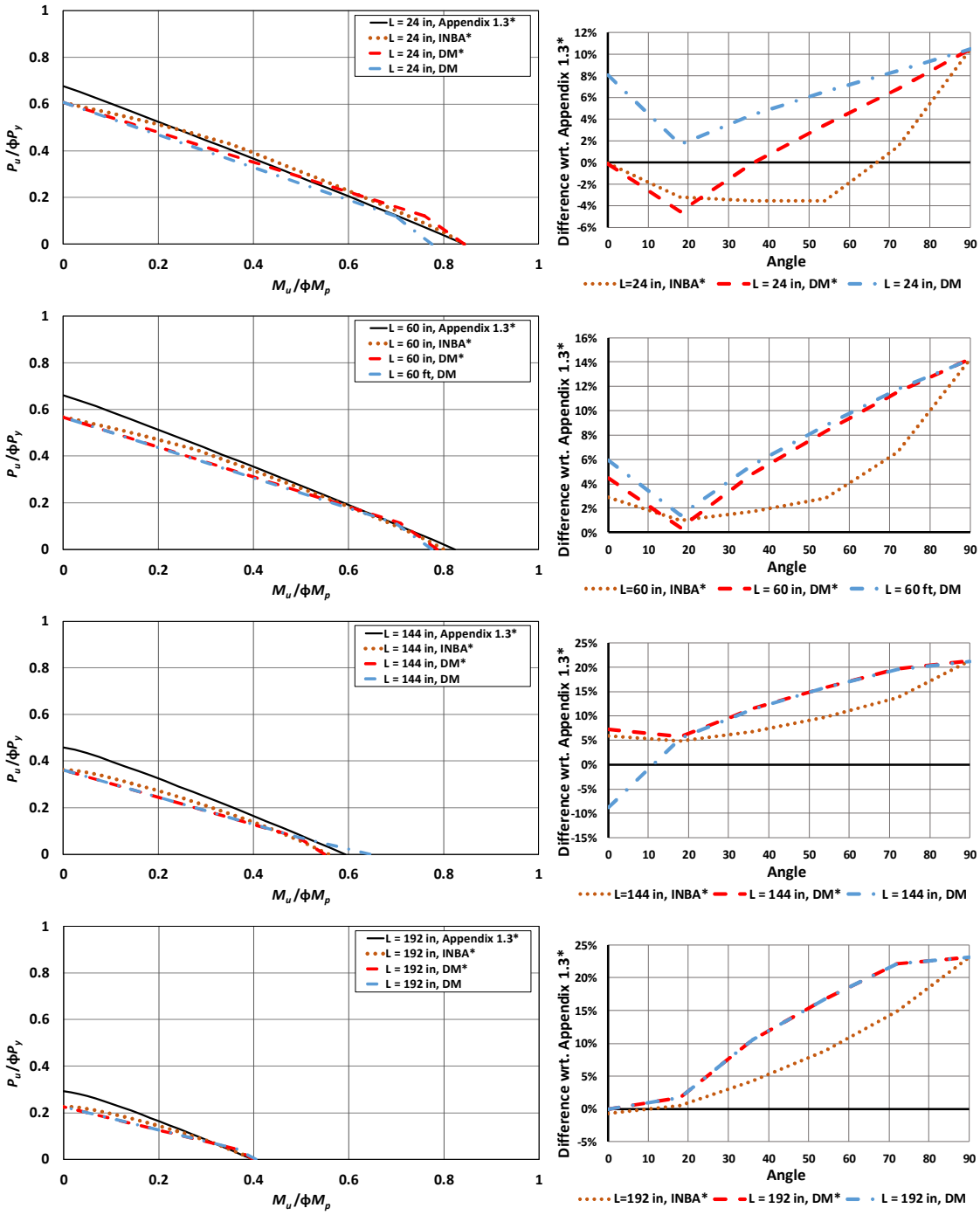

Figure 26. DS-7, uniform moment, beam-column strength curves and difference with respect to Appendix 1.3* curves (L_b=24 in, 60 in, 144 in, 192 in)

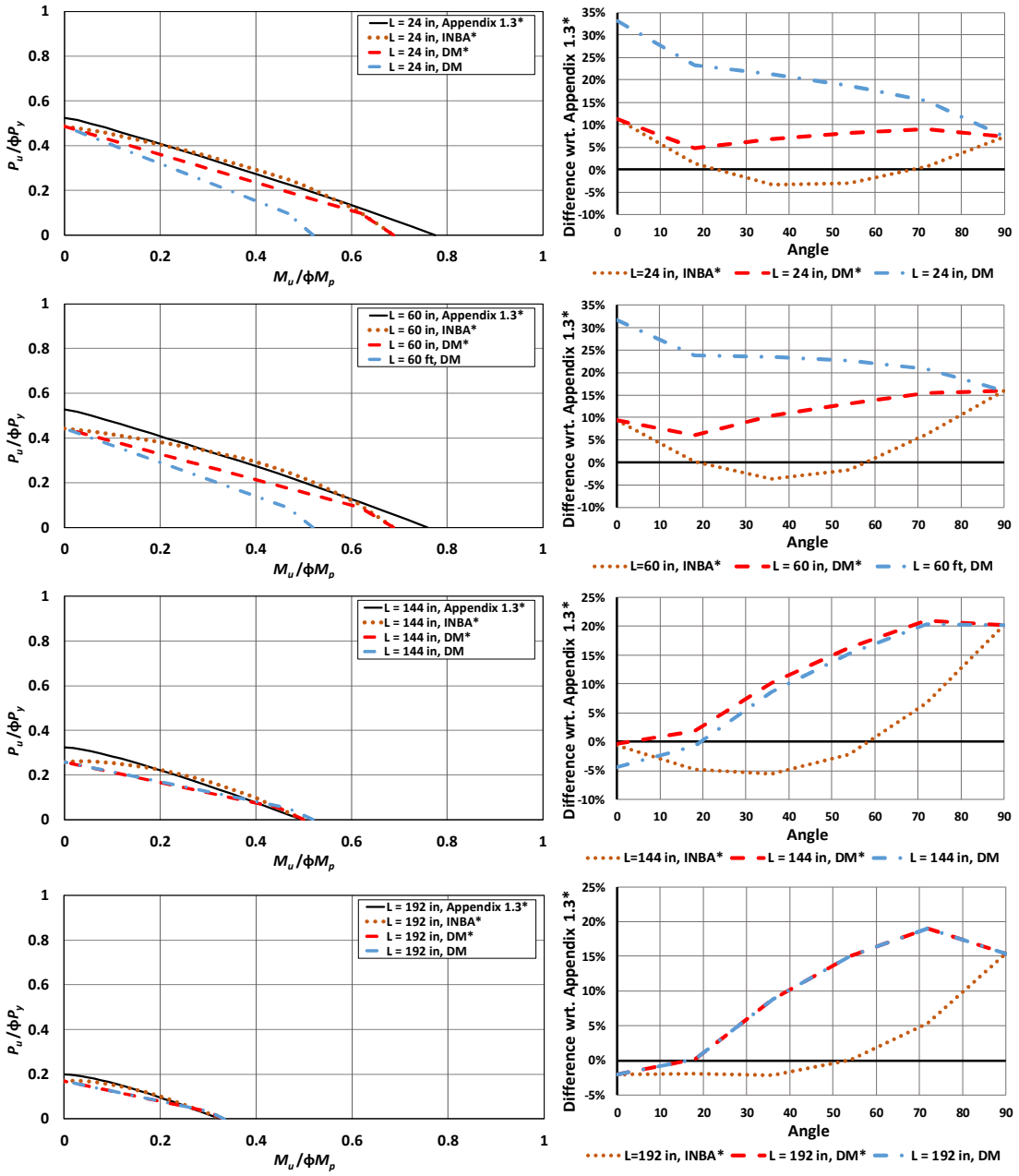

Figure 27. DS-8, uniform moment, beam-column strength curves and difference with respect to Appendix 1.3* curves (L_b=24 in, 60 in, 144 in, 192 in)

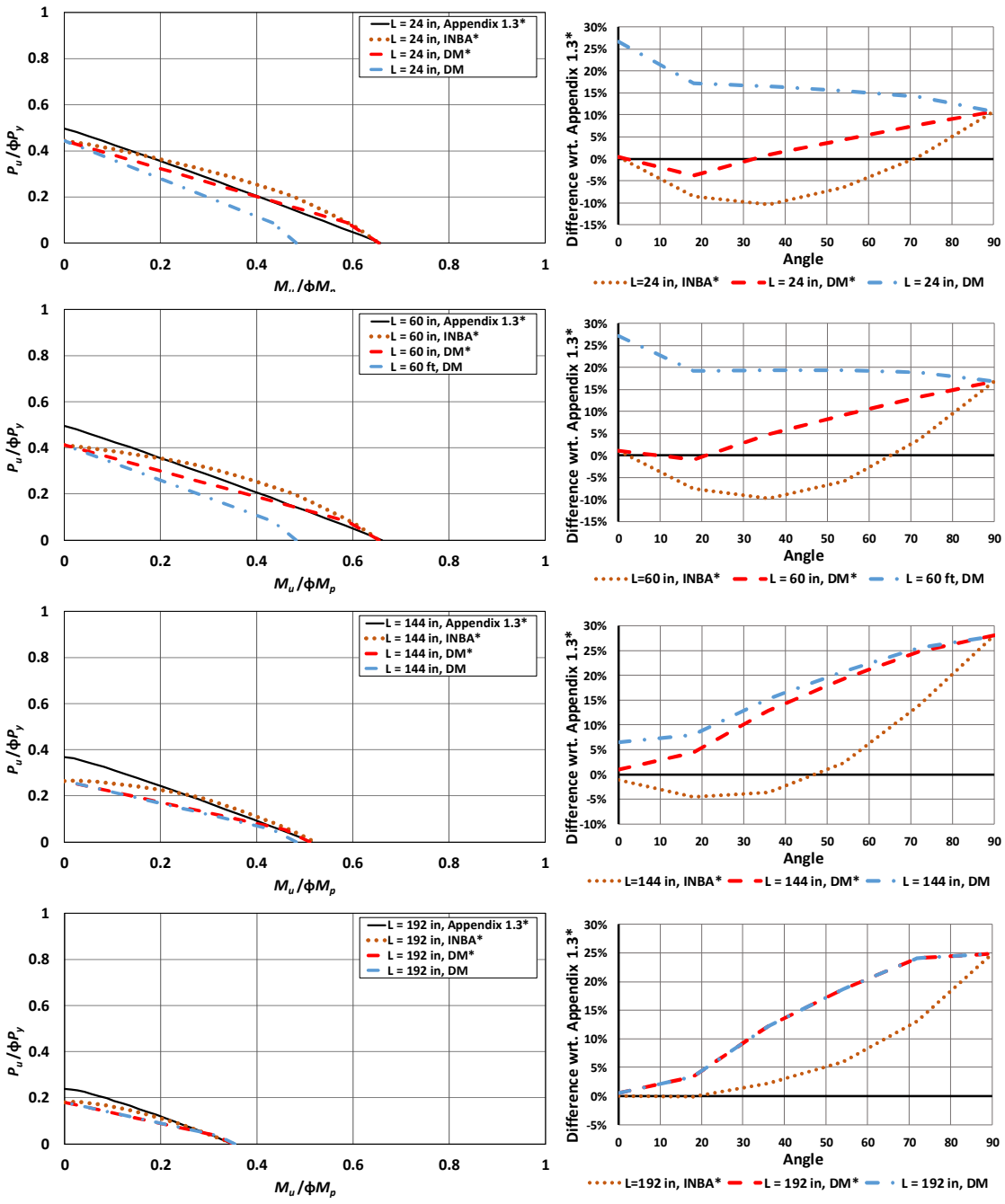

Figure 28. DS-9, uniform moment, beam-column strength curves and difference with respect to Appendix 1.3* curves (L_b=24 in, 60 in, 144 in, 192 in)

4.1.2.2 Data Analysis, Doubly-Symmetric Cross-Sections Subjected to Uniform Primary Bending

In this section, the results are discussed for the doubly-symmetric cross-section members listed in Table 1, subjected to the uniform primary moment (UM) load combinations (Figs. 20 to 28). The statistics the percent differences with respect to Appendix 1.3* are provided by the box and whiskers plot in Fig. 29.

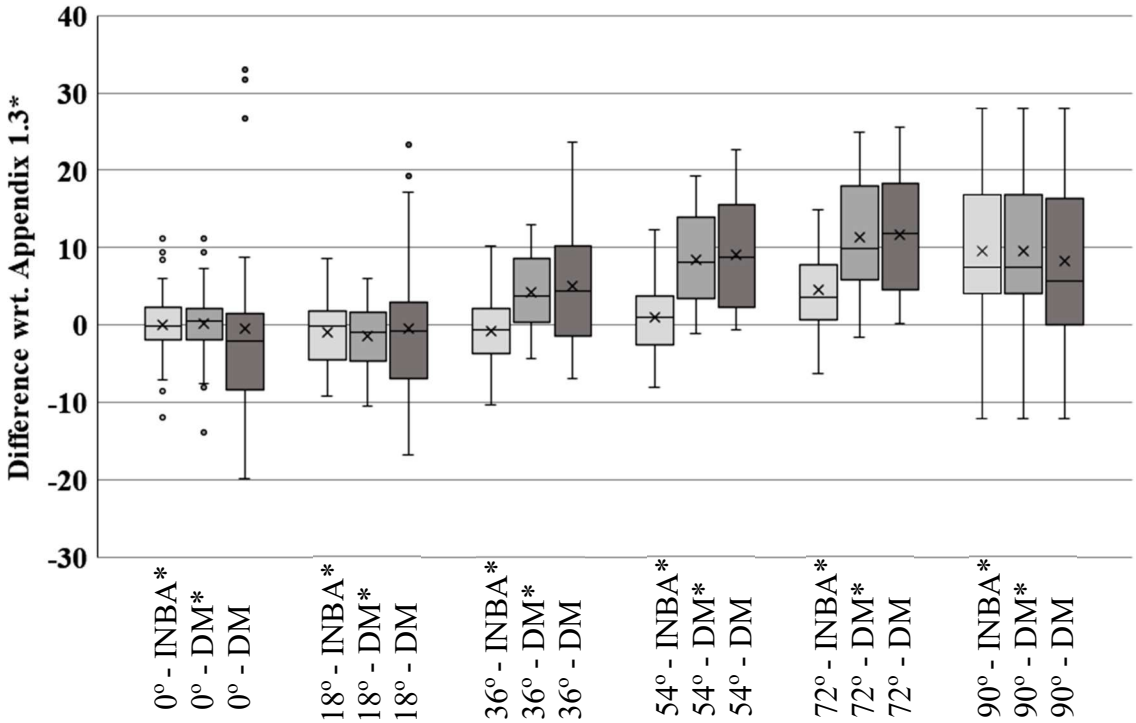

Figure 29. Comparison of INBA*, DM*, DM versus Appendix 1.3* solutions for Uniform Primary Moment Load Configuration

One important finding from Fig. 29 is that, for all the axial compression and moment combinations, the average and median of the data sets are within 2% of zero line. For the 0° (uniform primary moment only) and 90° (axial compression only) cases, the INBA* solutions and DM* solutions match exactly with one another. The derivation of the column and beam stiffness reduction factors of the INBA* procedure ensures this.

Another important general observation is that the unconservative predictions from the improved DM* procedures are significantly smaller than the current DM procedures compared to the Appendix 1.3* results. Furthermore, the INBA* calculations provide generally a slight reduction in the unconservative differences with the Appendix 1.3* results, compared to the DM* calculations. In addition, the INBA* calculations provide significant reductions in the conservative differences relative to the Appendix 1.3* in a large number of cases.

The LTB strengths for DS-8 and DS-9, cross-sections with slender elements (Table 1), classify as outliers in Fig. 29 for the 0^o and 18^o datasets for the DM analysis. This is caused by the flange local buckling (FLB) limit states equations of the AISC Specification, which are improved by the recommended FLB calculations presented in Section 3.1. The conservatism of the AISC FLB equations for these cases is due to the lack of consideration of the corresponding physical post-local buckling of the compression flange, which is accounted for by the use of the effective compression flange width in the recommended provisions.

In addition, the maximum unconservative difference with respect to Appendix 1.3* in the INBA* and DM* data set is measured as 12%. When the Appendix 1.3* test simulations are run with nominal elastic modulus (E) and nominal yield stress (F_y) instead of $0.9E$ and $0.9F_y$, this unconservatism is removed, and all cases except just one outlier are provide either 0% or higher positive difference with respect to Appendix 1.3* solutions. The one unconservative outliner case, DS-1 with 192 in. length, is at 12% difference (Fig. 20). Although one might expect the equivalent welded section (DS-2) has less capacity than the rolled section (DS-1), it is observed that the capacity of the DS-1 is smaller than

DS-2 for that particular length. This smaller capacity is mainly caused by the residual stress effects that are used in the test simulations. With the patterns that are used, the Lehigh residual stress (presented in Appendix A.3, Fig. 130) pattern is actually more critical. The reason for this behavior is that the Lehigh pattern is based on light column-type sections where the web tends to be entirely in residual tension. With this type of residual stress distribution, the section has a net residual compression force in the flanges, which tends to be relatively damning. It can be argued that the Lehigh residual stress pattern is not representative of beam-type wide flange sections. Subramanian and White (2016) show other more representative patterns, including a summary of past research measurements, but recommended the use of the Lehigh pattern with the reduced magnitude residual stresses as a single nominal pattern that can be applied for all rolled wide-flange shapes.

For the 90^o cases, with axial compression only, the percent difference values show a large variation. This is mainly caused by the use of only one column curve in the AISC provisions. Using more than one column curve would require more than one τ_a equation, but it would improve the results for both columns and beam-columns.

The point having a significant change in slope in the beam-column interaction plots is referred as the "knee" of the interaction plots. For the 18^o case, which is in the vicinity of the "knee" region, the INBA* solution shows a closer correlation with the Appendix 1.3* result than the DM*. The INBA* linear interaction equation for UC values helps to reduce the unconservative differences in beam-column resistances for these cases.

The intermediate angles (36^o, 54^o, 72^o) of the beam-column interaction curves show that, INBA* provides closer correlation with the Appendix 1.3* solutions.

4.1.2.3 Member Strength Envelopes and Plots of Differences Relative to Test Simulation Studies, Doubly-Symmetric Members Moment Gradient Loading

Beam-column interaction plots that compare the INBA*, DM*, and DM results with the Appendix 1.3* solutions are provided in this subsection. The plots are provided for all the cases for the moment gradient loading conditions shown in Table 1.

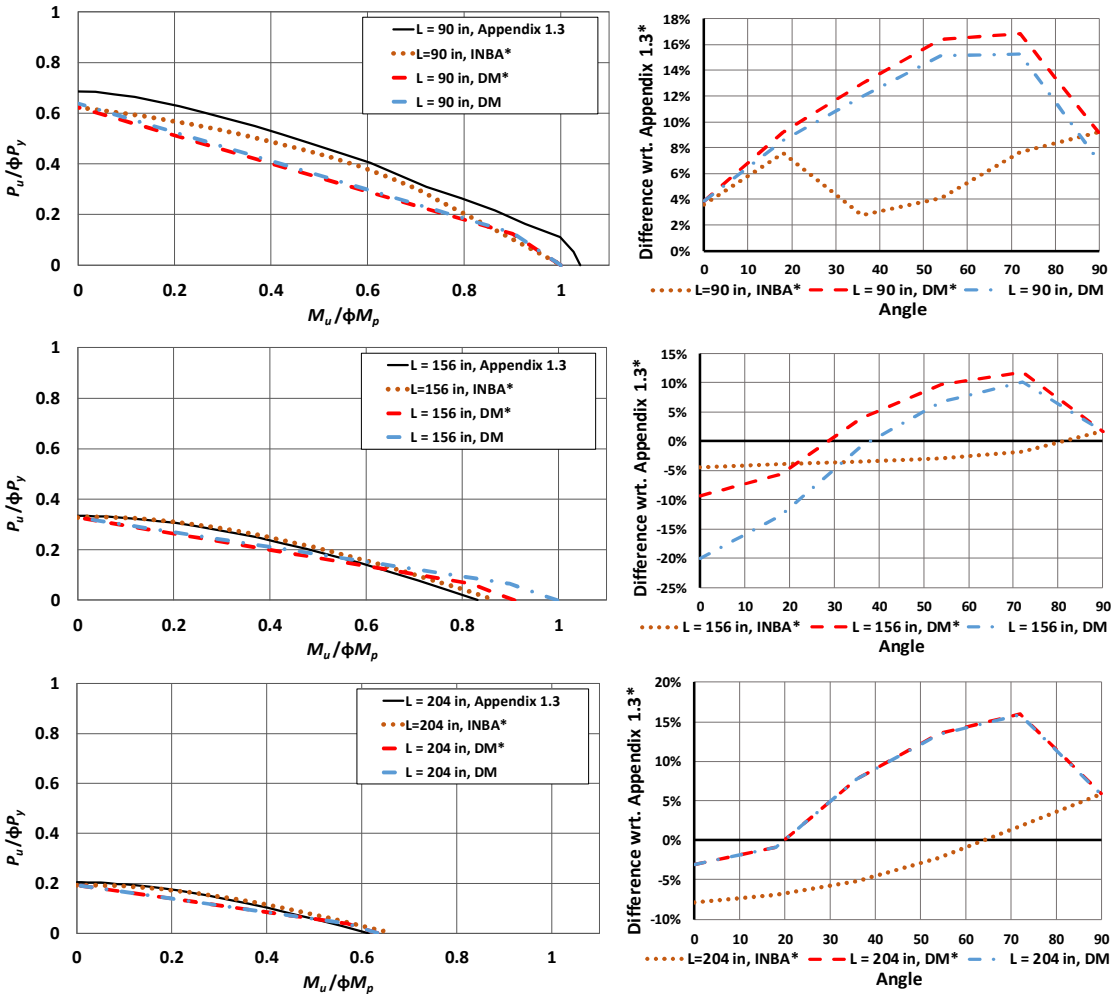

Figure 30. DS-1, moment gradient, beam-column strength curves and difference with respect to Appendix 1.3* curves (L_b=90 in, 156 in, 204 in)

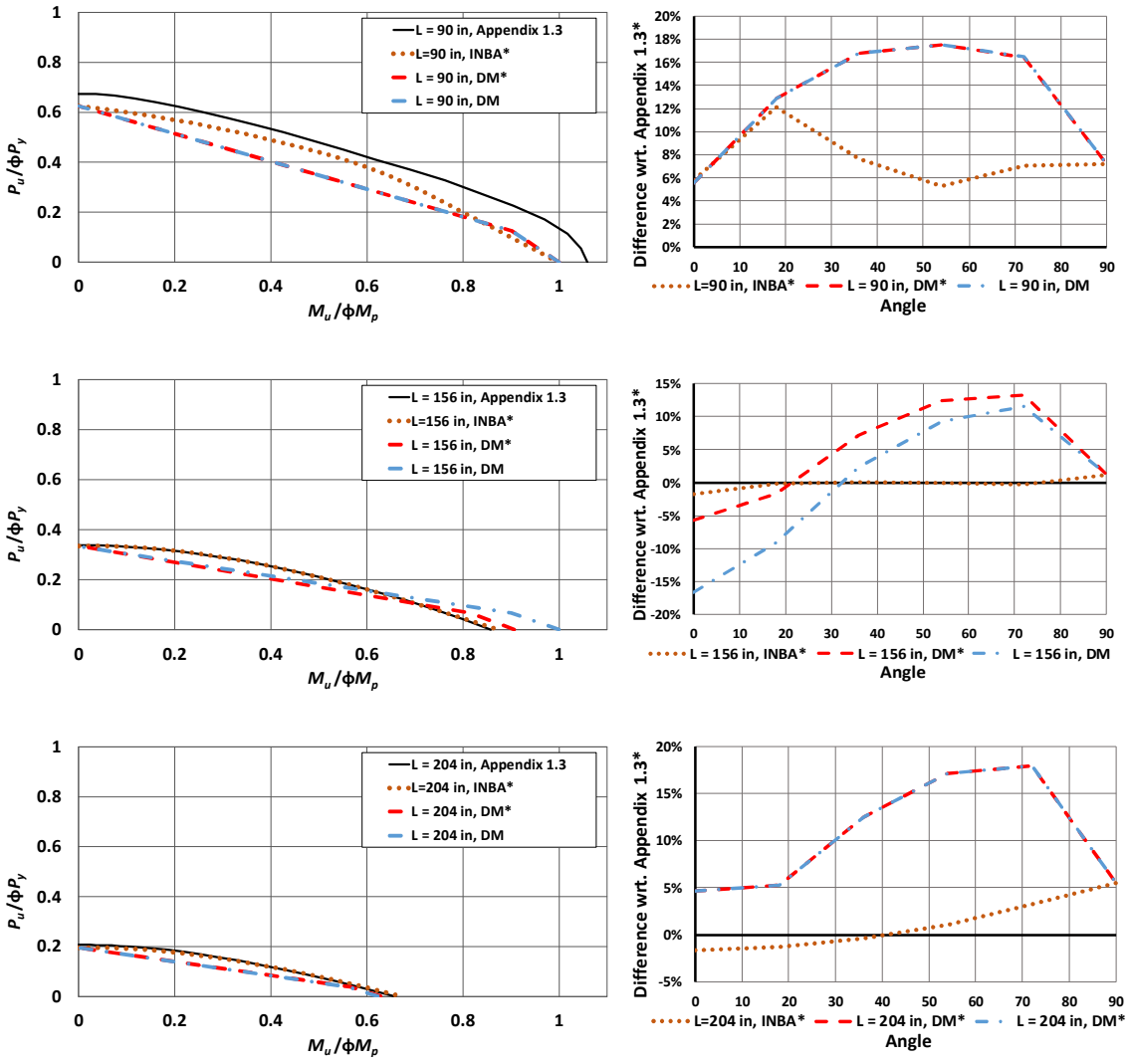

Figure 31. DS-2, moment gradient, beam-column strength curves and difference with respect to Appendix 1.3* curves (L_b=90 in, 156 in, 204 in)

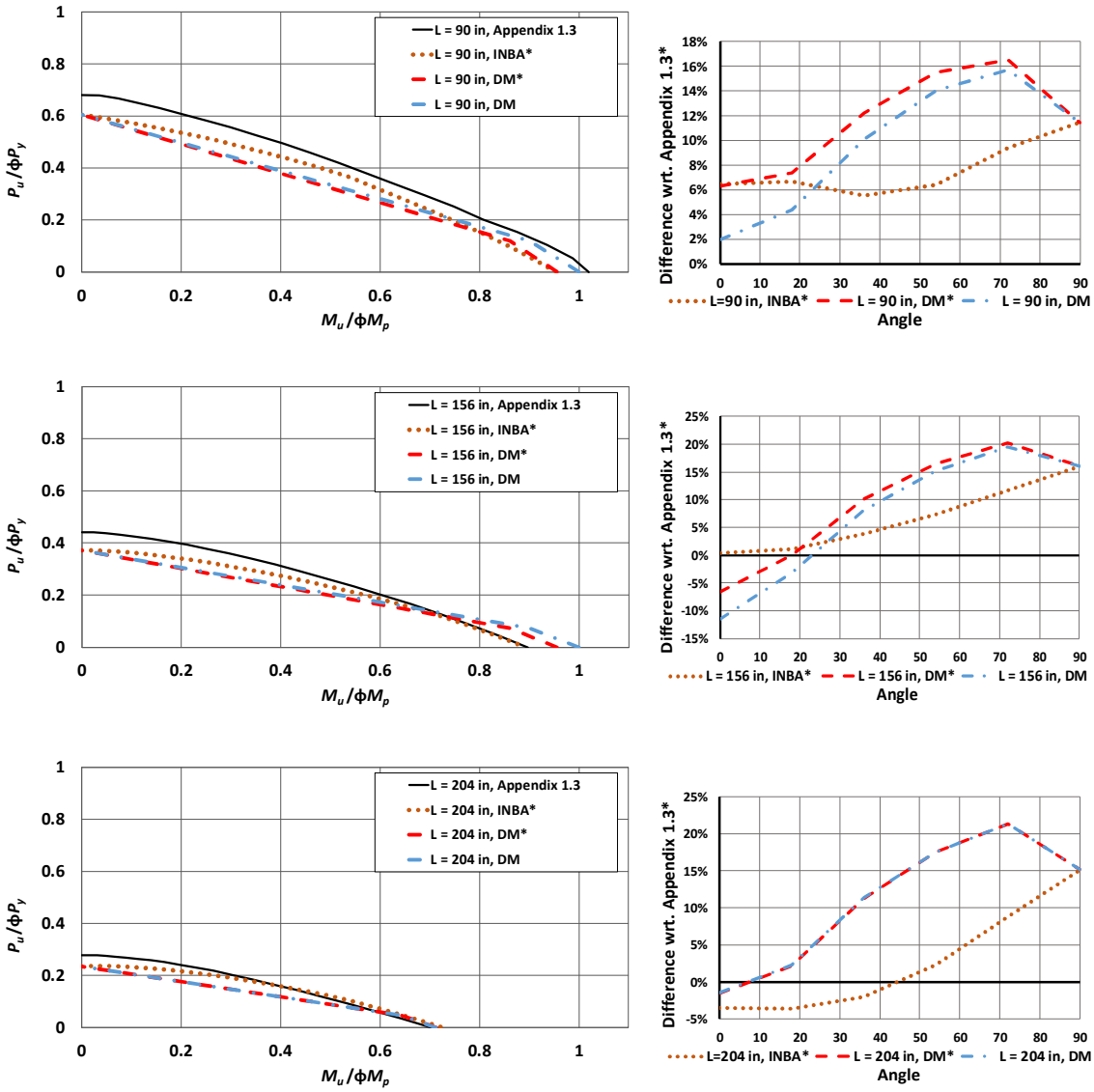

Figure 32. DS-3, moment gradient, beam-column strength curves and difference with respect to Appendix 1.3* curves (L_b=90 in, 156 in, 204 in)

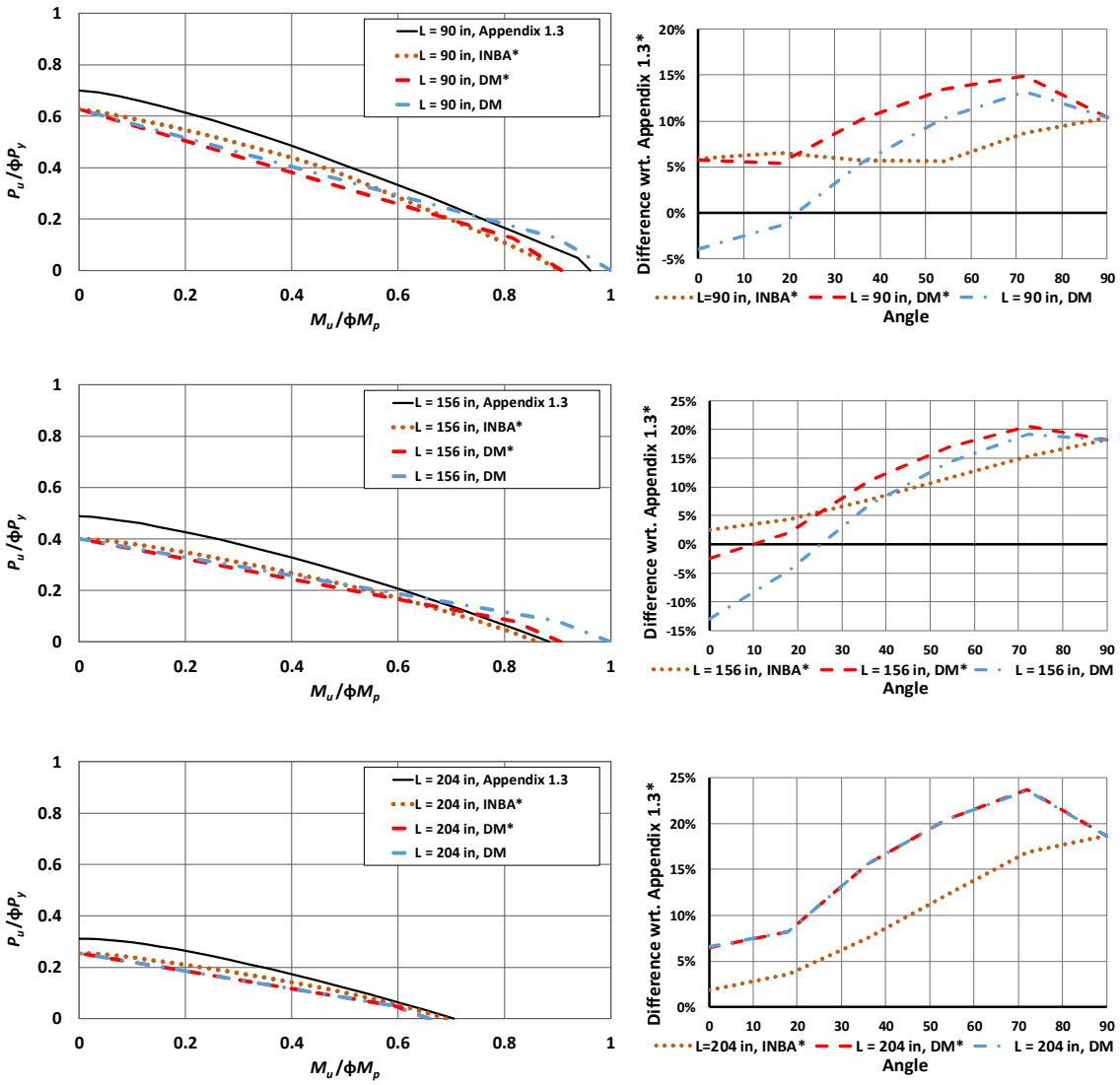

Figure 33. DS-4, moment gradient, beam-column strength curves and difference with respect to Appendix 1.3* curves (L_b=90 in, 156 in, 204 in)

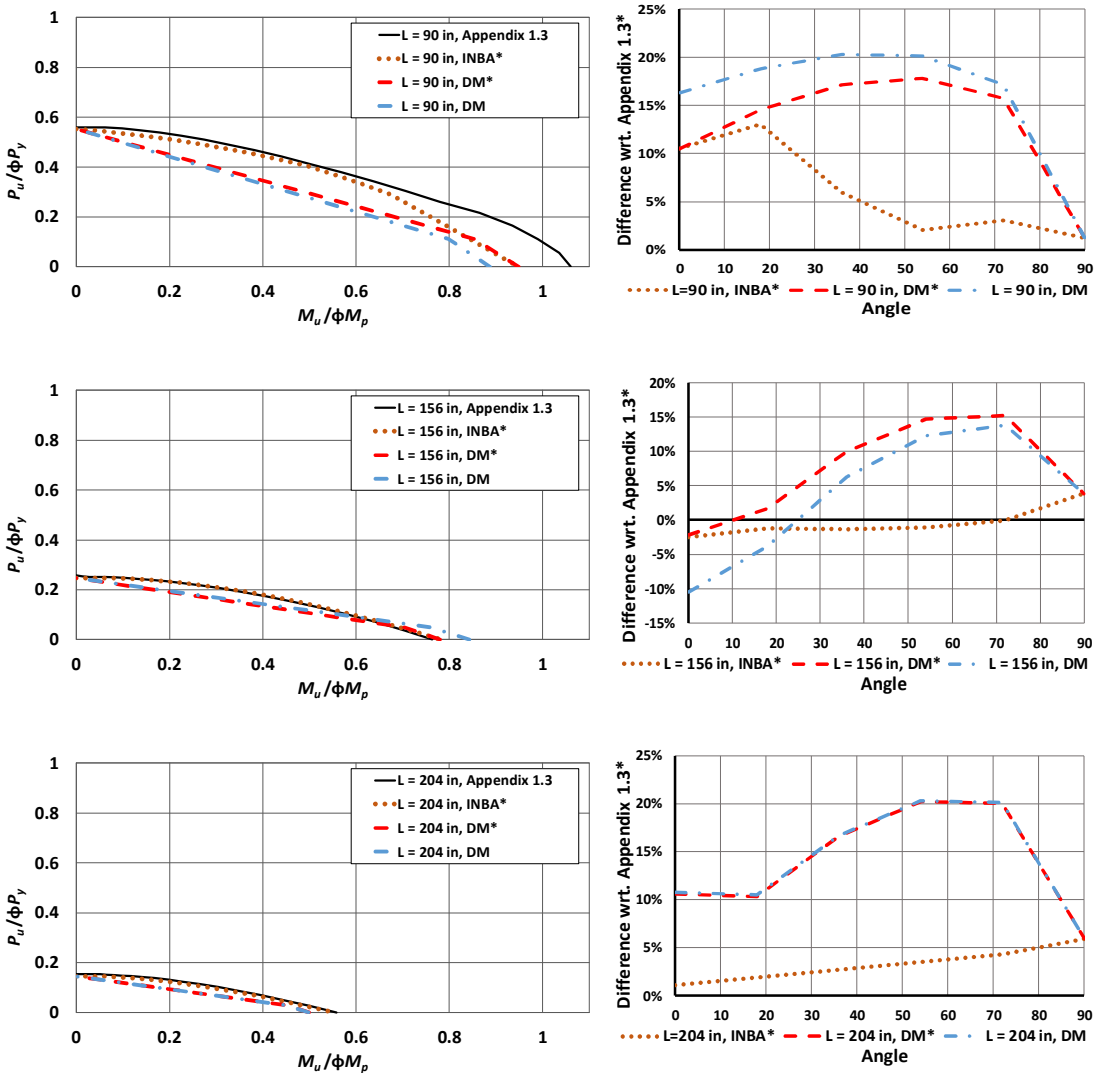

Figure 34. DS-5, moment gradient, beam-column strength curves and difference with respect to Appendix 1.3* curves (L_b=90 in, 156 in, 204 in)

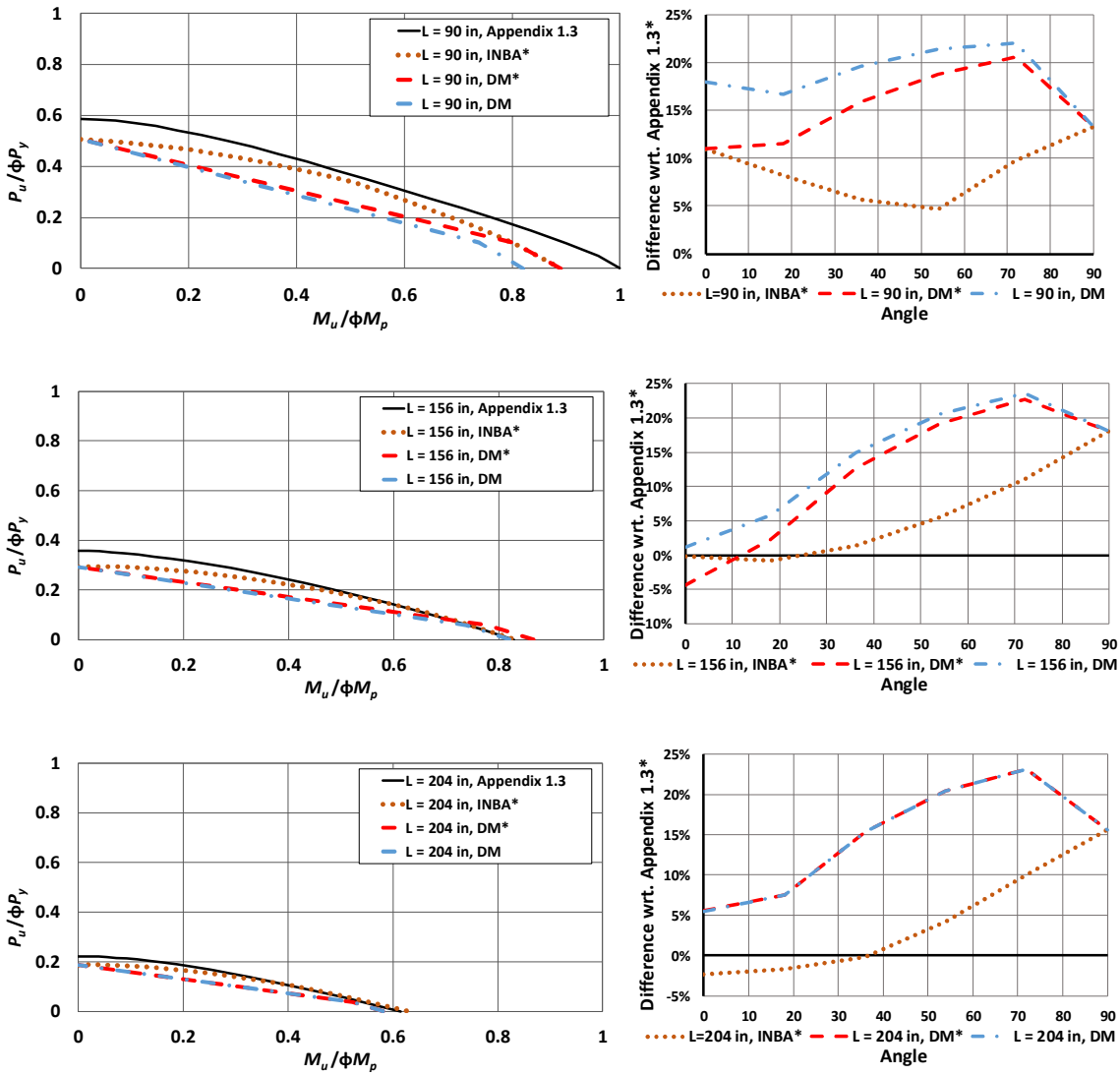

Figure 35. DS-6, moment gradient, beam-column strength curves and difference with respect to Appendix 1.3* curves (L_b=90 in, 156 in, 204 in)

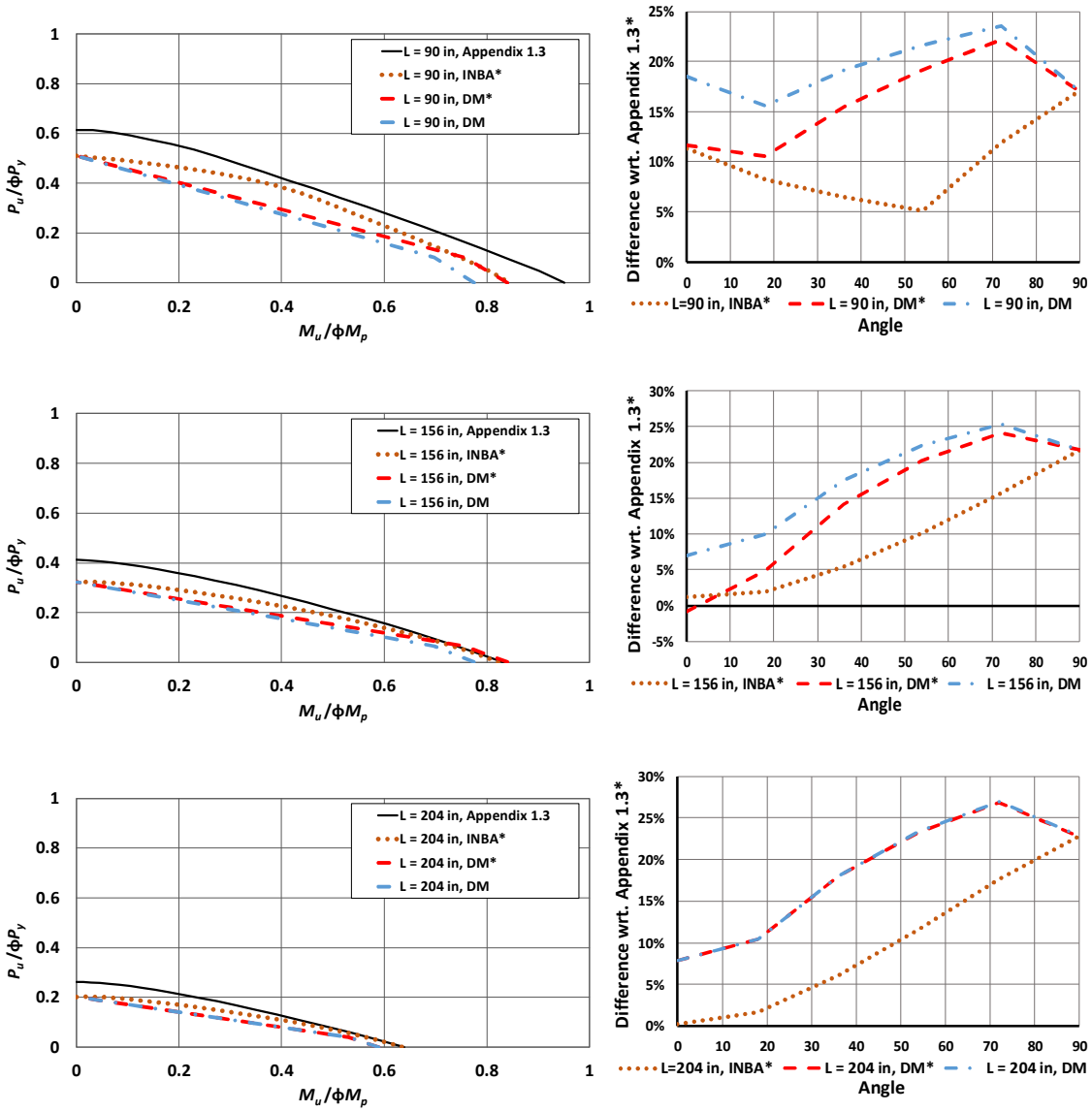

Figure 36. DS-7, moment gradient, beam-column strength curves and difference with respect to Appendix 1.3* curves (L_b=90 in, 156 in, 204 in)

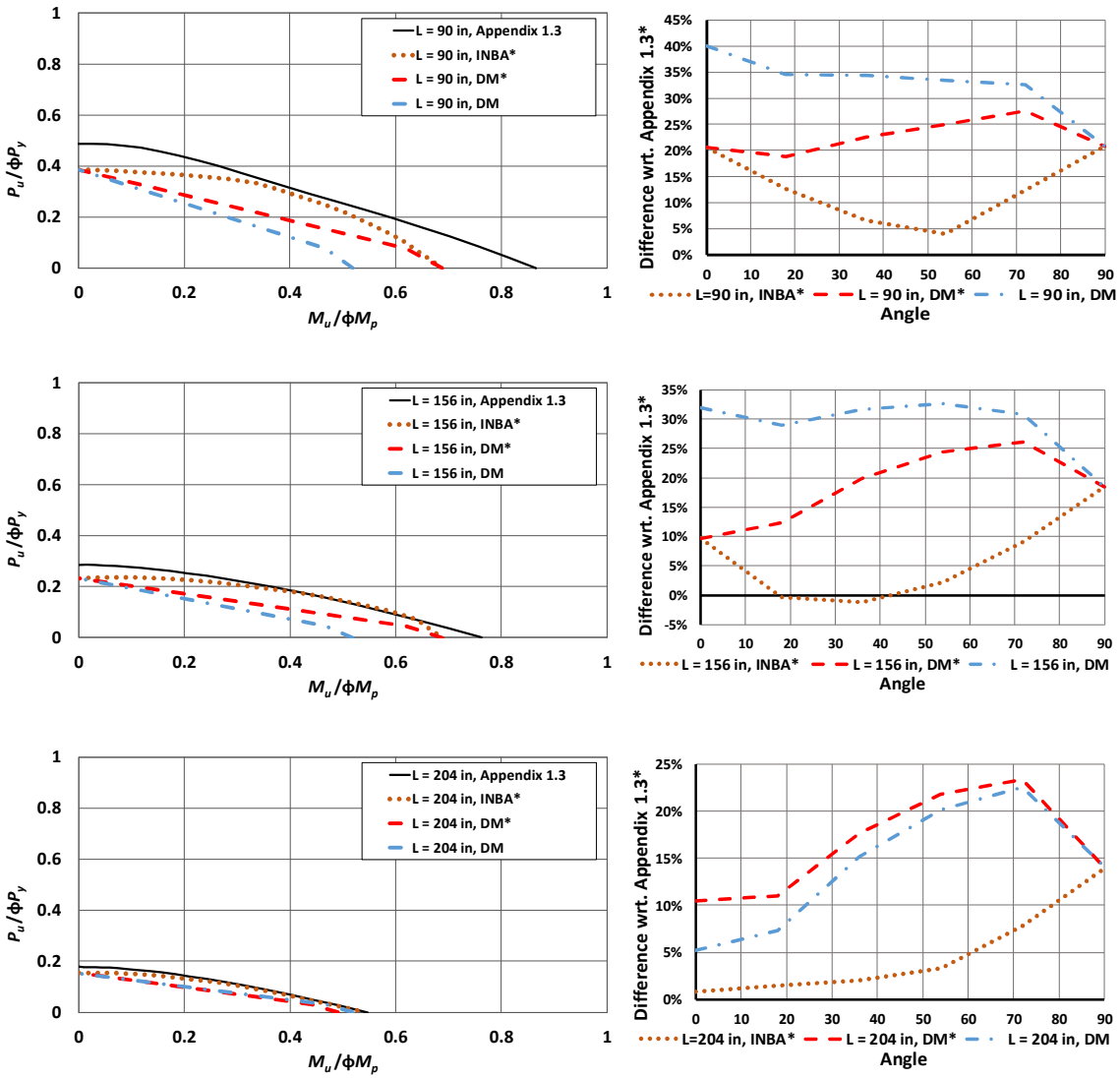

Figure 37. DS-8, moment gradient, beam-column strength curves and difference with respect to Appendix 1.3* curves (L_b=90 in, 156 in, 204 in)

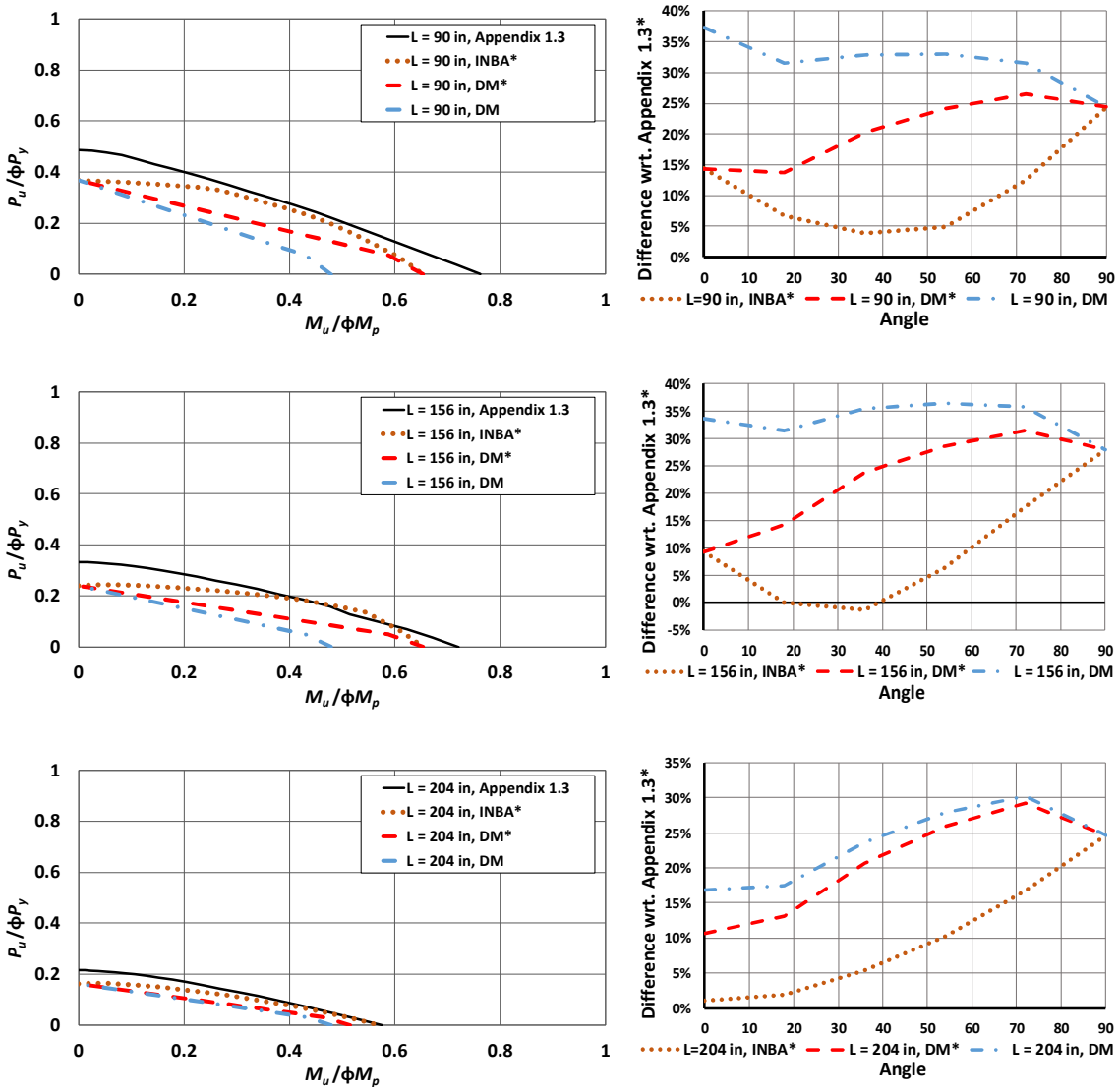

Figure 38. DS-9, moment gradient, beam-column strength curves and difference with respect to Appendix 1.3* curves (L_b=90 in, 156 in, 204 in)

4.1.2.4 Data Analysis, Doubly-Symmetric Cross-Sections Subjected to Moment Gradient Loading

In this section, the results are discussed for the doubly-symmetric cross-section members listed in Table 1, subjected to moment gradient (MG) load combinations (Figs.

30 to 38). The statistics for percent differences values are provided by the box and whiskers plot in Fig. 16.

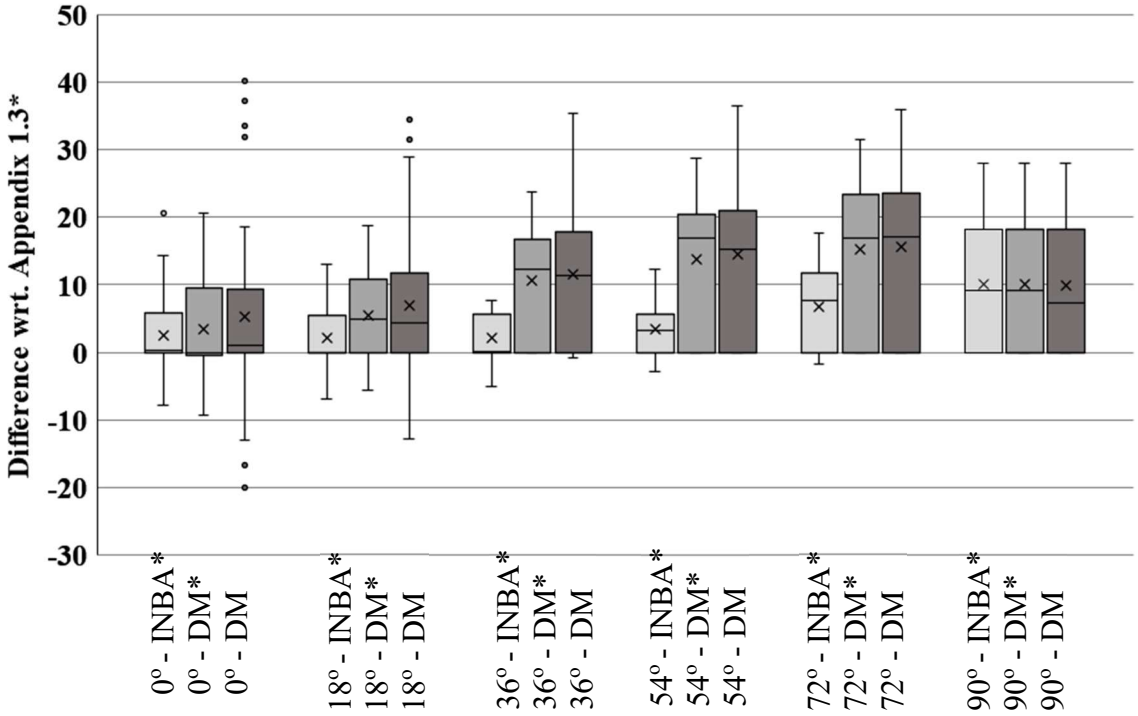

Figure 39. Comparison of INBA*, DM*, DM versus Appendix 1.3* solutions for Moment Gradient Load Configuration

For all the data sets in the moment gradient load configurations, the mean and average values of the INBA* solutions show a closer match with the Appendix 1.3* results than the DM* solutions. When the INBA* solutions are compared with the DM solutions, the mean value for INBA* results provide a closer results to 0%, which means INBA* is providing closer results to Appendix 1.3* solutions. The intermediate angles (18°, 36°, 54°, 72°) of the beam-column interaction curves show similar behavior to the corresponding uniform primary moment results. The average and mean values of the INBA* solutions are closer to zero than the DM* solutions for all the beam-column cases.

The INBA* and the DM* solutions are slightly different for the flexure only case with the moment gradient loading conditions (0° line on Fig. 16). The moment gradient factor of C_b is the main reason for this difference. The C_b that is employed in the moment gradient case the DM* solutions is provided by AISC (2016). As it can be observed from Fig. 39, the INBA* solutions provide better correlation with Appendix 1.3* solutions. This is because the INBA* solutions work directly with the inelastic *SRF* values along the member lengths.

The extremely conservative results for the 0° cases is from the slender sections (DS-8 and DS-9) in the DM dataset. Figures 37 and 38 show that the influence of the FLB limit states on the resistance of the cross-section. The recommendations prediction of the for FLB limit state are presented in Section 3.1. These recommendations account for the post-buckling strength of compression flanges using the effective length of it. One outliner case in the INBA* 0° and the DM* 0° data sets is presented in Fig. 37 for L_b = 90 in. For this case, the FLB recommendations helping the reduce conservatism with respect to Appendix 1.3* solutions from 35% to 20%, but still being an outlier since the top whisker is limited at around 15%.

Another important general observation is that the unconservative predictions from the improved DM* procedures are significantly smaller than the current DM procedures compared to the Appendix 1.3* results. Furthermore, the INBA* calculations provide generally a slight reduction in the unconservative differences with the Appendix 1.3* results, compared to the DM* calculations. In addition, the INBA* calculations provide significant reductions in the conservative differences relative to the Appendix 1.3* in a large number of cases.

4.1.2.5 Member Strength Envelopes and Plots of Differences Relative to Test Simulation Studies, Doubly-Symmetric Members Subjected to Uniformly Distributed Load

In this section, DS-1 (W21x44) is examined for uniformly distributed lateral load combinations with uniform axial compressions (Fig. 19). The difference values related to this loading configurations are listed in Figure 40. The findings for uniform primary moment load cases and moment gradient loads are consistent with the uniformly distributed lateral load cases. For the smallest member length of 90 in, the INBA* results show close correlation with the Appendix 1.3* results.

As in the moment gradient load studies, there is a difference between the INBA* and the DM* solutions for pure flexure cases. This difference is mainly caused by the moment gradient factor of C_b. The C_b equations that are used for the moment gradient load configuration is not suitable to use in the uniformly distributed loading case since its moment diagram is not linear. The C_b equation used in these cases is obtained with the AISC Eq. F1-1 (AISC 2016). Figure 40 shows that using the INBA* approach provides a better correlation with the Appendix 1.3* solutions.

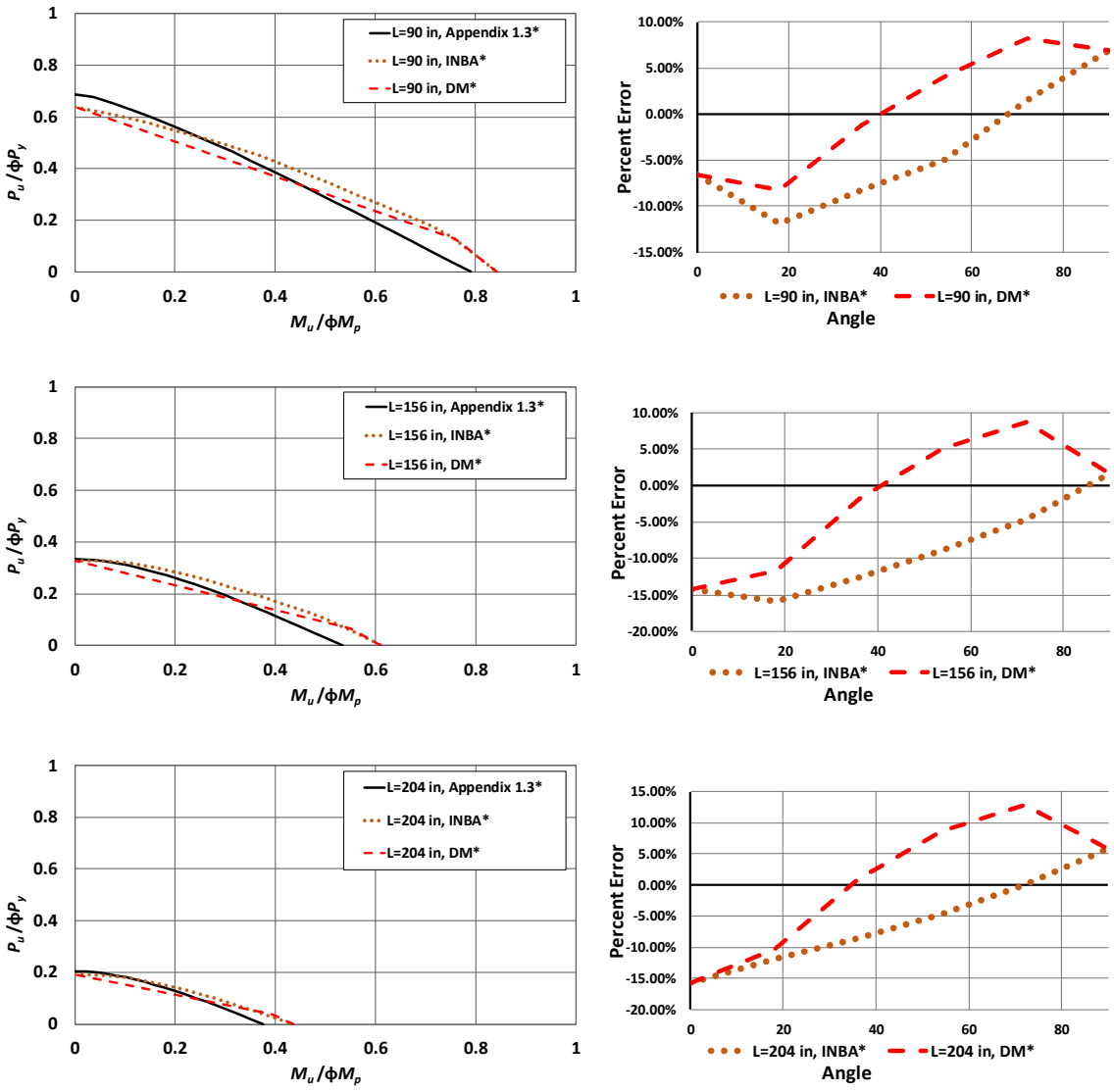

Figure 40. DS-1, uniformly distributed loads, beam-column strength curves and difference with respect to Appendix 1.3* curves (L_b=90 in, 156 in, 204 in)

4.1.3 *Singly-Symmetric Prismatic Beam-Columns*

Two different loading configurations are examined for singly-symmetric cross-sections. First, uniform positive primary moment cases with eight prismatic cross-sections are tested (Fig. 17). Second, moment gradient cases using the same prismatic cross-section set are evaluated (Fig. 18). A total of 524 + 524 = 1048 test simulations are conducted.

For the singly-symmetric cases, uniform negative primary moment and negative moment gradient loading are also applied on the member (Figs. 42 and 43). This helps to cover a wide spectrum of cross-section types. An example beam-column strength curve is presented in the Fig. 41. As indicated in the figure, while the left side of the strength curve is obtained by the application of negative moment load combinations, the right side of it is obtained by the application of positive moment load combinations.

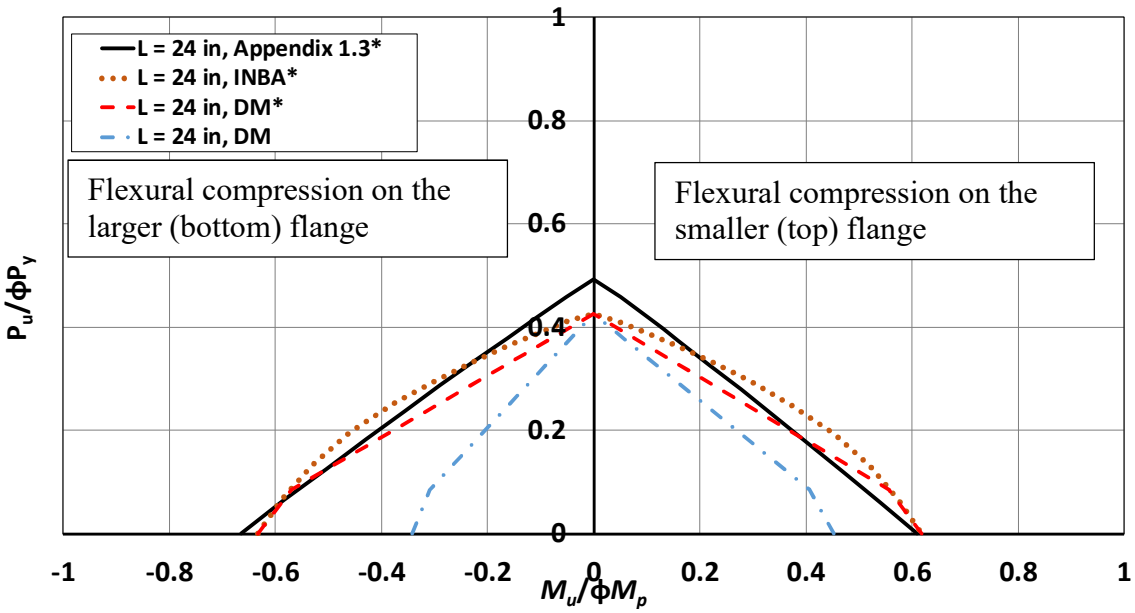

Figure 41. Example for singly-symmetric members beam-column strength curve

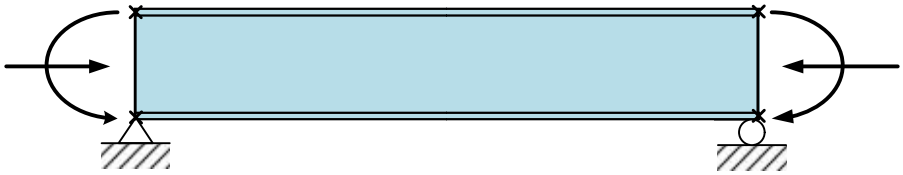

Figure 42. Uniform negative primary moment load configuration

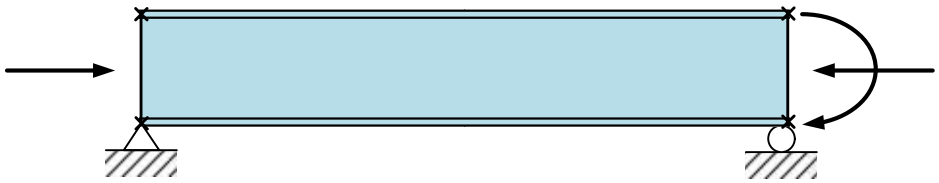

Figure 43. Negative moment gradient load configuration

All the members are flexurally and torsionally simply-supported at their ends and they have no intermediate lateral bracing. As such, their effective lengths $L_{cx} = L_{cy} = L_{cz}$ are all equal to their laterally unbraced length L. Eight different cross-sections are considered in this study as summarized by Table 2. Members with short, intermediate and long unbraced lengths are considered for each of these sections. To ensure singly-symmetric cross-sections, bottom flange is widened to 8 in, while the top flange remains 6.5 in.

Table 2. Singly-Symmetric I-sections considered in validation studies (bf_comp= 6.5 in and bf_ten = 8 in (M+) or bf_ten= 6.5 in and bf_comp = 8 in (M-), dw = 19.8 in).

Case	Description	t_f (in)	t_w (in)	$A_{fillets}$ (in^2)	$b_{f\_comp}/2t_f$ (M+)	$b_{f\_comp}/2t_f$ (M-)	d_w/t_w
SS-2	Equivalent Welded Section	0.4500	0.3500	0.00	7.22	8.89	56.57
SS-3	Noncompact Web	0.4500	0.1787	0.00	7.22	8.89	110.80
SS-4	Slender Web	0.4500	0.1238	0.00	7.22	8.89	160.00
SS-5	Noncompact Flange	0.2708	0.3500	0.00	12.00	14.77	56.57
SS-6	Noncompact Flange & Noncompact Web	0.2708	0.1787	0.00	12.00	14.77	110.80
SS-7	Noncompact Flange & Slender Web	0.2708	0.1238	0.00	12.00	14.77	160.00
SS-8	Slender Flange & Noncompact Web	0.1806	0.1787	0.00	18.00	22.15	110.80
SS-9	Slender Flange & Slender Web	0.1806	0.1238	0.00	18.00	22.15	160.00

Since the strength curve has two sides for singly-symmetric sections, number of lines used in the difference with respect to Appendix 1.3* is increased to 11 lines to cover both side of the curves.

4.1.3.1 Member Strength Envelopes and Plots of Differences Relative to Test Simulation Studies, Singly-Symmetric Members Uniform Bending

Beam-column interaction plots that compare the INBA*, DM*, and DM results with the Appendix 1.3* solutions are provided in this subsection. The plots are provided for all the cases for the uniform primary moment loading conditions shown in Table 2.

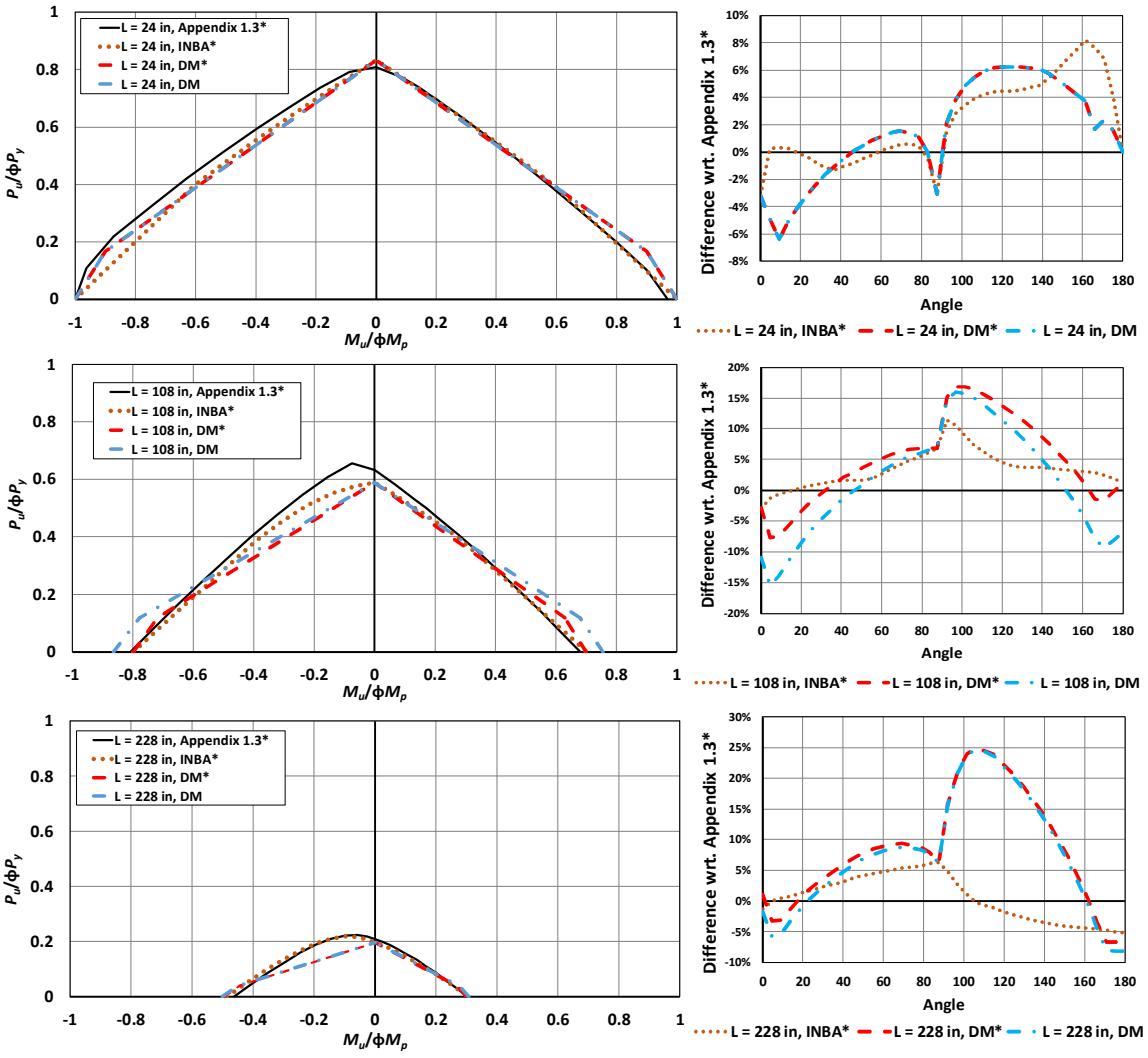

Figure 44. SS-2, uniform moment, beam-column strength curves and difference with respect to Appendix 1.3* curves (L_b=24 in, 108 in, 228 in)

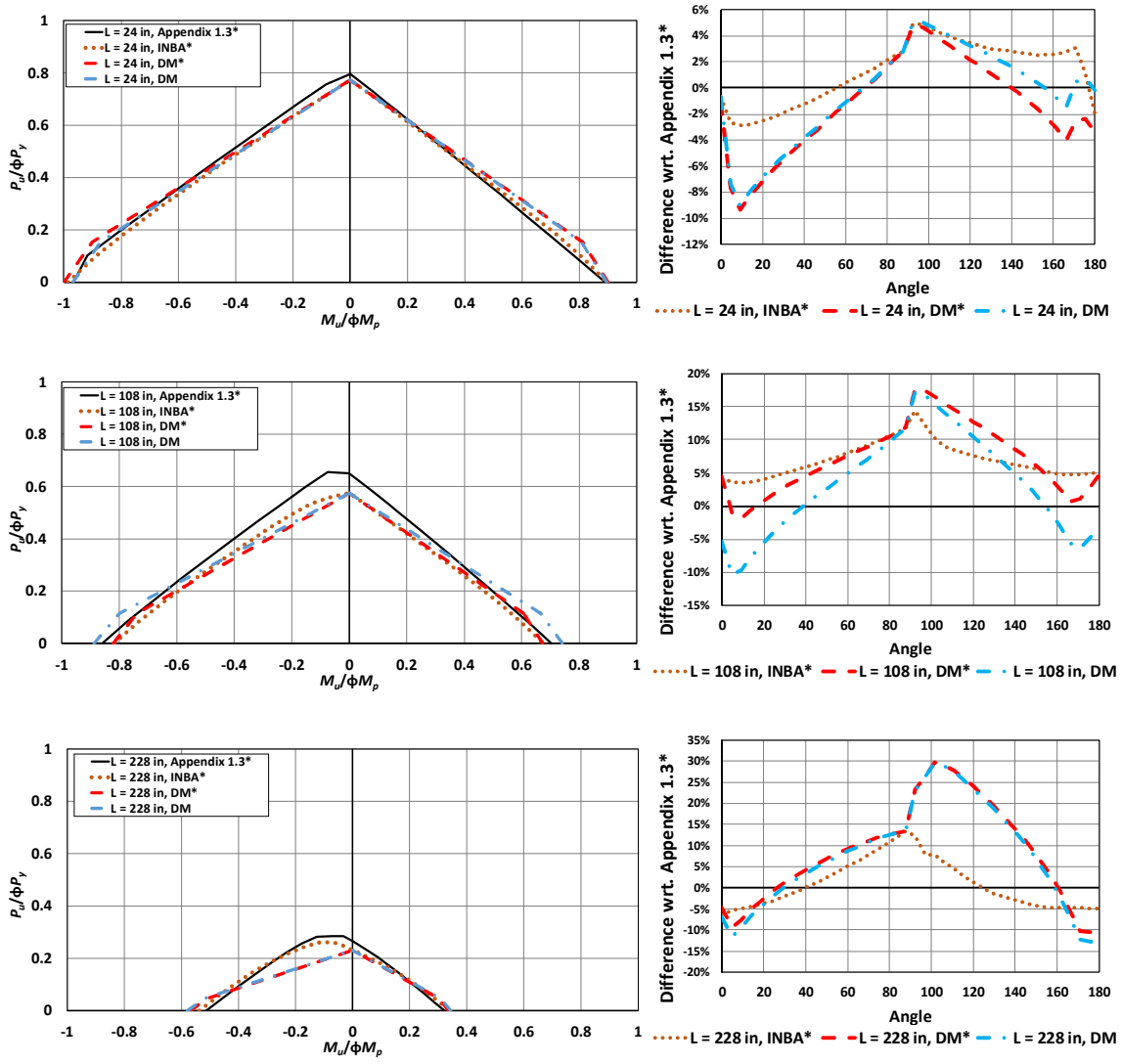

Figure 45. SS-3, uniform moment, beam-column strength curves and difference with respect to Appendix 1.3* curves (L_b=24 in, 108 in, 228 in)

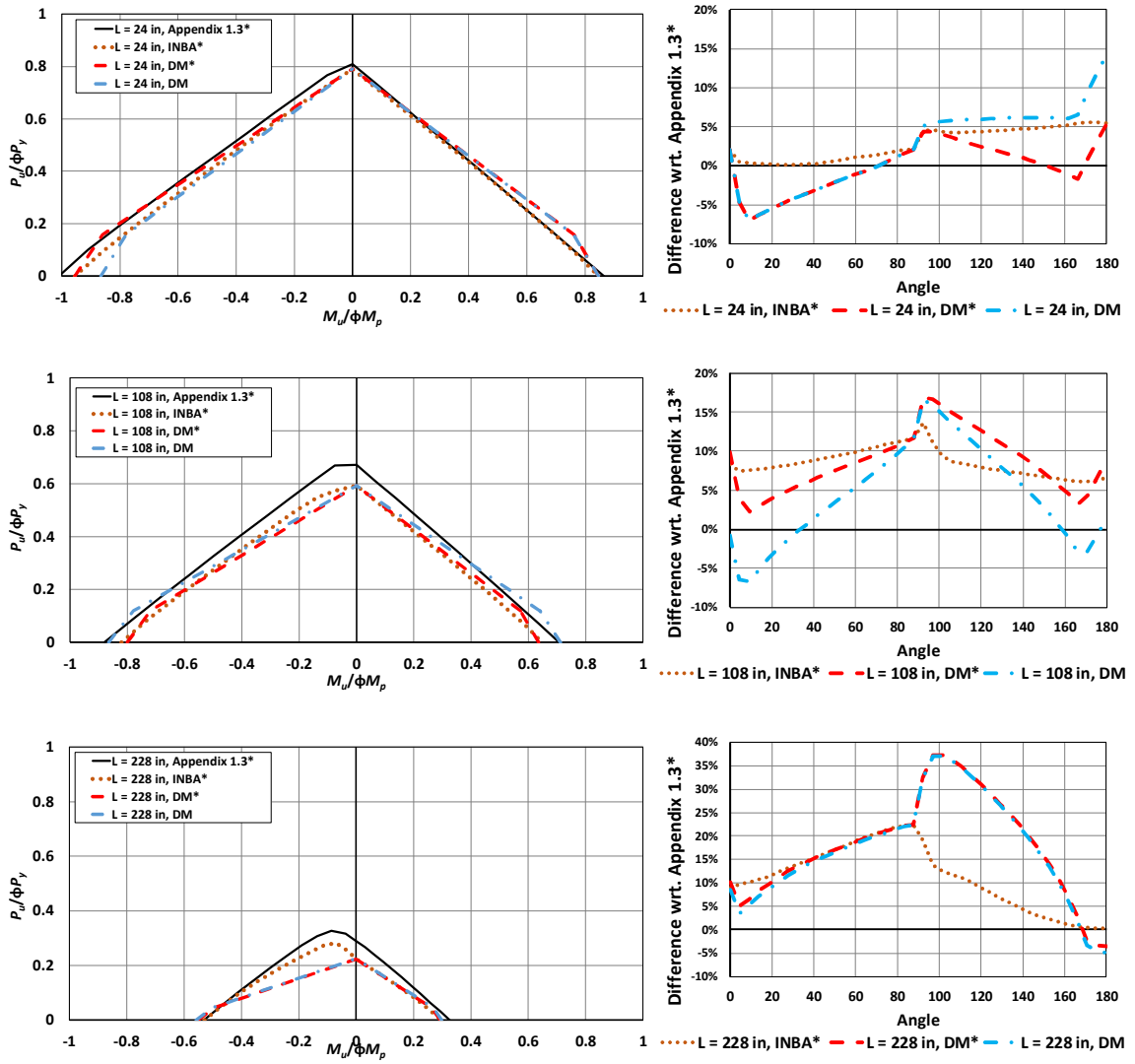

Figure 46. SS-4, uniform moment, beam-column strength curves and difference with respect to Appendix 1.3* curves (L_b=24 in, 108 in, 228 in)

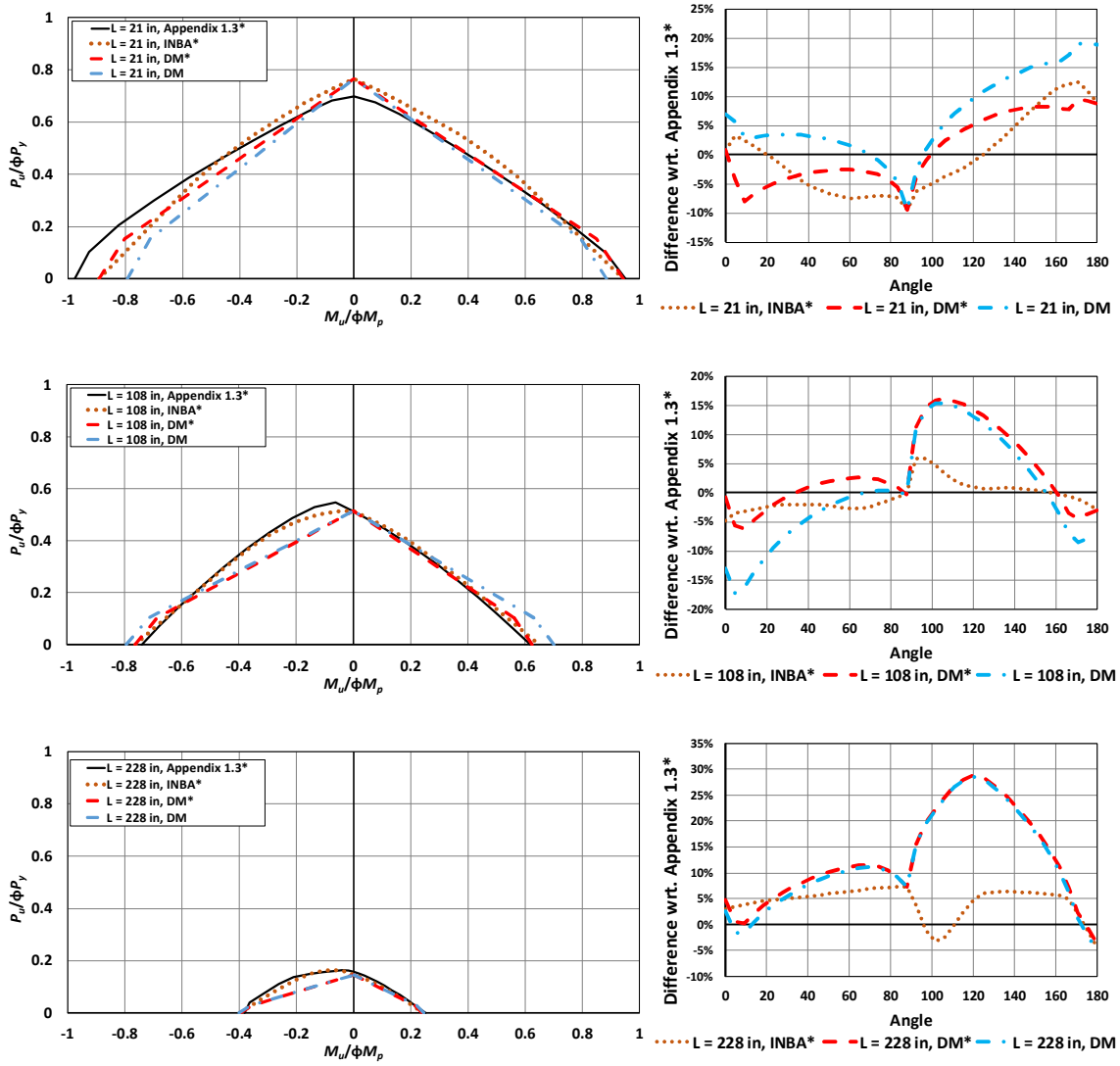

Figure 47. SS-5, uniform moment, beam-column strength curves and difference with respect to Appendix 1.3* curves (L_b=21 in, 108 in, 228 in)

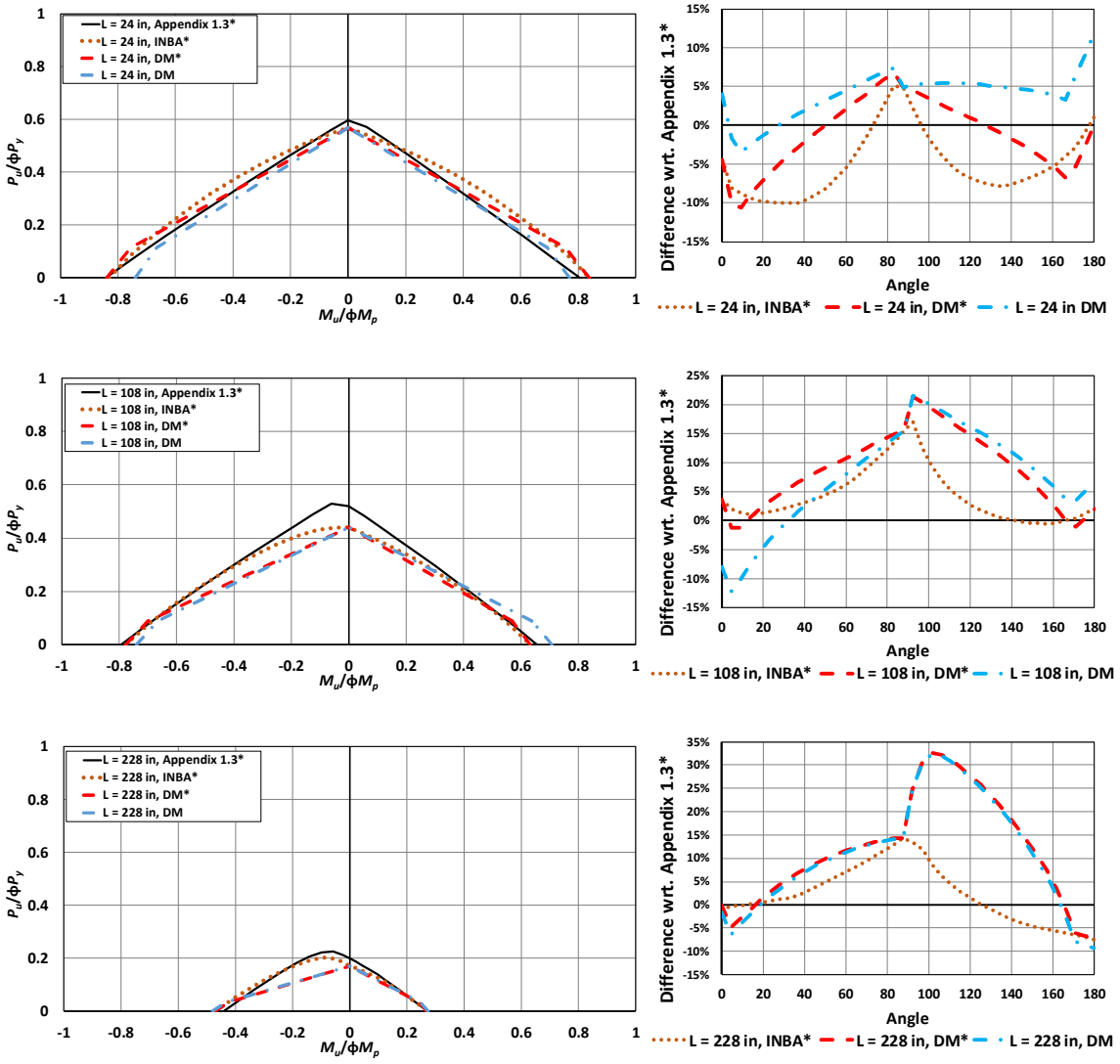

Figure 48. SS-6, uniform moment, beam-column strength curves and difference with respect to Appendix 1.3* curves (L_b=24 in, 108 in, 228 in)

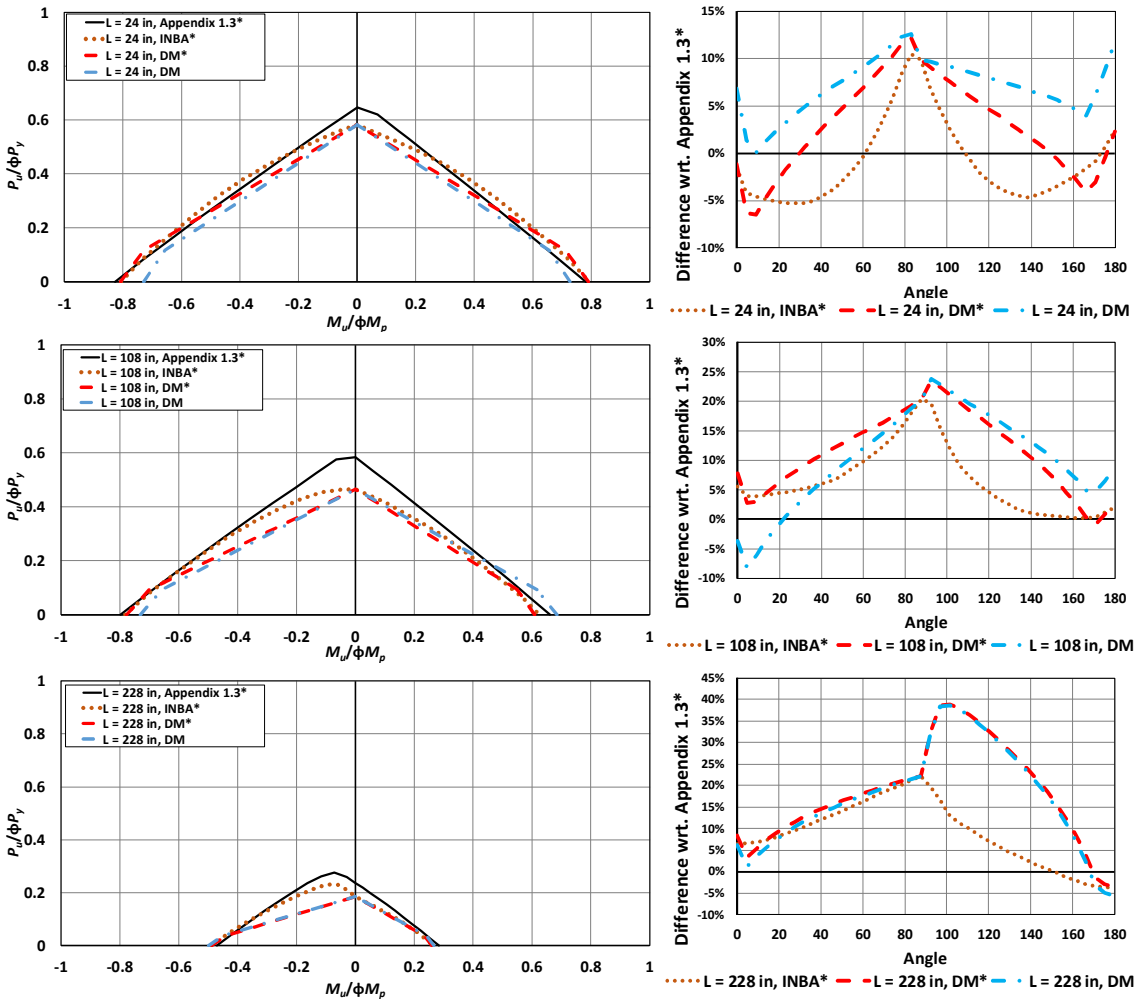

Figure 49. SS-7, uniform moment, beam-column strength curves and difference with respect to Appendix 1.3* curves (L_b=24 in, 108 in, 228 in)

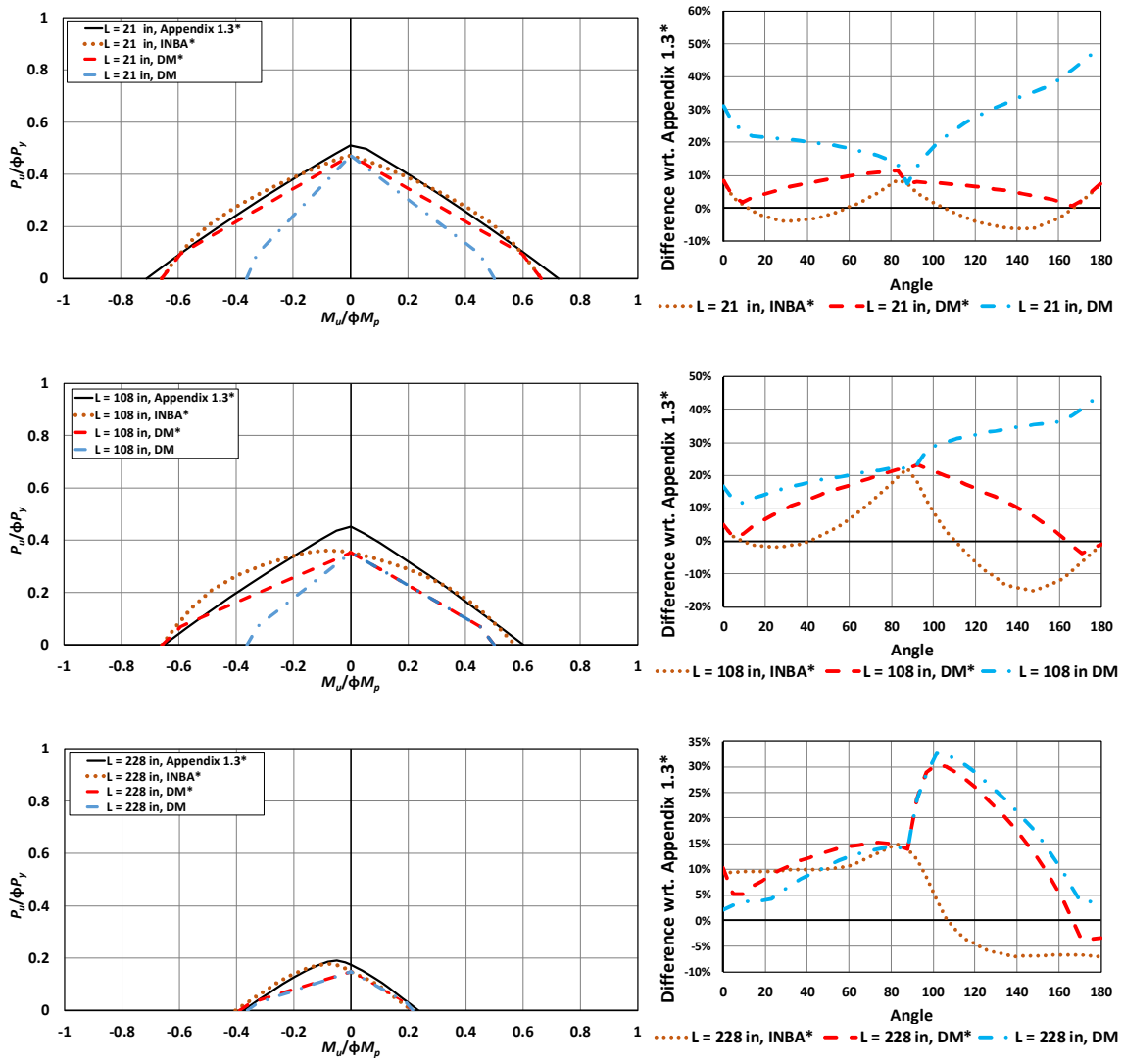

Figure 50. SS-8 uniform moment, beam-column strength curves and difference with respect to Appendix 1.3* curves (L_b=21 in, 108 in, 228 in)

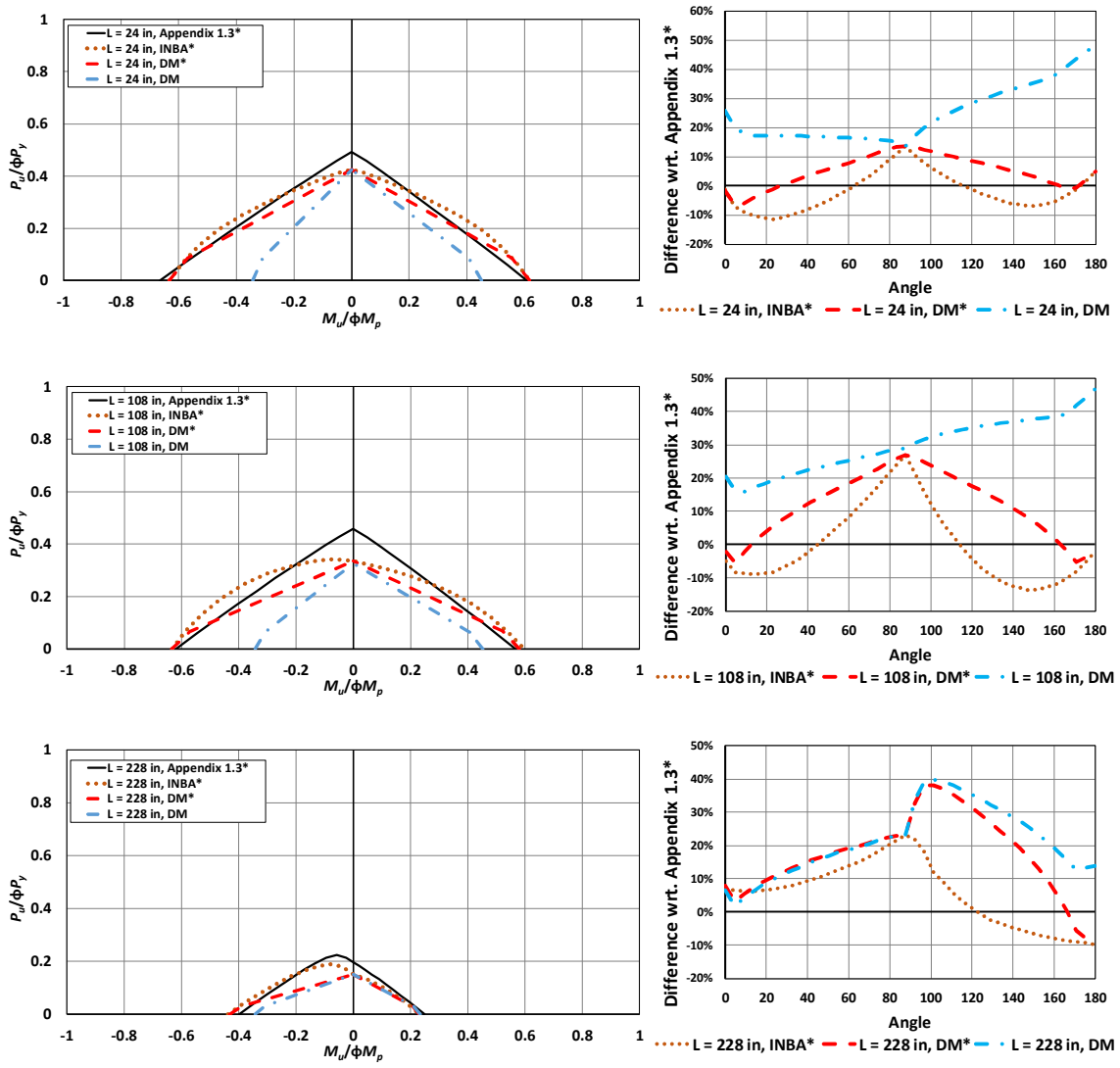

Figure 51. SS-9, uniform moment, beam-column strength curves and difference with respect to Appendix 1.3* curves (L_b=24 in, 108 in, 228 in)

4.1.3.2 Data Analysis, Singly-Symmetric Cross-Sections Subjected to Uniform Primary Bending

In this section, the results are discussed for the singly-symmetric cross-section members listed in Table 2, subjected to the uniform primary moment (UM) load combinations (Figs. 44 to 51). The statistics for the percent difference with respect to Appendix 1.3* are provided by the box and whiskers plot in Figs 52 and 53.

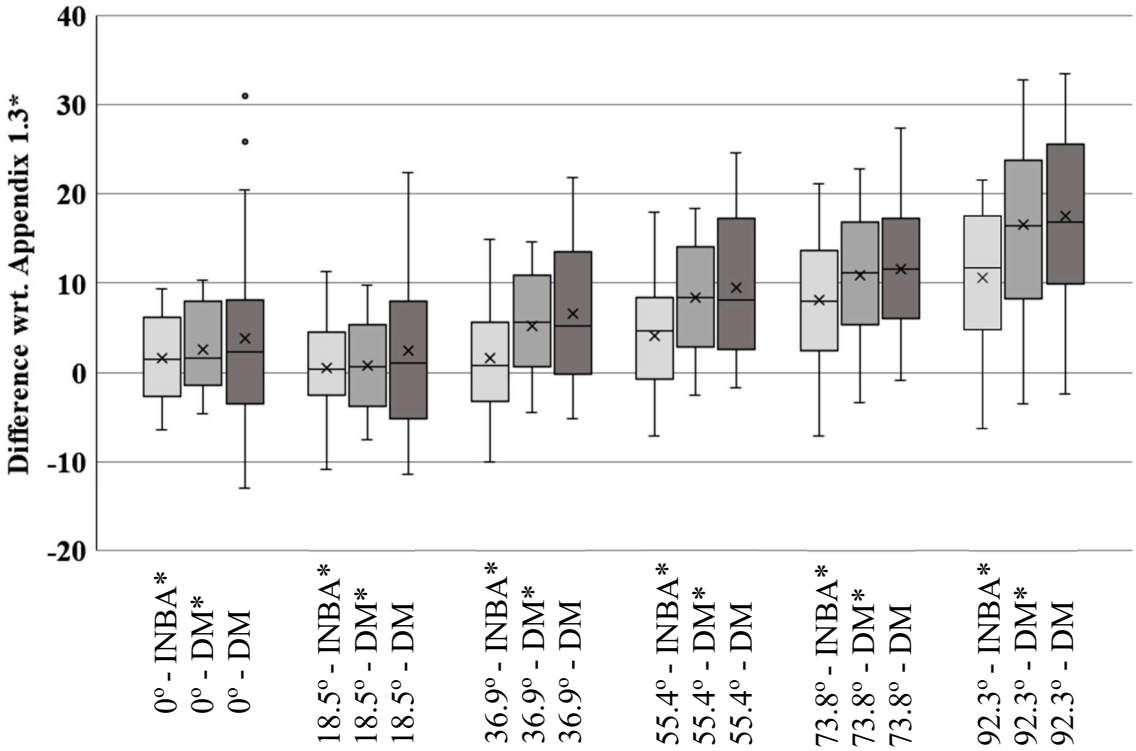

Figure 52. Comparison of INBA*, DM*, DM versus Appendix 1.3* solutions for uniform primary moment load configuration (part 1) (mostly right-hand quadrant of strength curves)

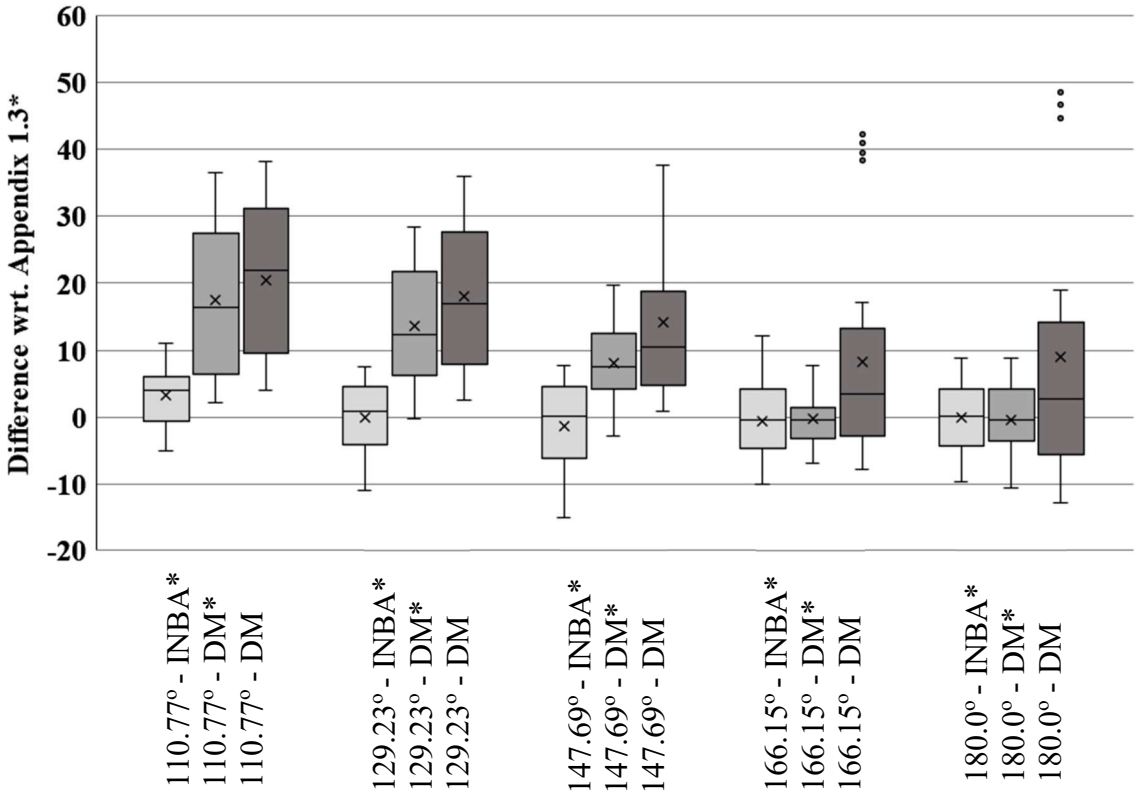

Figure 53. Comparison of INBA*, DM*, DM versus Appendix 1.3* solutions for uniform primary moment load configuration (part 2) (left-hand quadrant of strength curves)

The main finding from Figs. 52 and **53** is as similar to the doubly-symmetric cases, the average and median of all data sets for different angle lines are within 2% of the zero line, which means the data show close correlation with the Appendix 1.3* test simulation results. For the 0º (uniform primary positive moment only), the 90º (axial compression only) cases, and the 180º (uniform primary negative moment only) the INBA* solutions and DM* solutions match exactly with one another. The derivation of the column and beam stiffness reduction factors of the INBA* procedure ensures this.

For the 0º line in Fig. 52, the data dispersion is much lesser than the DM analysis. The main reason for this is the recommendations by Subramanian et al. (2018) and the

recommendations presented in Section 3.1 provides a better correlation with the results obtained by the Appendix 1.3* application.

The maximum unconservative difference with respect to the Appendix 1.3* solution for the 0° line is detected as 8%. This case is the SS9- L_b = 180 in. The case is governed FLB limit state for analysis types (INBA*, DM*, and DM). When the Appendix 1.3* test simulations for this case is run with nominal elasticity modulus (E) and nominal yield stress (F_y) instead of 0.9E and 0.9F_y, this conservatism is reduced, and the case becomes 1.5% conservative.

The most unconservative difference with respect to the Appendix 1.3* is detected as 15% for all the lines on the beam-column strength envelope. As stated previously, using the nominal stiffnesses instead of the stiffness values reduced by 0.9 coefficient is reducing this unconservatism at the maximum value of 5%.

For all intermediate angle lines except for the 92.3° line, which is the closest data point to the axial capacity, all INBA* data sets are showing closer correlation with Appendix 1.3* solutions than both DM* and DM solutions. Since DM* is using the recommended procedure for flexural strength of the member, the overall beam-column strength envelope procedure by this equations are also providing a better estimate than DM analysis solutions.

One key point that wasn't raised in the doubly-symmetric cases, the Tension Flange Yielding (TFY) limit states is governing limit state for negative moment application of the SS-4 case L_b = 24 in. The conservatism by the TFY current strength equations are reduced by half with the usage of the recommended procedure provided in Section 3.2.

All the outlier found in the DM analysis solutions for 0° line and 180° line (positive and negative moment applications) are caused by the current FLB limit state is being too conservative for especially slender flange section. This conservatism is removed by the recommended procedure, and that leads the INBA* set is having no outlier on these data sets.

4.1.3.3 Member Strength Envelopes and Plots of Differences Relative to Test Simulation Studies, Singly-Symmetric Members Moment Gradient Loading

Beam-column interaction plots that compare the INBA*, DM*, and DM results with the Appendix 1.3* solutions are provided in this subsection. The plots are provided for all the cases for the moment gradient loading conditions shown in Table 2.

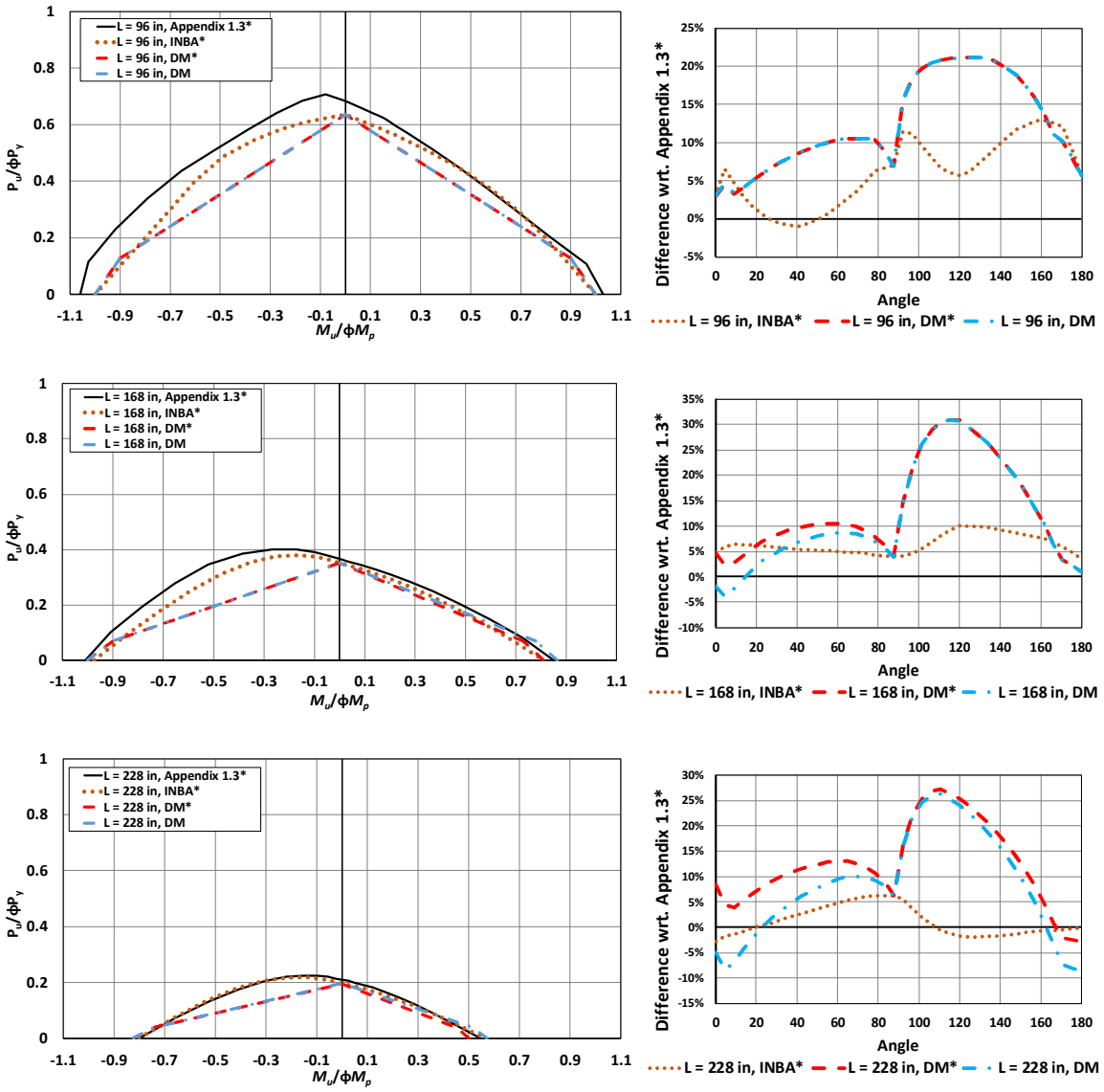

Figure 54. SS-2, moment gradient, beam-column strength curves and difference with respect to Appendix 1.3* curves (L_b=96 in, 168 in, 228 in)

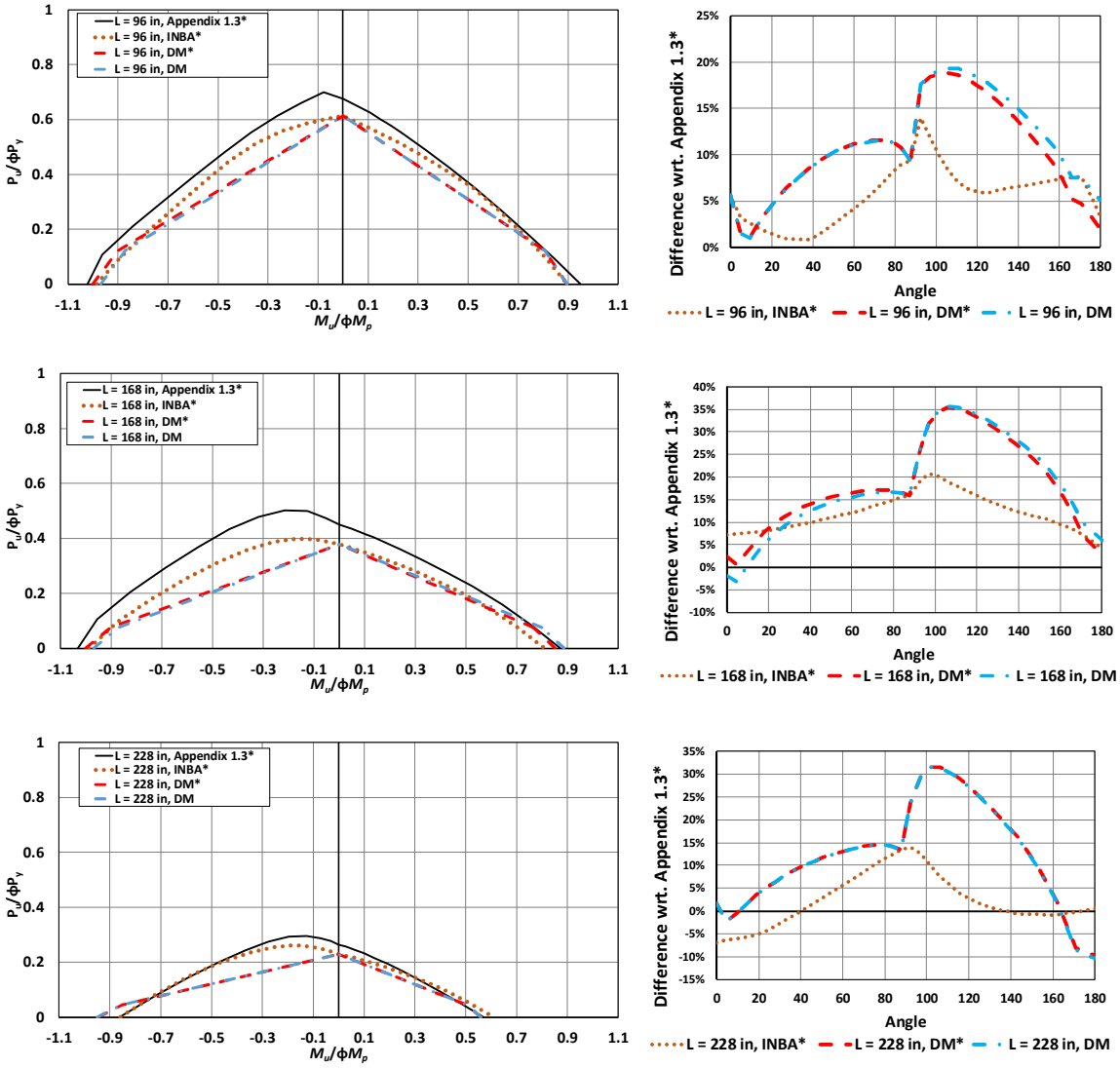

Figure 55. SS-3, moment gradient, beam-column strength curves and difference with respect to Appendix 1.3* curves (L_b=96 in, 168 in, 228 in)

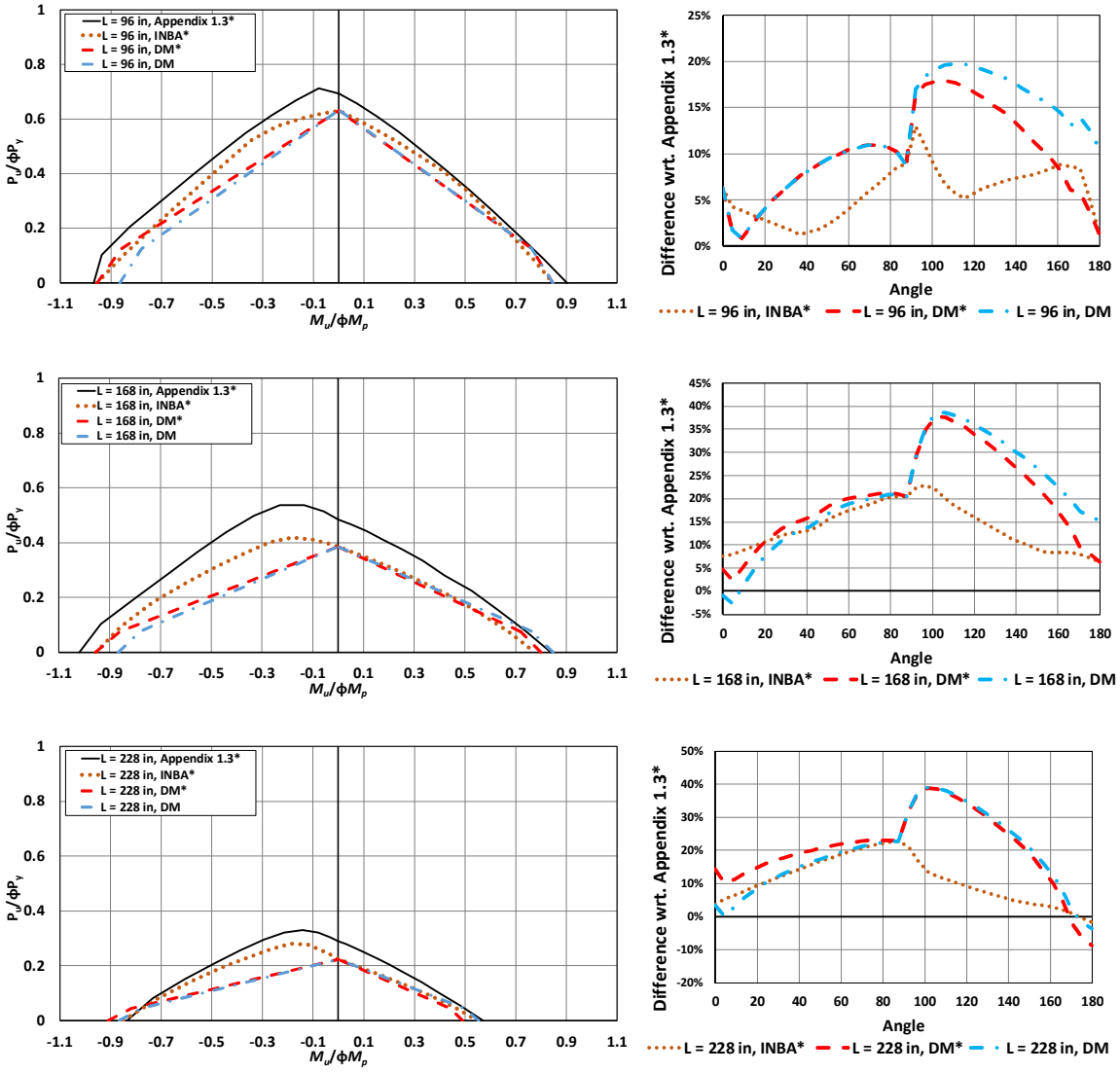

Figure 56. SS-4, moment gradient, beam-column strength curves and difference with respect to Appendix 1.3* curves (L_b=96 in, 168 in, 228 in)

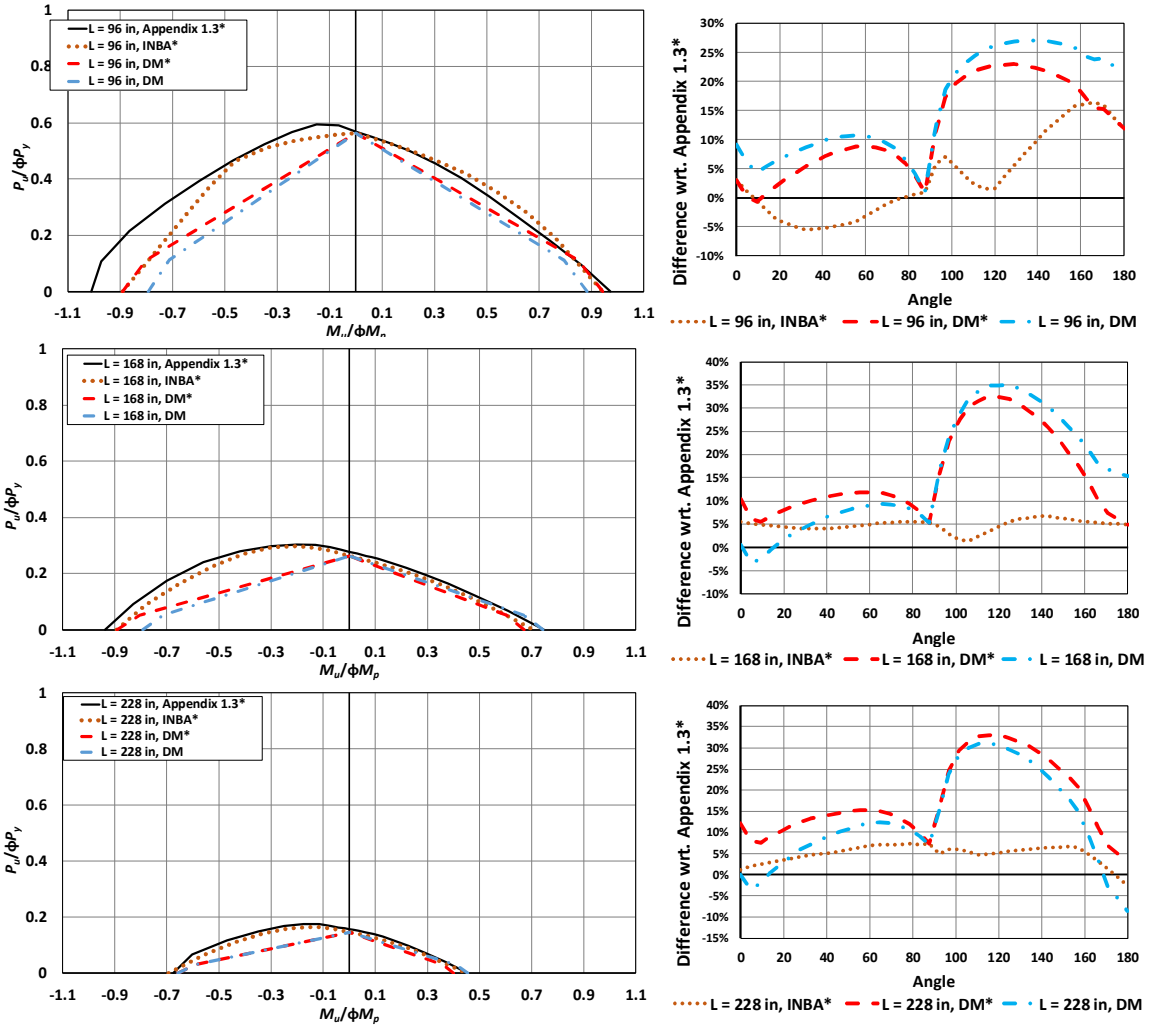

Figure 57. SS-5, moment gradient, beam-column strength curves and difference with respect to Appendix 1.3* curves (L_b=96 in, 168 in, 228 in)

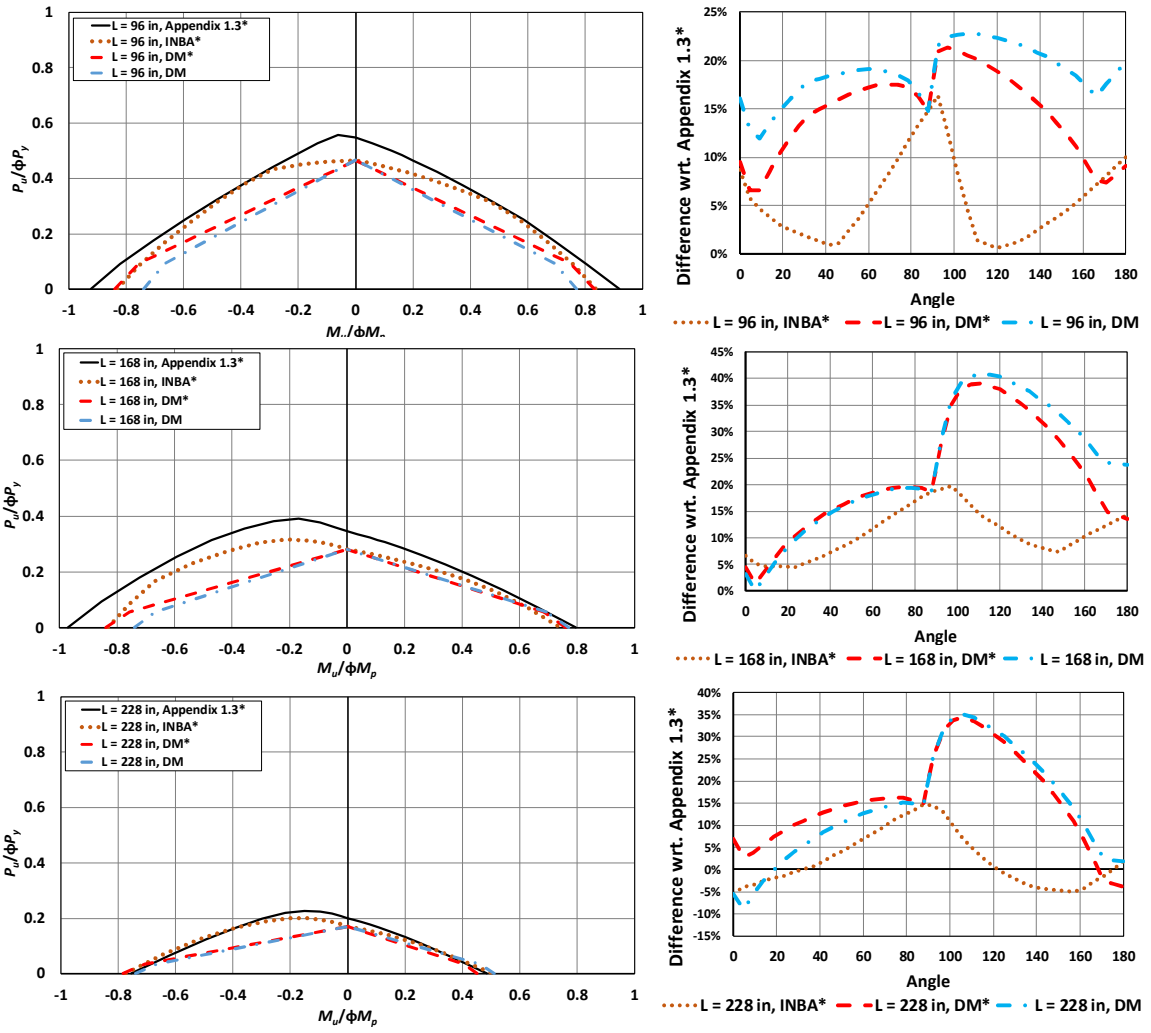

Figure 58. SS-6, moment gradient, beam-column strength curves and difference with respect to Appendix 1.3* curves (L_b=96 in, 168 in, 228 in)

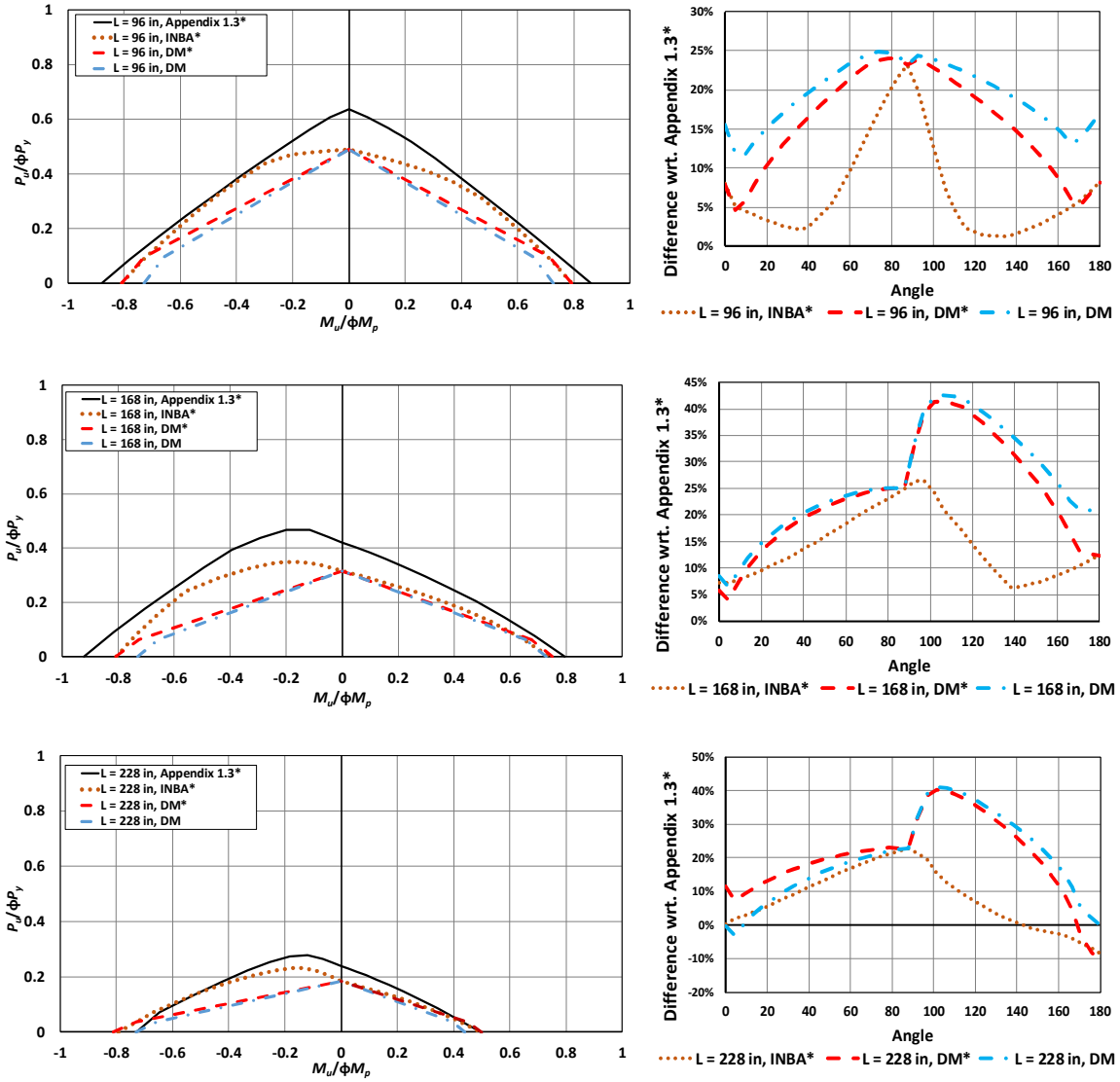

Figure 59. SS-7, moment gradient, beam-column strength curves and difference with respect to Appendix 1.3* curves (L_b=96 in, 168 in, 228 in)

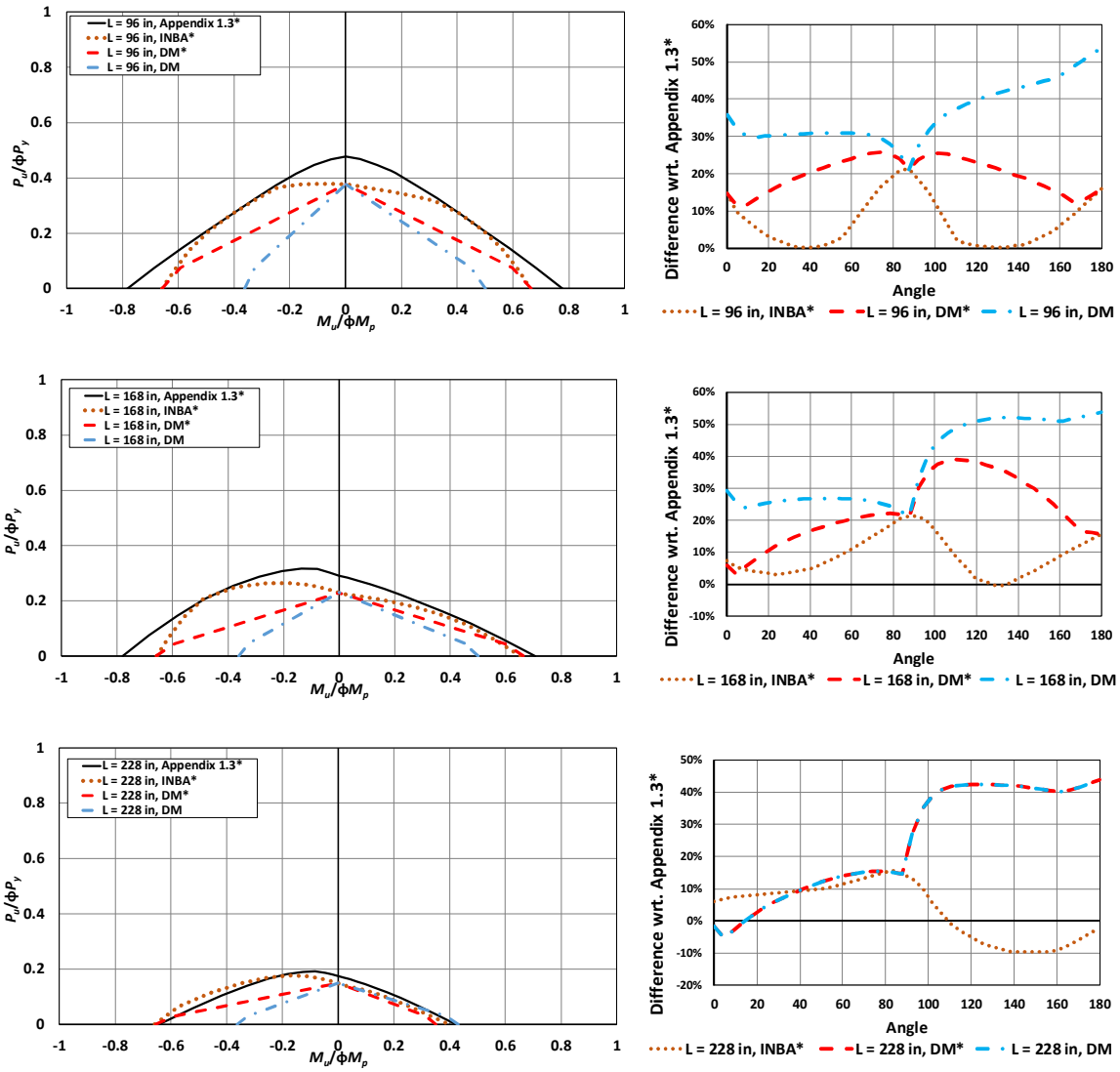

Figure 60. SS-8, moment gradient, beam-column strength curves and difference with respect to Appendix 1.3* curves (L_b=96 in, 168 in, 228 in)

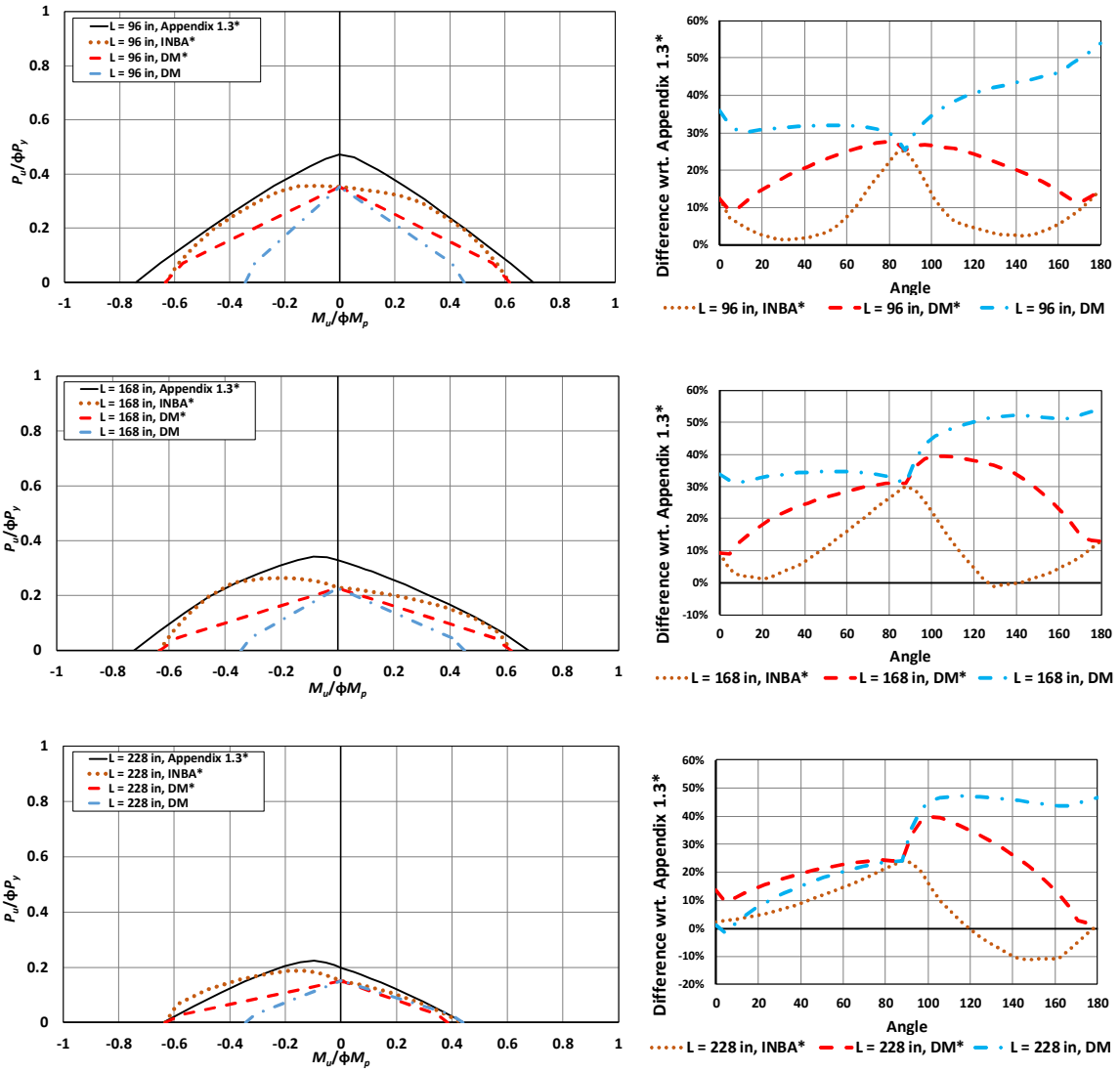

Figure 61. SS-9, moment gradient, beam-column strength curves and difference with respect to Appendix 1.3* curves (L_b=96 in, 168 in, 228 in)

4.1.3.4 Data Analysis, Singly-Symmetric Cross-Sections Subjected to Moment Gradient Loading

In this section, the results are discussed for the singly-symmetric cross-section members listed in Table 2, subjected to the moment gradient (MG) load combinations (Figs. 54 to 61). The statistics for the percent difference with respect to Appendix 1.3* are provided by the box and whiskers plot in Figs. 62 and 63 .

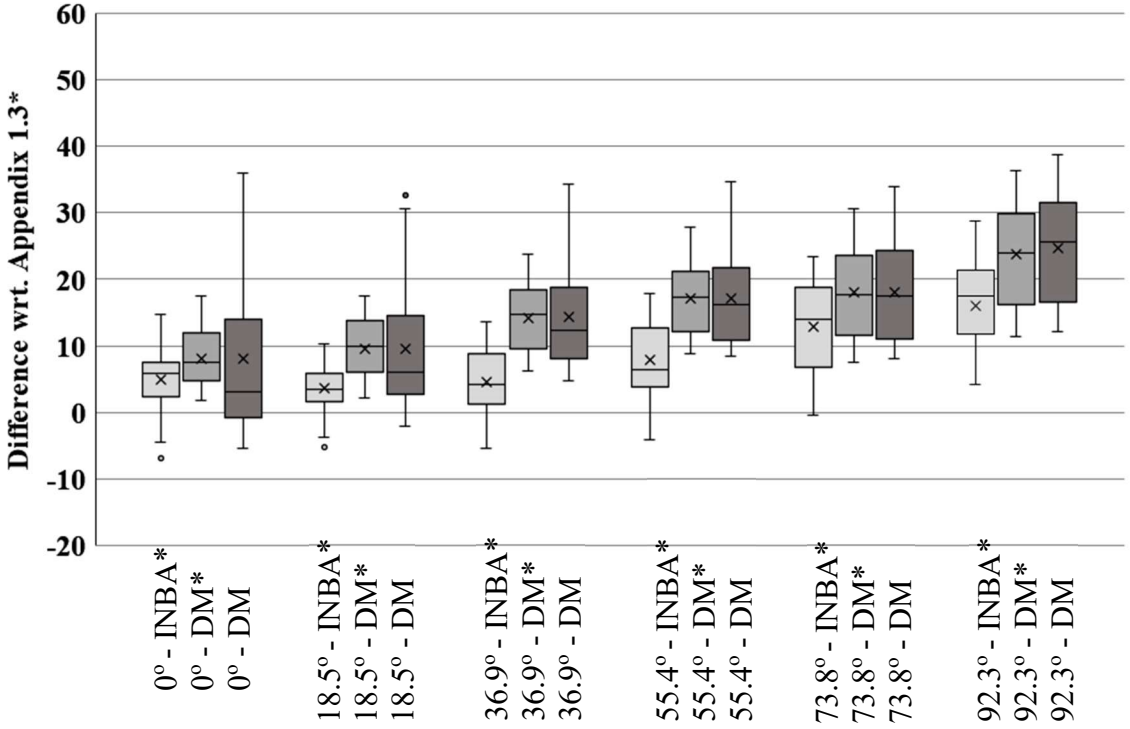

Figure 62. Comparison of INBA*, DM*, DM versus Appendix 1.3* solutions for moment gradient load configuration (part 1)

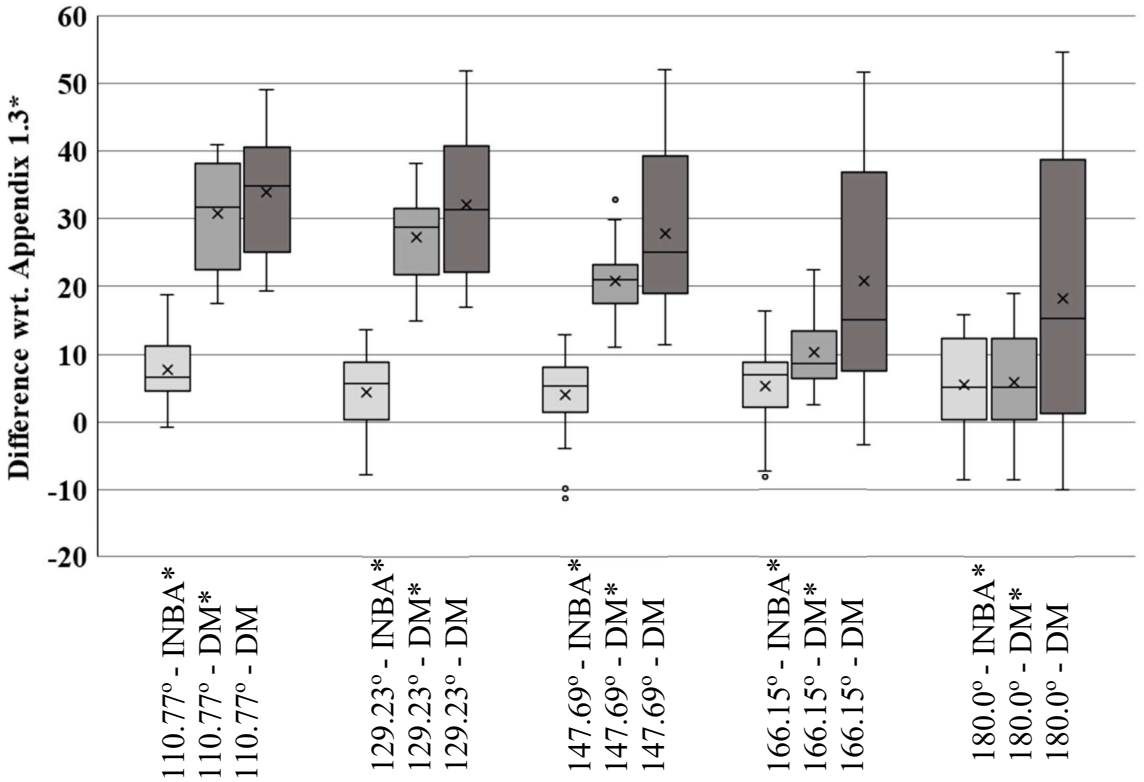

Figure 63. Comparison of INBA*, DM*, DM versus Appendix 1.3* solutions for moment gradient load configuration (part 2)

The main finding from Figs. 62 and 63 is that, for all the axial compression and moment combinations, the average and median of the data sets are greater than zero, which corresponds to the conservative prediction for these cases.

The outliers observed in the 0° line and the 180° line (positive and negative moment applications) are at the longest unbraced lengths of the SS3 and SS7. Although the extra capacity detected from the INBA* and the DM* is fairly small, this unconservative differences seems to be large since it is compared by normalized plots. As applied previously for the previous data sets, using the nominal stiffness values is also helping to wipe out these unconservative results.

Another unconservatism detected in the data set, which is a maximum of 11% is caused by the convexity of the beam-column strength curve generated by the INBA* procedure (Figs. 60 and 61). This unconservatism is also eliminated usage of the nominal stiffness in Appendix 1.3* solutions. In addition, this convexity is observed when the flexural capacity of the member is estimated correctly, but axial capacity is substantially less than the Appendix 1.3* solutions. When the axial capacity of the member is estimated more correctly, the beam-column strength curve generated by the INBA* is also following the Appendix 1.3* solutions (ex. Fig. 54, L_b = 228 in). For this purpose, more than one column curve should be used in the calculations of the axial resistance. This will also ensure that the τ_a (stiffness reduction factor for axial loading) is also more accurate as well.

For all intermediate angle lines, the DM* solution is better than the DM solution in terms of reducing the extra conservatism introduced by the FLB equations. In addition, the INBA* analysis shows overall the closest correlation with respect to Appendix 1.3* solutions. The 92.7^o angle is for the axial load case, which should be the same for all analysis types.

4.2 Web-Tapered Members – Comparison to Experimental Tests

This section considers the strength predictions for the web-tapered members tested experimentally in the study by Smith et al. (2013). This study includes a total of ten cases, which including two beam-column cases. The test matrix from this study is presented in Table 3.

Table 3.Test matrix, synthesized from (Smith et al. 2013)

Specimen	Taper Angle	CS		Notes:
		Flange	Web	
CF1	4.60°	C	S	constant taper, no transitions, full CS 2-sided weld, CS = 1st unbraced length, welded brace clips
CF2	4.60°	C	S	constant taper, no transitions, CS = 1st unbraced length, welded brace clips, slot in web
CF2-A	4.60°	C	S	constant taper, no transitions, axial load, CS = 1st unbraced length, welded brace clips, slot in web
PF1	9.59°	C	S	pinch point at end of CS, CS = 1st unbraced length, welded brace clips
PF2	14.48°	C/N	S	pinch point within CS, CS = 1st unbraced length, welded brace clips
CS1	5.62°	N	N	constant taper, no transitions, CS = 2nd unbraced length, bolted brace clips
CS1-A	5.62°	N	N	constant taper, no transitions, axial load, CS = 2nd unbraced length, bolted brace clips
CS2	4.60°	N	S	constant taper, flange splice, CS = 2nd unbraced length, bolted brace clips
CS3	4.60°	C/N	S	constant taper, flange splice and thickness change, CS = 2nd unbraced length, welded brace clips
CS4	4.60°	N	S	constant taper, shear stiffeners, CS = 2nd unbraced length, welded brace clips

a CS = Controlling Segment
b C = Compact, N = Non-Compact, S = Slender

As explained in Table 3, the PF1 and PF2 cases have pinch point within the Controlling Segment (CS), where the CS is the critical unbraced length with respect to the resistance calculations. From the drawings of these cases in the report, it is observed that there is no web stiffener at these pinch point locations. This makes these locations susceptible to a local web failure, and experimental tests indeed showed a local failure at these locations. Therefore, the various member strength calculations are not considered for these tests.

4.2.1 *Description of Experimental Tests*

The specimens listed in Table 3, were tested in an L-shaped frame configuration to apply moment at left side of the members. For this application the column fixture used in the left side of the Fig. 64 was designed to remain elastic during the tests.

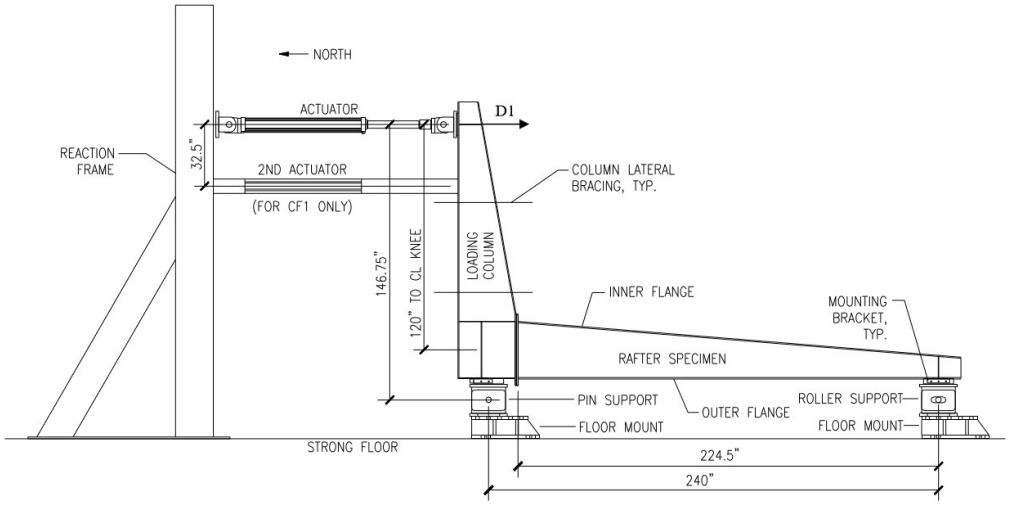

Figure 64. Test setup elevation (Adapted from Smith et al. 2013)

As illustrated in Fig. 65, the specimens listed in Table 3 are modeled as members with flexurally and torsionally simply-supported boundary conditions. At the brace point locations, the members are restrained both twisting and lateral out-of-plane displacements. This assumption is valid considering the rigid panel zone of the moment frame.

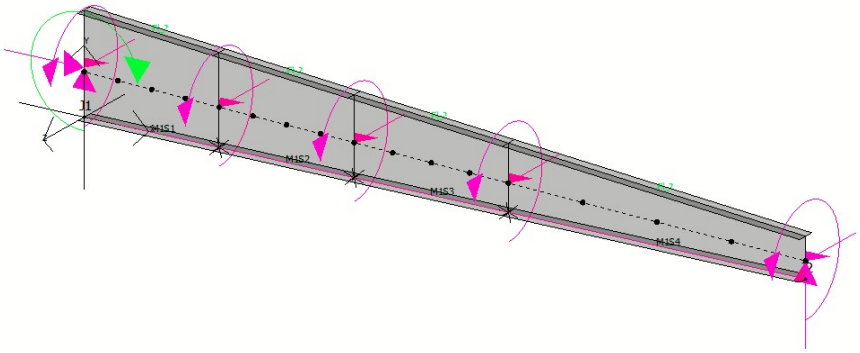

Figure 65. CF1 - SABRE2-V2 model

It is common for members to have different yield stresses for different plates. However, it should be noted that if the yield stress of the web is larger than the flange yield stresses, the recommended procedures set the web yield stress to the smaller of the flange yield stresses. Table 4 summarizes whether the section is classified as hybrid or homogenous after changing the web yield stress to the smaller of the flange yield stresses.

Table 4. Cross-section classifications

	F_{y_top}	F_{y_bot}	F_w	$F_{w\_adjusted}$	Hybrid?
CF1	62.5	60.0	61.9	60.0	Yes
CF2	57.6	57.6	71.9	57.6	No
CF2-A	57.6	57.6	71.9	57.6	No
CS1	61.6	61.6	62.1	61.6	No
CS1-A	61.6	61.6	62.1	61.6	No
CS2	69.8	69.8	61.9	61.9	Yes
CS3	69.7	67.0	61.9	61.9	Yes
CS4	54.5	54.5	71.9	54.5	No

4.2.2 *Summary of the Results*

A summary of results for the eight web-tapered members considered in this work is provided in Table 5. There are 4 different analysis procedures are conducted on the test cases listed in Table 4. The first analysis type is $INBA_{FULL,}$ which is the full member used in the analysis with the INBA procedures. The second analysis type is the $INBA_{FULL}$*, which is using the INBA* procedures, and again using the full member in the analysis. The third one is the $INBA_{CS}$ in which only the Critical Segment (CS) of the member modeled in the analysis without consideration of the continuity effects that can help the member from adjacent unbraced lengths, and is analyzed using the INBA procedures. Similarly, in the $INBA_{CS}$*, only the CS of the member is analyzed using the INBA* procedures. The CS

used in these analyses are obtained from the INBA* procedures, since this procedure is providing a better correlation to experimental results in Table 5.

Table 5. Summary of the results and failure types for using the full member modeling and only modeling the critical segment detected with INBA* procedures

	$INBA_{FULL}$	$INBA_{FULL}$ Failure	$INBA_{FULL}$*	$INBA_{FULL}$ *Failure	Critical Segment (CS)	$INBA_{CS}$	$INBA_{CS}$ Failure	$INBA_{CS}$*	$INBA_{CS}$* Failure
CF1	1.00	CFY	1.02	CFY	1st	1.00	CFY	1.02	CFY
CF2	1.09	CFY	1.12	CFY	1st	1.09	CFY	1.12	CFY
CF2-A	1.09	CFY	1.10	CFY	1st	1.09	CFY	1.10	CFY
CS1	0.99	FLB	0.92	LTB	2nd	0.96	FLB	1.02	LTB
CS1-A	1.05	FLB	0.99	LTB	2nd	1.02	FLB	1.09	LTB
CS2	0.84	FLB	0.81	FLB	1st	0.84	FLB	0.81	FLB
CS3	1.02	CFY	1.04	CFY	1st	1.02	CFY	1.04	CFY
CS4	1.01	FLB	0.99	FLB	2nd	1.01	FLB	1.05	LTB

When the INBA procedures are used, the calculated strengths for the tests are governed by either Flange Local Buckling (FLB) or Compression Flange Yielding (CFY). However, when the INBA* procedures are used, some of the cases change their failure mode, and are governed by LTB. It should be noted that the LTB resistances determined here from the INBA and INBA* procedures include the benefit of the continuity across the braced points, and the restraint provided to the critical segments from the other unbraced lengths. Table 5 provides results for test resistance divided by the predicted resistance from the related inelastic nonlinear buckling analysis resistance. For this ratio, while the value less than 1 means unconservative, greater than 1 means conservative results with respect to the experimental tests.

The strength of the members is obtained from the first positive cycle of 3% displacement ratio for the experimental results. These values are obtained for both axial and bending loads.

While the mean for INBA procedures is 1.00, and the mean of INBA* procedure is calculated as 1.01. The coefficient of variation (COV) for INBA is calculated as 7.77, and for INBA* is 9.96. It should be noted that the CS2 case is also listed as a possible outlier in the report without further explanation about the case (Smith et.al. 2013). After removing the CS2 considering the case outlier as well, the mean for INBA using the current AISC Specification Equations (2016) is calculated as 1.04, while the mean for INBA* using the recommended equations in Section 3 is calculated as 1.03. The COV is also reduced with the removal of the possible outlier CS2. The new COV values are for the INBA procedure 3.97, and for the INBA* procedure 6.69.

For the case CF1, the resistance is governed by the Compression Flange Yielding for both the INBA and INBA* procedures. Since the INBA* is using the recommendations by Subramanian et al. (2018), the reduction in the plateau of the LTB curve is reduced. This is resulting a little more conservative results for the INBA* than the INBA. For controlling segment detection, since the member is governed by a limit state, the Unity Check (UC) plot can be used to determine which unbraced length is critical. Figure 66 clearly shows that the max UC value is detected as 1.00 at the left support location. This indicates that the controlling segment for the CF-1 case is the first unbraced length.

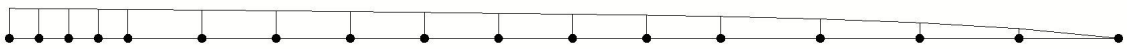

Figure 66. CF1 Unity Check (UC) plot using the INBA* procedures

When the deflected shape for CF-1 is investigated, the largest out-of-plane displacement is also detected in the first unbraced length as well (Fig. 67). It should be noted that, the buckled shape provided in Fig. 67. uses the eigenvectors which

corresponding to a higher load level than the limiting CFY limit state. However, this still provides an insight of how the member would behave under those loads.

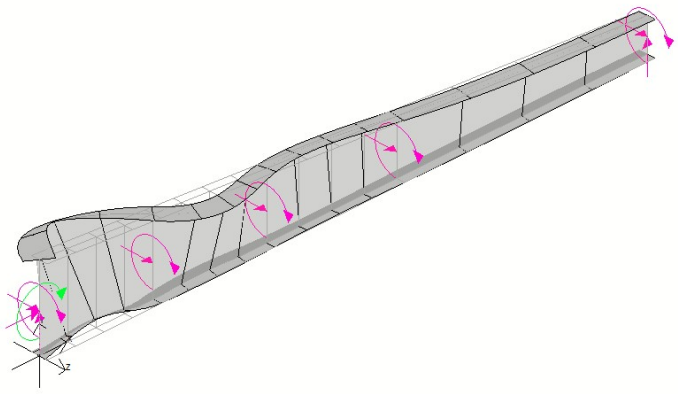

Figure 67. CF1 buckled shape (Load Proportionality Factor of 2.3)

Since the member behavior is governed by the limit state, the critical segment ratios are the same for both $INBA_{FULL}$ vs $INBA_{CS}$ and $INBA_{FULL}$* vs $INBA_{CS}$*.

Similar to the CF1 case, the CF2, CF2-A and CS3 cases are also governed by the CFY limit state, and the Critical Segments are detected as the first unbraced length of the member. The deflected shapes of these members are provided with the line representation and top-view, for better visualization of the out-of-plane displacements (Figs. 68 to 70). It should be noted from Fig. 70 that the critical segment of first unbraced length of the member displacement is showing very close to each other between first and second unbraced lengths.

Figure 68. CF2 buckled shape line representation (top view) (Load Proportionality Factor of 1.26)

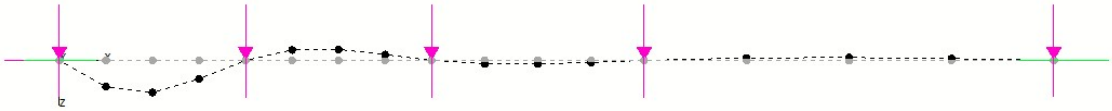

Figure 69. CF2-A buckled shape line representation (top view) (Load Proportionality Factor of 1.17)

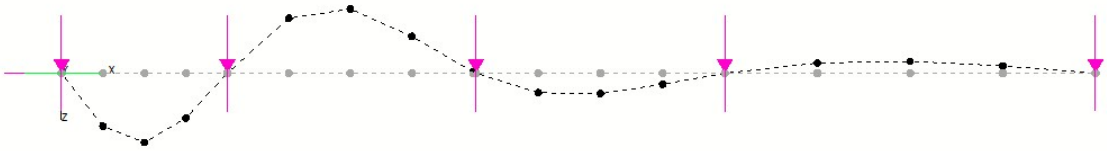

Figure 70. CS3 buckled shape line representation (top view) (Load Proportionality Factor of 1.30)

For cases CS1, CS1-A, while the INBA procedure is giving the failure mode as FLB limit state, the INBA* procedure provides this failure mode as LTB. The main reason for this limit state change is that the INBA* procedure utilizes the recommendation for FLB limit state provided in Section 3.1. Using these recommendations, since the FLB resistance become larger, the member is controlled by the LTB response. When the controlled segments are checked for these members using the INBA*, it is observed that the maximum out-of-plane displacements are detected at the second unbraced length for both members (Figs. 71 and 72)

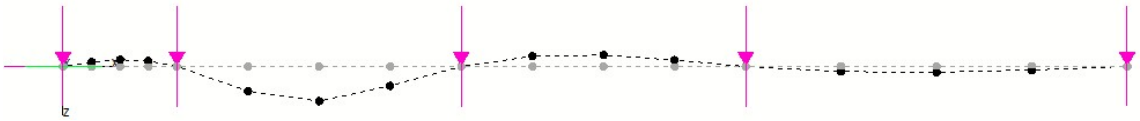

Figure 71. CS1 buckled shape line representation (top view) (Load Proportionality Factor of 0.98)

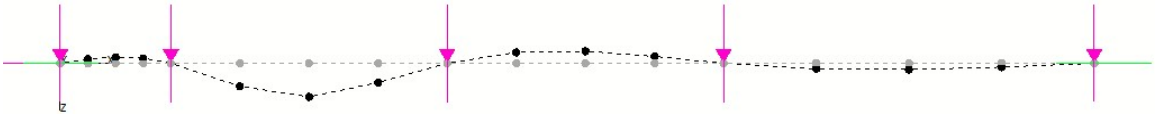

Figure 72. CS1-A buckled shape line representation (top view) (Load Proportionality Factor of 0.90)

When only the controlled segments are analyzed for these members, the $INBA_{CS}$ and $INBA_{FULL}$ are providing equal ratios with respect to the test results vs the predictions ratio from the buckling analyses performed with SABRE2. This is a similar behavior as seen in CF1, CF2, CF2-A, and CS3. However, if the controlled segments of these member are analyzed with the $INBA_{CS}$* procedure, it is observed that the results becoming conservative, which is caused because the segment cannot get the benefit from the adjacent unbraced lengths and fail with a smaller load level. Using the $INBA_{FULL}$* procedure is also a helpful tool in terms of using cross-sections with a higher unbraced length, considering the benefit from adjacent unbraced lengths.

For cases CS2 and CS4, the controlling limit state using the full member is resulting FLB failure for both the $INBA_{FULL}$ and $INBA_{FULL}$* procedures. The $INBA_{FULL}$* procedure provides a smaller test results vs the predictions ratio from the buckling analyses performed with SABRE2, because the recommendations presented in Section 3.1 provides a higher capacity for FLB limit state considering reserved post-buckling strength. The controlling segments are predicted the same with the experimental tests using the $INBA_{FULL}$* procedure. The deflected shapes for these members are provided in Figs. 73 and 74.

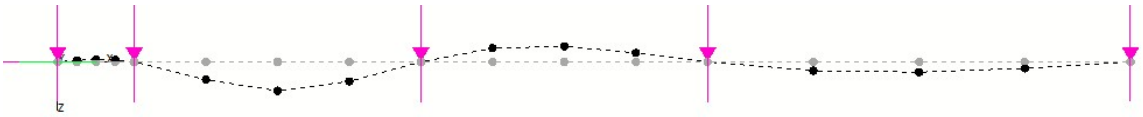

Figure 73. CS2 buckled shape line representation (top view) (Load Proportionality Factor of 1.11)

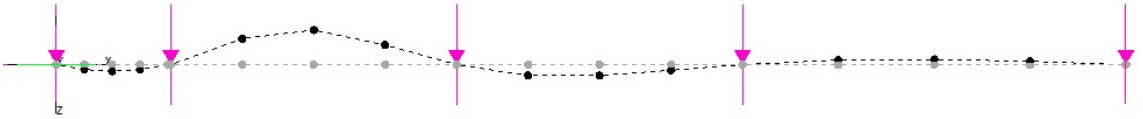

Figure 74. CS4 buckled shape line representation (top view) (Load Proportionality Factor of 0.91)

While the controlling limit state using the full member is resulting FLB failure for both the $INBA_{CS}$* and $INBA_{FULL}$* procedures for CS2 case, the failure type is changed in case CS4 using the controlled segment for recommended procedures. Since the FLB limit state is at a higher load level for the recommended procedure, the member can no longer reach that load level without the help from the adjacent unbraced lengths. This causes member to fail with LTB failure before reaching the cross-section limit state.

4.3 Extreme Singly-Symmetric Member Studies

4.3.1 *Beam, Column and Beam-Column Resistances in Uniform Primary Bending*

A detailed example is presented in this section to demonstrate the calculations outlined in Sections 3.1, 3.2 and 0, and to compare the resulting predictions to the limit states response determined by test simulation. This example is the same as in Fig. 8, except $L_b = L_x = L_y = L_z = 5$ ft here. The particular cross-section studied is from a clear-span metal building frame design provided to the author and discussed subsequently in Section 6.3. Similar to Fig. 8, Fig. 75 compares the current AISC (2016) and the recommended strength predictions to the results from test simulation.

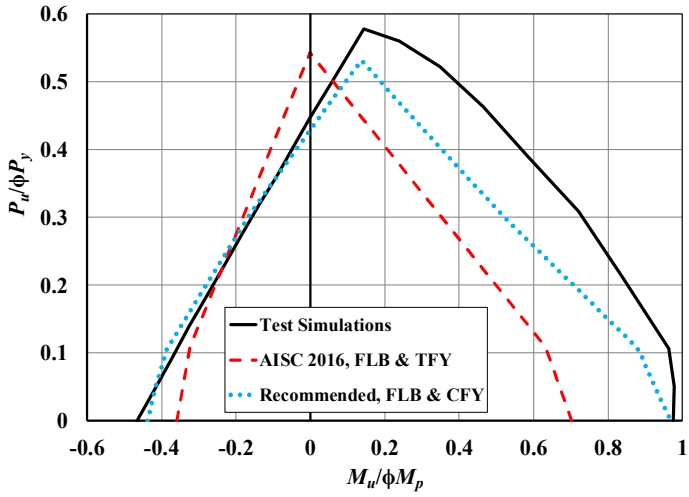

Figure 75. Strength envelopes from test simulation, the AISC (2016) column and flexural strength provisions, and the AISC column and recommended flexural strength provisions, torsionally and flexurally simply-supported singly-symmetric I-section members with $b_{fc} = b_{ft} = 8.0$ in., $t_{fc} = 0.75$ in. $t_{ft} = 0.25$ in., $h = 37.0$ in., $t_w = 0.1875$ in., and $L_x = L_y = L_z = L_b = 5$ ft, subjected to uniform primary bending moment and axial compression.

When the current AISC (2016) Specification is employed to assess this unbraced length, the flexural resistance for $P_u = 0$ is limited by TFY for flexure causing compression on the larger flange (i.e., for the curve in the right-hand quadrant of the plot). It is limited by FLB for flexure causing compression on the smaller flange (corresponding to the left-hand quadrant of the plot). However, with the recommended provisions, the flexural resistance in the right-hand quadrant is limited by LTB while the flexural resistance in the left-hand quadrant is limited by Flange Local Postbuckling (FLPB). The AISC (2016) TFY check is 28% conservative relative to the corresponding test simulation strength in the right-hand quadrant for $P_u = 0$ while the AISC (2016) FLB check is 23% conservative relative to the test simulation results in the left-hand quadrant. The recommended calculations are 0.5% and 6% conservative relative to the test simulation results for $P_u = 0$.

4.3.1.1 Results from intermediate and final resistance calculations

The results of the various intermediate and final resistance calculations are listed below:

- *Cross-section dimensions & width-to-thickness ratios*

  Top flange: $b_f = 8$ in., $t_f = 0.75$ in., $b_f/2t_f = 5.33$

  Bottom flange: $b_f = 8$ in., $t_f = 0.25$ in., $b_f/2t_f = 16.0$

  Web: $h = 37$ in., $t_w = 0.1875$ in., $h/t_w = 197$

  For bending causing compression on the larger flange:

  $D_c = 13.4$ in., $2D_c/t_w = 143$, $D_{cp} = 7.83$ in. (Eq. (54)), $D_{cT} = 1.09D_{cp}$

  (D_{cT} equation is given by Eqs. (54) and (51)), $2D_{cT}/t_w = 90.64$

  For bending causing compression on the smaller bottom flange: $2D_c/t_w = 252$

- *Overall cross-section properties*

  $F_y = 55$ ksi, $I_x = 3236$ in^4, $S_{xc} = 229$ in^3, $S_{xt} = 136$ in^3, $M_{y.top} = 1047$ ft-kip,

  $M_{y.bot} = 622$ ft-kip, $M_p = 886$ ft-kip, $M_p/M_{y.top} = 0.846$, $M_p/M_{y.bot} = 1.42$

  For bending causing compression on the larger top flange: $M_{ycT} = 852.5$ ft-kip

  Note that the yield moment to the top flange, $M_{y.top}$, is actually larger than the fully-plastic moment for this section. This is due to the neglect of the early onset of yielding at the bottom flange in this traditional calculation per AISC and AASHTO. The AISC and AASHTO resistance equations in whole account for the early yielding at the bottom flange in this type of section, but they tend to handle this

attribute of the strength behavior conservatively via a relatively elaborate implementation of the R_{pc} and R_{pt} factors.

- *Flange slenderness limits (Table B4.1 of the AISC (2016))*

  $\lambda_{pf} = 8.73$ and $\lambda_{rf} = 15.4$ (flexure), $\lambda_{rf} = 8.69$ (axial compression)

  The larger top flange of the subject cross-section is nonslender under uniform axial compression and compact under flexure. This means that local buckling of this flange is not a factor in the calculation of the resistances for any combination of axial load and moment.

  The smaller inside flange is slender under both uniform axial compression and flexure. This indicates that local buckling of this flange is a significant factor in the resistance under both uniform axial compression and flexure causing compression on the inside flange.

  The recommended provisions are the same as the AISC (2016) provisions with regard to the above limits, with the exception that the term F_L is expressed simply as $0.5F_y$ in the recommended provisions. This is made possible by the consideration of TFY directly in the calculation of M_{ycT}.

- *Web slenderness limits*

  AISC (2016) nonslender web limit for uniform axial compression: $\lambda_{rw} = 34.2$ (Table B4.1a of AISC (2016))

  This limit is the same for the recommended and the AISC (2016) calculations. The web is classified as slender under uniform axial compression.

AISC (2016) noncompact web slenderness limit in flexure:

$\lambda_{rw} = 5.7\sqrt{E / F_y} = 131$ (Table B4.1b of AISC (2016))

Recommended noncompact web slenderness limit in flexure (Subramanian and White 2017e):

When the larger top flange is in flexural compression:

$A_{fc} = 6$ in^2, $A_{wc} = 2.51$ in^2, $A_{fc} / A_{wc} = 2.39$, $c_{rw} = 5.7$ (Eq. F13-9),

$\lambda_{rw} = 131$ (Eq. F13-2)

(Note that the equation numbers with the prefix F13, F14 and F15 correspond to Figures 13, 14 and 15 of this dissertation; the prefixes do not denote Chapter F of the AISC Specification.)

When the smaller bottom flange is in flexural compression,

$A_{fc} = 2$ in^2, $A_{wc} = 4.42$ in^2, $A_{fc} / A_{wc} = 0.452$, $c_{rw} = 4.6$ (Eq. F13-9),

$\lambda_{rw} = 106$ (Eq. F13-2)

- *AISC (2016) compact web slenderness limit in flexure:*

  When the larger top flange is in flexural compression: $\lambda_{pw} = 85.2$ (Table B4.1b)

  When the smaller bottom flange is in flexural compression: $\lambda_{pw} = 40.3$ (Table B4.1b of AISC (2016))

- *Recommended compact web slenderness limit in flexure:*

  When the larger top flange is in flexural compression:

  m = 4.69 (Eq. F13-5), λ_{pw} = 108 (Eq. F13-4)

  When the smaller bottom flange is in flexural compression:

  m = 2.17 (Eq. 12), λ_{pw} = 49.8 (Eq. 11)

- *AISC (2016) web classification in flexure:*

  When the larger top flange is in flexural compression, since ($2D_c/t_w$ = 143) > (λ_{rw} = 131) the web of the subject cross-section is slender in flexure.

  When the smaller bottom flange is in flexural compression, since ($2D_c/t_w$ = 252) > (λ_{rw} = 131) the web of the subject cross-section is slender in flexure.

- *Recommended web classification in flexure:*

  When the larger top flange is in flexural compression, since ($2D_{cT}/t_w$ = 83.5) < (λ_{pw} = 108), the web is compact in flexure.

  When the smaller bottom flange is in flexural compression, since ($2D_c/t_w$ = 143) > (λ_{rw} = 106), the web is slender in flexure.

- *Governing FLB and FLPB flexural resistances for compression on the smaller bottom flange*

  AISC (2016) calculations:

  R_{pg} = 0.789 (Eq. F5-6 from AISC (2016)), a_w = 4.42 (Eq. F4-12 from AISC (2016)), F_{cr} = 35.7 ksi (Eq. F5-9 from AISC (2016)), $\phi_b M_n$(FLB) = 287 ft-kip (Eq. F5-7 from AISC (2016)), and $\phi_b M_{n(FLB)} / \phi_b M_p$ = 0.359

  Recommended calculations:

  R_{pg} = 0.744 (Eq. F13-10), a_w = 4.42 (Eq. F13-11), b_{fe} = 5.30 in. (compression flange) (Eq. (50)), S_{xce} = 114 in.^{3}, $\phi M_{n(FLB)}$ = 349 ft-kip (Eq. F14-8), and $\phi M_{n(FLB)} / \phi M_p$ = 0.438

- *Governing TFY and LTB flexural resistances for compression on the larger top flange*

  AISC (2016) calculations: $\phi M_{n(TFY)}$ = 560.05 ft-kip (Eq. F5-10 from AISC (2016))

  Recommended calculations: M_{ycT} = 853 ft-kip (Eq. (56)), m = 4.69 (Eq. F13-5), R_{pc} = 1.02, $\phi M_{n(LTB)}$ =767 ft-kip (Eq. F15-8), $\phi M_{n(LTB)} / \phi M_p$ = 0.96

- *Member axial compressive resistance*:

  AISC (2016) calculations: F_e = 227 ksi (Eq. E3-4 from AISC (2016)), F_{cr} = 49.7 ksi (Eq. E3-2 from AISC (2016)), b_e = 8.46 in. for the web (Eq. E7-3 from AISC (2016)), $b_e = b$ = 8.00 in. for the larger top flange (Eq. E7-2 from AISC (2016)), b_e = 5.54 in. for the smaller bottom flange (Eq. E7-3 from AISC (2016)), A_e = 8.97 in.^{2}, ϕP_n = 401 kips (Eq. E7-1 from AISC (2016)), $\phi P_n / \phi P_y$ = 0.54

4.3.1.2 Discussion of Overall Results

The following are key observations that can be highlighted regarding the final strength curves shown in Fig. 75:

- Members having the above dimensions are able to develop close to the factored plastic moment resistance of the cross-section at low axial force levels, when the larger compact (top) flange is in flexural compression. This is evidenced by the intersection of the solid curve with the horizontal axis on the right-hand side of the plot. The recommended modification of the AISC (2016) provisions predicts the test simulation strength in flexure alone quite well. The current AISC provisions are quite conservative for this loading case. This is due to the fact that the current provisions limit the flexural resistance of this cross-section to the nominal first yielding of the tension flange, $\phi_b M_{yt}$.
- Figure 76 shows the contours of the plastic equivalent strain (PEEQ) at the mid-surface of the component plates at the peak load, for the case of P_u = 0 and flexural compression on the larger top flange. The darkest contour indicates the locations that are still elastic at this stage. The other contours indicate different magnitudes

of yielding. It can be observed that at this load level, the bottom flange, the majority of the top flange, and more than half of the web have yielded. In Fig. 10, the recommended design model predicts the onset of yielding at a depth of $2a = 2D_{cT} + t_{fc}$ = 16.4 in. below the centroid of the top flange at the first yield to the compression flange for this section. This is 43% of the total depth between the flange centroids. This value matches well with the extent of the elastic region shown in Fig. 76. The internal moment from the test simulation at the peak load is only slightly less than ϕM_p, and it is in fact approximately equal to ϕM_{ycT}, which is itself only slightly less than ϕM_p.

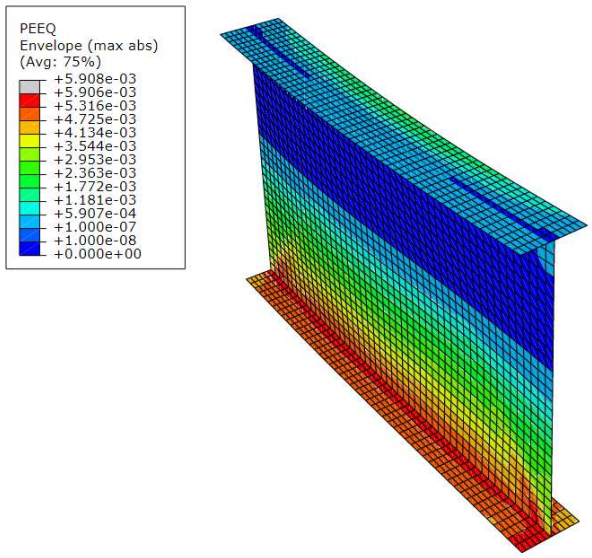

Figure 76. PEEQ (plastic equivalent strain) contours on the deflected shape for example singly-symmetric I-section member subjected to uniform moment loading causing compression on the top flange (P_u = 0).

- The flexural resistance for the above P_u = 0 case is predicted quite accurately considering the reductions for the noncompact web and for inelastic LTB, and the reductions due to extensive yielding in the tension zone captured by the yield

moment to the compression flange, M_{ycT}. It should be noted that if the AISC (2016) LTB equations are employed without the modifications in Eqs. F13-9, F13-8, F13-13 and F15-1, they generally tend to over-estimate the test simulation results (Subramanian and White 2017a, b, c, d, & e, Subramanian et al. 2018)

- For flexure causing compression on the larger compact (top) flange in the above members, there is a minor increase in the physical flexural resistance with the addition of a small amount of axial compression. This is due to a reduction in yielding on the side of the neutral axis in flexural tension, due to the added axial compression. However, the cross-section is already yielded extensively at these strength limits. Therefore, the enhancement in strength is minor compared to what one would expect by considering theoretical elastic stresses and strength of materials equations. The AISC Eqs. H1-1a and H1-1b are far from perfect in capturing this behavior. However, with the recommended enhancements in the flexural resistance calculations, the corresponding beam-column resistances are substantially larger than with the current provisions. Given that $P_u/\phi P_y$ is typically less than about 0.2 in metal building frames, the recommended enhancements are quite effective at capturing the true capacities in the context of metal building frame members.
- Considering the case of flexural compression on the smaller slender (bottom) flange with zero axial compression, the test simulations show 37 % larger strength than obtained using the AISC (2016) FLB equations (or as noted above, the AISC (2016) FLB check is 23% conservative relative to the test simulation results). This is due to the lack of recognition of compression flange local postbuckling strength in the

current provisions. The recommended provisions recognize this additional source of resistance, and predict the test simulation results with only minor conservatism. It should be noted that flexural compression on the smaller (bottom) flange is not a likely loading scenario for the cross-section considered in this example. However, the results are representative of those for more practical cross-sections, say in the vicinity of an inflection point in a frame, where both flanges may be relatively thin.

- The rigorous beam-column strength interaction shown by the solid curve on the left-hand side of the plot, obtained from the test simulation studies, is essentially linear for all practical purposes. Both the recommended and the current application of AISC Eqs. H1-1a and H1-1b extend slightly above this rigorous curve (i.e., they are slightly unconservative) at two different locations. The dotted (recommended) curve extends slightly above the rigorous curve within the vicinity of the "knee" of Eqs. H1-1. This is due to the fact that the true interaction is closer to linear. However, the conservatism of the AISC column strength curve (i.e., $\phi_c P_n$) for these members results in the predictions using Eqs. H1-1 still being reasonably good using the recommended calculations. Conversely, the current AISC (2016) prediction (i.e., the dashed curve) extends somewhat more markedly above the rigorous solid curve at high axial load levels. This is due to the fact that, under high axial compression, the small slender (bottom) flange and the web adjacent to this flange have a significant reduction in their effective areas. This effective area reduction, which occurs just on the bottom side of the members, results in a shift of the effective centroid and an introduction of an effective eccentricity of the axial compression force relative to this effective centroid. For the recommended (dotted)

interaction curve, the combination of the conservative $\phi_c P_n$ and the inclusion of this effective eccentric moment from the axial compression results in an accurate prediction, avoiding the unconservatism in the predictions from the current AISC (2016) provisions.

- It should be noted that the moment, M_u, on the horizontal axis of the plot does not include the above additional internal moment, due to the eccentricity of the applied axial loads with respect to the effective centroidal axis of the cross-section under high axial compression. The additional internal eccentric moment causes a shift in the strength curve. One can observe that the peak $P_u/\phi P_y$ point on both the dashed AISC (2016) curve and the dotted recommended curve are at the same value, i.e., approximately 0.54. This corresponds to the AISC (2016) axial compressive resistance of these members, governed by flexural-torsional buckling. The test simulations predict a somewhat larger axial compressive resistance of these members.
- The behavior of these members, if we consider the cases starting with $M_u = 0$ (where the strength curves cross the vertical axis) and as we start to apply small $M_u > 0$, causing flexural compression on the larger compact (top) flange, is that the resulting net compressive stresses on the smaller slender (bottom) flange are reduced. This results in an overall net increase in the axial compressive resistance due to the application of small $M_u > 0$ to the members. However, once we have applied a little less than $M_u = 0.2\phi M_p$ to the members, the increasing compression on the top flange becomes more dominant in its effect on the member ultimate strength. Hence, for

M_u larger than about $0.2\phi M_p$, the subject members start to support less and less P_u with increasing M_u.

- It appears that the maximum $P_u/\phi P_y$ point, on the dotted (recommended) design strength curve and on the solid (rigorous) test simulation based strength curve, occur at roughly the value of M_u that is equal and opposite to the eccentric moment caused by the axial force acting through the eccentricity between its line of action and the effective centroid of the cross-section (where we have lost significant effective area on the side of the cross-section corresponding to the smaller (slender) bottom flange.
- It should be noted that the AISC (2016) Specification and Commentary do not address the impact of the axial load eccentricity due to loss of effective area on singly-symmetric cross-section members. The AISI (2012) Specification did speak to this issue, although the AISI (2016) Specification is now silent about it. The original development of the unified effective width method (Peköz (1986)) showed that accurate predictions were obtained for general singly-symmetric and unsymmetric beam-columns, with the exception of slender angle sections, when the moment of the axial loads is taken about the centroidal axis of the effective section determined considering axial load alone. AISI (2016) relaxes the requirement that the bending moment should be defined with respect to the centroidal axis of the effective section. The increased eccentricity due to local buckling can have a measurable impact on the resistance of in an ideally pin-ended member; however, this effect tends to become minor in continuous members or members with ends restrained, where the rotations due to these eccentricities are restrained. As stated

above, AISC (2016) also neglects these effects. An additional eccentric bending moment may be included in Eqs. H1-1, to account conservatively for potential situations where shifting of the cross-section effective centroidal axis due to local buckling may have a measurable impact on compression member resistances. This practice parallels the handling of these effects in CEN (2005). It is included here to obtain the best correlation with the test simulation results, where the ends of the unbraced lengths are assumed to be flexurally and torsionally simply supported.

- The most important results in the above plot, pertaining to the design of common metal building frame members, are the results for small values of P_u. One can observe that with the recommended calculations, the strengths at small P_u are represented accurately.
- In addition to the improvements on the TFY and FLB limit states, when the improvement of beam-column strength interaction is considered, the unconservative results on the left hand quadrant of the section are eliminated. Fig. 77 labels these results as 'Recommended FLB & TFY Section 0' label.

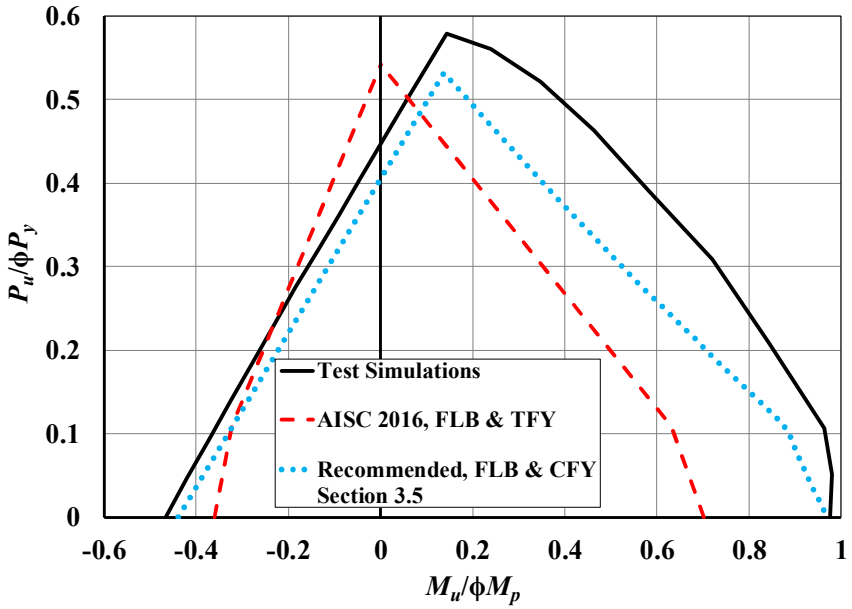

Figure 77. Strength envelopes from test simulation, the AISC (2016) column and flexural strength provisions, and the AISC column and recommended flexural strength provisions with recommendations from Section 3, torsionally and flexurally simply-supported singly-symmetric I-section members with $b_{fc} = b_{ft} = 8.0$ in., $t_{fc} = 0.75$ in. $t_{ft} = 0.25$ in., $h = 37.0$ in., $t_w = 0.1875$ in., and $L_x = L_y = L_z = L_b = 5$ ft, subjected to uniform primary bending moment and axial compression.

4.3.2 *Moment-Shear Interaction and Moment Gradient Studies*

Considering the changes made regarding the Tension Flange Yielding (TFY) limit state in Section 3.2), extensive yielding of the tension flange and the tension region of the web are permitted for all types of I-section members. Since most of the shear capacity is provided by the web of the cross-section, it is important to evaluate whether the consideration of substantial tension yielding within an I-section will result in interaction between the shear and moment resistances. Prior to the introduction of the AISC (2005) and AASHTO (2005) Specifications, the AISC and AASHTO provisions required the consideration of interaction between the flexural and shear resistances in the design of I-section members having transversely-stiffened webs. However, starting with AISC (2005) and AASHTO (2005), the AISC and AASHTO Specifications no longer required the

consideration of interaction between flexural and shear resistances for any cases. This change was based on the findings from White et al. (2008). The AASHTO (2005) Specification and subsequent AASHTO Specifications do require the consideration of a reduced tension field capacity for the shear strength, referred to as the "True Basler" shear resistance, when the flanges of a transversely-stiffened I-section member are smaller than a certain limit. The AISC (2016) Specification has now adopted these same tension field action equations for interior transversely-stiffened web panels in I-section members. For I-section members with unstiffened webs, the AISC and AASHTO provisions have never considered any interaction between the flexural and shear resistances. For sections with compact unstiffened webs, this is justified by the onset of significant strain-hardening prior to reaching the ultimate shear or flexural resistance (ASCE/WRC, 1971). For I-sections with noncompact and slender unstiffened webs subjected to significant combined flexure and shear, Daley et al. (2016), have shown that the interaction between the flexural and shear resistances is negligible, even in the context of significantly larger unstiffened web shear strengths that consider the web postbuckling response in shear.

For singly-symmetric members, all of the above conclusions are in the context of the current AISC and AASHTO provisions, which impose the Tension Flange Yielding (TFY) limit on the resistance of noncompact and slender-web I-section members exhibiting early yielding in flexural tension. As noted previously in Section 3.2, these current provisions limit the flexural resistances of slender-web I-section members to the moment at first nominal yielding of the tension flange, M_{yt}, and they limit the flexural resistance of noncompact-web I-section members to a value between M_{yt} and the plastic moment, M_p, depending on the web slenderness. Once the web is compact, the current AISC and

AASHTO provisions allow the use of a "plateau" nominal (unfactored) flexural resistance of M_p without any consideration of interaction between the flexural and shear resistances.

Hash (2001) has conducted one experimental three-point bending test in which the theoretical plastic neutral axis is located in the compression flange. White et al. (2008) show that this test exhibited negligible moment-shear strength interaction, based on the use of the unified flexural resistance equations from White (2008), combined with the recommended tension field action equations from Basler (1961). Both the original unified equations from White (2008) and the recommended equations developed in this research give a nominal flexural resistance of $M_n = M_p$ for this girder.

In addition, it is important to consider the impact of early tension on the flexural resistance when considering the influence of moment gradient on the flexural capacity. For manual resistance calculations, the influence of moment gradient is captured via the C_b factor in the AISC and AASHTO Specifications. The C_b factor in AISC (2016) and AASHTO (2017), and in prior AISC and AASHTO Specifications, is based on elastic lateral-torsional buckling theory (Yura et al. 1978). Yura et al. (1978) observed that there is some reduction in the LTB resistance due to the onset of yielding near the peak moment location, for members where the moment capacity becomes larger than $F_L S_{xc}$; however, they observed that the reductions in strength due to this inelasticity are minor and thus suggested that the uniform bending flexural resistance simply can be scaled by the elastic C_b equations up to the point where the "plateau" resistance is reached in flexure. Subramanian (2015) has shown that in some situations, where the maximum moment occurs other than at a brace point, some reduction in the resistance, due to yielding effects (i.e., inelastic C_b effects), can be observed. Eurocode 3 (CEN, 2005) recognizes this

behaviour in the context of their calculation procedures via a correction factor denoted as k_c. It is important to check whether there are any significant influences of early tension flange yielding on the LTB resistance of I-section members subjected to moment gradient loading. The test simulation cases discussed at the beginning of Chapter 3 and in Section 4.1 have already shown that the recommended provisions developed in Section 3.2 provide an accurate, significantly improved characterization of the resistance of I-section members subjected to uniform bending. Section 4.2 also shows the accurate prediction of the resistances of singly-symmetric I-section members subjected to moment-gradient loading. However, it is useful to consider an extreme case that may exacerbate these issues.

The extreme singly-symmetric I-section from Section 4.3, which has a significantly larger compression flange, is selected for the study in this section, and is subjected to three point bending using members with different lengths, causing a wide range of combinations of internal bending moment and shear (Fig. 78). The member is flexurally and torsionally simply supported at its endpoints. Bearing stiffeners are provided at the support points and applied load locations, preventing any significant web distortion at these locations.

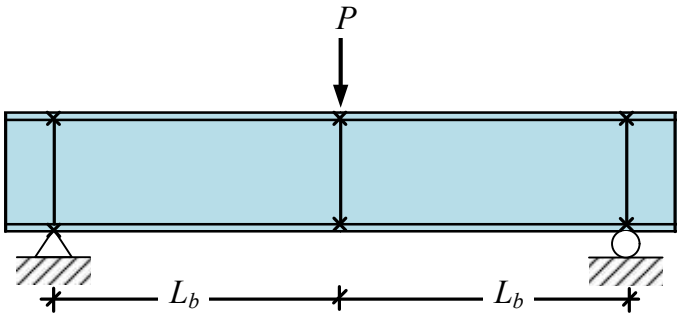

Figure 78. 3-Point bending test configuration

4.3.2.1 Suite of Test Specimens

The cross-section for the members studied in this section is the same as that considered in Section 4.3.1.1:

E = 29,000 ksi Elasticity Modulus

F_y = 55 ksi Yield Stress (Homogenous Member)

b_{top} = 8 in. top flange width (in compression)

t_{top} = 0.75 in. top flange thickness (in compression)

b_{bot} = 8 in. bottom flange width (in tension)

t_{bot} = 0.25 in. bottom flange thickness (in tension)

d = 37 in. web clear depth

t_w = 0.1875 in. web thickness

The following member unbraced lengths are considered for the three-point bending test simulation conducted in this study:

L_b = 2, 4, 6, 8, 9.25, 10, 12, 14, 16, 18, 19.4, 22, 26, and 30 ft

4.3.2.2 Analysis Types

The resistance of the members is determined using test simulation studies (Simulia 2014) as explained in the Appendix A. The members are subjected a point load at the top flange of the specimen at the mid-point and the maximum Load Proportionality Factor

(*LPF*) is recorded. The corresponding shear strength at the maximum *LPF* value is *LPF* × *P* / 2, and the moment is *LPF* × *P* × L_b / 2.

For the calculated shear strength of the member AISC Specification Chapter G.2 (AISC 2016) is used and it is denoted as V_{AISC} in the following plots. For calculation of the bending strength both hand estimate using AISC Specification Chapter F with current TFY, and Inelastic Buckling Analysis with the recommended TFY (INBA*) are used in the calculations.

4.3.2.3 Summary of Results

The moment shear interaction plot is provided in Fig. 79. In the plot both the AISC and INBA* is using the same shear strength calculations since the thin-walled open section (TWOS) frame element is not capable to analyze shear dominant cases. For longer lengths, since shear deformations are negligible due to lower shear demand TWOS estimate the overall capacity more accurate.

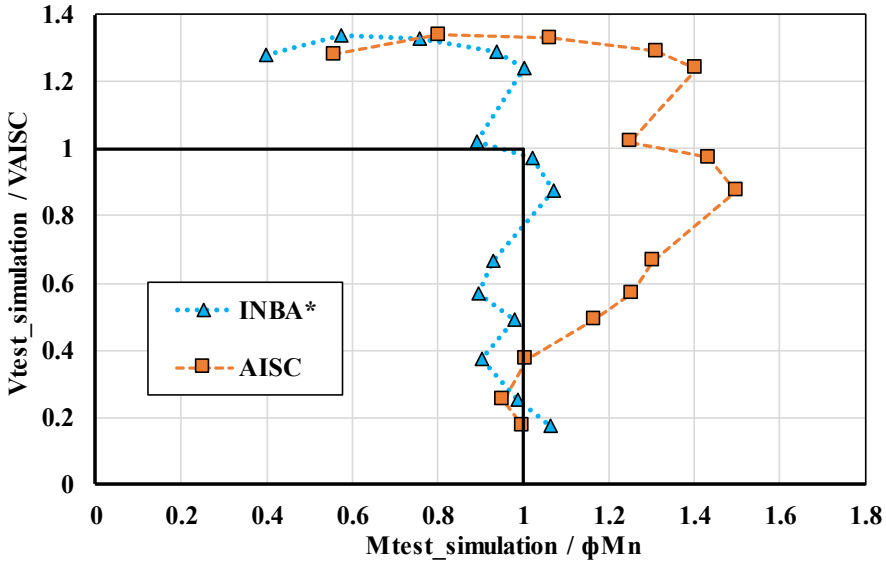

Figure 79.Moment-shear interaction plot

The lowest data point for INBA* is detected as 0.891 and 0.895 for Mtest/ϕMn ratio. These cases are the neighbours of L_b = 19.4 ft case which is the closest case to the elastic buckling limit of L_r = 19.1 ft. Considering the Finite Element Analysis (FEA) studies are conducted with $0.9F_y$ and $0.9E$, normalizing the values with respect to that will also remove the unconservative results around these points.

For the performance of the recommended TFY calculations, it is observed that maximum of 40% gain is obtained with respect to the current AISC approach.

When the moment strength curve is investigated it is also observed that INBA* is showing better correlation with test simulation results. For smaller lengths, the dominant failure mode is shear (Fig. 80). Additional PEEQ (plastic equivalent strain) plots for 10 ft case, which is failed with combined bending and shear failure. The longest length provided are provided to showcase for bending failure (Figs. 81 and 82)

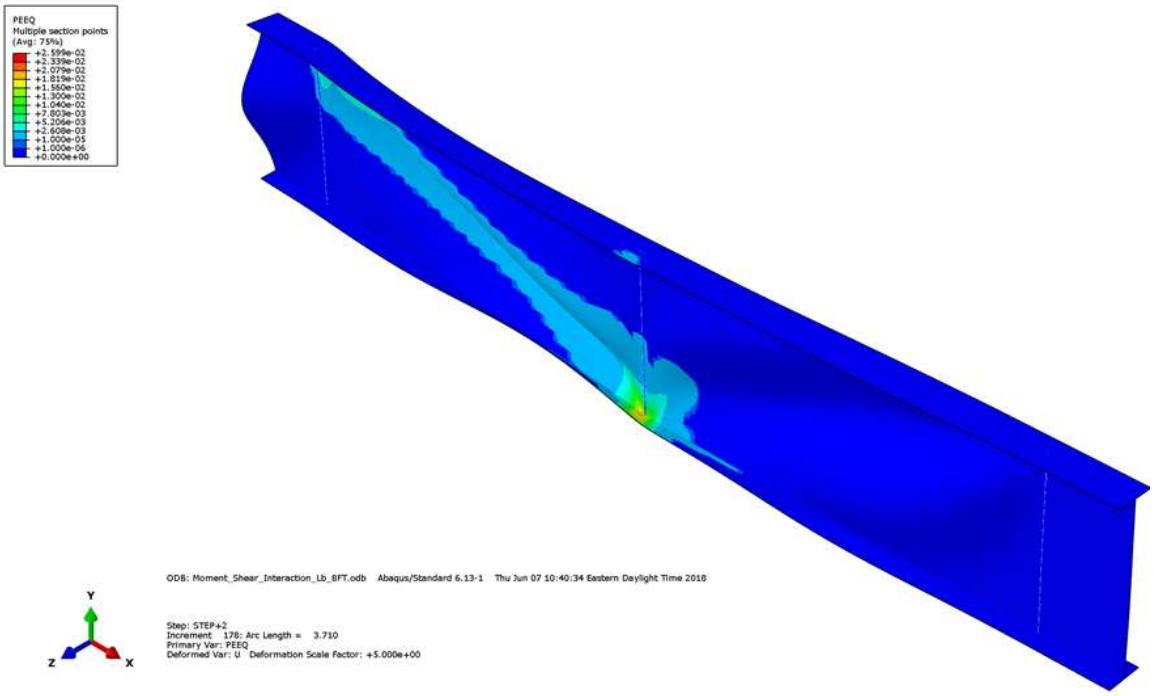

Figure 80. PEEQ (Plastic Equivalent Strain) contours on the deflected shape for extreme singly-symmetric i-section member subjected to 3-point bending test (L_b = 8ft, displacement scale factor = 5)

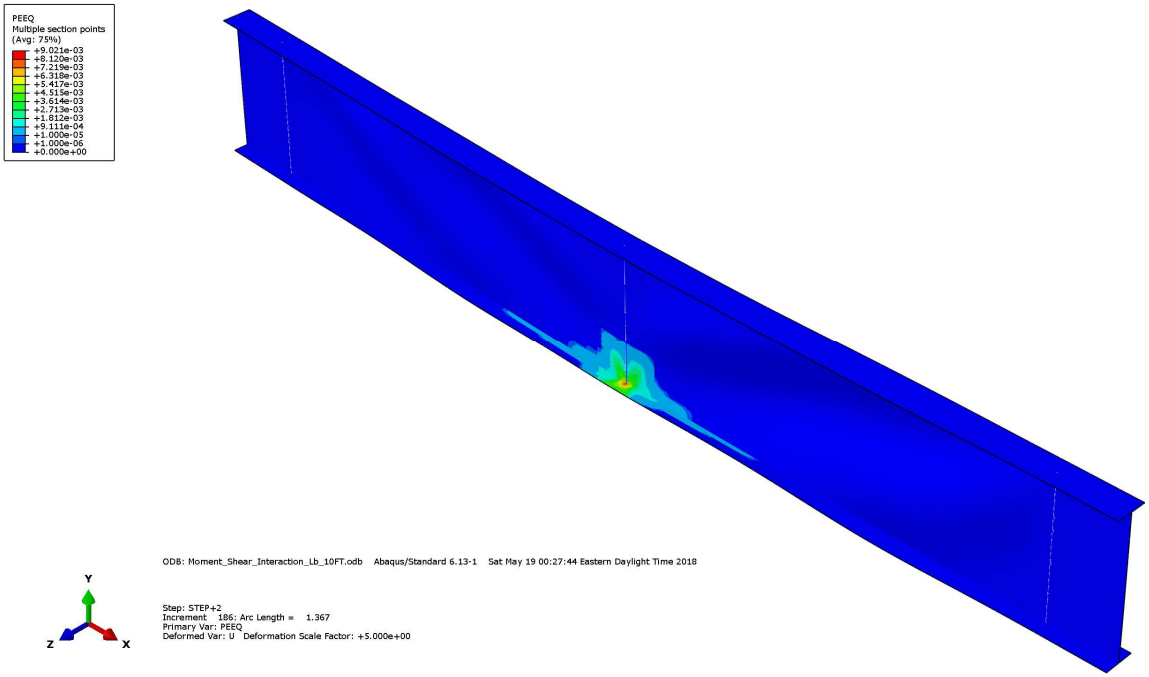

Figure 81. PEEQ (Plastic Equivalent Strain) contours on the deflected shape for extreme singly-symmetric i-section member subjected to 3-point bending test (L_b = 10 ft,displacement scale factor = 5)

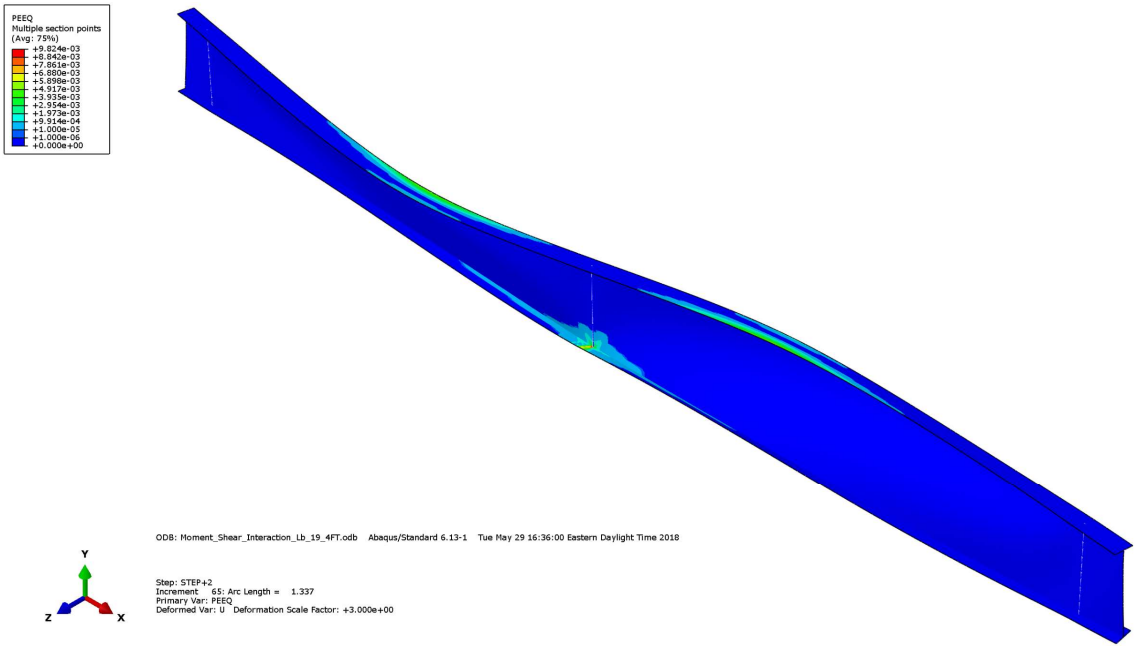

Figure 82. PEEQ (Plastic Equivalent Strain) contours on the deflected shape for extreme singly-symmetric i-section member subjected to 3-point bending test (L_b = 19.4 ft, displacement scale factor = 3)

CHAPTER 5. SOFTWARE SYSTEM AND PROGRAMMING FRAMEWORK FOR ADVANCED DESIGN EVALUATION OF STEEL FRAME STRUCTURES

Effective application of the methods developed in this research requires sophisticated software capabilities that facilitate the definition of the complex member, frame and bracing geometries and configurations, execution of the computations, assessment of the design behavior, and refinement of the design based on the advanced computational results. In addition, it is important that the programming framework provide for ease of expansion and adaptation to explore innovative involving the structural engineering application of the advanced evaluation tools. The following sections discuss a software system and programming framework developed to meet these goals.

5.1 Introduction to the SABRE2 Software System

SABRE2 is a structural analysis and design software system focused on efficient, rigorous assessment of the strength of frames composed of web-tapered and general nonprismatic steel I-section members. SABRE2 achieves these capabilities via innovative computational buckling analysis techniques implemented with frame finite elements based on open-section thin-walled beam theory. Specifically, SABRE2 handles:

- Single and multiple web taper,
- Steps in the cross-section geometry,
- Double- and single-symmetry of the member cross-sections, and

- Any combination of compact, noncompact and slender flanges and webs.

In addition, SABRE2 can be used to assess all types and combinations of doubly-symmetric prismatic I-section members. SABRE2 addresses all the AISC member strength limit states within its buckling calculations, and it can be used to model general lateral and/or torsional bracing, member continuity across braced points, any type of restraint at member ends (where there is no adjacent unbraced length), and the influence of load height (i.e., the position of transverse loads though the depth of the cross-section, e.g., shear center, mid-web, top flange, bottom flange, etc.). In this regard, SABRE2 represents a fundamental advancement in the design of steel I-section column, beam and beam-column members. With SABRE2, the consideration of attributes such as moment gradient, load height, end restraint, member continuity effects and beam-column strength interactions is handled via a rigorous computational framework, removing the need for tedious and relatively inaccurate Cb, K and beam-column strength interaction calculations.

Although SABRE2 can handle 3D systems subjected to general spatial loading, its primary emphasis is on the strength (in-plane and out-of-plane) of frames and/or their component members, subjected to loads that are nominally in the plane of the frame. Where desired, SABRE2 can capture the influence of off-axis loads, both axial loads as well as transverse loads applied at any position through the cross-section depth (i.e., “load height”).

SABRE2 has the capability to display a surface rendering of the deformed member geometries under load (pre-buckled, from an in-plane geometrically nonlinear load-deflection analysis, or buckled, corresponding to the out-of-plane, or in some cases in-

plane, buckling mode or modes determined from an eigenvalue buckling analysis), allowing for a more complete understanding of the warping (i.e., cross-bending) response of the I-section member flanges in resisting torsion.

SABRE2 may be used for design solutions where it is desired to assess the demands on the bracing system. In addition, it addresses members with any end conditions, and any combination of members and/or overall planar framing systems and in- and/or out-of-plane bracing of these members and/or systems.

Figure 83 shows a screen shot of the main viewing window and the main-level menus of its graphical user interface upon opening the program. Four main menu buttons appear at the bottom of the screen in this view: the main window, definitions, analysis, and viewing buttons. The last three of these buttons brings up the graphical user interfaces pertaining to problem definition, execution of the analysis, and visualization of the results respectively. The first of these buttons hides these other user interfaces such that only the main viewing window appears on the screen, as shown in the figure.

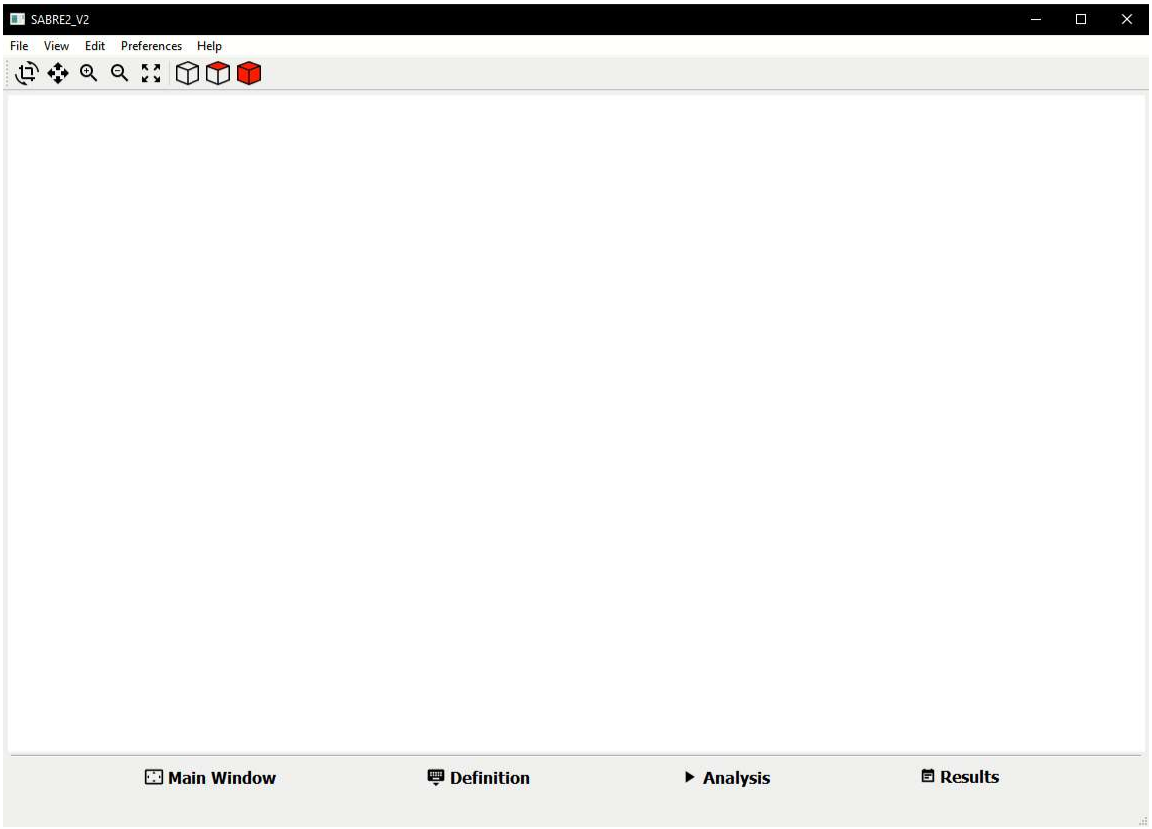

Figure 83. SABRE2 general program screenshot

5.2 Design Evaluation of a Representative Tapered I-Section Member

To illustrate the basic capabilities of SABRE2, the problem definition and design evaluation of the linearly tapered member shown in Fig. 84 is presented in this section and in the subsequent Sections 5.3 and 5.4. This problem is from Examples 5.6 through 5.8 of the AISC/MBMA Design Guide 25 (White and Jeong, 2019). Although this member is actually a building frame column, the member is shown in a horizontal position in the following to eliminate white space. This section focuses predominantly on the problem definition capabilities, but also touches on the analysis and results interpretation to some extent. Section 5.3 details a wide range of types of analysis available within SABRE2. The primary emphasis in this dissertation is on inelastic linear and nonlinear buckling analysis.

Flowcharts outlining the detailed inelastic linear and nonlinear buckling analysis procedures are provided in this section. Section 5.4 focuses on visualization and results interpretation from the various advanced design calculations.

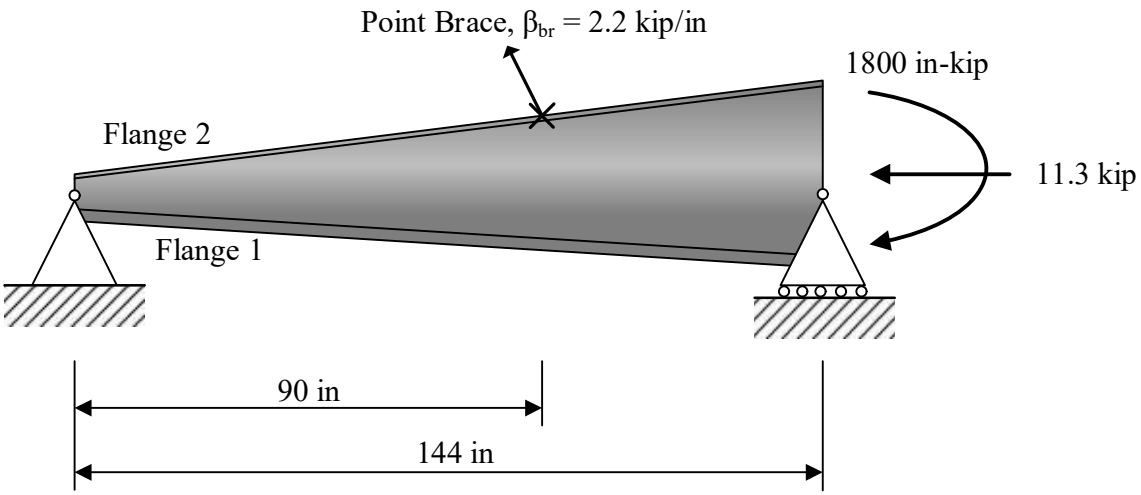

$d_{w\_i} = h$ = 12 in at left-hand end
$d_{w\_j} = h$ = 24 in at right-hand end
t_w = 1/8 in
b_f = 6 in, both flanges
t_{ft} = 7/32 in, Flange 2 (in flexural tension)
t_{fc} = 5/16 in, Flange 1 (in flexural compression)
E = 29,000 ksi
F_y = 55 ksi

Figure 84. Simply-supported web tapered member.

SABRE2 provides for the analysis and design of general members and frames, including the consideration of finite stiffness bracing. Design Guide 25 does not address the consideration of bracing stiffness and strength. A point brace with a stiffness of 2.2 kip/inch is defined at an intermediate purlin location in Fig. 84 to illustrate the consideration of finite bracing stiffness in SABRE2. The SABRE2 problem definition, analysis, and design checking of the member shown in Fig. 84 is explained below.

5.2.1 *Definition of Joint Coordinates*

Figure 85 shows the SABRE2 table user interface menu for defining the joint coordinates. Upon selecting the *Definitions* menu button in Fig. 83, the *Joints* dialog panel (Fig. 85) is displayed at the bottom of the screen. Each of the joint coordinates are entered using this dialog panel. Any updates made within this dialog panel are automatically reflected in the display. Joints are defined as points at the ends of any lengths that are defined as members. In this problem definition, we will consider the problem in Fig. 84 as a single member with end joint coordinates (0, 0, 0) and (144, 0, 0). Therefore, one can enter these coordinates using the *Joints tab* as shown in Fig. 85. Note that consistent units should be used throughout all problem definition steps in SABRE2. The default consistent units are US (inches and kips).

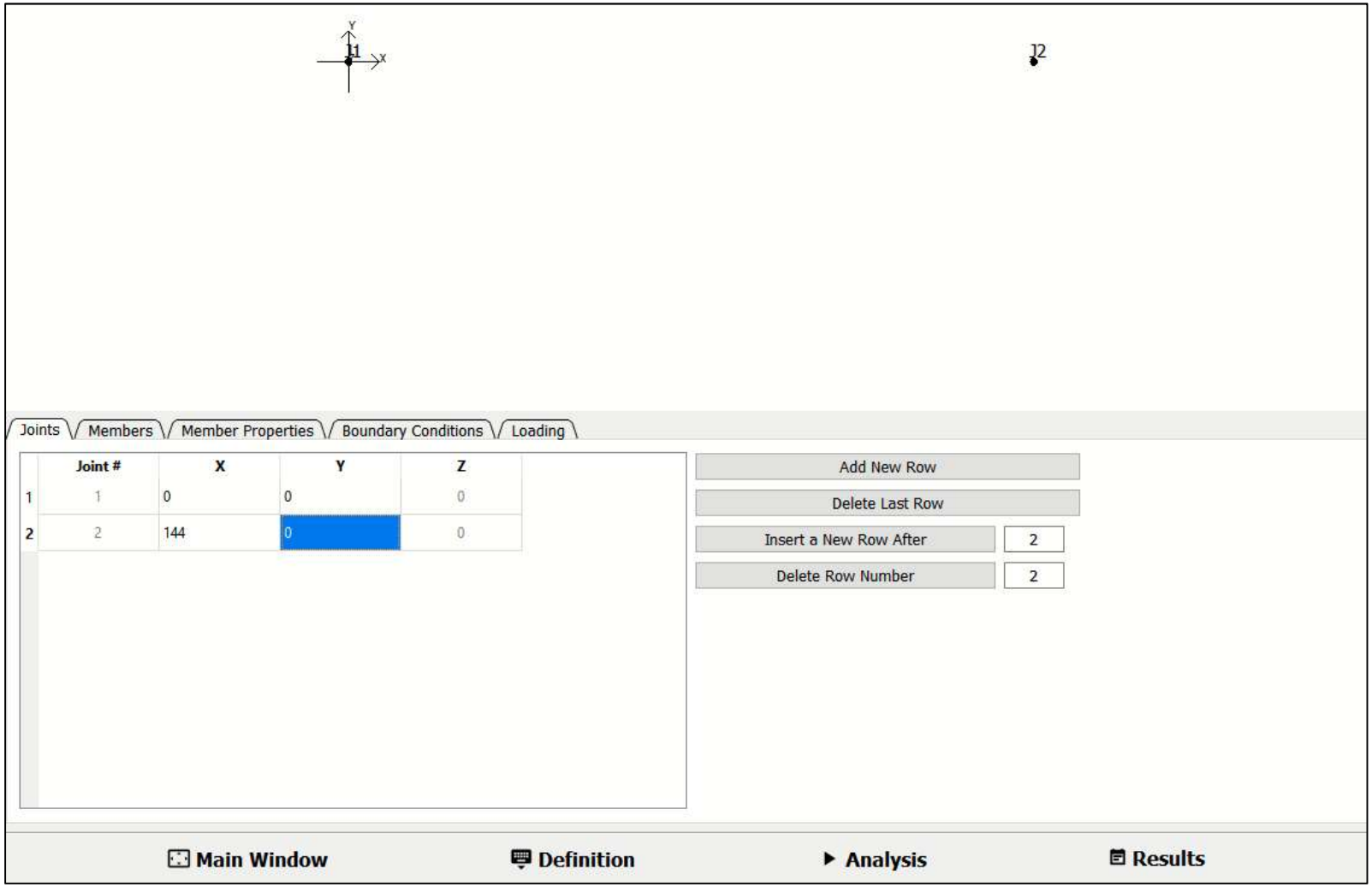

Figure 85. Definitions user interface showing the Joints table

5.2.2 *Definition of Member to Joint Connectivity and Member Cross-Section Dimensions*

The next step of the problem definition in SABRE2 is to define the member by specifying its connectivity to joints 1 and 2, and specifying its cross-section dimensions at each of these joints. This is accomplished using the *Members* tab, which is accessed at the top of the *Definitions* user interface in Fig. 85. Upon selecting the *Members* tab, the dialog panel shown in Fig. 86 appears. When joints 1 and 2 are selected in the corresponding *Members* table, the color of the selected joints changes to green.

SABRE2 uses the concept of a design axis to facilitate the problem definition for non-prismatic members. The *Design Axis* is simply a reference axis used to define the member geometry. The *Design Axis* is by default taken as the *Mid-web* depth. However, in metal building frames, it is often much simpler to define the geometry based on the lines along the outside edge of the member webs. The *Design Axis* also may be set as the inside edge of the web. The above edges are referred to as "Flange 1" and "Flange 2" in SABRE2. The cross-section depth is always measured perpendicular to the *Design Axis*. In this example, we will use the default *Mid-web* depth as the *Design Axis.*

Next, the user needs to input the section dimensions at the member start and end joints. SABRE2 provides a *Section Database* dialog, located just below the *Members* table, which can be used to select any rolled wide-flange section from the AISC Section Database. However, for general welded I-sections, the section dimensions at each of the joints is entered using the *Members* table, located the bottom right corner of the screen. Figure 86 Figure 86 shows this panel with the section dimensions entered for the member from Fig. 84.

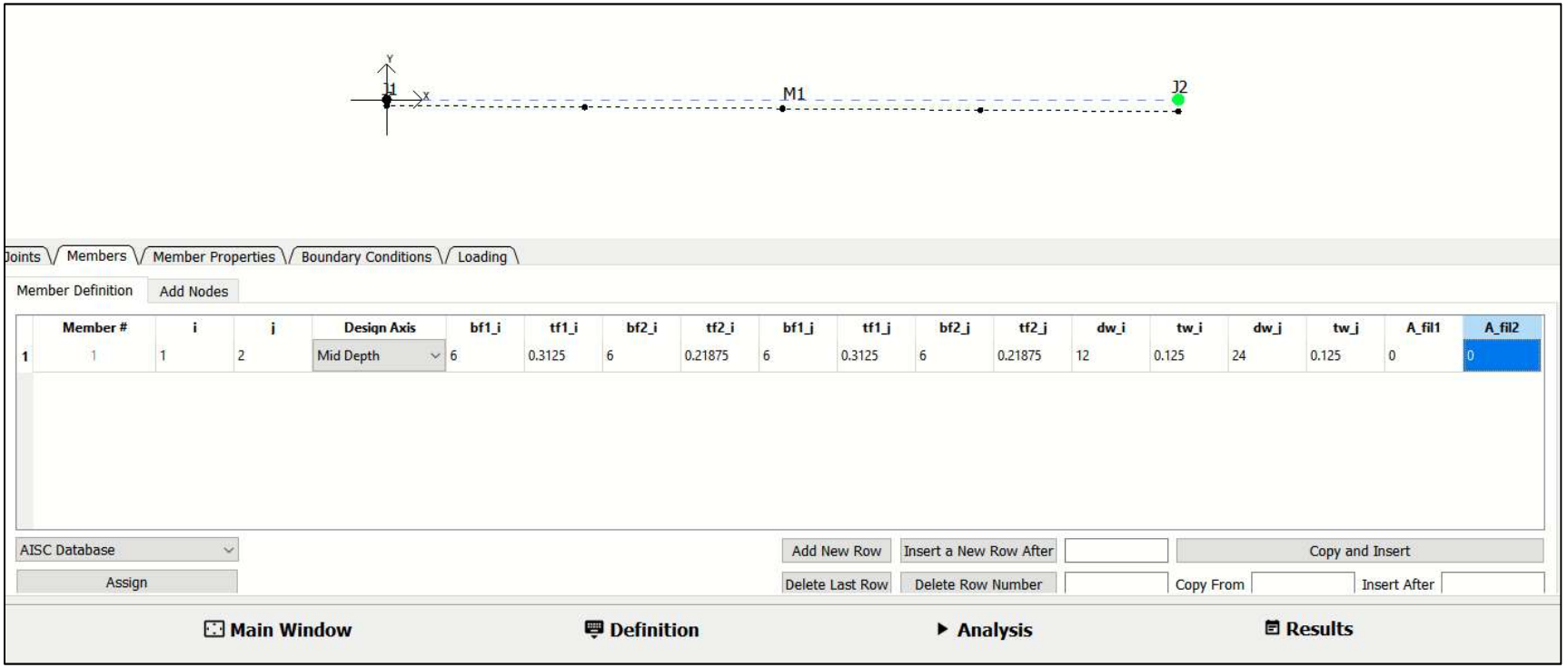

Figure 86. Line representation of member after applying the member-to-joint connectivity and the section definitions for the start and end joints.

Once the start and end member joints, referred to as Joints *i* and *j*, and the cross-section dimensions at these joints are specified, the changes appear automatically in the Main Window of the screen. This results in the final elevation view of the member shown in Fig. 87.

The default option for viewing of the model is the line element representation shown in Fig. 86. However, if one desires, the 3D rendered representation of the member or structure can be viewed by pressing the Filled Cube icon in toolbar at the top of the screen (shown in Fig. 83). Selection of the Empty Cube icon in Fig. 74 sets the display back to the line representation. Since the example considered in this section has only one member, the 3D rendered representation of the structure is used in the following sections. The 3D rendered representation is shown in Fig. 87.

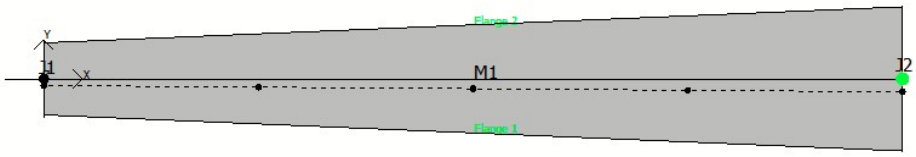

Figure 87. Elevation view of member after applying the member-to-joint connectivity and the section definitions for the start and end joints.

5.2.3 *Definition of Essential Nodes and the Cross-Section Dimensions at these Nodes*

The next step in the problem definition of the example beam-column in SABRE2 is to define an *Essential Node* at the braced location, 90 inches from the column base. This is accomplished by selecting the *Add Nodes* tab in Fig. 86. Essential nodes generally need to be placed at any brace location along the member length, as well as at changes in material properties, stepped changes in the cross-section plates, changes in member taper, etc. The

lengths between adjacent joints and/or essential nodes are referred to as member segments in this work. The user can select the member in the Add Node tab to indicate that this is the member for which it is desired to add a node. Following that, the Add Node push button is selected to add the additional essential node to the member. This activates a second drop-down menu. Next, the distance from joint *i*, at which this additional node is located, is entered within the dialog under the Add Nodes tab as shown in Fig. 88. When the Follow Taper push button next to this input cell is selected, SABRE2 creates the cross-section dimensions at this essential node based on a linear variation in values between joints 1 and 2 (or in general, between the adjacent joints and/or essential nodes) within the table on the bottom of dialog panel (Fig. 88). If these dimensions are the desired ones, which they are in this case, the user simply clicks Apply at the bottom right corner of the screen to add the essential node. This additional node is highlighted by an x symbol and lines representing the cross-section are shown on the member at the position of the essential node, as illustrated in the figure.

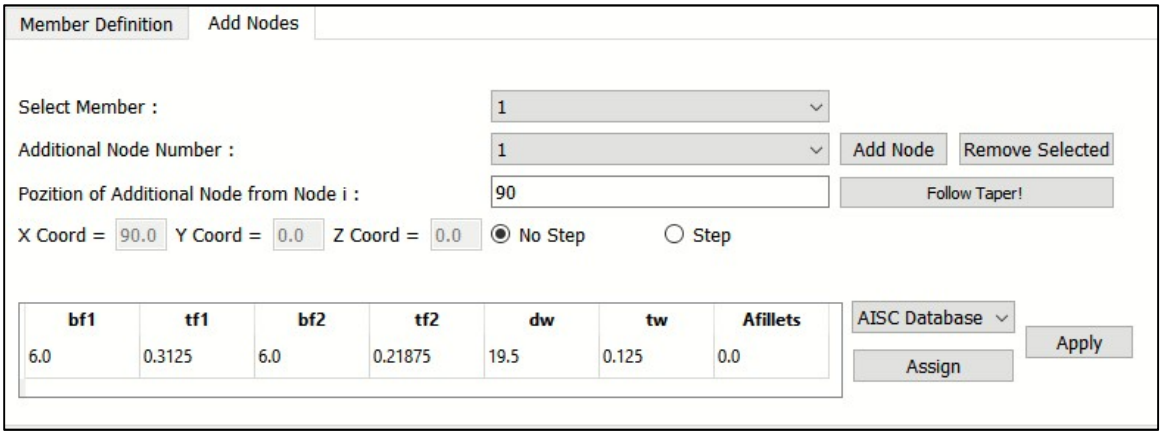

Figure 88. ***Add Nodes*** **user interface**

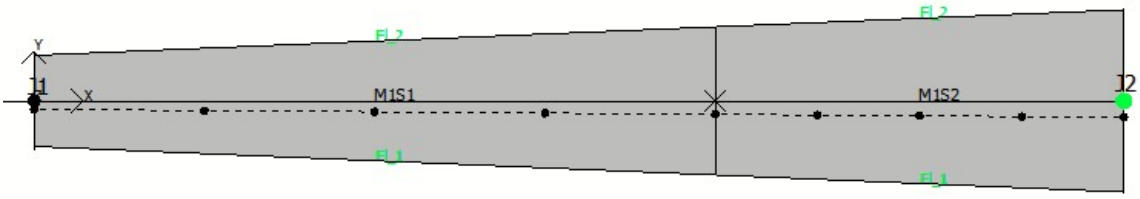

Figure 89. Elevation view of member after adding the *Essential Node* at the braced location.

5.2.4 *Subdivision of Member Segments and Material Assignment*

The fourth step of the problem definition in SABRE2 is to select the *Member Properties* tab from Fig. 85. SABRE2 considers the number of elements employed within each member segment, as a member property. In addition, the material elastic modulus, shear modulus, density, and yield strengths of the flanges and web are considered as member properties. Default values are provided in the table for each of the defined member segments; however, one can change these default values. As shown in Fig. Figure 9090, the number of elements is changed to 8 in the column labeled *# of Elements* and the default yield strength of *50* is changed to *55* in the cells labeled F_{yf1}, F_{yw}, F_{yf2} in the *Member Properties* table. Once all the values are as desired in this dialog panel the number of elements and yield stresses related to each panel are applied automatically, without need of confirming changes. If it is desired to apply the properties for a specific row to all members and their segments, this can be achieved by selecting the *Apply to all members* push button shown in Fig. 90.

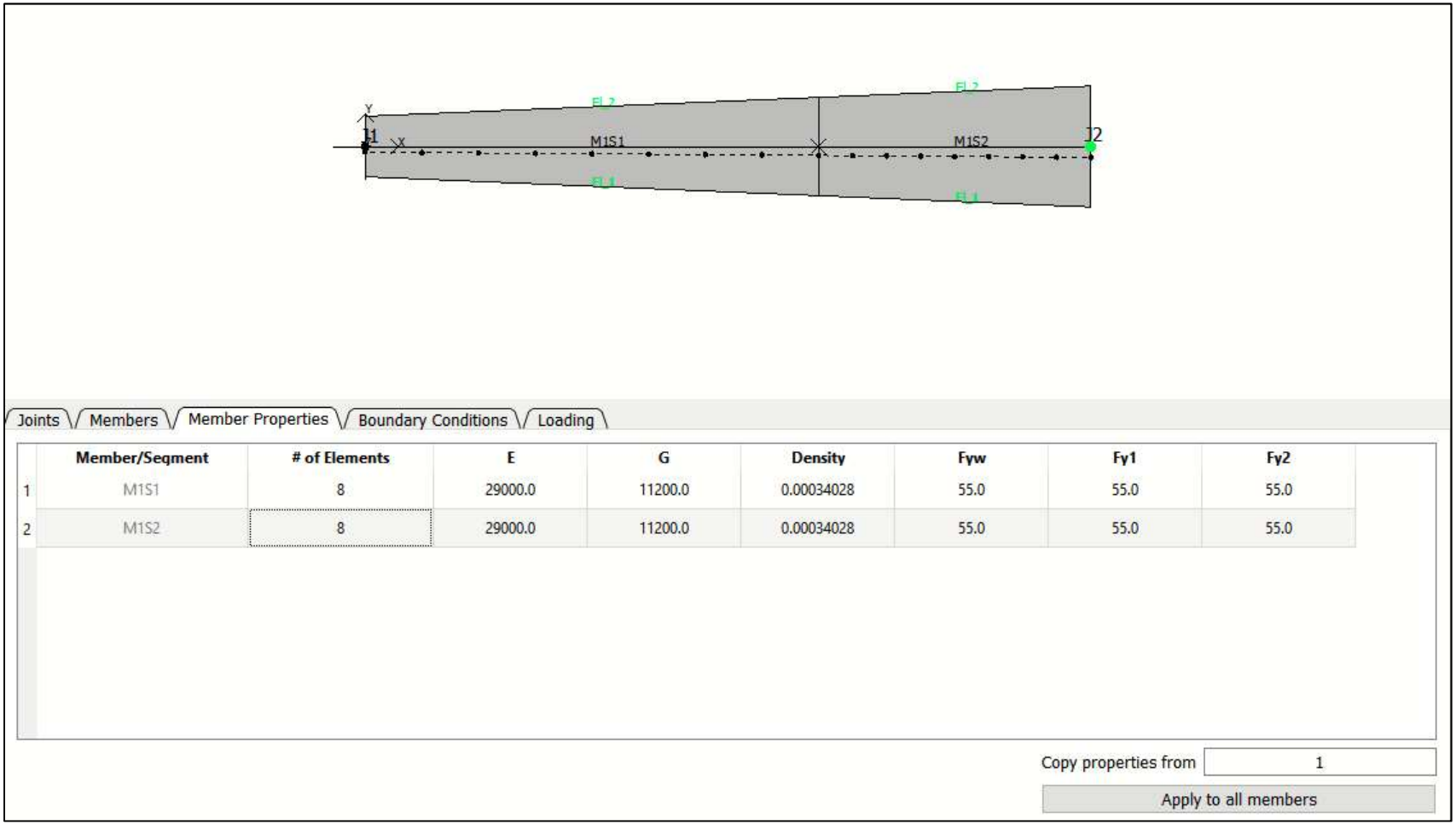

Figure 90. Member Properties user interface, showing application of 8 elements per segment and Grade 55 steel using the Apply to all members push button

Note that the material definition in Fig. 90 includes the weight density of the steel. The default weight density in SABRE2 is 1.2 times the nominal weight density of steel, equal to 1.2 x 0.490 kcf / 12^3 = 0.00034028 kip/in^3 in US units. If the self-weight of the steel is being considered in a load combination other than one corresponding to a dead load factor of 1.2, this value should be modified to the appropriate factored weight density of the steel.

5.2.5 *Definition of Boundary Conditions*

The fifth step of the problem definition in SABRE2 is to define the member displacement boundary conditions. One can define the loads as the fifth step, if desired, but we will address the displacement boundary conditions next in this example. The *Fixities* table is accessed, to define the displacement boundary conditions, by selecting the *Boundary Conditions* tab from the *Definitions* user interface. This brings up the *Fixities* table at the bottom of the screen. One can define fixities for different nodal locations, view information about the shear center location and define cross-section offsets of the fixities in this table. SABRE2 also displays a view of the structure showing the element discretization along the reference axis for the structural analysis when this table is displayed (the shear center axis is used as the reference axis for the structural analysis in SABRE2). This is shown in Fig. 91.

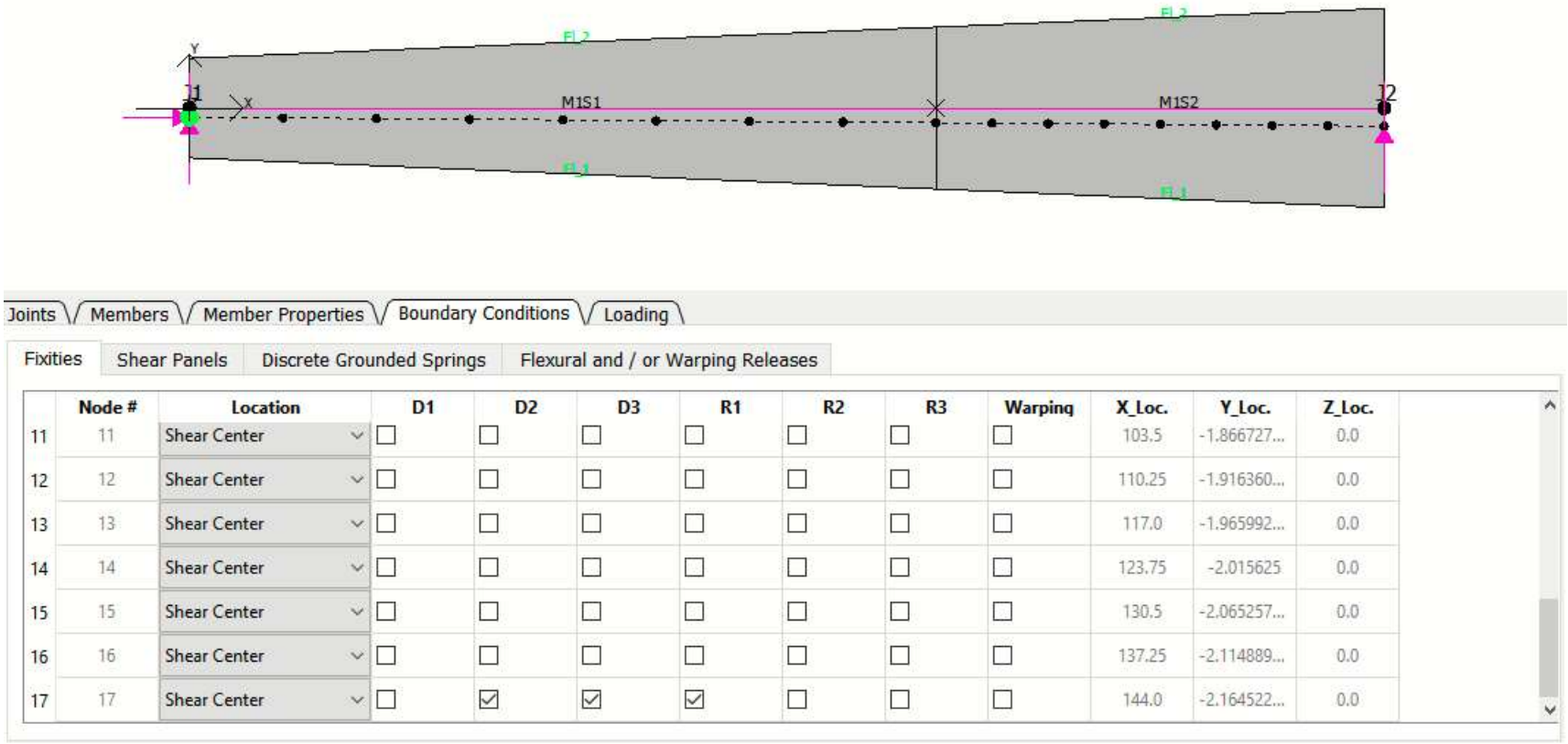

	Node #	Location	D1	D2	D3	R1	R2	R3	Warping	X_Loc.	Y_Loc.	Z_Loc.
11	11	Shear Center	☐	☐	☐	☐	☐	☐	☐	103.5	-1.866727...	0.0
12	12	Shear Center	☐	☐	☐	☐	☐	☐	☐	110.25	-1.916360...	0.0
13	13	Shear Center	☐	☐	☐	☐	☐	☐	☐	117.0	-1.965992...	0.0
14	14	Shear Center	☐	☐	☐	☐	☐	☐	☐	123.75	-2.015625	0.0
15	15	Shear Center	☐	☐	☐	☐	☐	☐	☐	130.5	-2.065257...	0.0
16	16	Shear Center	☐	☐	☐	☐	☐	☐	☐	137.25	-2.114889...	0.0
17	17	Shear Center	☐	☑	☑	☑	☐	☐	☐	144.0	-2.164522...	0.0

Figure 91. ***Boundary Conditions / Fixities*** **user interface**

One can assign the desired displacement constraints at any of the nodes by clicking on the related fixities check boxes in the table, which causes SABRE2 to display the related constraint at the *Main Window*. One then defines the location of the displacement constraint (shear center, Flange 1, Flange 2 or the cross-section centroid), and finally uses the check boxes in the *Fixities* table to indicate the degrees of freedom where the displacements are fixed. The default location of the displacement constraints is the shear center. Figure 92 shows an isometric view of our member, obtained by selecting the pull-down menu View > Defined Views > Isometric (XYZ) View after the above definitions are applied. Note that each of the displacement constraints is represented by a magenta colored arrow.

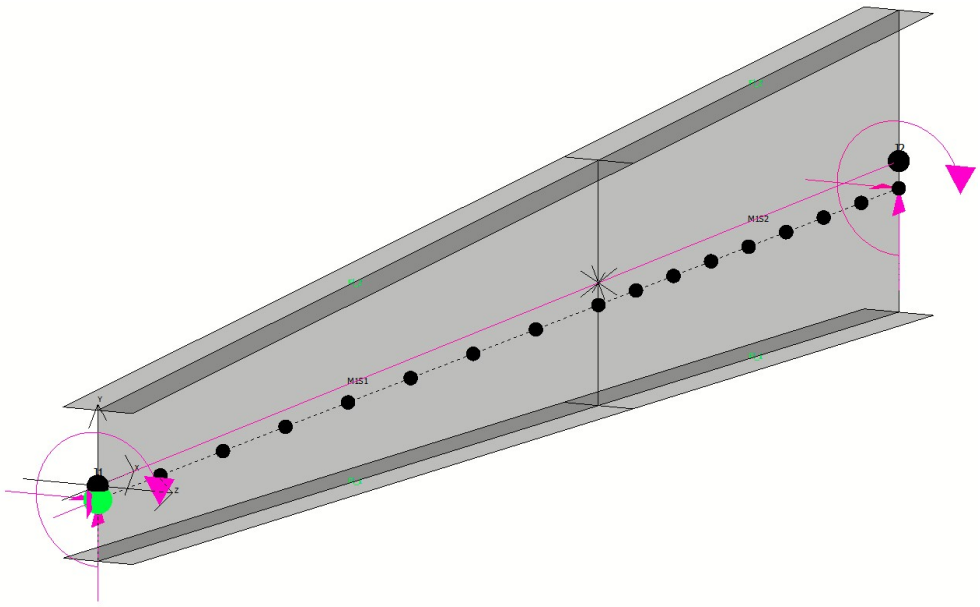

Figure 92. Isometric view of the member after the displacement boundary conditions are specified.

The intermediate brace in the example problem is defined as a grounded spring having a stiffness of 2.2 kip/in. This "provided" brace stiffness is assumed to be developed by wall panels and/or wall bracing connected at the level of an outset girt located at 90

inches above the column base. For the assessment of the effectiveness of this bracing stiffness by the 2016 AISC Appendix 6 procedures, this stiffness is divided by $2/\phi = 2/0.75 = 2.667$ for the buckling analysis. That is, a value of 2.2 kip/in / 2.667 = 0.825 kip/in is entered into SABRE2 for the buckling analysis. If the buckling analysis shows that this reduced bracing stiffness is sufficient to develop the required loads, the physical bracing stiffness of $\beta_{br} = 2.2$ kip/in is sufficient.

The point bracing at the *Essential Node* is defined in SABRE2 by selecting the *Discrete Grounded Spring* tab in Fig. 91 and selecting the *Essential Node* in the table. This action will turn the desired node color to green. Figure 93 shows the definition of the appropriate input values for our problem in the table. The modified stiffness value in the table is automatically applied to the selected essential node. This point brace is assumed to be oriented in the global z direction, and it is specified as being located at the top flange of the essential node in Fig. 93. (Torsional braces may be defined as being oriented either about the global X or Y axes or aligned with the local member x axis in SABRE2.)

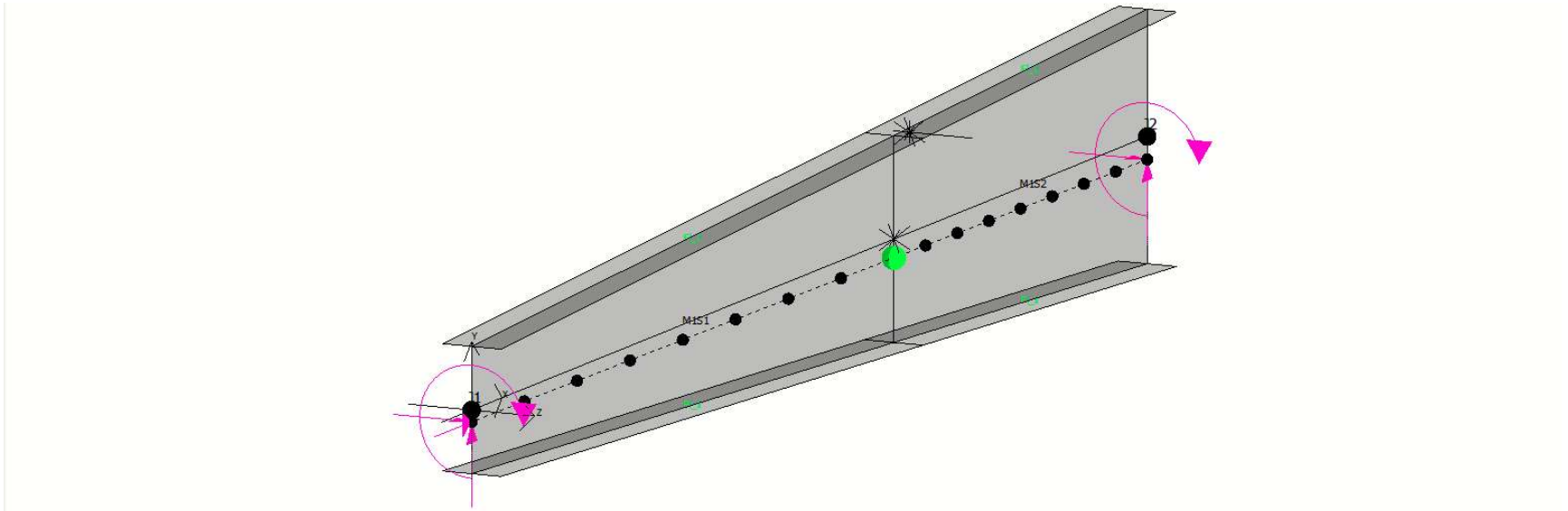

Joints | Members | Member Properties | Boundary Conditions | Loading

Fixities | Shear Panels | Discrete Grounded Springs | Flexural and / or Warping Releases

	Node #	Location	Perpendicular to	D1	Status	D2	Status	D3	Status	R1	Staus	R2	Status	R3	Status	Warping	Status
9	9	Flange 2	Global Coordinates	0	Constant	0	Constant	0.825	Constant	0	Constant	0	Constant	0	Constant	0	Constant

Figure 93. ***Discrete grounded springs*** **table associated with the definition of a point brace (grounded spring) stiffness at the selected essential node of the example problem, and isometric view of the member after the intermediate nodal brace has been defined**

5.2.6 *Definition of Load Conditions*

Figure 94 shows the *Loading* user interface table corresponding to the *Define Point Load* tab in SABRE2. In this example problem, these loads are the axial force of -11.3 kip, applied at the cross-section centroid at the right-hand end of the member, and the applied moment of -1800 in-kip about the global Z axis at this location. Upon selecting *Define Point Loads* in Fig. 94, the table shown in Fig. 94 appears at the bottom of the screen. To define the applied loads, the user clicks on the desired row in the table and the color of the node turns to green in the Main Window. In addition, the user can also see the location of the defined points in the last three columns of the table. Furthermore, the load height at the node can be defined to be at the *Shear Center,* at *Flange 1,* at *Flange 2,* at the *Centroid*, or at the *Mid-Web*.

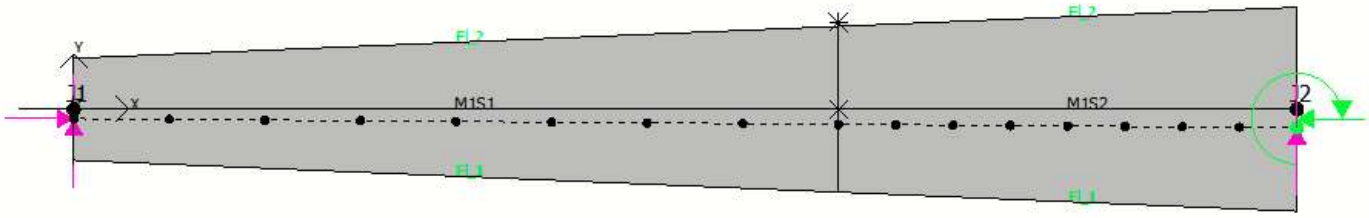

Joints | Members | Member Properties | Boundary Conditions | Loading

Load Combinations | Define Uniform Loads | Define Point Loads

	Node #	LC Name	Load Height	alpha	Fx	Fy	Fz	Mx	My	Mz	X_Loc	Y_Loc	Z_Loc
11	11	DL	Shear Center	0	0	0	0	0	0	0	103.5	-1.86672794...	0.0
12	12	DL	Shear Center	0	0	0	0	0	0	0	110.25	-1.91636029...	0.0
13	13	DL	Shear Center	0	0	0	0	0	0	0	117.0	-1.96599264...	0.0
14	14	DL	Shear Center	0	0	0	0	0	0	0	123.75	-2.015625	0.0
15	15	DL	Shear Center	0	0	0	0	0	0	0	130.5	-2.06525735...	0.0
16	16	DL	Shear Center	0	0	0	0	0	0	0	137.25	-2.11488970...	0.0
17	17	DL	Centroid	0	-11.3	0	0	0	0	-1800.0	144.0	-2.16452205...	0.0

Figure 94. ***Loading/Defined Point Loads*** **user interface**

5.2.7 *Definition of Structural Analysis Parameters*

Before running the structural analysis, it is important to check that the various analysis options available in SABRE2 are set to the desired values. In many situations, default parameters assigned by the software are sufficient. Figure 95 shows the SABRE2 user interface obtained when the *Analysis Parameters* tab is selected in this dialog window. Many of the parameters shown in this dialog window correspond to analysis capabilities other than Inelastic Nonlinear Buckling Analysis. These additional analysis capabilities in SABRE2 are discussed below and in Section 5.3. The various parameters accessed from this page are as follows:

- The member self-weight may be included. This is defined by the menu buttons in the upper left-corner of the dialog window. The *y* direction is taken as the gravity load direction if this option is turned *on*. The self-weight option is set to *off* by default. Note that when the self-weight is included, the appropriate factored weight density should be entered in the dialog shown in Fig. 90.
- The *J = 0 for Slender web* radio buttons defines whether the St. Venant torsional constant should be taken as zero or not for slender-web members when an Elastic Buckling Analysis (EBA) is employed. If *yes* is selected, then *J* is taken equal to zero in the buckling analysis, if the member web is slender under flexure per the AISC Specification Table B4.1b (AISC 2016). When an inelastic Linear or Nonlinear Buckling Analysis is employed, *J* is always taken equal to zero for slender web members (within any portion of the member length where the web is slender). This is because Section F5 of AISC uses $J = 0$ for these member types.

- The next analysis parameter defines whether the buckling and cross-section strength calculations should be based on the current AISC (2016) Specifications or on recommended member strength equations developed in recent research by Subramanian et al. (2018) as well as the recommended Flange Local Buckling (FLB) and Tension Flange Yielding (TFY) procedures developed in Sections 3.1 and 3.2. If *Current* is selected, the AISC (2016) based calculations are employed.
- The fourth analysis parameter specifies whether the stiffness reduction factor of 0.8, per the AISC Direct Analysis Method, should be applied to the elastic stiffnesses of the geometric nonlinear (pre-buckling load-displacement) analysis when an Elastic Nonlinear Buckling Analysis (ENBA) is employed. When an Inelastic Nonlinear Buckling Analysis (INBA) is employed, the software always uses the specified nominal elastic member stiffnesses.
- The increment size and maximum applied load ratio may be specified for first- and second-order load-deflection analyses. A value of 1.0 corresponds to application of the full specified load in one increment.

- Multiple buckling modes, rather than just the critical mode, may be requested for Elastic Linear Buckling Analysis.

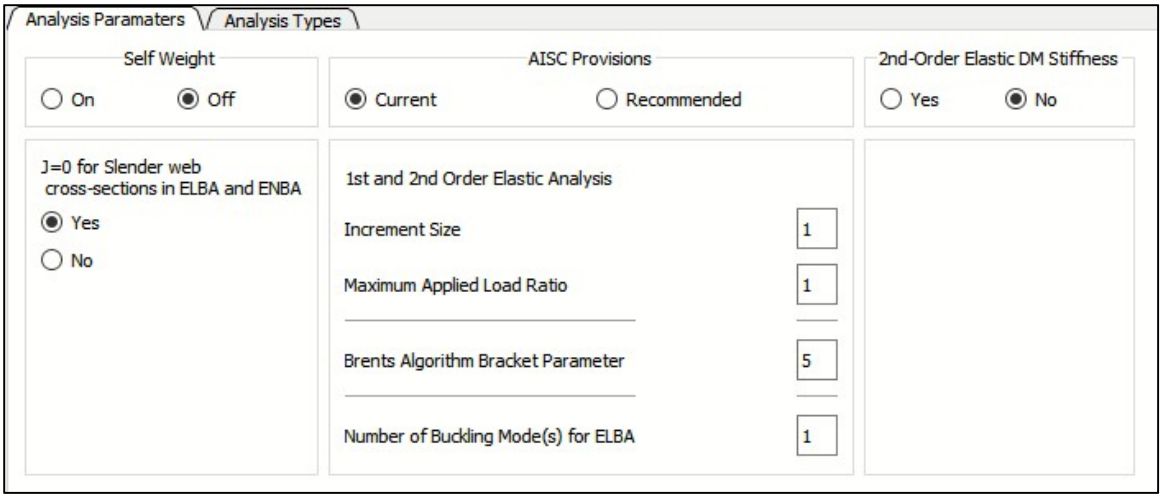

Figure 95. *Analysis Parameters* user interface

5.2.8 *Execution of Structural Analysis*

Given the completed problem definition, including the modification of any of the analysis parameters as appropriate, various types of analysis may be applied to the model of the member or structure in SABRE2. The available analysis types are listed via the push buttons inside the dialog window shown in Fig. 96, which is accessed via the *Analysis Types* tab in Fig. 95. Two types of load-deflection analysis may be conducted: first- and second-order elastic. In addition, four different types of buckling analysis are available within SABRE2. These different analysis types are discussed further in Section 0.

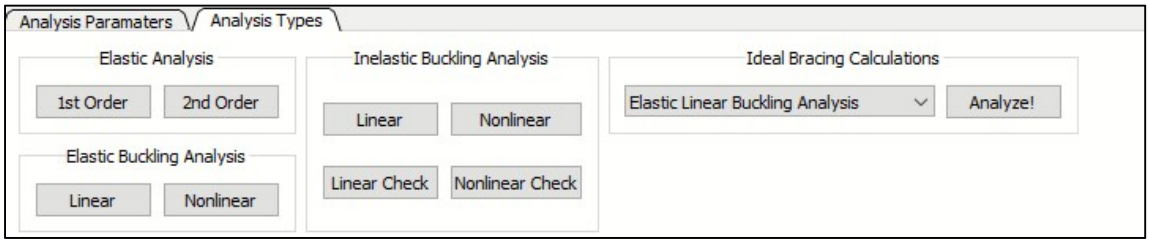

Figure 96. *Analysis Types* user interface, showing the various types of analysis available within SABRE2.

Given the selection of the analysis method from the dialog window shown in Fig. 96, SABRE2 executes the structural analysis, shows the corresponding displacement solution, for a load-displacement solution, or pre-buckling or buckling deflections from buckling analyses, and opens the corresponding Results dialog panel for further inspection of the responses.

5.2.9 *File Formats for Storage of Problem Definition and Results Data*

The problem definition and analysis results data are stored by SABRE2 in an h5 file format (Collette 2008). The h5 file format is a highly efficient binary format, and is discussed further in Section 5.5. The problem definition can also be defined or stored in a human readable problem definition text file format. SABRE2 can read and write both the h5 and text file formats for input of problem definitions. A given problem definition can be modified by changing the text file. Once either of these files is read in, the model can be modified using the graphical user interface as needed.

5.2.10 *Additional Modelling Considerations*

5.2.10.1 Fillet Areas

Cross-section fillet areas may be defined in the *Members -> Member Definition* tab (Fig. 86). For welded sections, this area is commonly taken equal to 0.0. For rolled sections, $A_{fillets}$ can be calculated as $A - 2b_f t_f - d_w t_w$, where A is the nominal cross-section area specified in the AISC Manual.

5.2.10.2 Application of Step in the Cross-Sections

If no step is defined, the cross-section dimensions are varied linearly between the adjacent joints and/or essential nodes (Fig. 88). When a step is defined at a given essential node, the change(s) in the cross-section dimensions between the previous joint or node and the essential node under consideration are implemented abruptly at this essential node. Important attributes of the corresponding "Step" function are as follows:

- The web depth is always varied linearly between adjacent essential nodes and/or joints in SABRE2, regardless of whether the geometry is stepped or not at a given essential node.
- SABRE2 models steps in the cross-section geometry by tapering the section dimensions over a short length. This is necessary to maintain continuity of the flange warping displacements. For cases where only one of the cross-section dimensions is stepped, the taper transition is always placed on the side of the splice that has the larger cross-section dimension. For cases where multiple cross-section dimensions are stepped, SABRE2 places the taper transition on the side of the step where the sum of the flange areas is larger. If the sum of the flange areas is the same, the taper transition is located on the side of the step where the total cross-section area is larger. This practice approximates the fact that, if a higher-order analysis such as a shell finite element analysis were conducted (i.e., with the flange and web plates modeled by shell elements), the section with the larger plate areas would tend to be only partially effective at the discrete physical step in the cross-section.

- Figure 97 shows several example graphs of how a given dimension, plotted on the vertical axis, varies along the length of the member when there is no step and when there is a step.

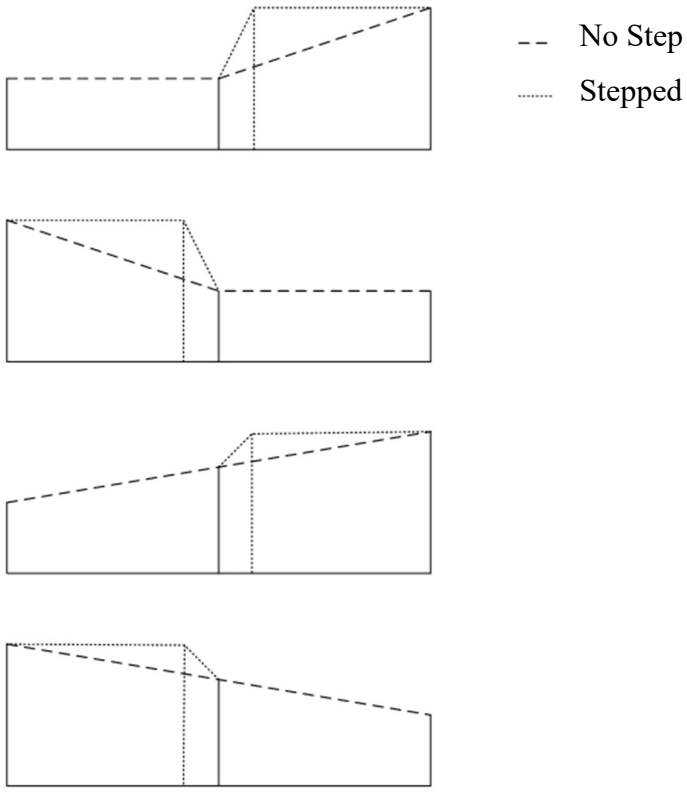

Figure 97. Example variations in a given cross-section dimension when there is no step versus when there is a step at an intermediate essential node.

- If desired, the user can model any taper transition explicitly by defining a taper. Taper transitions are defined by inserting essential nodes along the length of the member, and by providing the cross-section dimensions at each essential node.

5.3 Analysis Procedures in SABRE2

SABRE2 currently provides six analysis types:

1) First-Order Elastic Analysis –Load-deflection analysis in which second-order effects due to deformations are not taken into account; equilibrium is considered on the undeflected geometry of the structure and the material is idealized as linear elastic.
2) Second-Order Elastic Analysis – Load-deflection analysis in which second order effects due to deformations are taken into account for the analysis; equilibrium is considered in the deflected geometry of the structure; the material is modeled as linear elastic.
3) Elastic Linear Buckling Analysis (ELBA) – Eigenvalue buckling analysis of the ideal elastic structure neglecting the influence of pre-buckling displacements.
4) Elastic Nonlinear Buckling Analysis (ENBA) – Eigenvalue buckling analysis of the ideal elastic structure considering pre-buckling displacement effects. This is accomplished by a second-order elastic load-deflection solution to determine the pre-buckling deformed geometry and internal forces. Conversely, linear buckling analysis uses a first-order elastic load-deflection solution to estimate the underlying internal forces. The elastic buckling of the structural system is evaluated based on these forces.
5) Inelastic Linear Buckling Analysis (ILBA) – Eigenvalue buckling analysis of structure neglecting the influence of pre-buckling displacements but considering the buckling solution stiffness reduction factors developed in Chapter 2. This approach provides for the calculation of the buckling resistance of any type of I-section column, beam or beam-column member. The SABRE2 inelastic buckling algorithm can be used to produce a rigorous direct calculation of the AISC member axial resistance, $\phi_c P_n$, the

AISC member flexural resistance, $\phi_b M_n$, and/or the AISC-based beam-column resistance under combined axial compression (or tension) and flexure. SABRE2 can account for the influence of any type or combination of bracing, member end translational, rotational and/or warping restraint, and continuity with adjacent framing and across brace points within its calculation of the inelastic buckling resistance. The algorithm for the Inelastic Linear Buckling Analysis is presented by the flow chart in Fig. 98.

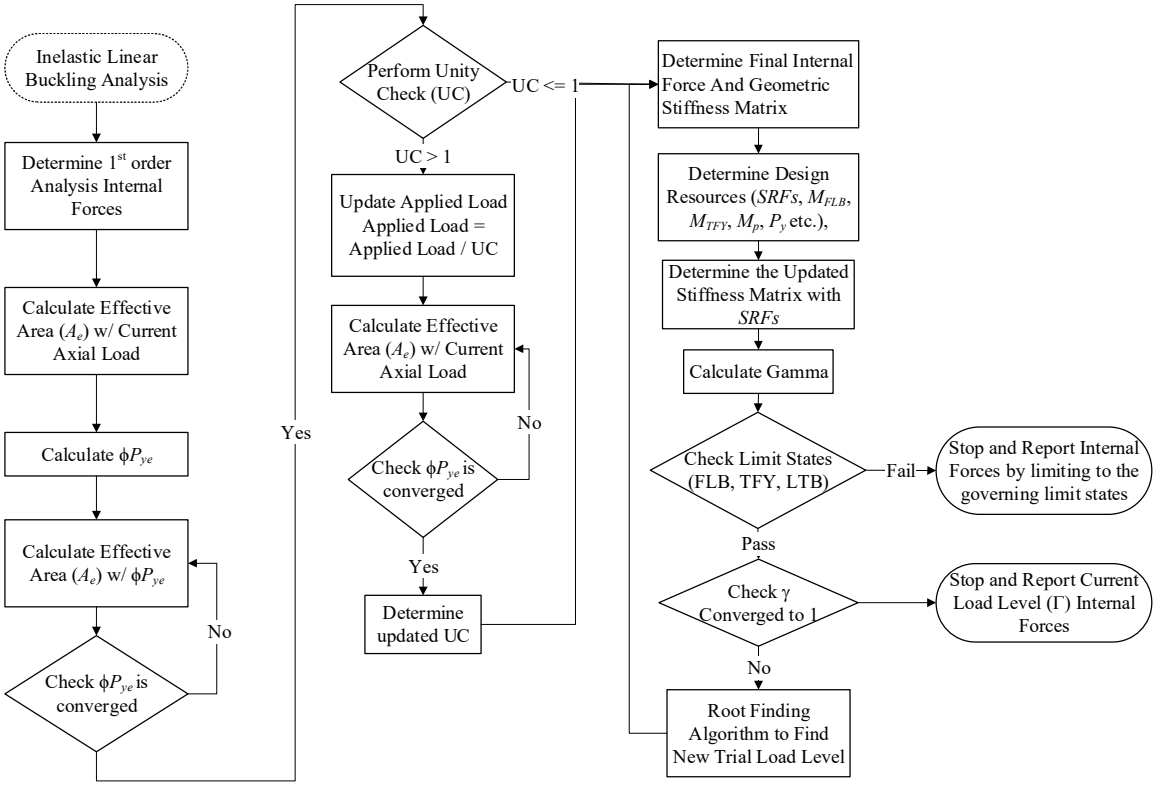

Figure 98. Inelastic Linear Buckling Analysis (ILBA) algorithm

6) Inelastic Nonlinear Buckling Analysis (INBA) – Eigenvalue buckling analysis of the structure considering pre-buckling displacement effects based on the AISC (2016) Direct Analysis Method idealization for the load-deflection analysis. For beam-type members, inelastic linear buckling analysis usually is sufficient to determine the

flexural resistance $\phi_b M_n$. In addition, column axial resistances, $\phi_c P_n$, can be obtained accurately from an inelastic linear buckling analysis in problems where the pre-buckling flexural and torsional displacements are relatively small. However, for general members and frames, the solution must track the changes in the structure's geometry under the applied load to satisfy the AISC design requirement that equilibrium must be considered on the deformed geometry of the structure. The SABRE2 INBA algorithm calculates the pre-buckling load-deflection response based on either the AISC Effective Length or Direct Analysis method rules. However, SABRE2 replaces the traditional checks of the member resistances via Specification algebraic resistance equations, which use various approximations such as C_b, K_x, K_y, K_z, etc., by the direct calculation of the buckling resistance of the structure with its members having reduced stiffnesses derived from the Specification resistance equations as discussed in Chapter 2. As a result, SABRE2 provides a rigorous calculation of $\phi_c P_n$, $\phi_b M_n$, and/or the beam-column resistances within the context of the Direct Analysis methods. The need to determine resistances from the AISC Specification strength equations is replaced by a more general buckling analysis calculation. This allows for a more accurate implementation of the Specification provisions. Algorithm for the Inelastic Nonlinear Buckling Analysis is presented the flowchart in Fig. 99.

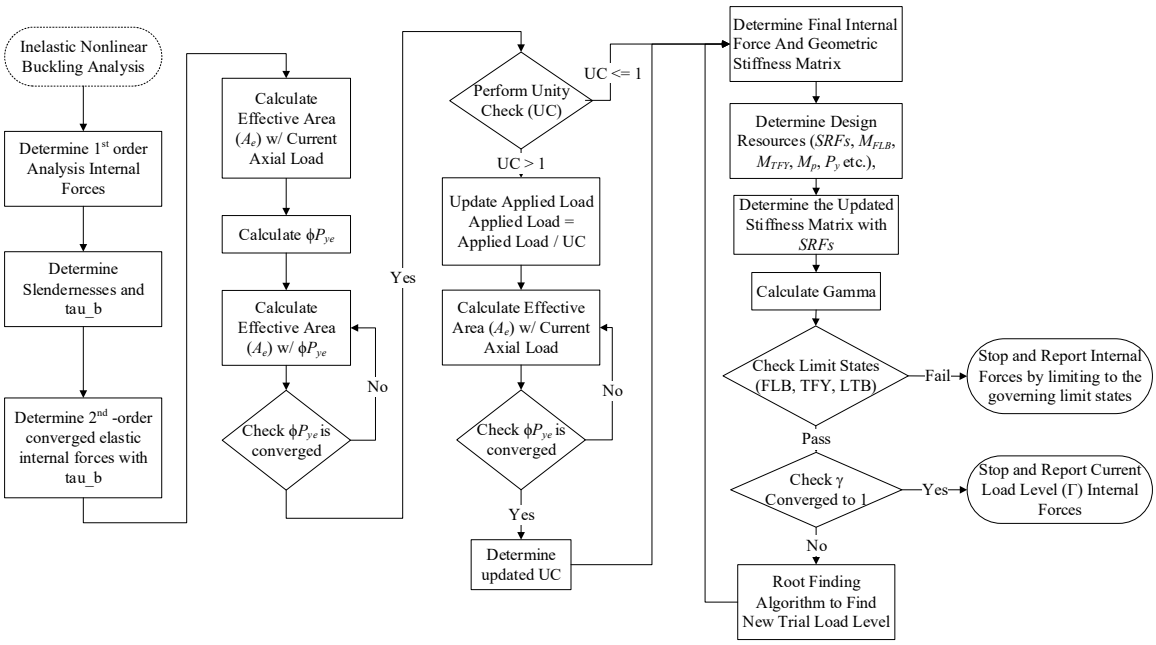

Figure 99. Inelastic Nonlinear Buckling Analysis (INBA) algorithm

SABRE2 is focused only on AISC Load and Resistance Factor Design (LRFD) at the present time. Allowable Strength Design (ASD) can be accommodated within the context of all the procedures implemented in SABRE2. The restriction to LRFD is simply a matter of focusing limited development resources. In addition, the current SABRE2 system is not aimed at "production design." Only one load case or load combination is accommodated at any one time. Similar to MASTAN2 (Ziemian and McGuire 2016), SABRE2 is focused on teaching, demonstration, and fundamental validation of structural analysis and design concepts.

5.4 Synthesis and Presentation of Results

Figure 100 shows the buckling mode for the example beam-column obtained from an Inelastic Nonlinear Buckling Analysis (INBA) in SABRE2. As one might expect, since the nodal brace is located on the flange subjected to flexural tension, and since the applied

bending moment causes significantly larger stresses than the applied axial load, the impact of considering the elastic stiffness of the brace is small. The γ_n is calculated as 1.18.

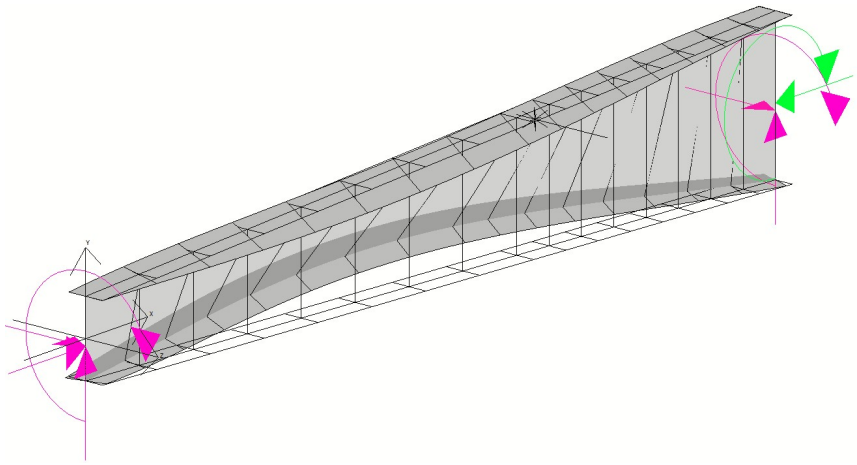

Figure 100. Member inelastic buckling mode

If the applied moment is set to zero such that the above member is subjected solely to concentric axial compression, the result shown in Fig. 101 is obtained. The member's inelastic buckling load is γ_n = 7.96 times the reference applied axial load (taken as the required LRFD load level). If the lateral brace at Flange 2 was taken as rigid (zero displacement) and the inelastic buckling load is obtained as 8.31 times the reference applied load. The small lateral brace stiffness is sufficient to develop a resistance of the member under uniform axial compression equal to 7.96/8.31 x 100 = 95.7 % of the resistance corresponding to rigid bracing. From Fig. 101, the member failure mode is clearly Constrained-Axis Torsional buckling (CATB). That is, the member is buckling by twisting about the top flange. One can observe that the CATB mode is similar in form to the LTB mode for this example.

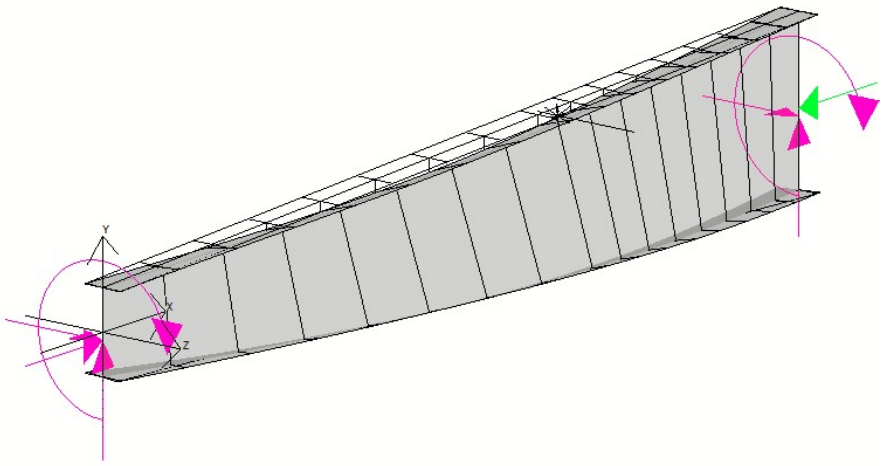

Figure 101. Constrained-axis torsional buckling of example member under concentric axial compression.

When the scale of the structural system is large, it is hard to distinguish a member's buckling mode due to the fact that the overall member dimensions may be quite small compared to the overall dimensions of the structure within the main viewing window. In these cases, it is typically more effective and more efficient to only display a line representation of the member and the overall structure. In addition, a line representation can be useful to better understand the lateral movement of the shear center reference axis associated with a given load-deflection analysis deflected shape or a buckling analysis buckling mode. For this purpose a line representation of the member deflected shape is also available. Figure 102 shows the corresponding SABRE2 *Deflected Shape* menu, accessed via the *Deflected Shape Options* tab of the *Results* user interface, along with a line representation of the undeflected and deflected shape of the member/structure. The *Results* user interface is accessed via the *Results* menu button shown in Fig. 83.

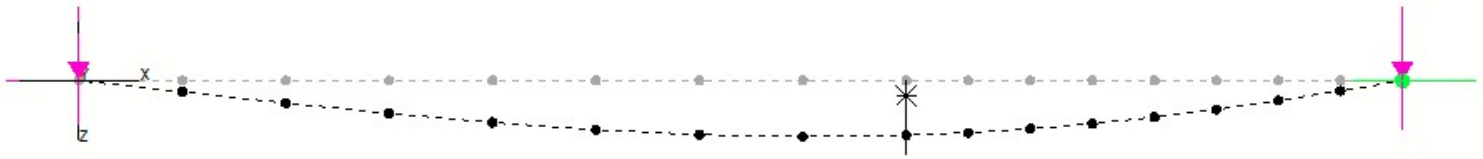

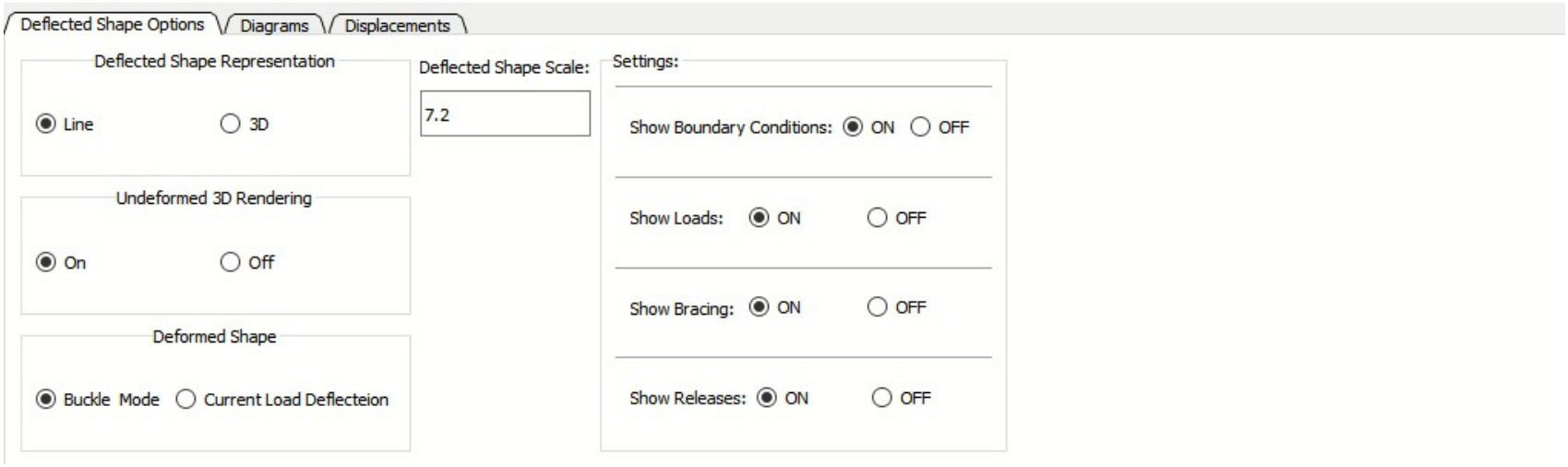

Figure 102. Line representation of the beam-column (top view) and *Deflected Shape Options* menu

In addition to the deflected shape of the analyzed structure, SABRE2 can also provide various response quantities and member/cross-section properties useful for design evaluation. These are referred to as "design resources" in SABRE2, and they include quantities such as the *SRF*, ϕM_{max}, ϕM_{FLB}, ϕM_{TFY}, and ϕP_y. These plots can be accessed through the *Diagrams* tab of the *Results* user interface. This information is available both as plots and as tabulated values.

Figure 103 shows a diagram of the beam-column Stiffness Reduction Factor (SRF) along the length of the member at the maximum design strength limit. The right-most element is the lowest SRF values. The sampling points for the five-point Gauss-Labatto numerical integration employed by the frame elements in SABRE2 is provided inside the plot.

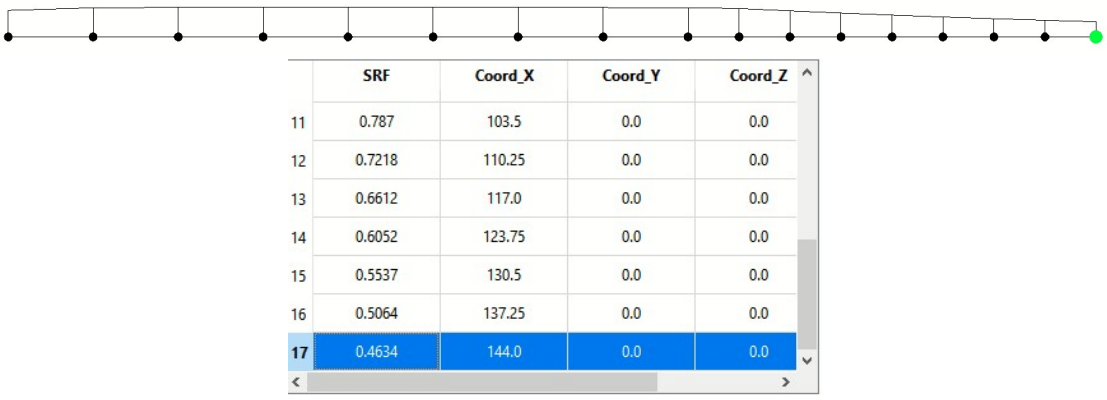

	SRF	Coord_X	Coord_Y	Coord_Z
11	0.787	103.5	0.0	0.0
12	0.7218	110.25	0.0	0.0
13	0.6612	117.0	0.0	0.0
14	0.6052	123.75	0.0	0.0
15	0.5537	130.5	0.0	0.0
16	0.5064	137.25	0.0	0.0
17	0.4634	144.0	0.0	0.0

Figure 103. Beam-column SRF diagram with values displayed using the diagrams tab highlighted from the SRF design resources table.

5.5 Software Framework

A previous Version 1 prototype of SABRE2 (White et al. 2017) was developed using the MATLAB (Mathworks 2016) environment. Using the programming framework provided by the Python (Python Software Foundation 2018) language and associated tools,

the features discussed in the previous section can be achieved with greater programming and execution efficiency. Therefore, a component of this research is to develop the software discussed in the above sections using the Python language, and to explore how the initial prototype can be improved. The selection of the Python language for this work is based on the considerations discussed below.

One of the most important advantages of Python pertaining to software such as SABRE2 is the "Garbage Collector", which allows the program to release the unused memory. This is essential for larger structural analysis and design solutions. Another advantage is the Python Libraries. There are many libraries available for any type of application in Python. For instance, the only user interface tool available for MATLAB is the GUIDE tool (Smith 2006) is available inside the MATLAB interface. This tool can be efficient for a basic user interface design, but it is limited in its ability to implement complex graphical user interfaces. For applications in Python, there are more than ten options available for this purpose. on the Python official web-site (Python Software Foundation 2018). In addition, the use of Python has become extensive in research institutes because of the shared tools available through its open source libraries.

For the development of the new SABRE2 interface, the use of QT Designer (The QT Company 2018) is selected for ease of coding. The Version 1 SABRE2 user interface is programmed at a low level, without any help from the MATLAB GUIDE tool, for its user interface design. This was necessary to achieve the desired user interface capabilities. The development of a user interface using lower-level programming can result in potential issues when implementing the software on different computer systems.

After the design of the SABRE2 user interface using the QT framework, the PyQT5 (v5.11.2) (Riverbank 2018) package, which translates the QT code into Python code, is used. This package provides High Definition (HD) capabilities that are compatible with the most current HD monitors and graphic processors. While it is compatible with current hardware systems, it is also back-compatible with older ones.

Additional software libraries selected for the SABRE2 Version 2 implementation are listed below with an explanation of their usage:

- Numpy (Oliphant 2006): The use of this package is essential for almost all mathematical operations performed in Python. This library provides better performance than inherited mathematical operations in Python.
- SciPy (Jones et al. 2001): This is a numerical tools package provided for Python language. The difference between Numpy and SciPy is that Numpy is used for array manipulations, and SciPy is used for all numerical operations
- h5py (Collette 2008): This package is used for internal storage and file save formatting and storage.
- PyOpenGL (Fletcher and Liebscher 2005): All graphical operations are performed using native OpenGL applications in the new version of SABRE2 developed in this research. To use these libraries, PyOpenGL supplies conversion from C code to the Python language. The PyOpenGL code is embedded inside PyQT5 code using the QGLWidget provided by PyQT5 package.
- os (Python Software Foundation 2018): This package handles all operating system processes and warnings

- sqlite3 (Häring G. 2006): This package is used for SQL database management. An SQL database is used to maintain AISC rolled I-section properties, as well as for storage of analysis parameters in the new version of SABRE2.

CHAPTER 6. ADVANCED DESIGN EVALUATION EXAMPLES

6.1 Beam Torsional Bracing Example

The grillage shown in Fig. 104, which is similar to a beam torsional bracing example presented in AISC (2002), supports glass roof panels subjected to uniformly distributed load. The W30x90 members (F_y = 50 ksi) are flexurally and torsionally simply-supported at their ends and are subjected to a maximum internal moment of M_u = 850 ft-kip (> $\phi_b M_n$ = 144 ft-kip for L_b = 60 ft and C_b = 1.14). Therefore, bracing is needed from the secondary W12x40 beams (F_y = 50 ksi).

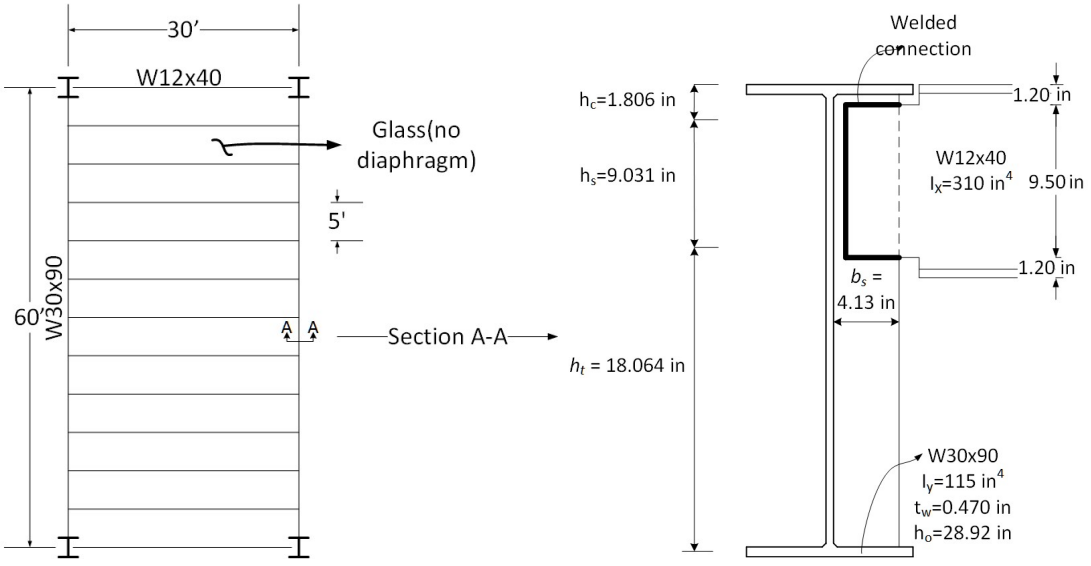

Figure 104. Beam torsional bracing example

The W12x40 beams have ample stiffness to brace the W30x90 members, but only if the connections are sufficient and the distortional flexibility of the W30x90 cross-section does not overly limit the effective torsional bracing stiffness.

The relevant properties and dimensions for this problem are as follows:

E = 29,000 ksi

L = 60 ft. overall length of the W30x90 beams

h_o = 28.9 in. distance between the mid-thickness of the W30x90 flanges

t_w = 0.470 in. web thickness of the W30x90 beams

I_y = 115 in^4 lateral bending moment of inertia of the W30x90 beams

I_b = 310 in^4 moment of inertia of W12x40 secondary beams

L_b = 30 ft. length of the secondary beams

Full-depth one-sided transverse stiffeners (4.13 in x 0.375 in) are used at each of the secondary beam locations as shown in Fig. 104. The height h_s is idealized as a length over which the web of the W30x90 is rigidly constrained to deflect in a straight line (due to the additional stiffening coming from the welded connection to the W12x40 beam webs). The torsional bracing is modeled as a rotational spring at the middle of this length.

6.1.1 *Assessment using AISC Appendix 6 with refinements from Yura (2001) and AISC (2002)*

Given the idealization summarized in Section 3.1, the effective torsional bracing stiffness provided by the secondary beams and their connection to the W30x90 girders may be calculated as follows (Yura 2001):

$$\beta_c = \frac{3.3E}{h_c}\left(\frac{h_o}{h_c}\right)^2\left(\frac{1.5h_c t_w^3}{12}+\frac{t_s b_s^3}{12}\right) = 30{,}180{,}000\ \frac{\text{in-kip}}{\text{rad}} \tag{62}$$

$$\beta_t = \frac{3.3E}{h_t}\left(\frac{h_o}{h_t}\right)^2\left(\frac{1.5h_t t_w^3}{12}+\frac{t_s b_s^3}{12}\right) = 33{,}030\ \frac{\text{in-kip}}{\text{rad}} \tag{63}$$

$$\beta_b = \frac{6EI_b}{L_b} = 149{,}800\ \frac{\text{in-kip}}{\text{rad}} \tag{64}$$

$$\beta_{Tprov} = \frac{1}{\frac{1}{\beta_c}+\frac{1}{\beta_t}+\frac{1}{\beta_b}} = 27{,}040\ \frac{\text{in-kip}}{\text{rad}} \tag{65}$$

Any distortional flexibility of the beam within the height of the connection region h_s, as well as the torsional flexibility of the overall girder system due to differential major-axis bending of the girders, is assumed to be negligible.

As explained in AISC (2002), the required torsional bracing stiffness can be determined most accurately from the following refinement of the AISC Specification Appendix 6 Eq. (A-6-11):

$$\beta_T = \frac{1}{\phi}\left[\frac{2.4L\left(M_u-\phi_b M_{no}\right)^2}{nEI_{yeff}C_b^2}\right] = 4508\ \frac{\text{in-kip}}{\text{rad}} \tag{66}$$

where:

$\phi = 0.75$

$L = 60$ ft.	overall W30x90 span length
$M_u = 850$ ft-kip	for the specified factored design loading
$\phi_b M_{no} = 144$ ft-kip	strength of the W30x90 in the absence of any intermediate bracing, including the associated moment gradient factor $C_{bu} = 1.14$
$n = 11$	number of intermediate brace points
$I_{yeff} = I_y = 115$ in^4	lateral bending moment of inertia of the W30x90 beams

and

$C_b = 1.0$	moment gradient factor based on near uniform bending at the mid-span unbraced lengths of the W30x90 beams

Therefore, it can be concluded that the W30x90 beam and the above bracing system has adequate stiffness to resist the required loads corresponding to $M_u = 850$ ft-kip. If an unstiffened connection detail such as the one evaluated in AISC (2002) is considered for this problem, the distortional flexibility of the W30x90 web severely limits the effective torsional bracing stiffness such that the unstiffened detail is not sufficient for the above level of loading.

From the AISC (2016) provisions, the bracing strength requirement for this case is

$$M_{br} = 0.02 M_u = 17.0 \text{ ft-kip} \tag{67}$$

The subsequent test simulation solutions indicate a strength requirement in this problem of 2.2 % of the maximum moment to develop the limit load capacity of the W30x90 beams. This is based on an out-of-alignment of the top flange of 30 ft x 12in/ft x 1/500 = 0.72 inches at the girder mid-span, which corresponds to a twist imperfection of θ_o = 0.72 in. / 28.9 in. = 0.0249 rad given that the bottom flange is assumed to have zero out-of-alignment. This twist imperfection is slightly smaller than the net rotation assumed in AISC (2002) considering movement in the bolted connections of the W12x40 beams due to hole clearances. However, 99 % of the flexural capacity is developed when the bracing moment reaches 2.0 %. Therefore, 2.0 % is considered an acceptable required strength for the stability bracing design in this problem.

Given the above strength requirement, a welded connection can be designed to transfer the required shears and moments to the W12x40 beams. The 4.33 x 0.375-inch transverse stiffeners on the W30x90 beam are sufficient to transfer the bracing moment M_{br} to the main girders, but they actually start to yield at slightly larger than 2.0 % bracing moment, as discussed subsequently. Also, the 9.5-inch depth of the coped W12x40 web is adequate to transfer the required moment.

6.1.2 *Assessment via Inelastic Buckling Analysis using SABRE2*

To perform a design assessment for this problem using the Inelastic Nonlinear Buckling Analysis capabilities in SABRE2, one can execute the following steps:

1. Construct a model of one of the W30x90 beams, including the modeling of the effective elastic rotational restraint at the attachments to the W12x40 secondary beams. Since M_u = 850 ft-kip is greater than $0.7\phi_b M_y$ = 643 ft-kip for the W30x90,

the primary beams have significant inelastic stiffness reduction at their mid-span at the required load level. Figure 105 shows the SRF values determined at the mid-length of each of the 24 elements used for the buckling analysis of the W30x90 beam. As discussed in Section 2.4, these SRF values are applied to *all* the beam cross-section rigidities associated with LTB (GJ, EC_w and EI_y).

2. Apply the factored loading of q_u = 1.890 klf to the model, which produces M_u = 850 ft-kip at the member's mid-span. This load can be applied with sufficient accuracy by applying concentrated loads of 9.444 kip at each of the W12x40 beam connection locations.

3. Analyze the beam using the Inelastic Nonlinear Buckling Analysis procedure in SABRE2.

4. Vary the effective elastic rotational stiffness at the secondary beam connection locations until the model buckles at the above required load. The corresponding bracing stiffness is the ideal bracing stiffness β_{Ti} required to develop the above applied loading. The ideal bracing stiffness obtained from this assessment is

$$\beta_{Ti} = 2463 \frac{\text{in-kip}}{\text{rad}} \tag{68}$$

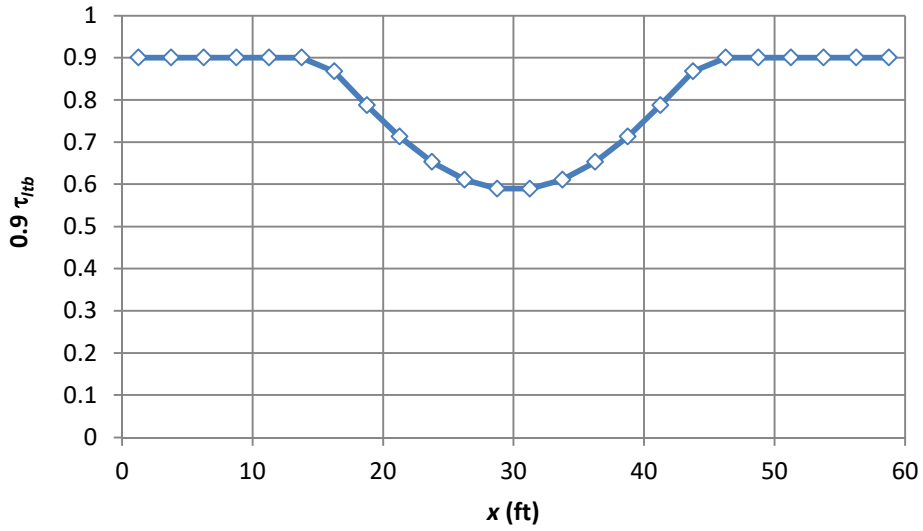

Figure 105. Variation of SRF along the length of the W30x90 primary beams due to the variation in $M_u/\phi M_n$ along the member length.

5. Apply the conventional factor 2/ϕ to the above ideal bracing stiffness (Eq. (68)) obtained from the above buckling analysis to obtain the required bracing stiffness. This value can be compared to the value of 4508 in-kip/rad obtained from Eq. (66) in Section 6.1.1 of Appendix 6 of AISC Specification (2016). The above value is considered to be a more accurate estimate of the required torsional brace stiffness, since it is obtained from a rigorous buckling analysis model, particularly since the rigorous buckling analysis accounts for LTB inelastic stiffness reduction as illustrated in Fig. 105 whereas Eq. (66) does not include any accounting for the effect of beam inelasticity. Equation (66) assumes that the W30x90 beam's elastic stiffness is available to resist the brace point lateral displacements throughout the member length. Prado (2014) and Lokhande (2014) show from extensive parametric test simulations that the torsional bracing requirements are indeed influenced by beam inelasticity.

6. Compare the above required torsional bracing stiffness to the provided torsional bracing stiffness, including the consideration of distortional flexibility of the stiffened W30x90 cross-section at the brace points. The calculation of the provided torsional bracing stiffness is given by Eq. (65).

Since β_{Tprov} is significantly greater than the above β_{br}, we can conclude that the W12x40 secondary beams combined with the one-sided 4.13 x 0.375 inch full-depth transverse stiffeners provide ample stiffness to develop the required design load associated with M_u = 850 ft-kip in the W30x90 beams.

Based on the AISC 2016 Appendix 6 provisions, the bracing strength requirement is the same as in Section 3.4 (White and Jeong 2019) Eq. (67), i.e., $M_{br} = 0.02M_u = 17.0$ ft-kip .

It should be noted that the above model provides a direct assessment of the W30x90 beam LTB resistances. No separate check of the Specification LTB strength equations is necessary once these calculations have been performed. Via the use of SABRE2, this assessment includes a rigorous assessment of the influence of the torsional bracing stiffnesses as well as continuity effects between the adjacent unbraced lengths along the span. As noted previously, strength limit states other than LTB must still be checked.

Another powerful feature of the inelastic buckling solution is that it can be used to justify the stiffening of the W30x90 web at only a selected number of secondary beam locations (rather than providing the same stiffening at each of W12x40 beams). This solution is not shown here in the interest of keeping the presentation brief. Equation (66) is based on the assumption of equally-spaced equal-stiffness torsional bracing throughout

the span of the beam that is being braced. In addition, Eq. (66) is an entirely elastic derivation, involving the implicit assumption that the elastic stiffness of the primary beam is available to help resist the brace point displacements, as well as the assumption that the beam strength is scaled by C_b, regardless of whether the "plateau LTB resistance" ($\phi_b M_p$ for a compact-section beam) is exceeded.

6.1.3 *Comparisons to Test Simulations*

Figure 106 plots the moment at the mid-span of the W30x90 beams versus the maximum bracing moment in the secondary beams, expressed as a percentage of the W30x90 mid-span moment. The curves in this plot are obtained from four separate test simulations. The results are generated considering the two different geometric imperfections shown in Fig. 107. The "larger" of these imperfections involves an equal out-of-alignment of 1/500 in all of the unbraced lengths on each side of the mid-span, resulting in an overall Δ_o of the top flange of 0.72 inch at the mid-span, as discussed previously. The "smaller" of these imperfections involves an out-of-alignment of 1/500 only in the L_{br} = 5 ft unbraced lengths on each side of the critical brace at the W30x90 mid-span. In addition, a top-flange out-of-straightness of $L_{br}/2000$ = 0.03 inch is specified in opposite directions in the unbraced lengths on each side of the mid-span (this imperfection is used, rather than $L_{br}/1000$, as a representative average out-of-straightness within the unbraced lengths). The bottom flange is modeled as perfectly straight in all of these simulations. Both of these imperfection patterns satisfy the AISC Code of Standard Practice (COSP) tolerances. In addition, results are generated with the one-sided stiffener

having the actual yield strength of F_y = 50 ksi and with the stiffener modeled as infinitely elastic.

For the residual stresses used in the test simulations, 0.9 times 0.5 of the Lehigh residual stress pattern is employed. The 0.9 factor corresponds to factoring of the material strength ordinates by 0.9 as required by Appendix 1 of the AISC Specification. One-half of the magnitude of the residual stresses in the Lehigh residual stress pattern is used because this value of the residual stresses tends to produce test simulation results that match reasonably well with the AISC LTB strength curves, which in turn capture close to the mean LTB resistances obtained from experimental tests (White and Jung 2008; White and Kim 2008a; Subramanian and White 2018).

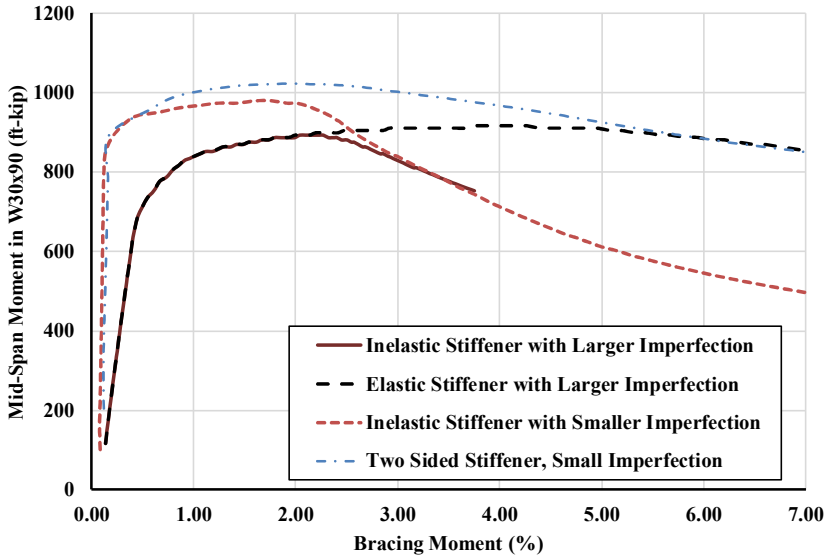

Figure 106. Mid-span internal moment in the W30x90 primary beams versus the largest bracing moment in the secondary W12x40 beams (occurring in the bracing beam attached at the mid-span) from four different test simulations.

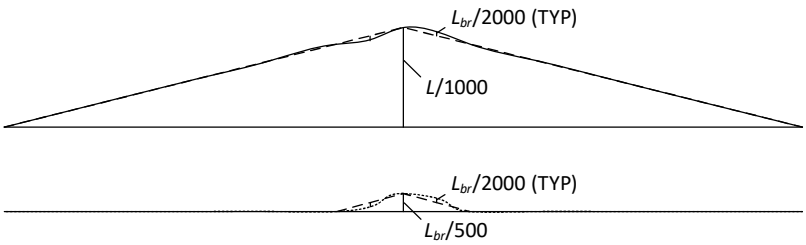

Figure 107. "Larger" and "smaller" out-of-plane initial geometric imperfection displacements considered on the top flange of the W30x90 beams (L_{br} = 5 ft and L = 60 ft).

Figure 106 shows that the W30x90 is sufficient to develop the required moment capacities for the design scenario considered. However, the maximum capacity of the W30x90 beams is less than $\phi_b M_p$ = 1061 ft-kip, although if one checks the AISC Appendix 6 bracing requirements to develop $\phi_b M_p$, it can be concluded that the bracing stiffness provided should be sufficient to develop the factored plastic moment capacity. The larger imperfection case with inelasticity modeled in the stiffener shows the smallest strength of M_{max} = 897 ft-kip. If the stiffener is assumed to be infinitely elastic, only a slightly larger strength of M_{max} = 915 ft-kip is developed. It is determined that the selected imperfection has a significant impact on the maximum capacity of the primary beams. If the smaller imperfection is considered, the system develops a M_{max} = 980 ft-kip in the W30x90 beams, still 8 % smaller than $\phi_b M_p$. Therefore, an additional test simulation is conducted with the smaller imperfection and in which a double-sided transverse stiffener is used that has a total width equal to the 10.4-inch width of the W30x90 flanges at each of the bracing locations. This case develops a M_{max} of 1024 ft-kips, which is within 3.5 % of the factored design plastic moment.

For the beams with the one-sided stiffener, larger imperfections, and either actual or infinitely elastic properties, the required bracing moment in the secondary beams is 1.4

% of M_u (11.9 ft-kip) at M_u = 850 ft-kip. If the maximum capacity of the "elastically-stiffened" beam of 915 ft-kip were utilized, a required bracing moment of 4.2 % (38.43 ft-kip) would be required. Nevertheless, 97 % of this member's moment capacity is developed (i.e., 886 ft-kip) when the bracing required moment reaches 2.0 % of the girder mid-span moment, and this result is obtained for both the solutions with the elastic as well as the inelastic stiffener. Generally, a required bracing moment of 2.0 % has been found to be acceptable as a simple estimate for all cases, based on the criterion that at least 95 % of the maximum moment capacity is developed in the member that is being braced (Prado 2014; Lokhande 2014).

Figure 106 shows that at slightly more than 2 % bracing moment, the actual 4.13 x 0.375 inch one-sided stiffener starts to yield in the case where the beam has the larger imperfection, thus limiting the maximum capacity of the W30x90 beams to 897 ft-kip and resulting in a bracing moment at the primary beam limit load of only 2.2 %.

In addition, Fig. 106 shows that the bracing moments are significantly smaller for the beams with the smaller imperfection until just before the maximum capacity of the beams is achieved. The torsional bracing moments at the limit load for the beams with the smaller imperfection are 1.8 % when the one-sided stiffener is used, and 1.9 % when the large two-sided stiffener is used. However, at 95 % of the maximum capacity of these beams, the torsional bracing moments are only 0.7 % and 0.4 % respectively.

6.1.4 *Additional Comparisons to Test Simulation Results*

Figure 108 shows the maximum strength of the W30x90 beams versus the total effective torsional bracing stiffness, obtained from: (1) the AISC Appendix 6 provisions,

(2) the above Buckling Analysis procedures, and (3) refined Test Simulation calculations. These curves consider a scenario in which the size of the secondary bracing beams is varied, giving an overall variation in β_{Tprov}. These types of curves are often referred to as "knuckle curves" in the literature. For the Appendix 6 calculations, given a total effective bracing stiffness β_{Tprov}, Eq. (66) is solved for M_u to generate the points along the Appendix 6 knuckle curve. For the Buckling Analysis calculations, the procedure outlined earlier is employed, but with a variable β_b. For the Test Simulation solutions, the 4.13 x 0.375-inch one-sided stiffener results are considered with the larger and smaller imperfections shown in Fig. 107. In addition, the 10.4 x 0.375-inch two-sided stiffener results are shown for the smaller imperfection.

Figure 108 is helpful to understand the behavior associated with the Appendix 6 and SABRE2 Buckling Analysis solutions, and the inability of the W30x90 beams to develop $\phi_b M_p$ in spite of the use of large torsional bracing stiffness values. The following points can be gleaned from this plot:

- The refined AISC Appendix 6 Eq. (65) suggests that the W30x90 beams are able to develop $\phi_b M_p$ = 1061 ft-kip at a relatively small effective torsional bracing stiffness value of only 7605 in-kip/rad. This behavior is related to the fact that Eq. (65) assumes fully elastic behavior of the W30x90 beams, whereas the beams have substantial inelastic stiffness reduction as they approach $\phi_b M_p$ = 1061 ft-kip at their mid-span.

- The Buckling Analysis solution, based on the use of reduced stiffnesses of (SRF) defined as a function of the internal moment levels along the W30x90 beams,

predicts that the primary beams are able to develop $\phi_b M_p$ = 1061 ft-kip at an ideal brace stiffness of β_{Ti} = 11,980 in-kip/rad., which then translates to a required bracing stiffness of

$$\beta_T = \frac{2\beta_{Ti}}{\phi} = 31{,}920 \frac{\text{in-kip}}{\text{rad}} \tag{69}$$

- The knuckle curve determined by the SABRE2 Buckling Analysis calculations does a good job of capturing the shape of the test simulation-based knuckle curves for the larger imperfection. However, the Buckling Analysis solution predicts that the W30x90 beams can achieve $\phi_b M_p$ for effective torsional brace stiffnesses β_T greater than 31,920 in-kip/rad, whereas the test simulations with the larger imperfection only achieve a maximum resistance of 897 and 915 ft-kip at an effective torsional bracing stiffness of approximately 22,000 in-kip/rad. With the smaller imperfection and the large two-sided transverse stiffener, the W30x90 beams reach a maximum strength of 1024 ft-kip at a β_T of approximately 22,000 in-kip/rad.

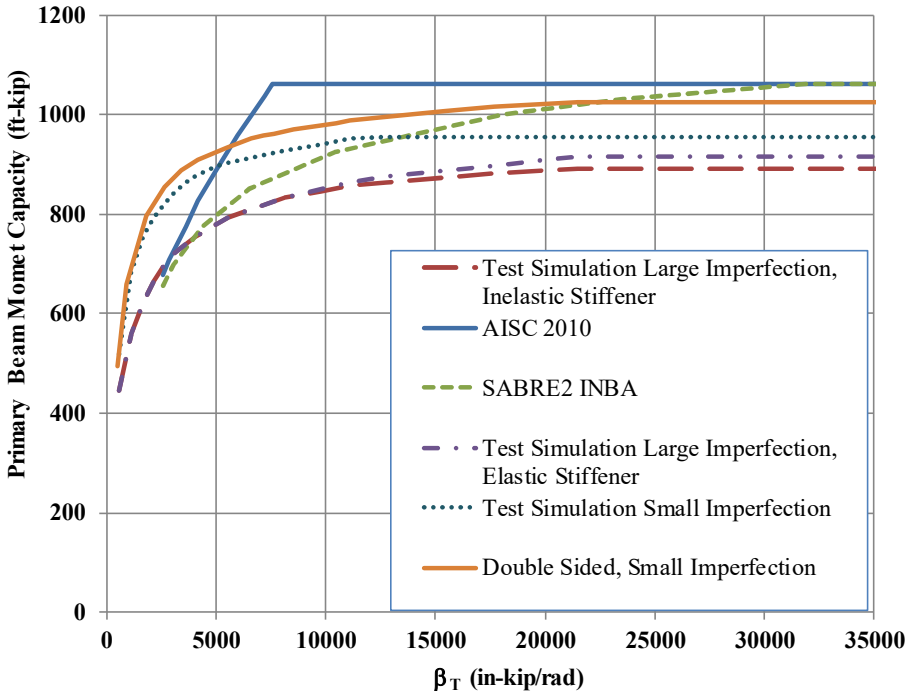

Figure 108. W30x90 beam design strength versus total effective torsional bracing stiffness knuckle curves from Appendix 6 and buckling analysis and test simulations

Several potential underlying reasons for the mid-span moment at the limit load being significantly smaller than $\phi_b M_p$ in the test simulations are as follows:

a) Test simulations based on geometric imperfections set at the AISC Code of Standard Practice maximum tolerances and using common traditional nominal residual stress patterns commonly indicate some difficulty in reaching $\phi_b M_p$ at unbraced lengths close to L_p for problems with uniform or near uniform bending. For the W30x90 beams used here, L_p = 7.38 ft however, whereas the unbraced length employed in this example is L_{br} = 5 ft. Therefore, the considerations appear to be deeper than just the conservative nature of typical test simulation results involving near uniform bending.

b) Rigid bracing benchmark results shown in Prado (2014)indicate that there is some minor variation in the maximum strength achieved for beams with both flanges restrained laterally, only the compression flange restrained laterally, or only twisting of the member restrained at the brace points. The rigid bracing strengths for torsional bracing are the smallest, and the rigid bracing strengths with both flanges restrained laterally are the largest. This type of behavior would appear to be a factor in the maximum strengths reached in this problem as well, but based on Prado (2014), it would not be expected that this behavior is the major reason why the W30x90 beams do not reach $\phi_b M_p$ in this example.

c) The "larger" imperfections result in a value of θ_o at the mid-span of the W30x90 girders that is relatively large compared to their 5 ft unbraced lengths. By considering the smaller imperfections, the strengths are increased measurably; however, the most substantial increase is obtained when the girders are also heavily stiffened at the torsional bracing locations. It is apparent that the test simulation beam strengths in this example problem are sensitive to both the overall geometric imperfection as well as the stiffening of the beam cross-section. As such, it is recommended that maximum limits on θ_o, or θ_o/L_{br} should be considered by the COSP. In addition, it is suggested that the sensitivity of beam strengths to cross-section distortion when torsionally-braced I-section beams are loaded to moment levels involving substantial cross-section plasticity

The above sensitivities to θ_o and the beam cross-section stiffening highlight the limitations of typical member resistance equations in design standards. These equations do

not capture any variation in the member capacity as a function of the above types of parameters. Refined test simulation solutions, which are permitted by AISC Appendix 1, can account for these effects. However, these types of solutions are certainly not routine.

6.2 Column Nodal Bracing Example

6.2.1 *Problem Description*

The wide-flange column shown in Fig. 109, taken from Appendix E.4 of Griffis and White (2013), is located in the middle of a mechanical shaft and supports a required strength of P_u = 1400 kip. Horizontal bracing members frame into the column in the weak-axis bending direction at each of the floor levels of the building, which are at 15 ft intervals along the column length. However, clearance is not available to provide any bracing over the entire 60 ft height of the column in its strong-axis bending direction. The efficiency of the design is improved by providing a "flying beam" AB across the shaft to restrain the column major-axis bending lateral deflections at its mid-height. A moment connection is provided in the anticipated lighter-weight flying beam member on each side of the column. The flying beam spans 30 ft across the width of the shaft and is simply-supported at its ends by a relatively rigid wall system. The flying beam is also a wide-flange section and is turned such that its strong-axis bending stiffness and strength braces the column. The column is simply-supported at its ends. A W14x145 is selected for the column, as discussed in Griffis and White (2013). In addition, Griffis and White (2013) show that a W14x43 flying beam is sufficient to brace the column, based on an assessment using the Direct Analysis Method. The W14x43 provides a nominal point bracing stiffness to the W14x145 column of

$$\beta = \frac{48EI_x}{L^3} = 12.77 kip/in \tag{70}$$

(E = 29,000 ksi, I_x = 428 in^4 and L = 30 ft = 360 inches) which is substantially smaller than the refined requirement for full bracing stiffness from the AISC (2016) Commentary, equal to

$$\beta_{brF} = \frac{2}{\phi}\left(4 - \frac{2}{n}\right)\frac{\phi_c P_{nF}}{L_{br}} = 22.5 \text{ kip/in} \tag{71}$$

where n = 1, ϕ = 0.75, $\phi_c P_{nF}$ = 1519 kips, and L_{br} = 30 ft = 360 inches.

In this example, the column and its bracing system are evaluated using the Inelastic Nonlinear Buckling Analysis (INBA) capabilities of SABRE2. The essential details of the corresponding analysis model are explained in Section 6.2.2.

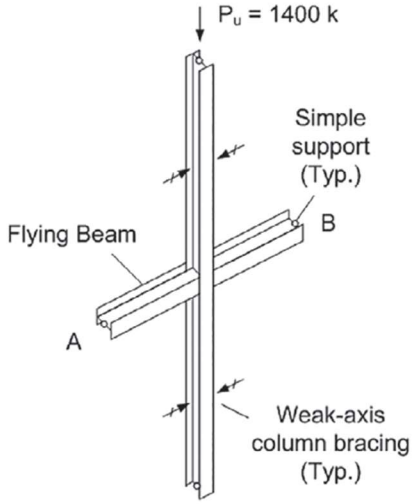

Figure 109. Griffis and White (2013) nodal bracing example – W14x145 column with a W14x43 flying beam brace, and with P_u = 1400 kip.

The relevant dimensions and properties for the W14x145 column are as follows:

$L_{br} = L_{cx} = 30$ ft $= 360$ in for full bracing

$r_x = 6.33$ in

$I_x = 1710$ in^4

$A = 42.7$ in^2

$F_y = 50$ ksi

$\phi_c = 0.9$

6.2.2 *Modelling of the Member with Inelastic Buckling Analysis*

The Inelastic Nonlinear Buckling Analysis model in SABRE2 uses the Direct Analysis Method (DM) to calculate the internal forces but replaces the resistance calculations by an eigenvalue buckling analysis. As such, all elastic contributions to the stiffness are to be multiplied by a stiffness reduction factor of 0.8 for the in-plane load-deflection analysis. For the buckling analysis, a stiffness reduction factor of 0.9 x 0.877 = 0.7893 is to be applied to any components that are nominally elastic. SABRE2 includes these stiffness reductions automatically when modelling any structural members. However, for the modelling of bracing components, SABRE2 intends for the user to provide the desired reduced stiffness to be employed for the bracing within the structural analysis model. This is due to the fact that engineers may wish to apply different stiffness reduction factors to the bracing, for example either 0.8 or 0.7893 as indicated above, or $\phi/2 = 0.375$ based on an interpretation of AISC (2016) Appendix 6. In this example, we will use a

stiffness reduction factor of 0.9 x 0.877 = 0.7893 both for the load-deflection calculation, which is slightly conservative relative to the required AISC stiffness reduction for the in-plane load-deflection analysis, and is equal to the required value for evaluation of the LRFD column factored resistance, $\phi_c P_n$ (see Section 2.2 of this dissertation). Therefore, the reduced bracing stiffness of the flying beam is taken as 0.9 x 0.877 x 12.77 kip/in = 10.08 kip/in in this example.

The column analysed in this example is expected to fail in an in-plane buckling mode rather than by out-of-plane buckling. Therefore, for the application of the DM to evaluate the in-plane strength, a key requirement is to define the imperfect column geometry that has the greatest destabilizing effect. The in-plane imperfection that produces the greatest destabilizing effect on the column is shown in Fig. 110. This imperfection involves an out-of-alignment of the middle brace point of L_{br} / 500 = 0.72 inches, and an out-of-straightness within each of the column unbraced lengths of L_{br} / 1000 = 0.36 inches.

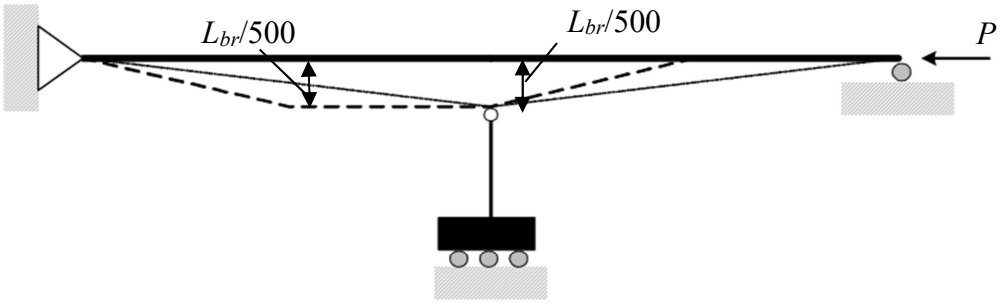

Figure 110. Critical in-plane imperfection for column maximum demand

The above column out-of-straightness needs to be applied in opposite directions in the two adjacent column unbraced lengths, basically forming an S-shaped out-of-straightness imperfection over the full column length (affine to the buckling mode of the fully-braced column). For practical purposes, it is sufficient to model these out-of-

alignment and out-of-straightness values in a chorded fashion, i.e., modelling the imperfect geometry by straight segments between the in-plane brace points and the middle of each of the unbraced lengths.

The column in-plane imperfection that produces the maximum destabilizing effect in terms of the strength demands on the flying beam brace is different than the above. This imperfection is as shown in Fig. 111. This imperfection pattern involves the same out-of-alignment and out-of-straightness values as above. However, the out-of-straightness is applied in the same direction in each of the unbraced lengths. Again, it is sufficient to model these imperfections in a chorded fashion.

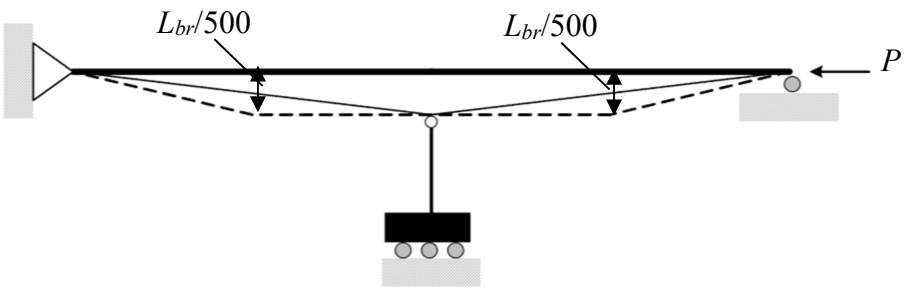

Figure 111. Critical in-plane imperfection for brace force demand

It should be noted that no out-of-plane imperfection is defined in the weak-axis bending direction of the column in the above models. The influence of out-of-plane geometric imperfections is accounted for implicitly in the SRF values employed within the Inelastic Nonlinear Buckling Analysis, as discussed in Chapter 2 of this dissertation.

Figure 112 shows the specified boundary conditions for the SABRE2 analysis model of the column. The column is shown in an isometric view, as if it were a horizontal member, to save on white space. The member is braced in the out of plane (Z) direction as well as against twisting at its ends and at every 15 ft along its length. These braces are

assumed to be rigid as specified by Griffis and White (2013). In addition, the member is assumed to be braced rigidly at its ends within the plane of the problem, as in Griffis and White (2013) (i.e., the member ends are flexurally and torsionally simply supported). All of these braces are indicated by the solid magenta arrows on the rendering of the member. The flying beam at the middle of the entire column length is modelled as a "bracing spring," and is denoted by the symbol with the "X" on it just below the column at its mid-length. This spring is oriented in the global Y direction in SABRE2. The concentrically applied axial loading at the top of the column is represented by the solid green arrow on the right-hand side of the figure.

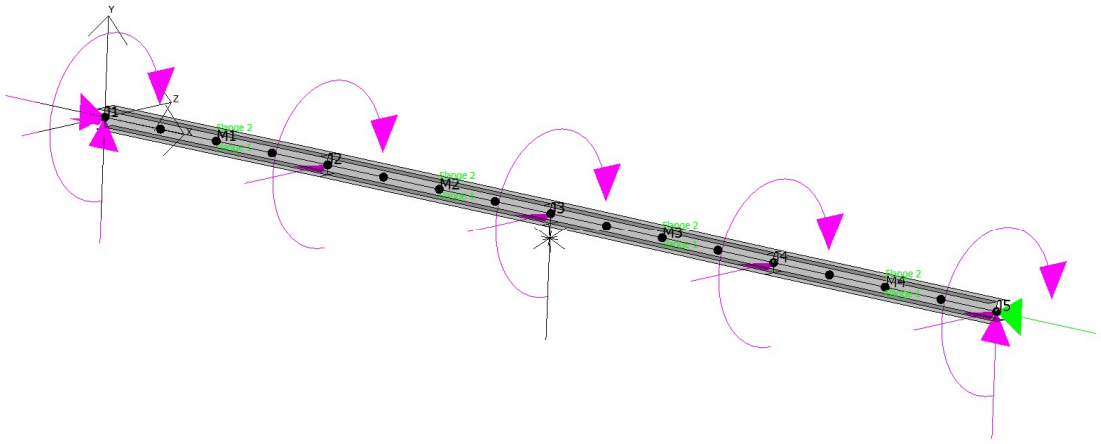

Figure 112. SABRE2 model of the column with the flying beam represented as a point bracing "spring."

6.2.3 *SABRE2 Results*

Figure 113 shows the failure mode of the column in this example when modeled with either of the geometric imperfections specified in Section 6.2.2. The strength of the column is predicted as $\Gamma P_u = \phi_c P_n = 1519$ kips to four significant digits for both of the above geometric imperfections. SABRE2 indicates that the failure of the column is by

buckling, with a Γ value of 1.085 (equal to 1519 / 1400). As such, this problem is an example of a case in which, although a DM solution with critical geometric imperfections is employed to determine the in-plane strength, the eigenvalue buckling solution based on the beam-column SRF defined in Section 2.4 governs before the DM solution reaches a unity check equal to 1.0 at any of the column cross-sections. The buckling mode in Fig. 113 confirms that the member is failing in an overall "fully-braced" fashion, with inflection points in the column at each of the brace locations.

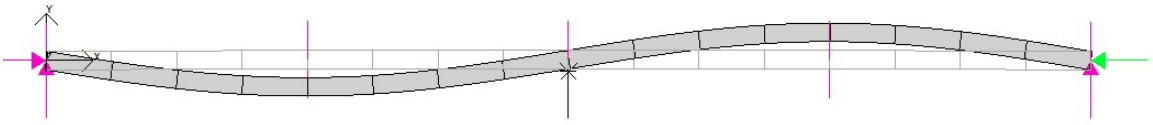

Figure 113. Buckling mode in SABRE2 corresponding to $\phi_c P_n$ = 1519 kip.

The internal bending moment diagram in the column model with the imperfection having the maximum destabilizing effect on the column strength, at the above strength condition, is shown in Fig. 114. The maximum bending moment is obtained in the left-hand unbraced length and is equal to 63.2 kip-ft = 759 kip-inches. The column cross-section resistance terms are $\phi_c P_y$ = 1922 kips and $\phi_b M_p$ = 975 kip-ft = 11,700 kip-inches. This gives a maximum cross-section unity check at the maximum strength condition of

$$\frac{P_u}{\phi_c P_y} + \frac{8}{9}\frac{M_y}{\phi_b M_p} = 0.848 \tag{72}$$

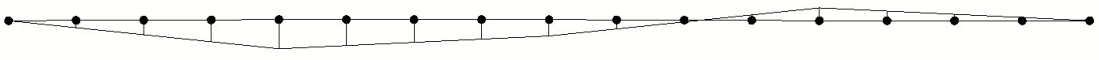

Figure 114. Internal bending moment along the length of the column

Figure 115 shows the variation of the cross-section unity check along the length of the column for the analysis with the geometric imperfection having the greatest destabilizing effect on the column. The corresponding variation of the SRF along the column length, due to the combined bending and axial compression, is shown in Figure 107.

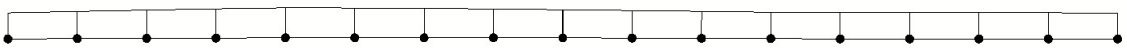

Figure 115. Plot of the cross-section unity check (UC) along the length of the column

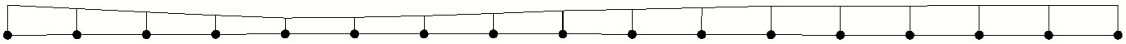

Figure 116. Plot of the SRF along the length of the column

Figure 117 shows a plot of the brace force versus the column axial load for the analysis with the geometric imperfection causing the maximum demand on the flying beam brace strength. The force applied to the flying beam brace at the calculated maximum system capacity is equal to 40.28 kips. This amounts to 2.5 % brace force, which is larger than the ordinary point brace requirement of 1.0 % in AISC (2016) Appendix 6. This is a slightly different value but is consistent with the results presented by Griffis and White (2013) for this column with the W14x43 flying beam brace (i.e., the brace force prediction is larger than 1.0 %). However, this brace force is well within the lateral bending capacity of the W14x43 beam. As discussed, by Griffis and White (2013), a W14x61 section is required for the flying beam brace in this problem, to develop the fully-braced strength of the column based on the more traditional Appendix 6 estimates. However, one can observe that, based on the above SABRE2 analysis prediction, the smaller W14x43 flying beam brace is sufficient to develop the column fully-braced strength.

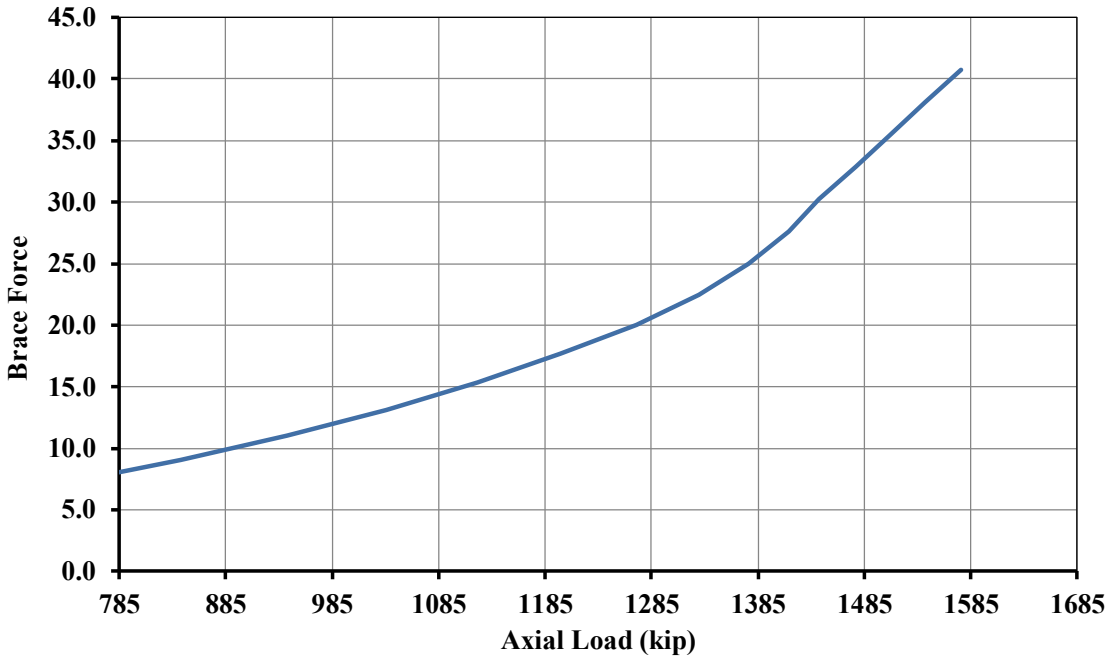

Figure 117. Brace force versus axial load in the column for the case with the geometric imperfection producing the largest brace force demand.

It is useful to consider an additional validation of the above results by the use of a refined 3D shell finite element test simulation using appropriate column residual stresses and geometric imperfections. For these test simulations, the column geometric imperfections are modelled as specified in Fig. 110. No additional local geometric imperfections are modelled, since the member cross-section is nonslender under uniform axial compression. No out-of-plane geometric imperfections are considered, since this problem is critical with respect to in-plane flexural buckling. The full Lehigh pattern, equal to two times the values shown in Appendix A.3, is employed for the column residual stresses.

Figure 118 shows the column strength versus the reduced brace stiffness (0.9 x 0.877 x nominal brace stiffness) "knuckle curve" for this problem generated by the refined test

simulation. One can observe that the largest column resistance is approached asymptotically as the brace stiffness is increased. At a reduced brace stiffness of 0.9 x 0.877 x 22.5 kip/inch = 17.8 kip/inch, corresponding to the traditional full-bracing stiffness from AISC (2016) Appendix 6 (Eq. A-6-10), the column strength is 1632 kip, equal to 98.5 % of the column strength for a rigid point brace. At the reduced brace stiffness for the W14x 43 flying beam of 0.9 x 0.877 x 12.77 kip/inch = 10.08 kip/inch, the column strength is 1554 kip, equal to 93.8 % of the column strength for a rigid point brace. It should be noted that the column axial compressive strength for rigid bracing, obtained from the test simulation, is slightly larger than the value of $\phi_c P_n$ = 1519 kips obtained from the AISC column curve for full bracing. This is due to the fact that the column fails due to major-axis in-plane flexural buckling in this problem. The actual column flexural buckling resistance generally tends to be larger for column major-axis flexural buckling compared to the column curve resistance and the weak-axis column flexural buckling strength for the same value of the column slenderness L_{br}/r (Salmon et al., 2009).

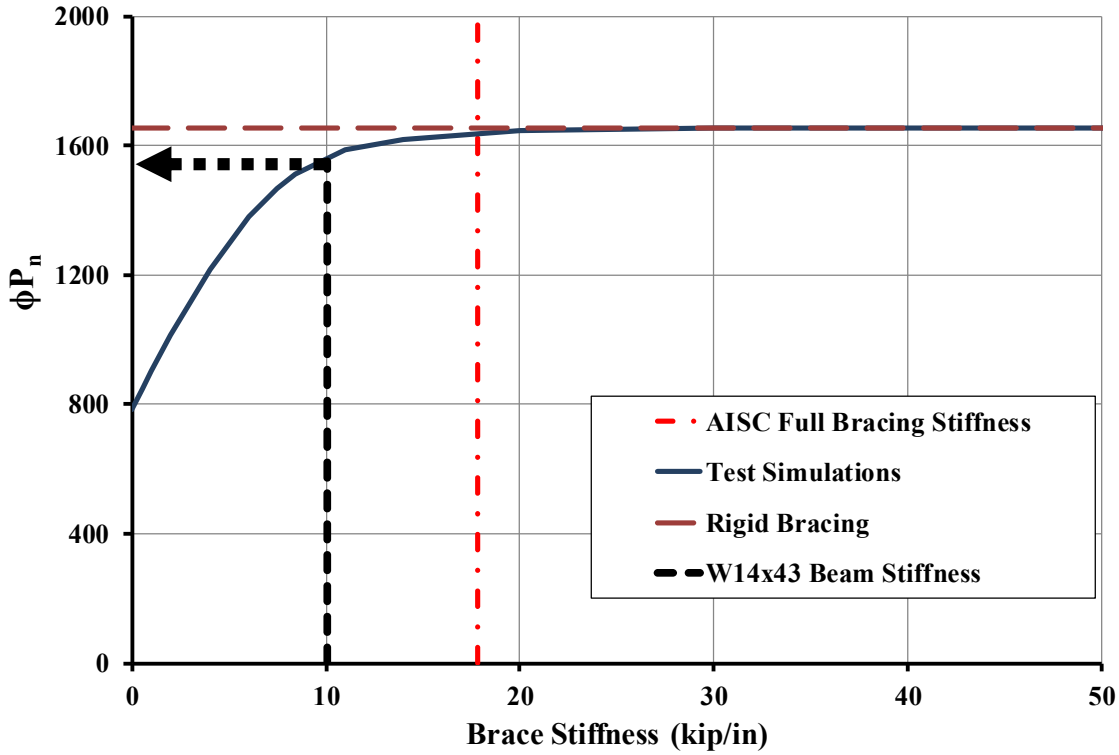

Figure 118. Brace Stiffness vs Axial Strength Curve (knuckle curve) for W14x145 column verus the reduced flying beam bracing stiffness of 0.9 x 0.877 x the nominal brace stiffness.

Therefore, it can be concluded that the W14x43 flying beam brace is indeed sufficient to develop both the applied axial load of P_u = 1400 kips in this problem, as well as the fully-braced column capacity of $\phi_c P_n$ = 1519 kips. The corresponding brace strength requirement is larger than the traditional Appendix 6 value of 1.0 %, but is well within the factored strength provided by the W14x43 beam.

6.3 Comprehensive Metal Building Frame Example

6.3.1 *Geometry*

Figure 119 shows the geometry of a representative interior frame of a clear-span building with a large span-to-eave height. The frame is symmetric about its ridge. Only its left half of is shown in the figure. The frame has a 180 ft span outside-to-outside between the outset girt lines, a 20 ft eave height and a roof slope of 0.5/12. Unless noted otherwise, the dimensions shown in the figure are to points along the outside edge of the column and roof girder webs, which are referred to as the design axes. These axes are employed as a primary reference for describing the geometry. The frame is assumed to have ideally simply-supported base conditions. That is, the frame analysis model assumes perfect pins at the centroid of the member cross-sections at the column bases. The locations where the girts and purlins are attached to the outside flanges are taken as braced points in the out-of-plane direction. In addition, twisting of the frame members is assumed to be prevented (i.e., both flanges are assumed to be braced in the out-of-plane direction) at the column bases and at the locations having diagonal braces between the purlins and the inside flanges. The diagonal braces are indicated by bold dashed lines in the figure. It should be noted that the roof girder outside flange is braced at a purlin location that falls within the width of the panel zone region. Table 6 lists the cross-section geometries of the frame. All of the web depths are measured perpendicular to the design axes.

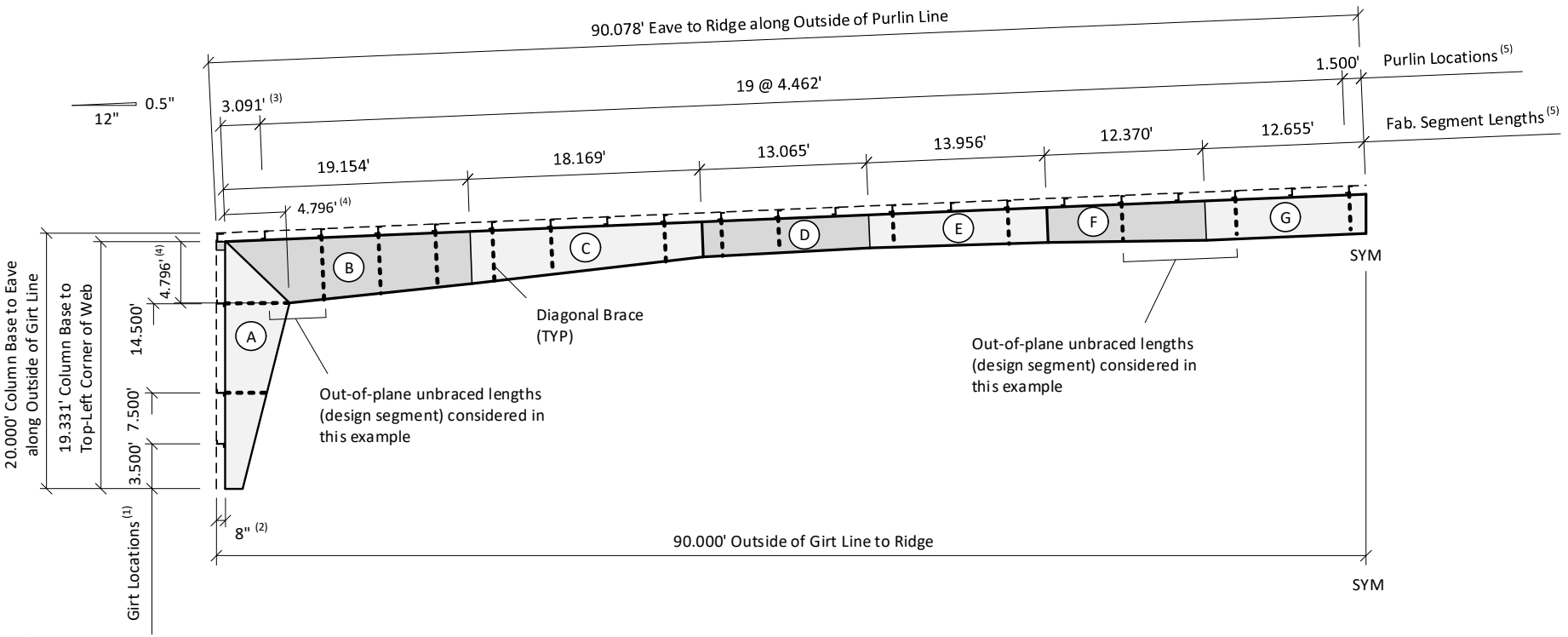

Footnotes:

(1) The girt locations are measured from the bottom of the column base plate to the bottom of the corresponding clip.
(2) The outset girts and purlins are 8 in. deep. The corresponding distance to the outside edge of the column web is 8.5 in.
(3) The first purlin location is measured from the top-left corner of the column web to the left side of the corresponding clip.
(4) The dimension shown is the length along the outside edge of the web, measured from the top-left corner to a line perpendicular to the design axis passing through the intersection of the inside edges of the webs of Segments A and B (i.e., the inside corner of the panel zone at the knee).
(5) The purlin locations and fab. segment lengths are measured on-slope along the top edge of the roof girder web.

Figure 119. Geometry of clear-span building frame with a large span-to-eave height

Table 6. Cross-section geometry of clear-span building frame with a large span-to-eave height.

Fabrication Segment	Length (ft)	Outside or Top Flg. b_f x t_f (in.)	t_w (in.)	Inside or Bottom Flg. b_f x t_f (in.)	Starting Web Depth h (in.)	Ending Web Depth h (in.)
A	19.231	10 x 0.50	0.50	10 x 0.50	16	60
B	19.154	10 x 0.375	0.3125	10 x 0.75	60	49
C	18.169	10 x 0.375	0.3125	10 x 0.50	49	33
D	13.065	6 x 0.375	0.2188	6 x 0.625	33	31
E	13.956	6 x 0.625	0.1875	6 x 0.375	31	33
F	12.370	8 x 0.75	0.1875	8 x 0.25	33	37
G	12.655	8 x 0.75	0.1875	8 x 0.25	37	37

At the knees of the frame in the structural analysis model, the edges of the panel zone and the ends of the physical members are taken as the cross-sections perpendicular to the design axes at the intersection of the inside edges of the webs of fabrication segments A and B, i.e., the inside corner of the panel zone at the knees. (The term “fabrication (fab.) segment” is employed in this example to refer to member lengths between changes in the web thickness, web taper angle and/or flange plate dimensions.) The web and flange plates of the column and of the roof girder are extended into the panel zone from the ends of the physical members to the point of intersection of the member shear center axes. The webs are arbitrarily taken as 60 in. deep within these short lengths. The finite size and deformation characteristics of the panel zones are not otherwise considered in the analysis model. This approach is consistent with the commonly employed frame analysis idealization in which the frame member representations are extended to the point where the member reference axes intersect, without directly modeling the responses within the finite-size panel zones. Nodes are positioned at the above defined location of the panel

zone edges and ends of the physical members. This facilitates the calculation of the member internal forces at these locations.

As stated above, the frame element reference axes are taken as the shear center axes within the SABRE2 software employed for these studies. The shear center is the natural reference axis for the modeling of three-dimensional member responses involving torsion. The influence of the offset of the cross-section centroid from the shear center axis is fully accounted for within the frame element formulation.

6.3.2 *Loading*

The ASD load combination producing the maximum positive and negative major-axis bending moments in the roof girder is selected to demonstrate the calculations in this example. This is the Dead + Collateral + Roof Live Load (reduced via the tributary area allowance) combination as summarized below:

- The dead plus collateral load is taken as 7.5 psf along the slope of the roof plus the self-weight of the frame.

- The reduced roof live load is taken as 12 psf along the slope of the roof.

The self-weight of the girts and the exterior wall panels, as well as other miscellaneous steel weight, is accounted for within the dead load allowance applied to the roof. The self-weight is calculated in the structural analysis based on the frame element lengths and areas in the analysis model.

The subject frame is symmetric about its ridge, and the above critical loading is symmetric about the ridge. The frame is modeled using an explicit initial out-of-plumbness of 1/500 to the right. That is, all the nodes of the analysis model are shifted by y/500 to the right, where y is the height above the base. The selected load combination is gravity-only. For gravity-only load combinations, the *Specification* requires the consideration of overall (out-of-plumbness) frame imperfections. The selection of out-of-plumbness to the right is arbitrary. Both the left and the right halves of the frame must be designed for the same maximum load effects.

The frame is evaluated under ultimate strength conditions using the general purpose second-order analysis capabilities with SABRE2. To represent the ultimate strength conditions, the second-order analysis is conducted at 1.6x the above specified ASD loadings. The resulting internal forces are divided by $\alpha = 1.6$ to determine the corresponding ASD required internal forces.

In summary, the loadings applied to the frame are as follows:

- As noted in the previous section, the frame in this example is an interior frame. The spacing between the frames in the out-of-plane direction is 25 ft. As such, the resulting purlin loads (ASD) are 2.175 kips downward with the exception of the purlins adjacent to the eave struts and the ridge.

- At the purlins adjacent to the eave struts, the resulting load is 2.007 kips downward, and at the purlins adjacent to the ridge, the resulting load is 1.819 kips downward.

- The corresponding load at the eave struts is 0.919 kips. The location of the eave struts is approximated as the outside of the building envelope for these calculations.

- A resultant moment of 0.919 kips x (8.5 in. + 29.922 in.) = 35.31 kip-in is applied at the intersection of the column and roof girder shear center axes, which is located 29.922 in. from the outside edge of the column web. This moment accounts for the position of the eave strut relative to the intersection of the frame element shear center axes.

- The above loads, as well as the steel self-weight (0.0002836 kip/in^3), are multiplied by α = 1.6 for the second-order analysis of the ultimate strength condition. The resulting internal forces are subsequently divided by 1.6 to obtain the ASD required internal forces. As such, the above loads corresponding to the ultimate strength condition are 3.482 kips, 3.211 kips, 2.910 kips, 1.471 kips, 56.52 kip-in, and 0.0004537 kip/in^3.

The total self-weight of the steel included in the structural analysis is 14.1 kips (a total factored load of 1.6 x 14.1 = 22.6 kips) based on the frame element lengths and areas in the structural analysis model. The actual weight of the frame and its miscellaneous steel is 15.6 kips (a factored weight of 25.0 kips). The difference between these loads is largely due to additional steel within the joint regions that is not included directly in the structural analysis model, as well as the weight of multiple end-plate splice connections. As noted above, this additional dead load is accounted for within the roof dead load allowance.

The sum of the factored vertical reactions from the structural analysis, equal to the total applied vertical load, is 162.9 kips.

The frame tends to sway to the right under the above load combination. As such, the frame is modeled using an explicit initial out-of-plumbness of 1/500 to the right. That is, all the nodes of the analysis model are shifted by y/500 to the right, where y is the height above the base. The selected load combination involves gravity load only. For gravity-only load combinations, the Specification requires the consideration of overall (out-of-plumbness) frame imperfections.

6.3.3 *Frame Analysis Discretization*

For the Inelastic Nonlinear Buckling Analysis (INBA) to determine the required ASD internal forces, a minimum of four frame elements is employed within each of the unbraced lengths as shown in Fig. **119**, Steps in the member cross-section geometry are represented by a short length in which the element cross-section is tapered from one geometry to the other. The corresponding analysis model is shown in Fig. 120. The nodal locations of the model are indicated by the dark circular symbols within the web depths. The frame analysis formulation employed for this study uses the cross-section shear centers as the reference axes; therefore, the nodes and the lines drawn between them, represent the variation of the shear center along the member lengths.

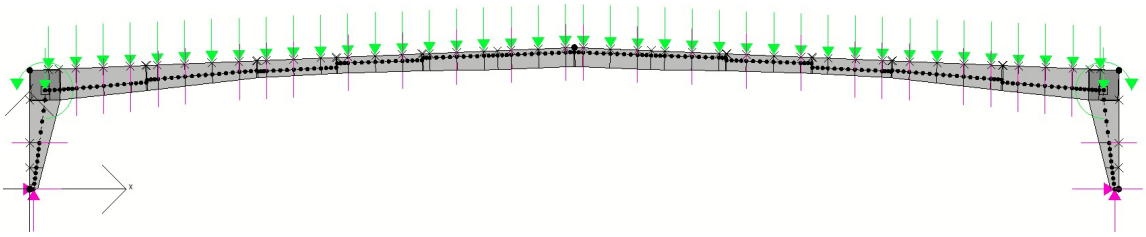

Figure 120. Frame analysis discretization of clear-span building frame with a large span-to-eave height.

The columns are represented by four segments below the inside corner of the panel zone at the knees, plus one additional segment within the panel zone. Correspondingly, the roof girder is represented on each side of the ridge with elements between the inside corner of the panel zone at the knees and the ridge, plus one additional element within the panel zone. There are four locations within each half-span of the roof girder that have a discrete change in the cross-section geometry. One can observe a significant shift in the shear center associated with these cross-section transitions between fabrication segments B and C, C and D, D and E and E and F in the roof girder (see Fig. **119** for the segment designations).

The concentrated loads from the purlins are applied at the top of the roof girder in the structural analysis model, at an offset from the frame element reference axes. The concentrated load from the eave strut, and the corresponding statically equivalent moment associated with the offset of the eave strut from the member shear center axes, are applied at the intersection of the column and roof girder shear center axes.

6.3.4 *Summary of Results*

The frame is evaluated using an Inelastic Nonlinear Buckling Analysis based on the AISC (2016) current Specification (INBA) as well as an Inelastic Nonlinear Buckling Analysis using the recommended equations by Subramanian et al. (2018) and Chapter 3 of this dissertation (INBA*). When INBA is conducted using the current equations the corresponding Load Proportionality Factor (LPF) is obtained as 0.800, and this load level is governed by the limit state of Tension Flange Yielding (TFY). When the recommended equations are used for the analysis, the governing limit state becomes cross-section yielding under flexure, which is given by the $\phi_b M_{yct}$ moment (Eq. (56)). The LPF value for INBA*

is equal to 0.958. This is a 19.8% increase in the strength of the overall frame. Similar increases in the resistances also are observed in the validation studies presented in the Section 4.1.3, when the recommended calculations are employed for members

The results are discussed first for the INBA solution. The mode shape obtained from the buckling analysis using INBA is provided in Fig. 121 and involves in-plane sidesway buckling. However, the maximum strength of the frame is governed by TFY; this sidesway buckling occurs at a higher load level than that corresponding to the critical TFY check.

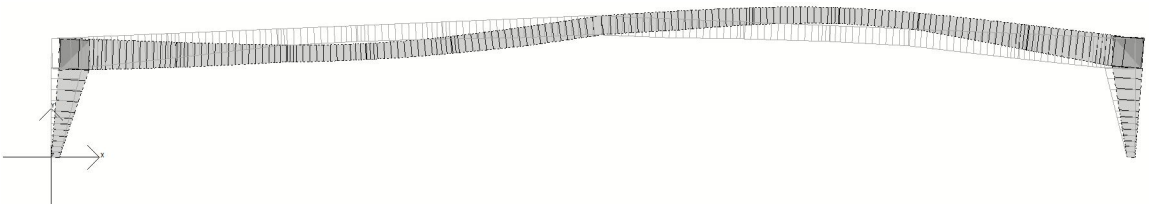

Figure 121. INBA buckling mode shape (3D rendered geometry)

A line representation of the buckling mode shape is helpful to convey the behavior (Fig. 122). The sidesway deflection is more apparent using the line representation of the deflected shape.

Figure 122. INBA buckling mode shape (line representation)

The critical cross-section of the frame, and the overall criticality of the cross-section checks throughout the frame, can be evaluated by plotting the Unity Check (UC) values of

each cross-section. For this purpose SABRE2 provides UC graph, that provides corresponding value at each of the five Gauss-Labatto integration points within each of the frame elements. The UC plot for the INBA solution is shown in Fig. 123. It can be observed from this figure that the critical section is a section just to the left of the ridge, where UC value is equal to 1.0. The fact that the maximum UC value is equal to 1.0 indicates that a cross-section limit state governs the member capacity at this location.

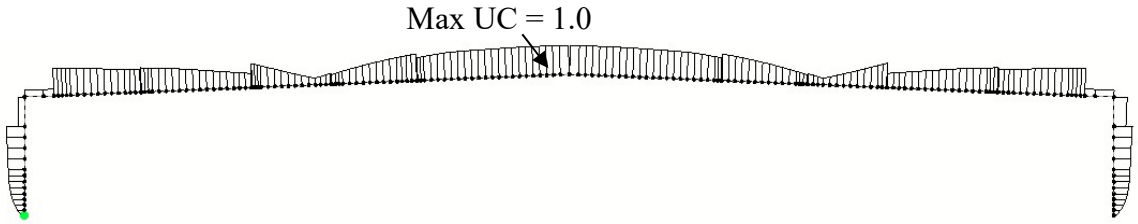

Figure 123. Cross-section unity checks (UC) throughout the frame for INBA

The moment and axial force diagrams at the maximum strength condition per the INBA are provided in Figs. 124 and 125. The bending component of the UC equation (Eq. (58)) consists of the moment and the bending resistance of the corresponding cross-section. Although the maximum bending resistance of the cross-sections ($\phi_b M_{max}$) (Fig. 126) and the maximum moment are detected near the knee joint, the critical cross-section is detected near the ridge location. The critical cross-section which is limited by the Tension Flange Yielding (TFY) limit state is Fab. Segment G from Table 6. According to the cross-section properties, the section is singly symmetric with $S_{xc}/S_{xt} > 1$ ratio. This section is the critical section associate with the governing TFY failure.

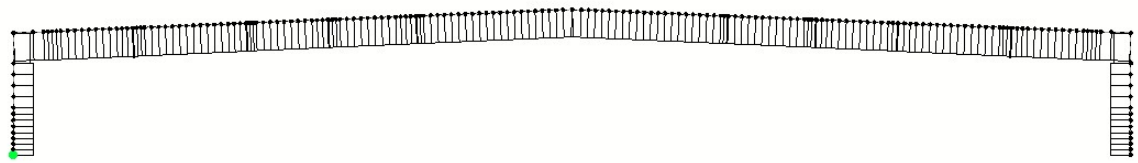

Figure 124. Axial force diagram

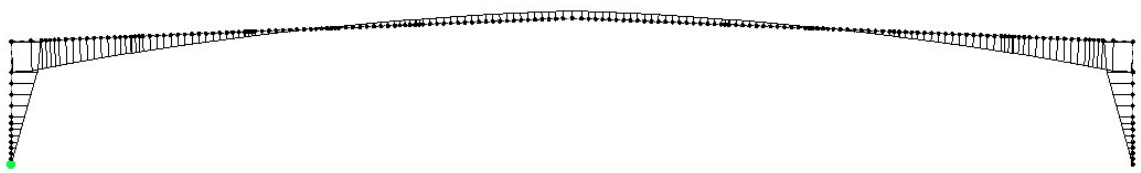

Figure 125. Moment diagram

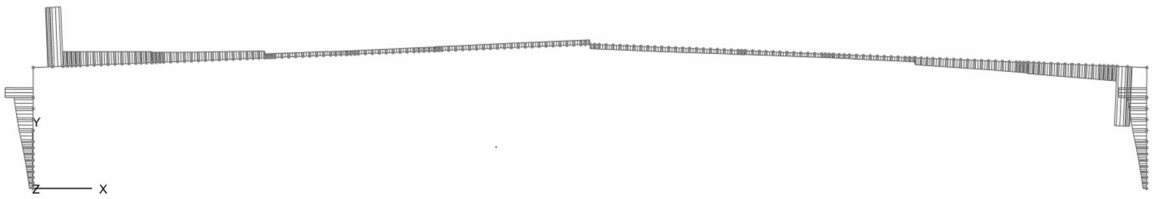

Figure 126. $\phi_b M_{max}$ diagram

Based on the INBA* solution, the maximum resistance is governed by cross-section yielding under flexure, which is equal to the $\phi_b M_{yct}$ moment (Eq. (56)). The UC plot for this solution is presented in Fig. 127. This figure indicates that the critcal cross-section changes to the section next to the right knee of the frame. This cross-section is section C from Table 6, with $S_{xc}/S_{xt} > 1$. The top flange is in tension at this location.

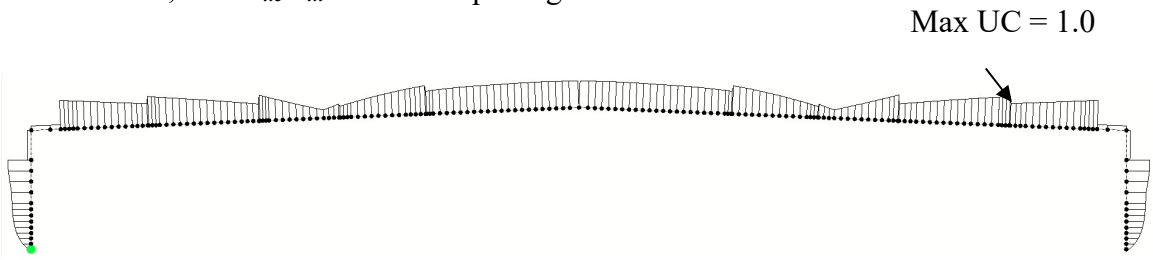

Figure 127. Cross-section unity checks (UC) throughout the frame for INBA*

From the INBA* solution, the buckling mode shape changes as well. While INBA indicates a sidesway buckling mode, INBA* indicates out-of-plane buckling for the critical buckling mode (Fig. 128). A top-view of the frame is shown in this figure using the line representation for drawing the buckled shape.

Figure 128. Frame deflected shape from buckling analysis for INBA*- top view (line representation)

The in-plane deflected shape from the INBA* load-deflection analysis at the strength condition is shown in Fig. 129. The INBA deflected shape at its strength condition is similar. These deflected shapes are both dominated by the vertical displacement of the roof girder at the ridge.

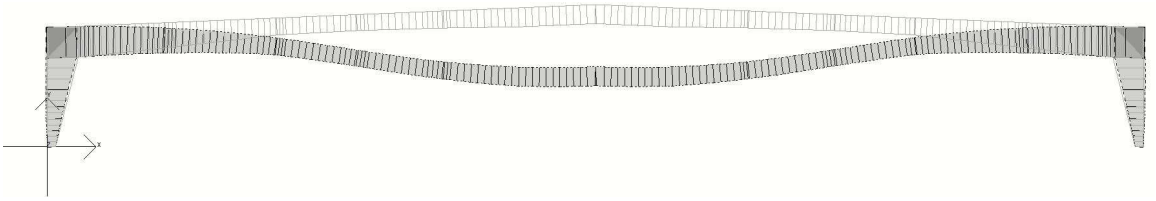

Figure 129. INBA* deflected shape at the strength condition (3D rendering) (scale factor = 5)

CHAPTER 7. CONCLUSIONS

In this chapter, the key contributions of the research are discussed. The future work is provided after the discussion of the contributions.

7.1 Key Contributions of This Research

The primary contributions of this research are as follows:

1) Stiffness Reduction Factors (SRF) for beams and beam-columns are developed based on the AISC (2016) Specification equations and recommended improvements to these equations. These SRFs can be employed for a proper configuration of a buckling analysis to determine the maximum buckling strength of columns, beams, and beam-columns directly. This analysis also rigorously accounts for restraints coming from bracing and bracing and unbraced length end conditions, without the need to separately evaluate the resistances using the AISC design strength equations. In addition to the beam and beam-column SRFs, column SRF (τ_a) for cross-sections that have slender elements are also presented. Basically, the effective area is used to reduce the SRF to account for the slenderness of the column.
2) Improved characterization for Flange Local Buckling (FLB) and Tension Flange Yielding (TFY) are provided. The updates provided in this research show promise to remove significant conservatism in the Flange Local Buckling (FLB) and Tension Flange Yielding (TFY) provisions of the current AISC (2016) Specification in certain cases. The FLB limit state check is improved by

implementing a form of the unified effective width approach (Peköz (1986)), which recognizes the postbuckling resistance of slender flange elements. For the TFY limit state, simple calculations is derived from mechanics of materials concepts, recognizing the ability of the region in flexural tension to develop extensive spread of yielding through the web.

Supporting contributions of this research are as follows:

1) Beam-column interaction curves are proposed to be linear when the section has slender plates under axial compression, or noncompact or slender plates under flexural compression. In the validation studies presented in Chapter 4, shows that for these types of section, the interaction between beam and column resistance is basically linear. Since the SRFs are basically derived from the Specification equations, using the bilinear curve for these members would result in unconservative estimates with Inelastic Buckling Analysis (INBA). Using the linear interaction curve shows a better correlation with test simulation strength.
2) Employing the above improvements along with the recommendations provided by Subramanian et al. (2018), an updated version of the Unified Flexural Resistance Equations are provided.
3) Validation and demonstration are performed using the all improvements explained with previous contributions. Doubly and singly symmetric prismatic and nonprismatic members are used. For the consideration of the TFY limit state improvement, moment-shear interaction is also observed.
4) A software framework of the key contributions is provided. The software, SABRE2, can perform Inelastic Buckling Analysis using the both current AISC

(2016) (INBA) or recommended equations provided in Section 0 (INBA*). The Software framework can analyze structure (members or frames) that are using:

a. Single and multiple web taper,
b. Steps in the cross-section geometry,
c. Double- and single-symmetry of the member cross-sections, and
d. Any combination of compact, noncompact and slender flanges and webs.

5) Three examples using the INBA with the above recommendations are provided. These examples aim to explain the key concepts with advanced design evaluation of members and framing systems, including the design of stability bracing.

7.2 Recommendations for Future Work

The future work recommendations below are recommended based on this research:

- The current modeling of joints in SABRE2 software is quite simplistic. Beam-to-column joints are usually modeled as infinitesimal size points. These models do not include sufficient detail to allow for complete assessment of the out-of-plane stability of the joint. In many programs, in the vicinity of the elements coming into the joint are commonly assumed located at the centroidal or mid-depth of the frame members coming into joint (i.e. girt, eve strut, bracing conditions etc.). However, to properly assess the out-of-plane stability of a joint, and model the joint location considering all its attributes, all the components need to be modeled at their actual position within the geometry of the joint.
- Further investigation of the innovative application of the INBA procedures for bracing design, and member design accounting for continuity across brace points

is needed. A study should be conducted to evaluate better the benefits gained by recognizing these sources of enhanced resistance.

- Better modeling of joint base conditions, both in-plane as well as the restraint to out-of-plane member buckling offered from the column bases is required for a complete assessment of the end restrains, and their effects on the buckling load level (Γ).
- SABRE2 currently accommodates only one load combination definition at a time. It would be desirable to provide a fully integrated graphical interface in SABRE2 that accommodates the solution for the multiple load combinations. Some widgets for implementing this feature are currently set in the program, but this tool needs to be enhanced to solve for hundreds of load combinations. SABRE2 needs to be enhanced to accommodate realistic design situations involving large numbers of load combinations.
- For given geometry, end restrains, bracing, and the applied load, SABRE2 currently provides a load level (Γ) that the structure is able to carry most. In fact, rather than solving for the buckling load for a given set of bracing stiffnesses, one can consider a given LRFD applied factored loading (with $\Gamma = 1$) and then solve for the required bracing stiffnesses necessary to develop the critical buckling strength equal to this factored load level. These bracing stiffnesses are commonly referred to as the *ideal bracing stiffness* values, β_i, corresponding to a given desired load level P_u. This ideal bracing application is prototyped in shell FEA program, SINBAD (White and Bishop 2014), by the author for member applications.

APPENDIX A.TEST SIMULATION PROCEDURES

In this dissertation, test simulation solutions based on AISC (2016) Appendix 1.3, using reduced residual stresses and geometric imperfections from commonly employed values, are employed as the "gold standard" for evaluation of the results from the recommended DM solutions using INBA as well as the solutions from routine DM solutions. This type of test simulation solution is denoted by Appendix 1.3*. In addition, the terms INBA* and DM* highlight the fact that these solutions are based on modified AISC 2016 flexural resistance equations using the recommendations from Section 3.1 and 3.2, and recommendations per Subramanian et al. (2018). In the following subsections, the attributes of the AISC Appendix 1.3* calculations employed in this study are detailed.

A.1. Finite Element Model

The ABAQUS 6.13 (Simulia 2014) finite element analysis software is employed to model the members considered in this section. In all cases, a full nonlinear shell finite element solutions using the S4R element is used to model for both webs and flanges. The S4R is a four-node quadrilateral large strain shell element formulation. The mesh is generated with 12 elements for the width of the flanges, and 20 elements for the web depth. The shell element aspect ratio is chosen approximately 1.0 in the web to calculate the number of the elements along the member lengths.

A.2. Material Properties

Homogenous material properties are used for all the members with the yield stress (F_y) of 50 ksi, and the modulus of the elasticity (E) of 29,000 ksi. The material properties

F_y and E are multiplied by 0.9, as required by AISC 2016 Appendix 1.3. The factored properties are denoted by F_y* and E*. For the yield plateau of the material, the tangent stiffness is modeled as E/1000 up to ten times the yield strain (ε_y). After this point, the strain hardening modulus is taken as E/50. At the levels of the strains that are observed in the test simulations, true stress versus log strain and engineering stress versus engineering strain are essentially the same.

A.3. Residual Stresses

Residual stress patterns of one-half the commonly-assumed Lehigh pattern (Galambos and Ketter 1959) for rolled sections and the Best-fit Prawel (Kim 2010) pattern for welded sections are provided in Figs. 130 and 131. These residual stresses are recommended by Subramanian and White (Subramanian and White 2016) as appropriate values necessary for close correlation with lateral torsional buckling experimental test results.

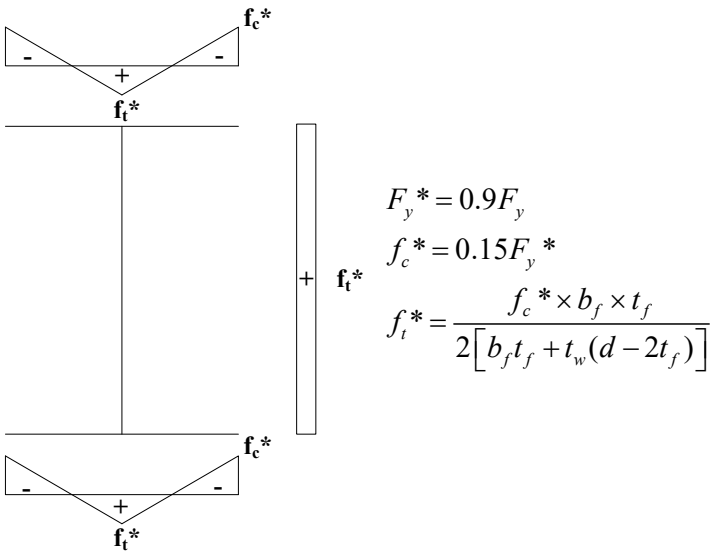

Figure 130. One-half of lehigh residual stress pattern, for rolled I-sections

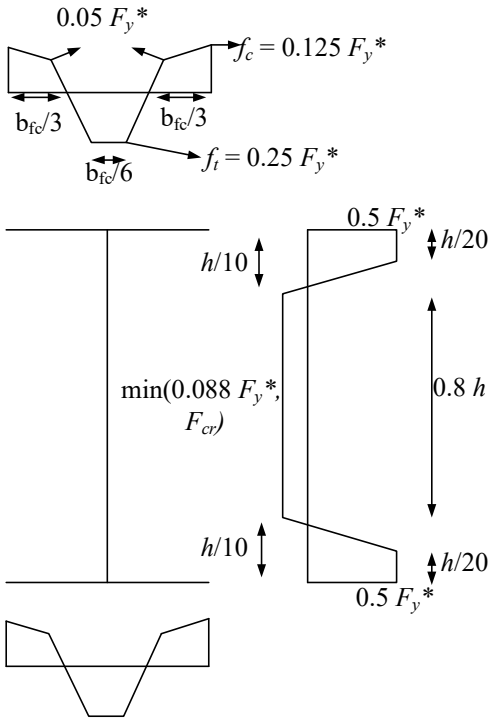

Figure 131. One-half of best-fit prawel residual stress pattern, for welded I-sections

A.4. Geometric Imperfections

The test simulations are based on out-of-straightness patterns with one-half of the AWS (2010)/AISC Code of Standard Practice (COSP) geometric imperfection tolerance values unless noted otherwise. Subramanian and White (2017a) show that these reduced geometric imperfections are necessary for close correlation with experimental results.

Flange tilt and web out-of-flatness patterns are obtained by elastic eigenvalue buckling analysis of the members with the out-of-plane displacements restrained at the top and bottom flange-web juncture points, and with the members being subjected to uniform axial compression. Given the resulting buckling modes, the flange tilt and web-out-flatness are isolated and scaled to one-half the tolerance values as illustrated in Fig. 132

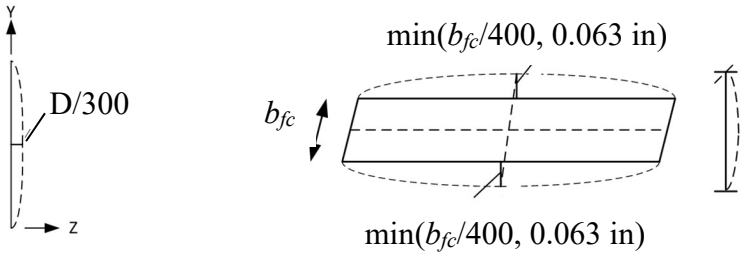

Figure 132. Web out-of-flatness and flange tilt imperfection

The resulting flange tilt and web out-of-flatness imperfections are combined with a flange sweep that is applied at web-flange juncture points. If the flange under consideration is subjected to flexural compression, a sinusoidal flange sweep is applied to the flange in flexural compression. For a flange that is in flexural tension, zero sweep ($IF = 0$) is applied if the net force in the flange is tension (Fig. 133). Otherwise a flange sweep between zero to $L_b/2000$ is applied as a linear function of IF. This handling of the sweep in flexural tension is illustrated by the IF factor shown in Fig.

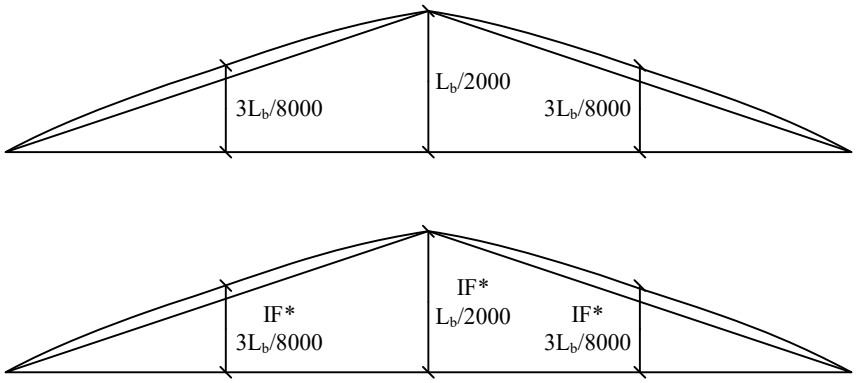

Figure 133. Applied imperfections (one-half of the AWS/AISC COSP flange sweep tolerance)

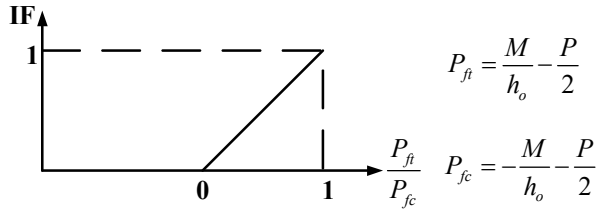

Figure 134. IF (tension flange sweep scale factor) calculation

REFERENCES

AASHTO (2005). AASHTO LRFD Bridge Design Specifications. 3th Edition. Washington, DC, American Association of State Highway and Transportation Officials.

AASHTO (2017). AASHTO LRFD Bridge Design Specifications. 8th Edition. Washington, DC, American Association of State Highway and Transportation Officials.

Abe, H. and N. Mizukoshi (1973). "Buckling tests on plate girders under bending." Annual Meeting of the Japanese Society of Civil Engineers, preprint(Japan Society of Civil Engineers, Tokyo).

AISC (2002). "Example Problems Illustrating the Use of the New Bracing Provisions – Section C3, Spec andCommentary." Ad hoc Committee on Stability Bracing, November.

AISC (2005). Specifications for Structural Steel Buildings, ANSI/AISC 360-05. Chicago, IL, American Institute of Steel Construction.

AISC (2010). Specifications for Structural Steel Buildings, ANSI/AISC 360-10. Chicago, IL, American Institute of Steel Construction.

AISC (2016). Code of Standard Practice for Steel Buildings and Bridges, AISC 303-16. Chicago, IL, American Institute of Steel Construction.

AISI (2012). North American Specification for the Design of Cold-Formed Steel Structural Members, ANSI/AISI S100-12. Washington, DC, American Iron and Steel Institute.

AISI (2016). North American Specification for the Design of Cold-Formed Steel Structural Members, ANSI/AISI S100-16. Washington, DC, American Iron and Steel Institute.

ASCE/WRC (1971). Plastic Design in Steel. ASCE Manual 41. , The Welding Research Council and the American Society of Civil Engineerins, 2nd ed.

AWS (2010). Structural Welding Code–Steel, AWS D1.1: D1.1M, 22nd ed, AWS Committee on Structural Welding.

Basler, K., B. T. Yen, J. A. Mueller and B. Thurlimann (1960). Web Buckling Tests on Welded Plate Girders. WRC Bulletin No. 64. New York, NY., Welding Research Council**:** 63.

Basler K. (1961). "Strength of plate girders in shear." Journal of Structural Division **87(7)**: 151-180.

Carskaddan, P. S. (1968). "The bending behavior of slender-web girders with A514 steel flanges." Applied Research, Rep. No. 57.019-904 (5) (AS-EA-23-ps), U.S. Steel Corporation, Pittsburgh.

CEN (2005). Design of Steel Structures, Part 1-1: General Rules and rules for buildings, EN 1993-1-1:2005:E, Incorporating Corrigendum February 2006. Brussels, Belgium, European Committee for Standardization.

Chang, C. J. (2006). Construction Simulation of Curved Steel I-Girder Bridges. PhD, Georgia Institute of Technology.

Collette, A. (2008). "HDF5 for Python <http://h5py.alfven.org>."

Daley, A. J., D. B. Davis and D. W. White (2016). "Shear Strength of Unstiffened Steel I-Section Members." Shear Strength of Unstiffened Steel I-Section Members **143**(3).

Dibley, J. E. (1969). "Lateral Torsional Buckling of I-Sections in Grade 55 Steel." Proceedings of the Institution of Civil Engineers **43**(Aug): 599-&.

Dibley, J. E. (1970). A Preliminary Investigation into the Use of High Strength Structural Steel in Structures Designed Plastically. BIRSA Open Report EG/A/13/70. London, British Steel Corporation**:** 25.

Disque, R. Q. (1973). "Inelastic K-factor for column design." Engineering Journal, AISC **10(2)**: 33-35.

Fletcher, M. and R. Liebscher (2005). the Python OpenGL binding <http://pyopengl.sourceforge.net>.

Galambos, T. V. and R. L. Ketter (1959). "Columns Under Combined Bending and Thrust." Journal of the Engineering Mechanics Division, ASCE **85**(EM2): 135-152.

Geschwindner, L. F. (2010). "A Case for a Single Stiffness Reduction Factor in the 2010 AISC Specification." Engineering Journal (New York) **47(1)**: 41-46.

Greiner, R. and P. Kaim (2001). Comparison of LT-Buckling Design Curves with Test Results, ECCS TC8, Report 23**:** 23.

Griffis, L. and D. W. White (2013). "Stability Design of Steel Buildings, AISC Design Guide 28." American Institute of Steel Construction, Inc. Chicago, IL.: 175 pp.

Hajjar, J. F. and D. W. White (1997). "Effective Length Approaches,." Chapter 2 of Effective Length and Notional Load for Assessing Frame Stability: Implications for American Steel Design, Technical Committee on Load and Resistance Factor Design, Task Committee on Effective Length, ASCE, pp. 33-129.

Häring G. (2006). "sqlite3 <https://docs.python.org/3.7/library/sqlite3.html>."

Hash, J. B. (2001). Shear Capacity of Hybrid Steel Girders. MS Thesis M.S. Thesis, University of Nebraska.

Holtz, N. M. and G. L. Kulak (1973). Web Slenderness Limits for Compact Beams. Structural Engineering Report No 43. Alberta, Canada, University of Alberta**:** 41 pp.

Holtz, N. M. and G. L. Kulak (1975). Web Slenderness Limits for Non-compact Beams. Structural Engineering Report No 51. Alberta, Canada, University of Alberta**:** 41 pp.

Janss, J. and C. Massonnet (1967). "The Extension of Plastic Design to Steel A52." Publications of the IABSE **27**: 15-30.

Jeong, W. Y. (2014). Structural analysis and optimized design of general nonprismatic I-section members. PhD, Georgia Institute of Technology.

Johnson, D. L. (1985). An investigation into the interaction of flanges and webs in wide flange shapes. Proc., Annual Technical Session, Structural Stability Research Council, U. Univ. of Missouri-Rolla, Rolla, Mo.**:** 395–405.

Jones, E., T. E. Oliphant, P. Peterson and others. (2001). "SciPy: Open Source Scientific Tools for Python , http://www.scipy.org/ [Online; accessed 2018-11-09]."

Kim, Y. D. (2010). Behavior and Design of Metal Building Frames Using General Prismatic and Web-Tapered Steel I-Section Members Doctoral Dissertation, Georgia Institute of Technology.

Kucukler, M., L. Gardner and L. Macorini (2015a). "Lateral Torsional Buckling Assessment of Steel Beams Through a Stiffness Reduction Method." Journal of Constructional Steel Research **109**: pp. 87-100.

Kucukler, M., L. Gardner and L. Macorini (2015b). "Flexural-Torsional Buckling Assessment of Steel BeamColumns Through a Stiffness Reduction Method." Engineering Structures **101**: pp. 662-676.

Lew, H. S. and A. A. Toprac (1968). "The static strength of hybrid plate girders." Structures Fatigue Research Laboratory, Dept. of Civil Engineering, Univ. of Texas, Austin, Texas **S.F.R.L. Technical Rep. No. P550-11**.

Lokhande, A. M. (2014). Evaluation of Steel I-Section Beam and Beam-Column Bracing Requirements by Test Simulation. Master of Science, Georgia Institute of Technology.

MathWorks Inc. (2016). MATLAB R2016b : the language of technical computing : computation, visualization, programming Natwick : Math Works Inc., 2016.

McDermott, J. F. (1969). "Plastic Bending of A514 Steel Beams." Journal of the Structural Division, ASCE **95**(9): 1851-1871.

Oliphant, T. E. (2006). A guide to NumPy. USA, Trelgol Publishing.

Peköz, T. (1986). "Development of a Unified Approach to the Design of Cold-formed Steel Members." International Specialty Conference on Cold-Formed Steel Structures.

Prado, E. (2014). Assessment of Basic Steel I-Section Beam Bracing Requirements by Test Simulation. Master of Science, Georgia Institute of Technology.

Python Software Foundation (2018). "Python Language Reference, version 3.7 <http://www.python.org>."

Riverbank (2018). PyQT5 v5.11.2 Reference Guide <http://pyqt.sourceforge.net/Docs/PyQt5/>.

Salmon, G. S., J. E. Johnson and F. A. Malhas (2009). Steel Structures Design and Behaviour Emphasizing Load and Resistance Factor Design, 5th Edition. Upper Saddle River, NJ, Pearson Education, Inc.

Seif, M. and B. W. Schafer (2009). Finite Element Comparison of Design Methods for Locally Slender Steel Beams and Columns. SSRC Annual Stability Conference. Phoenix, AZ. .

Simulia (2014). ABAQUS/Standard Version 6.14-2. Providence, RI, Simulia, Inc.

Smith, M. D., A. K. Turner and C.-M. Uang (2013). Experimental study of cyclic lateral-torsional buckling of web-tapered I-beams. Department of Structural Engineering University of California, San Diego**:** 268 pp.

Smith, S. T. (2006). MATLAB Advanced GUI Development. Indianapolis, IN, Dog Ear Publishing.

Subramanian, L. P. (2015). Flexural Resistance of Longitudinally Stiffened Plate Girders Doctoral Dissertation, Georgia Institute of Technology.

Subramanian, L. P., W. Y. Jeong, R. Yellepeddi and D. W. White (2018). "Assessment of I-Section Member LTB Resistances Considering Experimental Test Data." Engineering Journal **55**: 15-44.

Subramanian, L. P. and D. W. White (2016). "Resolving the Disconnect between I-Section Member Lateral Torsional Buckling Resistance Equations and Test Simulation Results." Submitted for Consideration by the Journal of Constructional Steel Research.

Subramanian, L. P. and D. W. White (2017a). "Resolving the disconnects between lateral torsional buckling experimental tests, test simulations and design strength equations." Journal of Constructional Steel Research **128**: 321-334.

Subramanian, L. P. and D. W. White (2017b). "Reassessment of the Lateral Torsional Buckling Resistance of I-Section Members: Uniform-Moment Studies." Journal of Structural Engineering **143**(3): 04016194.

Subramanian, L. P. and D. W. White (2017c). "A Reassessment of the Lateral Torsional Buckling Resistance of Rolled I-Section Members – Moment Gradient Tests." Journal of Structural Engineering, ASCE **143**(4).

Subramanian, L. P. and D. W. White (2017d). Flexural Resistance of Longitudinally Stiffened Plate Girders. Updated Report to AASHTO and AISI. School of Civil and Environmental Engineering, Georgia Institute of Technology, January, 392 pp. .

Subramanian, L. P. and D. W. White (2017e). "Improved Noncompact Web-Slenderness Limit for Steel I-Girders." Journal of Structural Engineering **143**(4): 04016216.

The QT Company. (2018). "QT Designer v5.11 <https://www.qt.io/edu/>." v5.11.

Toğay, O. and D. W. White (2017). Comprehensive Stability Design of Steel Members and Systems via Inelastic Buckling Analysis – Beam-Column Validation Studies. Proceedings of the Annual Stability Conference Structural Stability Research Council. San Antonio, TX.

Toğay, O. and D. W. White (2018). Toward the Recognition of Unaccounted for Flange Local Buckling and Tension Flange Yielding Resistances in the ANSI/AISC 360 Specification. Proceedings of the Annual Stability Conference Structural Stability Research Council. Baltimore, Maryland.

Toğay, O., D. W. White and S. Ryan (2018). SABRE2-V2. <white.ce.gatech.edu/sabre>.

Trahair, N. and G. Hancock (2004). "Steel Member Strength by Inelastic Lateral Buckling." Journal of Structural Engineering **130**(1): 64-69.

Trahair, N. S. (2009). "Buckling analysis design of steel frames." Journal of Constructional Steel Research **65(7)**: pp. 1459-1463.

Trahair, N. S. (2010). "Steel cantilever strength by inelastic lateral buckling." Journal of Constructional Steel Research **66(8-9)**: pp. 993-999.

Vlasov, V. Z. (1963). Thin-Walled Elastic Beams. Jerusalem, Published for the National Science Foundation, Washington, D.C., by the Israel Program for Scientific Translations.

White, D. W. (2008). "Unified flexural resistance equations for stability design of steel I-section members: Overview." Journal of Structural Engineering-American Society of Civil Engineers **134**(9): 1405-1424.

White, D. W., G. B. Barker and A. Azizinami (2008). "Shear Strength and Moment-Shear Interaction in Transversely Stiffened Steel I-Girders." Journal of Structural Engineering **134**(9): 1437-1449.

White, D. W. and C. Bishop (2014). "SINBAD." (Aug 3, 2014).

White, D. W. and W. Y. Jeong (2019). "Steel Design Guide 25 Second Edition; Frame Design Using Web-Tapered Members." American Institute of Steel Construction, Inc. Chicago, IL. .

White, D. W., W. Y. Jeong and O. Toğay (2016). "Comprehensive stability design of planar steel members and framing systems via inelastic buckling analysis." International Journal of Steel Structures **16**(4): 1029-1042.

White, D. W., W. Y. Jeong and O. Toğay (2017) "SABRE2-V1 User Manual."

White, D. W. and S.-K. Jung (2008). "Unified Flexural Resistance Equations for Stability Design of Steel I-Section Members: Uniform Bending Tests." Journal of Structural Engineering **134**(9): 1450-1470.

White, D. W. and Y. D. Kim (2008a). "Unified Flexural Resistance Equations for Stability Design of Steel I-Section Members: Moment Gradient Tests." Journal of Structural Engineering **134**(9): 1471-1486.

White, D. W. and Y. D. Kim (2008b). "Unified Flexural Resistance Equations for Stability Design of Steel I-Section Members: Uniform Moment Tests." Journal of Structural Engineering.

Yura, J. A. (1971). "The effective length of columns in unbraced frames." Engineering Journal, AISC, **8(2), 37-42**.

Yura, J. A. (2001). "Fundamentals of Beam Bracing " Engineering Journal **38**: 11-26.

Yura, J. A., T. V. Galambos and M. K. Ravinda (1978). "The bending resistance of steel beams." Journal of Structural Division **104(9)**: 1355-1369.

Ziemian, R. D. and W. McGuire (2016). "Mastan2 V3.5." http://www.mastan2.com/index.html.

VITA

Oguzhan Togay was born on August 18, 1988 in Ankara, Turkey. He received his Bachelor Degree in Civil Engineering in 2010 from Dokuz Eylul University, Izmir, Turkey. He joined to Georgia Institute of Technology with the graduate scholarship awarded by Turkish Ministry of Education in Fall 2012, and received the Master's degree in Civil Engineering in Fall 2013. He worked as a Research Assistant from 2010 to 2012 at Usak University, Turkey. He entered the PhD program at Georgia Institute of Technology in January 2014.

Email: togayoguzhan@gmail.com